DISSERTATION

Commissioning of the New CERN PS Booster Charge Exchange Injection System: Optimising and Automating Transverse Phase Space Painting

Ausgeführt zum Zwecke der Erlangung des akademischen Grades einer Doktorin der technischen Wissenschaften unter der Leitung von

Privatdoz. Dipl.-Ing Dr. techn. Michael Benedikt
E141, Atominstitut
Technische Universität Wien

Dr. Chiara Bracco
CERN, SY-ABT-BTP

eingereicht an der Technischen Universität Wien
Fakultät für Physik

von

Elisabeth Renner
Matrikelnummer 01026129

04/10/2022

Wien, am

Unterschrift Verfasser/in

Kurzfassung der Dissertation

Die LHC Injektoren am CERN wurden im Rahmen des LHC Injectors Upgrade (LIU) Projektes neu ausgerüstet um einen Teilchenstrahl mit hoher Brillianz für das Upgrade des LHCs, den High Luminosity LHC (HL-LHC), bereitstellen zu können. Ein Schwerpunkt dieser Erneuerungen war der Anschluss des neu installierten 160 MeV H$^-$ Linearbeschleunigers Linac4 an den ersten Kreisbeschleuniger in der CERN Beschleunigerkette, den Proton Synchrotron Booster (PSB). Damit wird die Injektionsenergie des Boosters von 50 auf 160 MeV erhöht und der relativistische Faktor $\beta_r\gamma_r^2$ verdoppelt. Dies ermöglicht es, leistungsbeeinträchtigende Raumladungskräfte trotz verdoppelter Strahlbrillanz auf dem gleichen Niveau wie vor dem Upgrade zu halten. Die neuen Systeme wurden im Winter 2020/2021 in Betrieb genommen. Ein wesentlicher Teil der Verbindung zwischen Linac4 und PSB ist das neu installierte 160 MeV Ladungsaustausch-Injektionssystem. In diesem werden während der Injektion die Elektronen des H$^-$ Strahles mittels einer Kohlenstofffolie gestrippt, sodass ein Protonenstrahl in den PSB injiziert wird. Während der Injektion wird der Orbit des PSB lokal in der horizontalen Ebene verändert, um den zirkulierenden Strahl zum injizierten Strahl zu leiten. Bei Variation der Amplitude dieser Orbitbeule während des Injektionsprozesses wird der transversale Abstand zwischen dem injizierten und dem bereits zirkulierenden Teilchenstrahl verändert. Der zeitliche Verlauf des Amplitudenabfalls kann je nach Strahltyp individuell eingestellt werden. Dies beeinflusst die Verteilung der Teilchen im transversalen Phasenraum. Die individuelle Anpassung der Phasenraumverteilung während der Injektion wird *phase space painting* genannt. Diese Technik wird im adaptierten PSB benutzt, um die transversalen Eigenschaften der verschiedenen Strahltypen, welche CERN für die Experimente bereitstellt, zu produzieren.

Diese Dissertation beschäftigt sich mit Lösungsansätzen, um die Inbetriebnahme und den Betrieb des neuen Injektionssystems, sowie die Konfiguration der Injektionsschemata zu optimieren und automatisieren. Im ersten Teil der Arbeit werden selbstkonsistente Vielteilchensimulationen durchgeführt um adäquate Injektionsschemata für die unterschiedlichen Strahltypen auszuarbeiten. Diese wurden während der Inbetriebnahme angewandt und die Simulationen mit den experimentellen Ergebnissen verglichen. Der Fokus dieser Studien liegt dabei auf der Reduktion der Strahlverluste, welche bei der Produktion von Strahltypen mit hoher Intensität ein limitierender Faktor sind.

Der zweite Teil der Arbeit untersucht Anwendungsmöglichkeiten maschinellen Lernens und numerischer Verfahren zur Leistung- und Effizienzsteigerung des neuen Systems. Im Zuge dessen wird die Realisierbarkeit, Injektionsparameter mithilfe numerischer Algorithmen online zu optimieren, demonstriert. Ein Ersatzmodell des Injektionsprozesses wird mittels maschinellen Lernens erstellt und verwendet, um die Leistungsfähigkeit unterschiedlicher Optimierungsalgorithmen offline zu untersuchen. Die Optimierung der Strahldynamik während des Injektionsprozesses wird abschließend durch Untersuchungen zur Regelung der Generatoren der Injektionskickermagnete ergänzt. Diese Studien untersuchen die Parametrisierung und Modellierung komplexer elektronischer Schaltkreise mittels Neuronaler Netzwerke.

Abstract

The CERN injector complex was upgraded within the framework of the LHC Injectors Upgrade project to produce high-brightness beams for the High Luminosity era of the LHC (HL-LHC). A key aspect of this upgrade is the connection of the newly built Linac4 to the Proton Synchrotron Booster (PSB) and the related installation of a new 160 MeV H^- charge exchange injection system. Increasing the PSB injection energy from 50 to 160 MeV increases the relativistic factor $\beta_r\gamma_r^2$ by a factor of two, which allows doubling the beam brightness while keeping space charge forces as before the upgrade.

The new PSB charge exchange injection system was commissioned in winter 2020/2021. It comprises a graphite foil for electron stripping and a horizontal injection bump to move the circulating beam to the stripping foil. Customising the field decay of this injection bump during beam accumulation, also called *phase space painting*, enables tailoring the transverse beam characteristics for the different experiments at CERN.

This thesis investigates solutions for commissioning the new system and pushing its performance by efficiently relating the requested transverse beam distributions to optimised operational paintings and required hardware parameterisations. In the first part, painting schemes for the different users are developed using self-consistent multi-particle simulations and benchmarked experimentally during beam commissioning. These studies mainly focus on optimising phase space painting to reduce space charge effects and minimise losses during the production of high-intensity fixed target beams.

The second part of the thesis explores novel applications of machine learning and numerical optimisation techniques to enhance the efficiency and performance of the new system. The feasibility of applying numerical optimisation algorithms for configuring the painting functions is demonstrated on the machine. The performance of different optimisation algorithms is assessed and compared offline on a data-driven surrogate model. The beam dynamics studies are complemented by first investigations towards using deep learning concepts to define the electronic circuit parameterisation of the phase space kicker magnet pulse generators.

Contents

Acknowledgements

First of all, I am grateful to my university supervisor Privatdoz. Dr. M. Benedikt for accepting me as a student and enabling me to do my doctorate at CERN. I was fortunate to learn a lot on the professional and personal levels and would not like to miss this time.

I would particularly like to thank Dr. C. Bracco for taking on my supervision, the many discussions and the great guidance throughout this project. I am grateful that you gave me the once-in-a-lifetime opportunity to take part in commissioning the upgraded PSB. It was an honour to perform the first measurements with a new system, which so many people have planned, designed and constructed over the last decade. Further, I will always benefit from your valuable feedback on scientific, technical and communication competencies.

I also thank F. M. Velotti for taking on an active part in my supervision and sharing his broad knowledge and creative ideas related to automation and machine learning techniques with me. I further thank W. Bartmann for the unconditional support and for providing a good atmosphere in SY-ABT, despite the Corona pandemic, lockdowns and a stressful period during LIU commissioning. A big ‘thanks’ goes to everyone from the SY-ABT-BTP section, for creating a passionate, motivated and innovative environment. The many discussions and open ears not only improved my technical understanding but will always be remembered as a good time with great colleagues.

This thesis would not have been possible without collaborating with many people across all of the CERN accelerator groups. I would like to say *many thanks, danke, grazie, gracias, merci, obrigada and efcharistó* to numerous colleagues, which are listed below in no particular order:

- The *Space Charge Working Group* for introducing me to the world of incoherent effects and working so closely with me on the PSB beam production schemes. I would like to particularly thank H. Bartosik, F. Asvesta, F. Antoniou and T. Prebibaj for the many welcoming, enlightening and inspiring discussions.

- The BE-OP-PSB and BE-OP-PS teams for the priceless support in the CERN Control Centre. Thank you to G. P. Di Giovanni, B. Mikulec, P. Skowronski and particularly all the operators for sharing the secrets of the machine with me.

- S. Albright and A. Findlay for help with the RF system, showing me the beauty of longitudinal dynamics and the great collaboration regarding the post-LS2 beam production schemes.

- V. Kain, B. Goddard and the *Machine Learning Working Group* for radiating enthusiasm during all the discussions on optimisation and machine learning topics. Their constant drive for innovation is truly inspiring. I further thank N. Madysa for his help with the Generic Optimisation Framework.

- J.B. Lallement, A. Lombardi and the entire Linac4 team for the collaboration on the connection of the Linac4 to the PSB.

- F. Roncarolo and A. N. Fernandez for exciting measurements with the H0/H- monitor.
- J. Emery, S. Di Carlo, A. Guerrero Ollacarizqueta, F. Roncarolo and J.-F. Comblin for the support with the new LIU wire scanners, which belong to the ‘most valuable players’ of this thesis.
- J. Bellemann and E. Maclean for help with the BPM settings and the Turn-by-Turn measurements.
- P. Van Trappen, G. Gräwer, N. Magnin and M. Pedro De Sousa Pimentel for introducing me to the secrets of the KSW generator hardware and controls software.
- W. Weterings, M. Atanasov, T. Stadlbauer and B. Balhan for sharing their knowledge about the transfer line and injection system hardware with me.
- L. Jorat for the positive collaboration on the stripping foils.
- A. Lechner for discussing the foil scattering simulations with me.
- Y. Dutheil and M. Lettrich for the valuable and patient help with all the ‘tiny’ IT issues throughout the last years.
- A. Huschauer and B. Salvant for providing me with sufficient beam time thanks to their flexible coordination of the machine development schedule.
- M. Pari and L. Stoel for being my PhD predecessors in SY-ABT-BTP and passing their wisdom onto me.
- C. Bracco, F. Asvesta, F. M. Velotti, P. Van Trappen, R. Ramjiawan and H. Lohninger for carefully proofreading parts of this manuscript.

Great experiences would not be of as much worth if there was no one to share them with: thank you to all the amazing friends, who went on so many adventures with me over the last years. Last, but definitely not least, a big hug and thank you is owed to my family and partner for the endless support, encouragement, distraction, enthusiasm and positivity.

Thank you, Elisabeth.

This work was funded by the Austrian Federal Ministry of Education, Science and Research in the framework of the Austrian Doctoral Student Programme.

List of Figures

List of Tables

List of Acronyms

Notation	Description	Page List
AD	Antiproton Decelerator	1
ANM	Adaptive Nelder Mead simplex search	118
ANN	Artificial neural network	109
BB	Black-box (optimisation problem)	115
BCT	Beam current transformer	24
BI	PSB injection line	45
BI.DIS	Distributor magnet (BI line)	45
BI.SMV	Septum magnet (BI line)	45
BLM	Beam loss monitor	37
BOBYQA	Bound Optimisation BY Quadratic Approximation	118
BPM	Beam position monitor	37
BSW	PSB injection chicane magnets	40
CEI	Charge exchange injection	3
CERN	European Organization for Nuclear Research	1
COBYLA	Constrained Optimisation BY Linear Approximation	118
DF	Derivative-free (optimisation problem)	117
FFT	Fast Fourier transform	28
GO	Global optimisation / optimiser	117
HL-LHC	High Luminosity Large Hadron Collider	1
ISOLDE	ISOLDE Radioactive Ion Beam Facility (Isotope Separator On Line DEvice)	1
K-V	Kapchinsky–Vladimirsky	23
KSW	Phase space painting kickers in the PSB injection system	40
LHC	Large Hadron Collider	1
LHCINDIV	PSB beam type: LHC individual bunch physics beam	96
LHCINDIV_VDM	PSB beam type: LHC individual bunch physics beam for the Van der Meer scan	96
LHCPROBE	PSB beam type: low-intensity LHC single bunch beam for beam commissioning	96
Linac2	Linac2 accelerator	3
Linac4	Linac4 accelerator	1
LIU	LHC Injectors Upgrade	1
LO	Local optimisation / optimiser	117
LS2	Long Shutdown 2	1

Notation	Description	Page List
ML	Machine learning	107
MLP	Multilayer perceptron	111
NM	Nelder Mead simplex search	118
nTOF	Neutron time-of-flight facility	1
PC	Principal component	144
PCA	Principal component analysis	143
PD	Proportional and derivative (feedback loop)	141
PGNN	Physics-guided neural network	137
PIC	Particle-In-Cell code	28
Pilot	PSB beam type: low-intensity LHC single bunch beam for beam commissioning	96
PINN	Physics-informed neural network	137
PS	Proton Synchrotron	1
PSB	Proton Synchrotron Booster	1
ReLU	Rectified linear unit (activation function)	110
RF	Radiofrequency	9
RFQ	Radiofrequency Quadrupole	35
RFR	Random Forest regressor	114
SBO	Surrogate-based optimisation	119
SPS	Super Proton Synchrotron	1
TbT	Turn-by-turn BPM acquisitions	56
WP	Working point	16

List of Symbols

Sign	Description	Unit	Page List
a_n	Skew multipole component with $n = 1, 2, \ldots$	-	11
$\mathbf{A}$	Magnetic vector potential	Vs/m	11
$\alpha_u(s)$	Twiss parameter $\alpha_u = -0.5 \cdot d\beta_u/ds$	rad	14
α	Noise level (optimisation)	-	116
AUC	Area under the curve	arb. unit	132
B	Beam brightness	p+/mm mrad	24
$\mathbf{B}$	Magnetic field, $\mathbf{B} = -\mathbf{\nabla} \times \mathbf{A}$	T	9
$\beta_u(s)$	Twiss parameter (betatron amplitude function)	m	14
β_r	Relativistic factor $\beta_\mathrm{r} = v/c$	-	2
b_n	Normal multipole component with $n = 1, 2, \ldots$	-	11
c_{4a}, c_{4b}	Painting kicker pulse generator: control bits to define the stage 4 capacitance	s	140
C_i	Painting kicker pulse generator: capacitor number C_i	-	139
CF	Chopping factor	-	39
c_i	Bounds and constraints (optimisation)	arb. unit	115
CR	Clearance rate	-	132
δ	Fractional momentum deviation, $\delta = \Delta p/p$	-	10
$\tilde{\delta}$	Canonical long. momentum, scaled with p_0	-	12
d	Foil thickness	m	31
$D_u(s)$	Dispersion in the transverse planes	m	13
$\mathbf{E}$	Electric field	V/m	9
E	Total relativistic particle energy	eV	10
E_0	Rest energy	eV	10
E_kin	Kinetic particle energy	eV	10
$\epsilon_{u,\mathrm{fit}}$	Transv. emittance based on Gaussian fit	mm mrad	22
ϵ_0	Vacuum permittivity	As/Vm	25
$\epsilon_{u,\mathrm{n}}$	Transv. normalised emittance	mm mrad	22
$\epsilon_{u,\mathrm{rms}}$	Transverse rms beam emittance	mm mrad	22
$f(\mathbf{x})$	Unknown function f which is approximated by the machine learning model $\hat{f}(\mathbf{x})$	arb. unit	107
$\hat{f}(\mathbf{x})$	Machine learning model of function f	arb. unit	107

Sign	**Description**	**Unit**	**Page List**
$\mathbf{F}_\mathrm{L}$	Lorentz force	$\mathrm{kg\,m\,s^{-2}}$	9
f_0	Noise-free objective function (optimisation)	arb. unit	115
$\tilde{f}_0$	Noisy objective function (optimisation)	arb. unit	116
g	Quadrupole gradient	T/m	12
$\gamma_u(s)$	Twiss parameter $\gamma_u = (1+\alpha_u^2)/\beta_u$	$\mathrm{m^{-1}}$	14
γ_r	Relativistic factor $\gamma_\mathrm{r} = E/E_0$	-	2
h	Harmonic number of RF frequency	-	19
$\tilde{H}$	Accelerator Hamiltonian	-	12
I	Beam current	A	39
I_KSW	Painting kicker magnet current	A	139
J_u	Transverse betatron action	m	16
k_n	Normalised normal multipole component with $n = 0, 1, 2, \ldots$	$\mathrm{m^{-(n+1)}}$	11
$k_n^{(s)}$	Normalised skew multipole component with $n = 0, 1, 2, \ldots$	$\mathrm{m^{-(n+1)}}$	11
$K_x(s)$	Horizontal focusing function $K_x(s) = -k_1(s) + 1/\rho^2$	$\mathrm{m^{-2}}$	13
$K_y(s)$	Vertical focusing function $K_y(s) = k_1(s)$	$\mathrm{m^{-2}}$	13
$\lambda(s)$	Longitudinal line density	$\mathrm{m^{-1}}$	20
$\mathcal{L}$	Loss function (machine learning, optimisation)	arb. unit	107
$\mathcal{M}(s_1 \leftarrow s_0; \mathbf{x_0})$	Betatron transfer map from s_0 to s_1	-	13
m_0	Proton rest mass	kg	10
$\mu_u(s)$	Betatron phase	rad	14
n_acq	Total number of function acquisitions during an optimisation run, $n_\mathrm{SA} \cdot n_\mathrm{steps}$	-	120
N_F	Number of foil passages	-	32
$N_\mathrm{p+}$	Intensity; number of particles	p+	2
n_SA	Number of acquisitions used for statistical resampling per optimisation step	-	119
n_steps	Number of optimisation steps	-	120
N_T	Number of decision trees in a random forest	-	113
ω_RF	RF frequency	$\mathrm{s^{-1}}$	19
ω_0	Synchtrotron revolution frequency	$\mathrm{s^{-1}}$	19
p	Total particle momentum, $p = m_0\gamma_\mathrm{r}\beta_\mathrm{r}c$	m/s	10
p_0	Reference momentum, $p_0 = m_0\gamma_{r,0}\beta_{r,0}c$	m/s	10
$\mathbf{\Phi}$	Electric potential	V	155
$\mathcal{P}$	Optimisation problem	-	115
$\tilde{p}_u$	Canonical transv. momentum, scaled w. p_0	-	12
Q_u	Betatron tune	-	16
q	Particle charge	C	9

Sign	**Description**	**Unit**	**Page List**
Q'_u	Chromaticity	-	17
R	Machine radius of the synchrotron	m	26
r_0	Classical particle radius	m	26
L_{rad}	Radiation length (scattering)	m	32
ρ	Positive pairwise correlation between individual decision trees (random forest)	-	112
s	Longitudinal location (reference particle)	m	10
$\sigma_{u,\mathrm{rms}}$	Transverse rms beam width	mm	22
t	Time	s	10
τ	Tolerance (optimisation)	-	117
$\sqrt{< \Theta^2_{\mathrm{MC}} >}$	Multiple Coulomb scattering: rms angle	rad	32
t_{rev}	PSB revolution time	s	4
$t_{\mathrm{LEN},s}$	Painting kicker pulse generator: duration of stage s being switched on	s	140
$t_{\mathrm{R},s}$	Painting kicker pulse generator: start time of stage s being switched on (rising edge)	s	140
$\left(\overline{u}, \overline{u'}\right)$	Normalised betatron phase space coord.	$\mathrm{m}^{1/2}$	16
$\mathbf{v}$	Particle velocity	m/s	9
$V(t)$	RF Voltage	V	19
$\boldsymbol{w}$	Weights of an artificial neural network	arb. unit	110
x, y, z	Coordinates in the Frenet-Serret system	m	10
$x_{\mathrm{L}}, y_{\mathrm{L}}, z_{\mathrm{L}}$	Coordinates in laboratory system	m	10
ξ_u	Normalised chromaticity	-	17
$\mathbf{x}^*$	Incumbent solution (optimisation)	arb. unit	117
$\mathbf{x}_{\mathrm{oob}}$	Out-of-bag / bootstrap samples	arb. unit	112
$\mathbf{x}_{\mathrm{train}}, \mathbf{y}_{\mathrm{train}}$	Input and output variables of a training data set	arb. unit	107
$\mathbf{x}_{\mathrm{test}}, \mathbf{y}_{\mathrm{test}}$	Input and output variables of a test data set	arb. unit	108
$\mathbf{x}_{\mathrm{val}}, \mathbf{y}_{\mathrm{val}}$	Input and output variables of a validation data set	arb. unit	107

Introduction

CERN Injector Complex

The accelerator complex of the European Organization for Nuclear Research (CERN) comprises a succession of machines which accelerate charged particle beams to different energies over several orders of magnitude, as illustrated in Fig. A. The first machine is the linear accelerator Linac4, which provides an H^- ion beam with a kinetic energy of 160 MeV, corresponding to approximately 50 % of the speed of light. Subsequently, a chain of synchrotrons (i.e. a type of cyclic accelerators) continues to increase the particle energy before transferring it to the next machine. After passing through the Proton Synchrotron Booster (PSB), the Proton Synchrotron (PS) and the Super Proton Synchrotron (SPS), the beam is injected at 450 GeV into CERN's largest accelerator, the Large Hadron Collider (LHC). LHC increases the particles' energy up to 7 TeV.

The injector chain can be configured to provide beams with user-specific energy, intensity and beam size to the LHC and the different fixed target experimental facilities (ISOLDE [1], nTOF [2], East Area [3], North Area [4], AD [5], ...).

LHC Injectors Upgrade

In 2021 the LHC enabled the experimental proof of one of the missing pieces of the Standard Model: the discovery of the Higgs Boson was announced by both the CMS and the ATLAS experiments [7, 8]. With this first key to understanding the origin of mass and electroweak symmetry breaking, one of the major goals of the LHC was fulfilled, opening the path for further studies. A higher number of collisions increase the statistics of these experiments, which allows observation of rare processes with higher precision. To fully exploit the 14 TeV energy regime, an upgrade of the LHC, the High-Luminosity LHC (HL-LHC), is scheduled to start operation in 2029. The aim is to increase the luminosity (a measure for the collision rate) by a factor of 5 beyond the design value of LHC [9]. Fulfilling these specifications requires to already inject beams with twice the beam brightness, i.e. the intensity per cross-section, into HL-LHC. Providing such beams necessitated massive upgrades of all injectors, which were conducted in the framework of the LHC Injectors Upgrade (LIU, [10]) project. In addition to doubling the beam brightness of HL-LHC beams, the upgraded machines also facilitate improved beam characteristics for the various fixed target experiments, such as an increased intensity for the ISOLDE experiment. The upgrades were installed during a shutdown in 2019-2020 (Long Shutdown 2, LS2) and commissioned in winter 2020/2021. The machines provided and exceeded the challenging beam specifications for the various users at CERN already during the first operational year in 2021 [11].

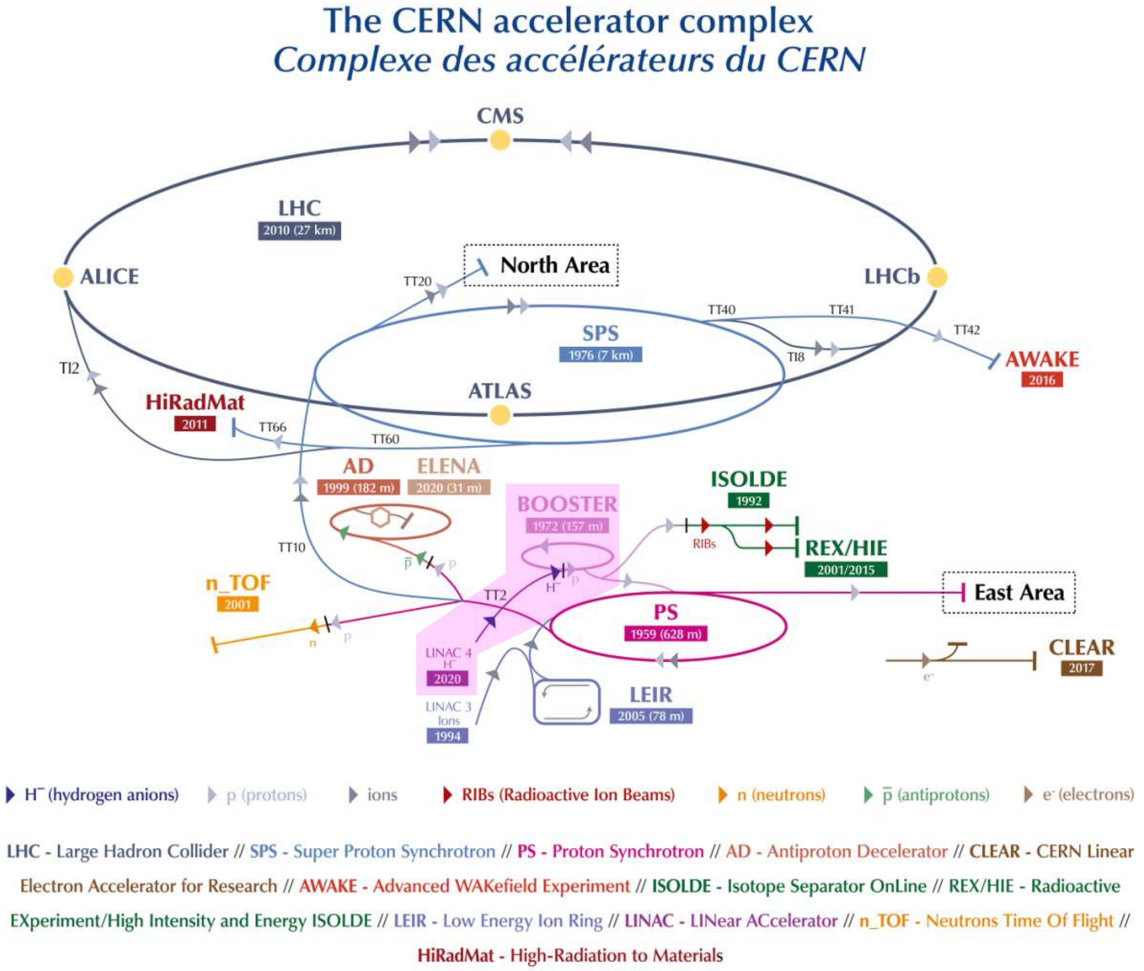

Figure A: The CERN accelerator complex after the LIU upgrades during LS2 [6]. The PSB and Linac4 are highlighted in purple shades.

Space Charge in Low Energy Machines

A driving force behind many of the LIU upgrades is direct space charge, which describes the interaction of the particles with one another in an accelerator (see Section 1.5). The repelling Coulomb forces between the particles have perturbing defocusing effects on the particle motion, which depend on the local charge density. The magnitude of the perturbation is proportional to

$$\Delta Q \propto -\frac{N_{\mathrm{p}+}}{\epsilon_{\mathrm{n}}\beta_{\mathrm{r}}\gamma_{\mathrm{r}}^{2}},$$

with $N_{\mathrm{p}+}$ being the intensity of the particle distribution and β_{r} and γ_{r} the relativistic factors. The normalised emittance ϵ_{n} is a measure for the transverse beam size, as introduced in Eq. (1.34).

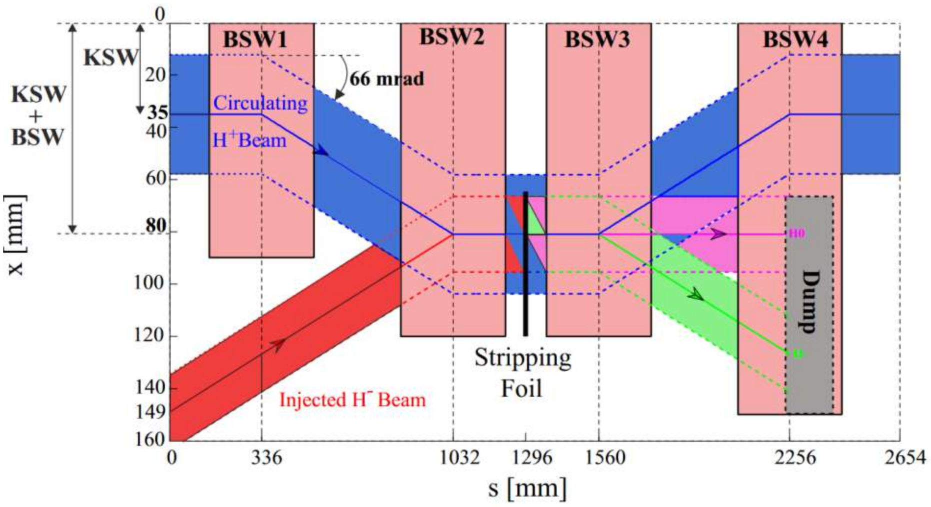

Figure B: Schematic of the PSB H^- injection system (KSW: painting kicker magnets, BSW: injection chicane). The injected H^- beam is marked in red, the circulating p+ beam in blue, the partially stripped H^0 beam in pink and the unstripped H^- beam in green [10].

This relation shows, that space charge is strongest when producing high-brightness beams (high charge density) in low energy machines. Optimising the transverse beam distribution to minimise the local charge density helps to reduce disturbing space charge effects.

The New PSB Injection System and Phase Space Painting

A major aspect of the LIU upgrades was, therefore, to overcome the space charge limitations at the PSB injection by installing Linac4 [12]. Linac4 replaces Linac2, which injected protons at 50 MeV into the PSB before retiring in 2018. The connection to Linac4 increases the PSB injection energy from 50 to 160 MeV and hence increases $\beta_r \gamma_r^2$ by a factor of two. This allows doubling the beam brightness, as required for HL-LHC, while keeping space charge forces at the same level as pre-LS2.

A key part of the connection to the PSB is the installation of a new charge exchange injection system (CEI, Fig. B), which replaces a conventional proton multiturn injection. The fundamental feature of a CEI is the conversion from H^- ions to protons during the injection process. The injected beam passes through a stripping foil, which removes the electrons. The stripped proton beam is merged to the PSB orbit. Partially (H^0) or unstripped (H^-) particles are deposited in the H^0/H^- dump, an absorber in the injection region. The circulating beam trajectory, i.e. the reference orbit in the PSB, is deflected horizontally towards the foil by a closed orbit bump during the injection process.

This system not only facilitates the production of beams with higher brightness for HL-LHC but is also used for tailoring the wide range of requested transverse beam characteristics for the different fixed target experiments. The various CERN users require intensities from $N_{p+} \approx 10^{10}$ to $> 10^{13}$ p+ per ring and normalised transverse emittances from $\epsilon_{n,rms} < 0.7\,\mu m$ (LHC-like beams) to $\approx$ 9-10 µm (high intensity, e.g. for the ISOLDE [1] or nTOF [2] experiment). To deliver the requested intensity, beam can be accumulated in the PSB over up to 150 turns, which corresponds to an injection over $t_{\text{inj}} = 150\,\mu\text{s}$ considering the PSB revolution period at injection energy $t_{\text{rev}} \approx 1\,\mu\text{s}$. The transverse beam characteristics for each user are customised by defining the programmable field decay of the horizontal injection bump and hence the offset between the injected beam and the circulating beam orbit during the injection process. This controlled tailoring of the transverse beam distribution during injection is referred to as *phase space painting*. It enables a reduction of the charge density during beam accumulation, particularly when injecting high-intensity beams and hence mitigates space charge-induced beam size growth.

Phase Space Painting and Charge Injection Schemes Worldwide

The concept of the H^- injection was first demonstrated experimentally at the Novosibirsk Institute of Nuclear Physics in 1964 by using gas jets for electron stripping [13]. A CEI based on a stripping foil was first demonstrated at the Zero Gradient Synchrotron Booster ring at Argonne National Lab in 1972 [14], starting operation in 1976 [15]. Consequently, in the following decades CEI systems have been implemented in various high-intensity proton machines, covering injected beam powers ranging from $< 0.1\,\text{kW}$ to $\approx 1.5\,\text{MW}$. Overviews of the various facilities are given, for example, in [16–19].

The newly gained flexibility of CEI injection systems triggered theoretical and experimental studies concerning transverse phase space painting. Spallation neutron sources and other high power facilities have led the way for related multi-particle simulation studies, as the record power requirements motivated continuous efforts to reduce losses[†]. These efforts mainly focus on optimising the injected beam distribution to satisfy the beam requirements at the target, while mitigating space charge effects, beam halo formation, losses and foil heating.

The modulation of the injected beam position relative to the orbiting beam during phase space painting can be technologically implemented in different ways. One option is to modulate the field decay of an injection bump field, another to vary the dispersive orbit due to variation of the synchrotron guide field. The Spallation Neutron Source accumulator ring at Oakridge National Laboratory, for example, features exponentially decaying painting bumps, which allow for phase space painting in both transverse planes.

Suitable transverse painting schemes strongly depend on the system implementation, the machine state and the requested beam parameters. Although the peak intensity targeted by the PSB is lower than in the high-power machines mentioned above, it should be noted that the PSB is a multi-user accelerator. The broad range of transverse beam characteristics requires increased operational flexibility of the injection system. In the PSB the field decay of the painting bump is not given by an exponentially decaying function but by a programmable, piece-wise linear current decay. The CEI at CERN further differs from the facilities mentioned above by the fact that transverse phase space painting is only possible in the horizontal plane. Implementing a system for vertical phase space painting as well was not possible given the tight spatial restrictions.

[†] Related studies were performed e.g. at the ISIS Neutron and Muon Source at Rutherford Appleton Laboratory [20, 21], the Spallation Neutron Source at Oakridge National Laboratory [22–26], the Chinese Spallation Neutron Source [27–31], the Japan Proton Accelerator Research Complex Rapid Cycling Synchotron [32, 33], in the KEK Booster Ring [34] or Fermilab [35]. Complementary to simulation results, analytical approximations of the beam dynamics during CEIs are summarised e.g. in [36, 37].

However, it is also not required to provide the requested beam intensities in the PSB.

Machine Learning and Numerical Optimisation for Particle Accelerators

The availability of large data sets and computing power is causing a paradigm shift towards data-driven approaches for modelling and controlling complex systems. Numerical optimisation and machine learning techniques are increasingly employed in many engineering and industrial processes, such as particle accelerator technologies. A summary of machine learning opportunities related to particle accelerators is given e.g. in [38]. The range of applications is broad and ranges from efficient optimisation of the machine configurations, anomaly detection and time series forecasting to the substitution of time-consuming simulations and measurements with machine learning models.

Research Question and Objectives

The new PSB CEI was commissioned during winter 2020/2021. This CEI system is unique in its flexibility and needs to provide a wide range of user-requested brightness targets. A pulse generator with a complex circuit parameterisation is required to provide such a programmable, but precise field decay. This system had not been previously operated at CERN. The drive to fully profit from the flexibility of programming different phase space painting schemes raises the following questions:

- What are the *optimised phase space painting schemes* for the different users?
- Can novel methods from *machine learning and numerical optimisation* be used to automatically, reliably and efficiently define required phase space painting functions based on beam instrumentation feedback?

To answer the above questions, studies in both domains, beam dynamics and automation techniques, are of interest:

- Self-consistent space charge simulations of the injection process were performed to develop phase space painting schemes for the various users and analyse the beam evolution during the injection process. The developed beam production schemes were implemented during the beam commissioning period and compared experimentally with first beam measurements.

  Several previous references provide a strong base for these beam dynamics studies[†]. First painting functions for the different users are presented for example in [44–48]. However, adapting these concepts to the current machine configurations and furthering the understanding of the beam evolution is essential in view of interpreting the beam measurements during commissioning.

- The application of novel automation methods is investigated to enhance the efficiency and performance of the new CEI. Derivative-free optimisation algorithms are explored to assess the potential of optimising the injection painting online using beam instrumentation

---

[†] For example benchmarking the simulation set-up [39], assessing sources of brightness degradation of LHC beams due to injection errors and space charge effects [39–42] or specifying the required characteristics and flexibility of the KSW field decay [43].

feedback. Supervised machine learning algorithms (Artificial Neural Networks and Random Forest Regressors) are applied to create data-driven models of the injection process. Systematically studying the performance of different optimisation algorithms without using beam resources is one application of such models. Another use case is modelling the complex dynamical behaviour of the injection kicker generator.

Overall, both enhancing the comprehension of the beam evolution during the injection process and finding solutions towards automating the phase space painting will enable pushing the beam performance. Automating the injection set-up will improve also the stability and reproducibility of results. It will be a key aspect to operating the new PSB and keep improving the performance in the coming years.

Structure of the Thesis

The thesis is structured into two main parts. Part I investigates the beam dynamics when tailoring the brightness targets for the various users using numerical simulations, which are compared to beam measurements during the beam commissioning period. Chapter 1 introduces the main concepts of beam dynamics and intensity effects. Chapter 2 gives a system layout of the PSB, its new CEI system and introduces the procedures used for phase space painting. Chapter 3 characterises and quantifies the main error sources during the PSB injection process using hardware and beam measurements. The estimated errors are subsequently used as an input for the phase space painting studies in Chapter 4. This chapter discusses the beam production schemes of different beam types using self-consistent space charge simulations and measurements. The main focus of Chapter 4 is the optimisation of the painting schemes, which is required to reduce the losses during high-intensity beam production.

Part II examines novel concepts using machine learning and numerical optimisation algorithms to increase the efficiency and performance of the new CEI system. A brief theoretical background on such methods is given in Chapter 5. Chapter 6 examines the automated optimisation of the transverse phase space painting for high-intensity beams using numerical optimisers. Finally, Chapter 7 complements the beam physics studies and investigates the feasibility of applying deep learning concepts to control the circuit parameterisation of the phase space kicker magnet pulse generators. A conclusion and outlook to further studies is provided in Chapter 8.

Part I

Phase Space Painting with the New PS Booster Charge Exchange Injection System

CHAPTER 1

Beam Dynamics and Intensity Effects in Synchrotron Accelerators

The particle motion in an accelerator is mainly driven by the external guiding fields of magnets and cavities. Additionally, the Coulomb forces between the charged particles generate a self-field. These so-called space charge forces depend on the beam distribution and can cause perturbations to the designed particle motion.

This chapter briefly introduces the main beam dynamics concepts which are relevant for analysing the beam evolution during the PSB CEI process. More detailed derivations can be found in Appendix A as well as the resources this chapter is based on, i.e. [49–54].

1.1 Particle Motion in an Accelerator and Frenet-Serret Coordinate System

The force acting on a moving particle with velocity **v** and charge q in electric (**E**) and magnetic (**B**) fields is the Lorentz force $\mathbf{F}_\mathrm{L}$:

$$\mathbf{F}_\mathrm{L} = q \cdot (\mathbf{E} + \mathbf{v} \times \mathbf{B}). \tag{1.1}$$

In particle accelerators, electric fields **E** are used to accelerate the particle longitudinally and are generated by radiofrequency (RF) cavities. Magnetic fields **B** deflect a moving particle orthogonally to both **B** and **v** and are thus used to guide the transverse particle motion (see Fig. 1.1). Dipoles are used to bend the particle trajectory. Quadrupoles do not affect the design trajectory but keep the particles close to it through fields, which are focusing in one and defocusing in the other plane. Installing a sequence of quadrupoles with alternating gradients allows for the achievement of a net focusing effect in both planes. Higher-order multipoles are used to correct errors, such as chromatic aberrations. The ensemble of elements in an accelerator is referred to as the *accelerator lattice*.

In beam dynamics, one expresses the particle motion through an accelerator lattice as deviation from a reference orbit. This trajectory is given by the motion of a particle with ideal parameters in ideal fields and is mainly dictated by the deflecting dipole magnets. Due to spatial and momentum offsets or field errors, real particles move close to - but not on - the reference orbit (Fig. 1.2).

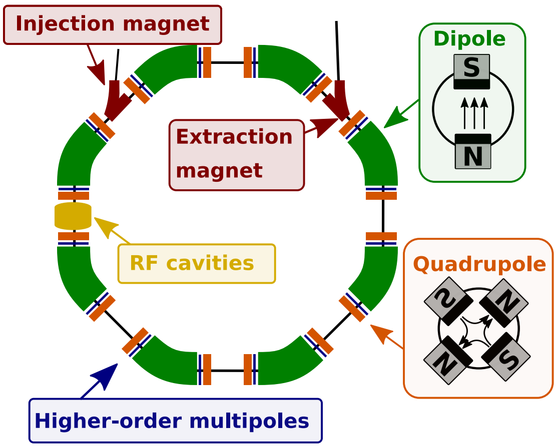

Figure 1.1: Schematic illustration of the main components of a synchrotron accelerator (not to scale).

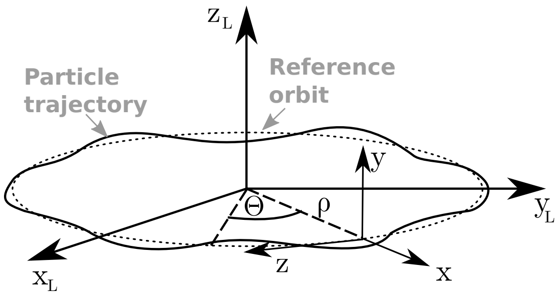

Figure 1.2: Deviation of the particle trajectory (solid) from the reference orbit (dashed). Particle motion is described in the moving Frenet-Serret coordinate system (x, y, z) instead of the laboratory reference frame $(x_\mathrm{L}, y_\mathrm{L}, z_\mathrm{L})$.

The transverse non-nominal trajectories can be stabilised by the restoring focusing forces of quadrupole magnets. Consequently, the particle performs an oscillating transverse movement around the reference orbit, which is called *betatron oscillation*. It is beneficial to describe these particle oscillations in the *Frenet-Serret coordinate system* (x, y, z), which is moving with the reference particle, rather than the laboratory coordinate system $(x_\mathrm{L}, y_\mathrm{L}, z_\mathrm{L})$. The guiding fields are functions of the location s and periodic in a synchrotron. Therefore, it is useful to express the particle motion using s instead of the time t. Details regarding this transformation to a curved reference trajectory with independent variable s are provided in e.g. [50, Chp. 4.3].

The particle state at location s is fully described in the Frenet-Serret coordinate system by the *state vector*

$$\mathbf{x}(s) = \begin{pmatrix} x(s) \\ x'(s) \\ y(s) \\ y'(s) \\ z(s) \\ \delta(s) \end{pmatrix}. \tag{1.2}$$

Here, the angle $u' = du/ds$ in the transverse planes $u = x, y$ is used to characterise the transverse component of the particle momentum $p_u = u' \cdot p_0$, with $p_0 = m_0 \gamma_\mathrm{r} \, |\mathbf{v}| \approx p_z$ being the reference momentum of the particle with rest mass m_0. Longitudinally, the particles are described using the coordinate pair (z, δ), with

$$\delta = \frac{p - p_0}{p_0} = \frac{1}{\beta_\mathrm{r}^2} \frac{\Delta E}{E} \tag{1.3}$$

being the fractional momentum offset of the particle with momentum p from the reference momentum. An alternative measure for the momentum offset is the fractional difference of the particle energy $E = E_\mathrm{kin} + E_0$, $\Delta E / E$.

1.2 Transverse Single Particle Motion

1.2.1 Magnetic Multipole Fields

As mentioned above, the transverse motion is directed by the transverse magnetic fields $\mathbf{B} = \nabla\times\mathbf{A} = (B_x, B_y, 0)$. The magnetic field a particle sees depends on the field type and the transverse position, i.e. the vertical field component as a function of the horizontal beam position is

$$B_y(x,y) = B_y(0,x) + x\frac{\partial B_y}{\partial x}\,|_{0,y} + x^2\frac{\partial^2 B_y}{\partial x^2}\,|_{0,y} + \dots\,. \tag{1.4}$$

For long and straight multipole magnets (i.e. neglecting edge effects, no longitudinal component), the magnetic field can be decomposed into multipole fields of different orders n

$$B_y(r) + iB_x(r) = B_{\text{ref}}\sum_{n=1}^{\infty}(b_n + ia_n)\left(\frac{x+iy}{R_{\text{ref}}}\right)^{n-1}\,, \tag{1.5}$$

with $r = x + iy$ (European convention, see e.g. [55, Chp. 1.2]). $n = 1$ describes a dipolar field component, $n = 2$ a quadrupolar and so on. The coefficients b_n and a_n are called the normal and skew multipole components and are given relative to a reference dipole field component B_{ref}, which is quantified at the (arbitrary) reference radius R_{ref}. They are connected to the derivatives of the field components through

$$\frac{\partial^n B_y}{\partial x^n}\,|_{x,y=0} = n!\frac{B_{\text{ref}}}{R_{\text{ref}}^n}b_{n+1} \quad \text{for } n = 0, 1, \dots,. \tag{1.6}$$

To facilitate a field description independent of the reference momentum p_0 and charge q, it is common to scale the multipole fields with p_0/q, which yields the normalised multipole strengths

$$k_n = \frac{q}{p_0}\frac{\partial^n B_y}{\partial x^n}\,|_{x,y=0} = n!\frac{B_{\text{ref}}}{R_{\text{ref}}^n}b_{n+1} \quad \text{for } n = 0, 1, \dots \tag{1.7}$$

and normalised skew multipole strengths

$$k_n^{(s)} = -\frac{q}{p_0}\frac{\partial^n B_x}{\partial x^n}\,|_{x,y=0} = -n!\frac{B_{\text{ref}}}{R_{\text{ref}}^n}a_{n+1} \quad \text{for } n = 0, 1, \dots\,. \tag{1.8}$$

Dipole

A dipole with a horizontally deflecting field $\mathbf{B} = (0, B_y = \text{const.}, 0)$ bends a particle with momentum $p_z = m_0\gamma_r v_z \approx p$ and charge q onto a circular trajectory with bending radius ρ. Equating the Lorentz and centrifugal force

$$\mathbf{F}_{\text{L}} = \mathbf{F}_{\text{CF}} \quad \text{i.e.} \quad \frac{m_0\gamma_r v_z^2}{\rho} = |q|\,v_z B \tag{1.9}$$

yields the relation

$$\rho B = \frac{p}{|q|}. \tag{1.10}$$

ρB is called *beam rigidity* and describes the "stiffness" of the particle motion given by its momentum and charge. The normalised multipole strength is

$$k_0 = B_{\mathrm{ref}} b_1 = \frac{B_y}{p_0/q} = \frac{1}{\rho}. \tag{1.11}$$

Quadrupole

A normal quadrupole with gradient $g = \frac{\partial B_y}{\partial x}\,|_{x,y=0} = \frac{\partial B_x}{\partial y}\,|_{x,y=0} =$ const. and field $\mathbf{B} = (yg, xg, 0)$ is characterised by the normalised quadrupole strength

$$k_1 = \frac{B_{\mathrm{ref}}}{R_{\mathrm{ref}}} b_2 = \frac{1}{p_0/q}\frac{\partial B_y}{\partial x}\,|_{x,y=0} = \frac{g}{p_0/q}. \tag{1.12}$$

Higher-Order Multipoles

Similar considerations are valid for higher-order multipoles. Note that different from dipoles and quadrupoles, the field of higher-order multipoles is no longer a linear expressions of the transverse positions x and y.

1.2.2 Accelerator Hamiltonian

Whereas Newtonian mechanics can be used to derive the equations of motion of a particle in such external fields, it is beneficial to apply the Hamiltonian formalism instead (see Appendix A.1, [55, Chp. 2] or [56, Chp. 3.7] for more details). When considering only small deflections from the reference orbit (*paraxial approximation*), the Hamiltonian for elements with respective normalised multipole strengths k_n can be approximated as

$$\tilde{H} \approx \overset{\text{kinematic}}{\boxed{\frac{1}{2}\left(\tilde{p}_x^2 + \tilde{p}_y^2\right)}} + \overset{\text{dipole}}{\boxed{\frac{x^2}{2\rho^2} - \frac{1}{\beta_{\mathrm{r}}\rho} x\tilde{\delta}}} + \overset{\text{quadrupole}}{\boxed{\frac{k_1}{2}\left(x^2 - y^2\right)}} + \overset{\text{sextupole}}{\boxed{\frac{k_2}{6}\left(x^3 - 3xy^2\right)}} + \ldots. \tag{1.13}$$

Here, $\tilde{p_u}$ and $\tilde{\delta} = \beta_{\mathrm{r}} \Delta p / p_0$ are the transverse and longitudinal canonical momenta normalised to p_0, as introduced in Appendix A.1.

1.2.3 Linear Transverse Particle Motion

The equation of the particle motion through a magnetic element can be derived by applying Hamilton's equations Eq. (A.7) to Eq. (1.13). For a lattice consisting only of dipolar and quadrupolar fields, this yields a linear equation of motion, also known as *Hill's equation*

$$x'' - \left(k_1(s) - \frac{1}{\rho^2}\right) \cdot x = x'' + K_x(s) \cdot x = \frac{\delta}{\rho}. \tag{1.14}$$

It describes the betatron motion of a particle in the horizontal plane. The homogeneous part of this equation can be interpreted as the equation of a harmonic oscillator with varying focusing strength $K_x(s)$. $K_x(s)$ depends on the position s in the lattice and is given by the normalised quadrupole strengths $k_1(s)$ and the weak focusing effect $1/\rho^2$ of the dipolar fields. The transverse motion is coupled to the longitudinal plane by the inhomogeneity δ/ρ. This causes *dispersive effects*, which are described in more detail below.

If there are no dipoles in the vertical plane, i.e. no bending and $\rho \to \infty$, the vertical Hill's equation simplifies to the homogeneous equation

$$y'' + k_1(s)y = y'' + K_y(s)y = 0. \tag{1.15}$$

The homogeneous solution of these linear differential equations is a quasi-harmonic oscillation in the transverse planes, with s-dependant amplitude. This motivates the common ansatz

$$u(s) = \sqrt{2J_u\beta_u(s)}\cos\left(\mu_u(s) + \phi_{u,0}\right). \tag{1.16}$$

J_u and $\phi_{u,0}$ are integration constants determined by the transverse initial conditions of the particle at s_0 (compare [49, Chp. 2.II]). The parameters $\beta_u(s)$ and $\mu_x(s)$ are functions of s and depend on the focusing properties $K(s)$. $\beta_u(s)$ describes the amplitude modulation and $\mu_u(s)$ the phase. Floquet's theorem [57] states that the amplitude of oscillations with periodic focusing strength $K(s) = K(s+L)$ has the same periodicity and hence $\beta(s) = \beta(s+L)$ (see [49, Chp. A.1] for details).

1.2.4 Dispersion

Particles with a fractional momentum offset δ experience a non-nominal deflection by a dipole. These dispersive effects are formalised in the inhomogeneity of Hill's equation Eq. (1.14). The solution

$$u(s) = u_H(s) + u_I(s) = \sqrt{2J_u\beta_u(s)} \cdot \cos\left(\mu_u(s) + \phi_{u,0}\right) + D_u(s) \cdot \delta \tag{1.17}$$

couples the longitudinal plane (δ) to the transverse plane (u). $D_u(s)$ is a property of the bending and focusing elements of the lattice and is called *Dispersion* function (compare [49, Chp. 2.IV]). If there are no bending dipoles in the vertical plane $D_y = 0$.

1.2.5 Transfer Maps

The solution to Hill's equation can be summarised in the *transfer map*

$$\mathbf{x}(s_1) = \mathcal{M}(s_1 \leftarrow s_0; \mathbf{x_0}), \tag{1.18}$$

which propagates a particle with state vector $\mathbf{x}(s_0)$ from s_0 to s_1. In the particular case of linear motion, the transfer map takes the form of a matrix

$$\mathbf{x}(s_1) = \mathcal{M} \cdot \mathbf{x}(s_0). \tag{1.19}$$

The propagation from location s_0 to s_N is obtained by combining the transfer matrices of the passed sequence of elements

$$\begin{pmatrix} u(s_N) \\ u'(s_N) \\ \delta \end{pmatrix} = \mathcal{M}(s_N \leftarrow s_{N-1}) \dots \mathcal{M}(s_2 \leftarrow s_1) \cdot \mathcal{M}(s_1 \leftarrow s_0) \cdot \begin{pmatrix} u_0(s_0) \\ u_0'(s_0) \\ \delta \end{pmatrix}. \tag{1.20}$$

1.2.6 Twiss Parameters

The analytic expressions one obtains by combining transfer matrices for a long sequence of elements between two observation points become rather complex. This motivates the *Twiss parameterisation*, a formalism which simplifies the propagation of a particle with initial conditions $(u, u')(s_0)$ to any location s_1.

The basis for the Twiss formalism is to write the betatron motion as an oscillation with s-dependant amplitude proportional to $\beta(s)$, as introduced in Eq. (1.16). Inserting this ansatz into Hill's equation Eq. (1.14) yields the relation

$$\beta_u(s)\mu_u'(s) = 1 \tag{1.21}$$

between the phase $\mu_u(s)$ and the amplitude $\beta_u(s)$. With the knowledge of $\beta_u(s)$ along the ring, the phase difference $\Delta\mu_u$ between two locations can be integrated as

$$\Delta\mu_u(s_1, s_0) = \mu_1 - \mu_0 = \int_{s_0}^{s_1} \frac{ds}{\beta_u(s)}. \tag{1.22}$$

Two further parameters

$$\alpha_u(s) = -\frac{1}{2}\frac{d\beta_u}{ds} \quad \text{and} \quad \gamma_u(s) = \frac{1+\alpha_u^2}{\beta_u} \tag{1.23}$$

are introduced, which allows the expression of the transfer matrix between s_0 and s_1 through $\beta_u(s_i), \alpha_u(s_i), \gamma_u(s_i) = \beta_{i,u}, \alpha_{i,u}, \gamma_{i,u}$ (here listed without the dispersive contribution)

$$\begin{aligned}
&\mathcal{M}(s_1 \leftarrow s_0) = \\
&\begin{pmatrix} \sqrt{\frac{\beta_{1,u}}{\beta_{0,u}}}(\cos\Delta\mu_u + \alpha_{0,u}\sin\Delta\mu_u) & \sqrt{\beta_{1,u}\beta_{0,u}}\sin\Delta\mu_u \\ \frac{\alpha_{0,u}-\alpha_{1,u}}{\sqrt{\beta_{1,u}\beta_{0,u}}}\cos\Delta\mu_u - \frac{1+\alpha_{0,u}\alpha_{1,u}}{\sqrt{\beta_{1,u}\beta_{0,u}}}\sin\Delta\mu_u & \sqrt{\frac{\beta_{0,u}}{\beta_{1,u}}}(\cos\Delta\mu_u - \alpha_{1,u}\sin\Delta\mu_u) \end{pmatrix} = \\
&\begin{pmatrix} \sqrt{\beta_{1,u}} & 0 \\ -\frac{\alpha_{1,u}}{\sqrt{\beta_{1,u}}} & \frac{1}{\sqrt{\beta_{1,u}}} \end{pmatrix} \cdot \begin{pmatrix} \cos\Delta\mu_u & \sin\Delta\mu_u \\ -\sin\Delta\mu_u & \cos\Delta\mu_u \end{pmatrix} \cdot \begin{pmatrix} \frac{1}{\sqrt{\beta_{0,u}}} & 0 \\ \frac{\alpha_{0,u}}{\sqrt{\beta_{0,u}}} & \sqrt{\beta_{0,u}} \end{pmatrix} = \\
&\mathcal{T}(s_1)^{-1}\mathcal{R}(\Delta\mu)\mathcal{T}(s_0).
\end{aligned} \tag{1.24}$$

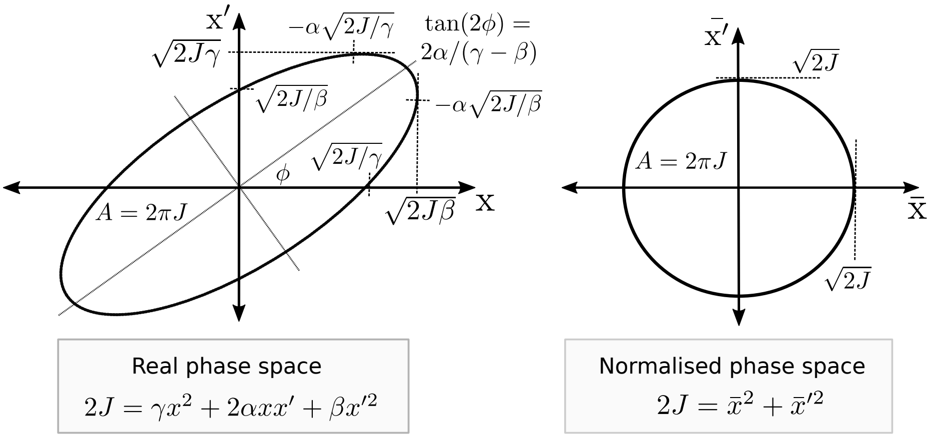

Real phase space
$2J = \gamma x^2 + 2\alpha x x' + \beta x'^2$

Normalised phase space
$2J = \bar{x}^2 + \bar{x}'^2$

Figure 1.3: Real (left) and normalised (right) trace space ellipse of a particle beam.

It has to be noted, that this expression is valid for multiple elements with different focusing and deflecting properties between the two observation points. The variables α_u, β_u and γ_u are uniquely defined at each location s by the properties of these lattice elements and are called *Twiss parameters* or *Courant-Snyder parameters*. One can compute the Twiss parameters for a lattice using different optics codes, such as MAD-X [58]. Using the computed parameters, the coordinates $u(s_1)$ and $u'(s_1)$ can be determined at any location in the accelerator for a particle with initial conditions $u(s_0)$ and $u'(s_0)$.

1.2.7 Phase Space

The conjugate coordinate pairs (x, p_x), (y, p_y) and (z, δ) can be illustrated in a *phase space* portrait, which is specific for each location s along the synchrotron. Recording the phase space coordinates of a particle over multiple revolutions $(x, p_x)(s + n \cdot L)$ results in the phase space trajectory of this particle at the respective location, also called *Poincaré map*. In linear beam dynamics, the resulting trajectory in phase space is an ellipse with orientation and eccentricity, which are specific for the location s in the lattice and given by the Twiss parameters $\alpha(s), \beta(s), \gamma(s)$ (Fig. 1.3, left).

In many practical applications it is useful to work with the space (u, u') instead. Despite this being technically called *trace space*, it is often referred to as *phase space* as well.

1.2.8 Normalised Coordinates and Normalised Phase Space

Eq. (1.24) shows that one can decompose the transfer matrix into a transformation $\mathcal{T}(s_i)$, which is a function of the local lattice properties, and a rotation matrix $\mathcal{R}$, which depends on the phase advance $\Delta\mu_u = \mu_u(s_1) - \mu_u(s_0)$. Applying this local transformation to the phase space vector yields the so-called *normalised coordinates* $\left(\overline{u}, \overline{u'}\right)$

$$\begin{pmatrix} \overline{u} \\ \overline{u'} \end{pmatrix} = \mathcal{T}(s) \cdot \begin{pmatrix} u \\ u' \end{pmatrix} = \begin{pmatrix} \frac{1}{\sqrt{\beta_{0,u}}} & 0 \\ \frac{\alpha_{0,u}}{\sqrt{\beta_{0,u}}} & \sqrt{\beta_{0,u}} \end{pmatrix} \cdot \begin{pmatrix} u \\ u' \end{pmatrix}. \tag{1.25}$$

The respective *normalised phase space* is illustrated in Fig. 1.3 (right). Note that for linear motion $\mathcal{R}$ describes a clockwise rotation on a circle in normalised phase space.

1.2.9 Propagation of the Phase Space Ellipse, Courant-Snyder Invariant and Action

The eccentricity and orientation of the ellipse depend on the local focusing properties and propagate along the accelerator (see e.g. in [50, Chp. 8.1.2]). The area of the phase space ellipse is a constant of motion under the influence of only conservative forces, also known as *Courant-Snyder Invariant*,

$$\gamma u^2 + 2\alpha_u u u' + \beta_u u'^2 = \text{const.} = 2J_u. \tag{1.26}$$

In normalised phase space, this yields

$$\overline{u}^2 + \overline{u'}^2 = \text{const.} = 2J_u. \tag{1.27}$$

$\sqrt{2J_u}$ is the radius of the circle in normalised phase space. J_u, first introduced as integration constant in Eq. (1.16), is the *action* of the particle with the initial conditions $(u, u')(s_0)$ and is constant for linear motion. Nonlinear forces, however, distort the phase space trajectory and $J_u \neq \text{const.}$

1.2.10 Tune and Working Point

One betatron oscillation has a phase advance of $\Delta\mu = 2\pi$. The number of betatron oscillations during one revolution is called *betatron tune*, or simply *tune*, and is given by the normalised phase advance over an entire turn

$$Q_u = \frac{1}{2\pi} \int_s^{s+L} \frac{ds}{\beta_u(s)}. \tag{1.28}$$

The tune pair (Q_x, Q_y) in a machine is determined by the chosen quadrupole settings and is called *working point* (WP). Typical WPs of the PSB during post-LS2 operation are $Q_x = 4.1 - 4.4$ and $Q_y = 4.17 - 4.45$.

1.2.11 Chromaticity

The focal length of quadrupoles, similar to the bending angle of a dipole, changes with the beam energy. Off-momentum particles experience a non-nominal focusing, which results in a deviation

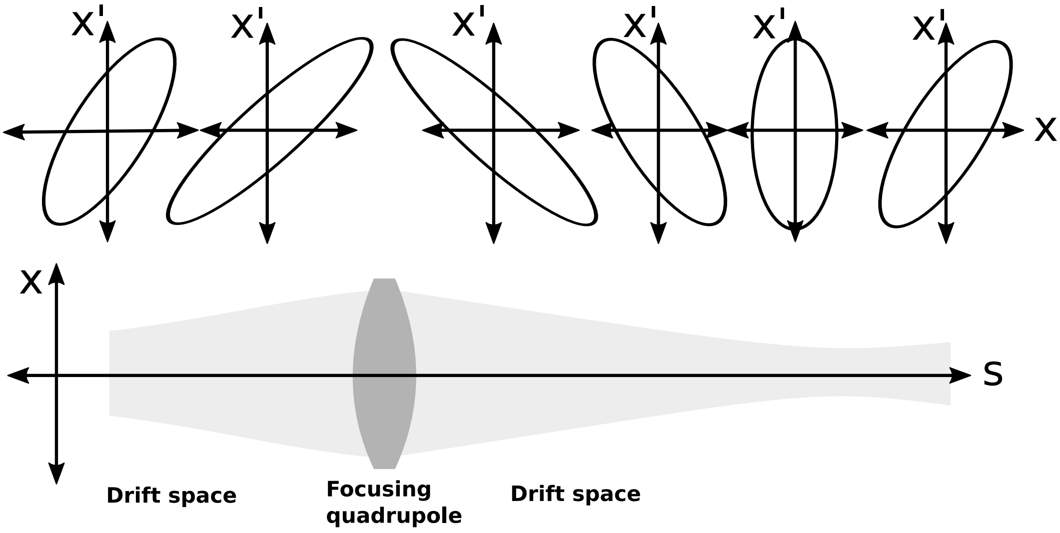

Figure 1.4: Propagation of the trace space ellipse when passing drift spaces and a focusing quadrupole. The shaded area illustrates the beam envelope.

of the particle tune. The chromaticity

$$Q'_u = \frac{\partial Q_u}{\partial \delta} = \frac{1}{4\pi} \int_s^{s+L} \beta_u \Delta K_u(s) ds. \tag{1.29}$$

describes the difference of a particle tune from its nominal tune due to a momentum offset. The normalised chromaticity is

$$\xi_u = \frac{Q'_u}{Q_u}. \tag{1.30}$$

Beams have a finite momentum spread, as outlined in Section 1.3. In a machine with non-zero chromaticity, this results in a spread of tunes around the WP. Generally, sextupoles can be used to correct the chromaticity. However, the available sextupole correctors in the PSB only allow for chromaticity correction in one plane, either horizontal or vertical.

1.2.12 Perturbed Particle Motion and Resonances

Up to this point, a perfect machine without imperfections or nonlinearities has been assumed when describing the linear betatron motion. However, imperfections such as alignment errors, field errors or power converter ripples perturb the particle motion. Consideration of such errors is crucial as the particle experiences erroneous kicks at every revolution. The respective kicks can add up or cancel each other over multiple turns, depending on the characteristic of the field error (dipolar, quadrupolar etc.) and the particle tune.

Formally, such imperfections and deviations from the linear motion are included in the Hamiltonian treatment by means of perturbation terms (see Appendix A.1.2). It is instructive to compare these perturbation terms to external driving forces of a harmonic oscillator: if the eigenfrequency

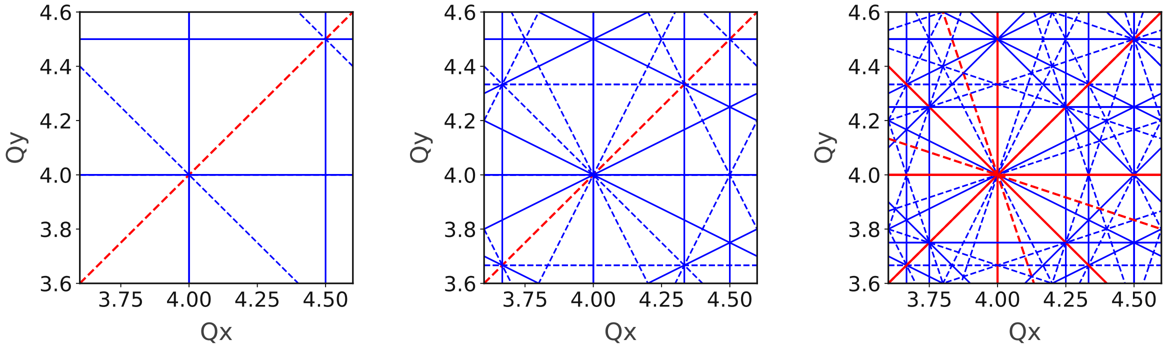

Figure 1.5: Tune diagrams displaying resonances up to 2^{rd} order (left), 3^{rd} order (center) and 4^{th} order (right). Systematic resonances are displayed in red. Solid lines refer to normal and dashed to skew resonances.

of the driving term matches the harmonic oscillation frequency (tune), the motion can get excited and particles lost. Such instabilities are called *resonances*.

The frequencies driven by the perturbations must differ from the betatron frequencies to provide a stable particle motion. From the Hamiltonian treatment, one can derive the *resonant condition*

$$m \cdot Q_x + n \cdot Q_y = p, \quad \text{with integers } n,\ m \text{ and } p > 1. \tag{1.31}$$

It defines the tunes (Q_x, Q_y), at which particles are excited by a specific resonance. The various resonances can be visualised in the tune diagram, Fig. 1.5.

The parameters n, m and p classify the type of the resonance: $|m| + |n|$ is the *order*. 1^{st}-order resonances are mostly driven by dipolar errors and are also called *integer resonances*. 2^{nd}-order resonances, also called *half-integer resonances*, are mostly driven by quadrupolar errors. Resonances, for which m and n have the same sign are called *sum resonances*. *Difference resonances* have different signs of m and n. Additionally, one distinguishes between *normal* (n is even) and *skew* (n is odd) resonances, which are respectively driven by normal and skew multipole components. If $p = j \cdot P$ is a multiple $j = 0, 1, \ldots$ of the periodicity P of the machine ($P = 16$ in the PSB, compare Section 2.2), resonances are called *systematic*. Resonances, for which both $n \neq 0$ and $m \neq 0$, impact the betatron oscillation in both transverse planes and are called *coupling resonances*.

The WP (Q_x, Q_y) of a synchrotron is chosen to stay clear of resonances. Fortunately, not all resonances are present in a machine: the relevant resonances depend on machine-specific errors and the effectiveness of the compensation schemes and vary in strength. Integer and half-integer resonances are the most dominant. Further, note that rather than being a line as illustrated in Fig. 1.5, resonances exhibit a finite thickness. This so-called *stopband width* depends on the strength of the resonance.

Resonances in the PS Booster

Figure 1.6 illustrates the dominant resonances observed post-LS2 in the upgraded PSB (ring 3), which are experimentally determined using loss maps [59]. For the first time, these studies reveal resonances up to the 4^{th} order in all rings. Whereas compensation schemes are successful in

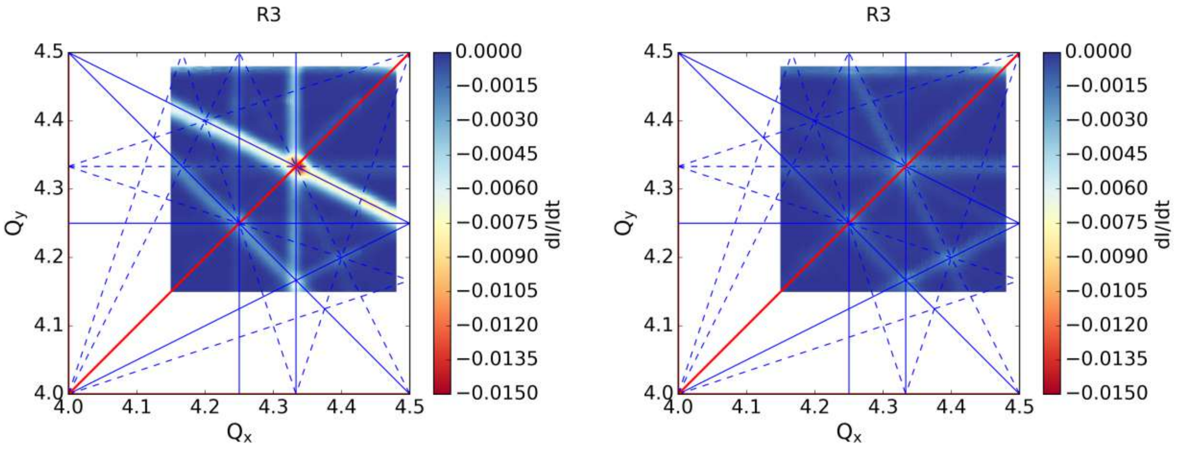

(a) Without correction.

(b) With octupoles and sextupoles for the simultaneous correction of the 3rd and 4th-order normal resonances.

Figure 1.6: Loss maps resulting from dynamic tune scans in PSB ring 3. The transverse tune space is colour-coded using the loss rate variation. Resonance lines up to the 4th order are plotted, normal in solid lines and skew in dashed. The non-systematic resonance lines are plotted in blue and the systematic, the coupling resonance in this case, in red [59].

globally compensating 3rd-order resonances (skew and normal), 4th-order resonances could only be partially compensated due to limitations in the octupole corrector strength [59].

1.3 Longitudinal Particle Motion

The longitudinal particle motion is predominantly driven by the electric field of the RF cavities, which has a sinusoidal form

$$V(t) = \hat{V}\sin\left(\omega_{\mathrm{RF}}\cdot t\right) = \hat{V}\sin\left(\Phi(t)\right) \tag{1.32}$$

with frequency ω_{RF} and amplitude $\hat{V}$. The frequency must be a multiple of the synchrotron revolution frequency ω_0 of the reference (*synchronous*) particle, i.e.

$$\omega_{\mathrm{RF}} = h\cdot\omega_0. \tag{1.33}$$

h is the *harmonic number* of the applied RF field. The synchronous particle passes the cavity always at the same phase $\Phi_s(t)$. Particles in a real distribution, however, differ from the reference particle by δ and Δz. Δz can be equally expressed as time difference Δt or phase offset $\Delta\Phi$, with which the particle arrives at the RF cavity, and δ by ΔE.

Figure 1.7 [60] illustrates the sinusoidal RF voltage (top) and the longitudinal phase space (bottom) for a beam, which is not accelerated. The synchronous particle with ω_0 arrives every turn at $\Phi_s = 0$ and $V = 0$ (no acceleration). Asynchronous particles arriving with $\Delta\Phi$ experience a different voltage and hence acceleration (or deceleration) compared to the reference particle.

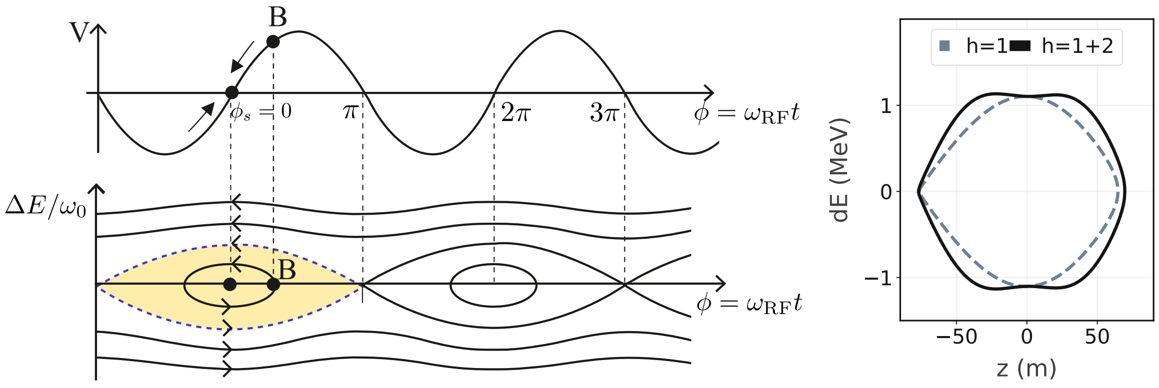

(a) **(b)**

Figure 1.7: A) Longitudinal particle motion for a single harmonic non-accelerating RF bucket. Particles, which arrive before or after the synchronous particle experience a voltage other than the reference voltage and conduct synchrotron oscillations. Top: RF voltage with ω_{RF}. Bottom: longitudinal phase space with stable particle trajectories (closed lines inside the yellow bucket) and unstable trajectories of off-bucket particles [60]. B) Separatrix of a single harmonic ($h = 1$) and double harmonic ($h = 1 + 2$) bucket.

Particles with $\Delta E \neq 0$ have a revolution time different from the reference particle due to differences in velocity and/or path length (dispersion) and arrive each turn at a different phase.

There is a range of acceptable $\Delta\Phi$ and ΔE combinations, which yield stable oscillations around the reference particle (*synchrotron oscillation*). The stable region in phase space is called *bucket* (yellow in Fig. 1.7) and is characterised by the RF voltage and frequency. Off-bucket particles become unstable and get lost in the machine aperture due to transverse dispersive effects. The separation between stable and unstable motion is called *separatrix* (dashed line in Fig. 1.7). In a multi-harmonic RF system, one combines RF waves with different harmonics, phases and voltages. The shape of the separatrix changes significantly when superposing the different potentials, as illustrated in Fig. 1.7b.

1.3.1 Longitudinal Filamentation, Line Density and Coasting Beam

The beam is injected from Linac4 into the PSB in chopped bunches (see Section 2.1), which have an approximately parabolic energy profile and uniform phase population. This distribution is not perfectly matched to the bucket, as illustrated in Fig. 1.8a (40 turns after injection, when injecting beam over 35 turns). Longitudinal forces are nonlinear, which yields a spread in synchrotron oscillation frequencies for particles with different longitudinal actions. This drives a redistribution in phase space until equilibrium is reached (*longitudinal filamentation*). The histograms in Fig. 1.8 (top) illustrate the evolution of the longitudinal density, also called *line density* $\lambda(s)$, during the filamentation process. In the PSB, double (or even triple) harmonic buckets are commonly used to reduce the line density along the bunch. If the RF system is switched off, the bunch spreads out over the entire circumference. The resulting unbunched distribution is uniform with $\lambda(z) = \text{const.}$ and is called a *coasting beam*.

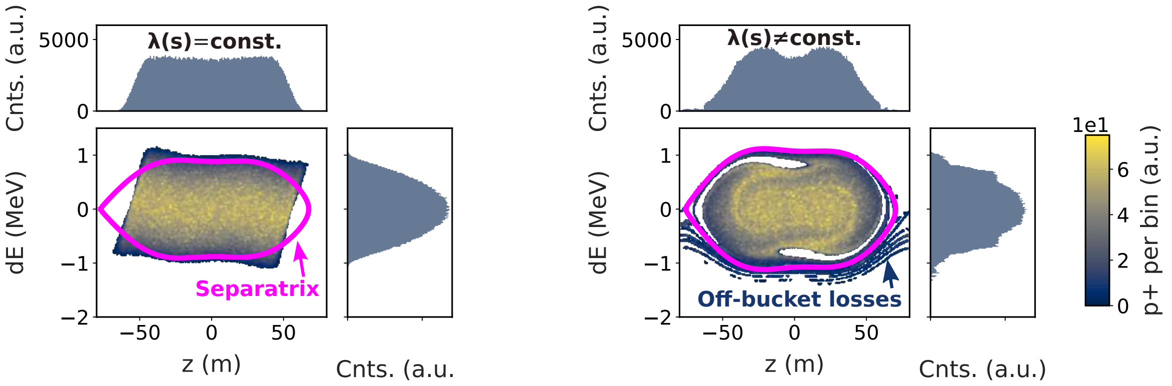

(a) Turn 10.

(b) Turn 2000.

Figure 1.8: Longitudinal filamentation in a double harmonic bucket, for the injection of an LHC-type beam into the PSB. Beam is injected over 32 turns. The line density $\lambda(z)$ changes during filamentation. Particles, which are injected outside the bucket (corners in a) become unstable (off-bucket particles in b) and will be lost around turn 5000 due to increased energy offsets and dispersive effects.

1.4 Transverse Beam Distributions

The descriptions of the transverse dynamics up to now concerned the motion of a single particle in external fields. The multiple particles of a beam are distributed in phase space, each with different betatron actions and phases and respective Courant-Snyder invariants. This section introduces quantities and methods to characterise the transverse properties of the entire particle distribution.

1.4.1 Emittance

The area A of the ellipse circumscribing the phase space occupied by all the trajectories of the individual particles is a measure for the beam size. It is quantified by the *beam emittance* ϵ

$$A = \pi\epsilon. \tag{1.34}$$

For decoupled planes, one can define three independent emittances (ϵ_x, ϵ_y for the transverse and ϵ_z for the longitudinal plane). The transverse emittances are given in units of πmm mrad (when referring the area A) or mm mrad, which is also noted as µm. It is often compared to the temperature of the particle beam. The more diffuse a beam, the larger its area in phase space and thus its emittance. ϵ_{rms} is constant for linear motion, similar to the Courant-Snyder invariant of a single particle.

There are various ways to quantify the emittance from measurement and simulation results. In this thesis, the following two descriptions are used:

- **Root-mean-square (rms) emittance**: The statistical way to describe the area occupied in phase space is

$$\epsilon_{u,\mathrm{rms}} = \sqrt{\left\langle u^2 \right\rangle \left\langle u'^2 \right\rangle - \left\langle u \cdot u' \right\rangle^2}. \tag{1.35}$$

The second moments of the betatronic distribution are related to the $\alpha_u(s)$, $\beta_u(s)$ and $\gamma_u(s)$ by

$$\sigma^2_{u,\mathrm{rms}} = \left\langle u^2 \right\rangle = \epsilon\beta_u \quad (\mathrm{mm}^2) \tag{1.36}$$

$$\left\langle u'^2 \right\rangle = \epsilon\gamma_u \quad (\mathrm{mrad}^2) \tag{1.37}$$

$$\left\langle uu' \right\rangle = -\epsilon\alpha_u \quad (\mathrm{mm\,mrad}). \tag{1.38}$$

- **Emittance based on Gaussian fit:** Populated tails, measurement noise or simulated large amplitude particles can distort the rms width $\sigma_{u,\mathrm{rms}}$ estimates significantly. Therefore, it is also common to retrieve $\sigma_{u,\mathrm{fit}}$ by fitting a Gaussian function to the profile. The resulting emittance reconstruction using Eq. (1.36) is labelled as $\epsilon_{u,\mathrm{fit}}$ in this thesis.

The Courant-Snyder invariant and the emittance are only invariant for constant p_0. When accelerating a particle beam, u' decreases due to $p_u = p_0 u' = m_0 c \beta_\mathrm{r} \gamma_\mathrm{r} u'$. The related decrease of the transverse beam size is known as *adiabatic damping*. However, the area enclosed by (u, p_u) stays constant also for varying p_0. One therefore defines the *normalised emittance*

$$\epsilon_{u,\mathrm{n}} = \beta_\mathrm{r}\gamma_\mathrm{r}\epsilon_u \tag{1.39}$$

as energy independent measure for the beam size. ϵ is referred to as *geometric emittance* in this context. Normalised emittances requested by the post-LS2 PSB users span ≈ 1 to 9 µm.

Dispersive Beam Size

The definition above is based on the second moment of the *betatronic* distribution. However, dispersion D causes an additional transverse spread proportional to the relative momentum spread $\delta \neq 0$. When reconstructing the emittance from measured transverse beam distributions, it is, therefore, necessary to deconvolve the dispersive contribution prior to computing the emittance. Assuming a Gaussian betatronic and momentum distribution, one can use the *standard Gaussian subtraction*

$$\sigma^2_{u,\beta} = \sigma^2_{u,\mathrm{meas}} - \sigma^2_{u,\mathrm{disp.}} = \sigma^2_{u,\mathrm{meas}} - \left(\left(\frac{dp}{p} \right)_\mathrm{rms} \cdot D_u \right)^2. \tag{1.40}$$

This approach is experimentally also applied in first order when measuring non-Gaussian betatronic and/or momentum distributions, but it has to be kept in mind that errors are introduced, as analysed in detail in [61]. Deconvolution algorithms are proposed to provide higher accuracy in emittance reconstructions [62]. However, these algorithms also assume either the betatronic or momentum distribution to be Gaussian. More details are given in the overview in [63].

Emittance Measurements

Emittance measurements are conducted by measuring the beam width σ_{rms} or σ_{fit} using intercepting devices such as *wire scanners* or *scintillator screens* screens (see e.g. [64]). Knowing the β_u and D_u at the location of the measurement device (e.g. the wire scanner), one can compute the emittance using

$$\epsilon_{u,\text{n}} = \frac{\sigma_\beta^2}{\beta_u}\beta_\text{r}\gamma_\text{r}. \tag{1.41}$$

Without prior knowledge of the optics functions, one requires profile acquisitions at multiple locations or with different focusing settings to reconstruct the emittance (e.g. quadrupole scan, 3 or 4 screen method, see [49, Chp. 2.5]).

1.4.2 Transverse Distributions

Control over the transverse distribution is essential to provide the specification for the respective experiments. Additionally, different distributions significantly impact the forces within the particle bunch, such as space charge forces, as will be discussed in Section 1.5.2.

A common distribution in many machines is the *bivariate Normal distribution*, i.e. Gaussian in both planes $u = x, y$,

$$n(x, x', y, y'; s) = \frac{1}{4\pi^2 a_x a_y} e^{-\frac{1}{2}\left(\frac{J_x}{2a_x}+\frac{J_y}{2a_y}\right)}. \tag{1.42}$$

The factors a_x and a_y are scaling factors for the respective plane. Several nonlinear effects such as space charge forces can drive the population of non-Gaussian tails. Such tails can be quantified in various ways e.g. using residuals, the ratio between σ_{fit} and σ_{rms} or fits with the q-Gaussian distribution (see Appendix A.2 or e.g. [65] for details on the q-Gaussian distribution).

Particle beams are called *rms equivalent* in case of equal ϵ_{rms} and intensity, despite being distributed differently (see e.g.[66] for more details). Many properties of real beams can be assessed using a simplified theoretical rms equivalent distribution, such as the *Kapchinsky–Vladimirsky distribution* (K-V, Fig. 1.9a)

$$n(x, x', y, y'; s) = \frac{1}{\pi^2 a_x a_y}\delta\left(\frac{J_x}{2a_x} + \frac{J_y}{2a_y} - 1\right). \tag{1.43}$$

This distribution is purely theoretical and cannot be realised in practice. However, it is commonly used for analytic derivations of e.g. space charge forces in rms equivalent beams. The particles are uniformly distributed in the transverse phase spaces. Each particle has the same sum of horizontal and vertical action $J_x + J_y$. In the 4-D space (x, x', x, y'), it describes a hollow hyper-ellipsoid with uniform surface density. Note that here δ is the Dirac delta function. There is no 6-D variant of a K-V distribution.

Figure 1.9 illustrates rms equivalent Gaussian and K-V distributions for optics parameters in the PSB injection system. The maximum charge density is lower for a K-V than the Gaussian distribution, which will be of importance when discussing space charge effects.

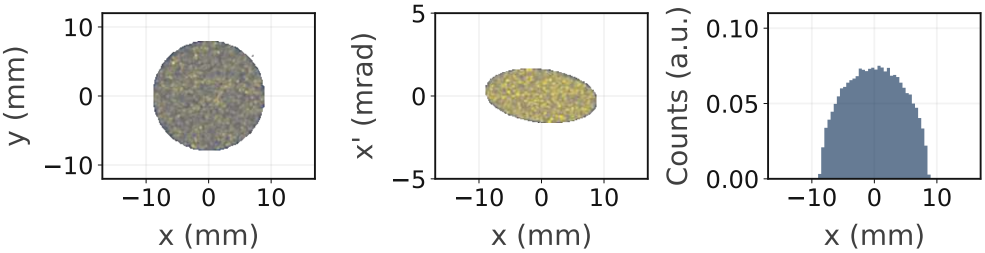

(a) Kapchinsky–Vladimirsky distribution.

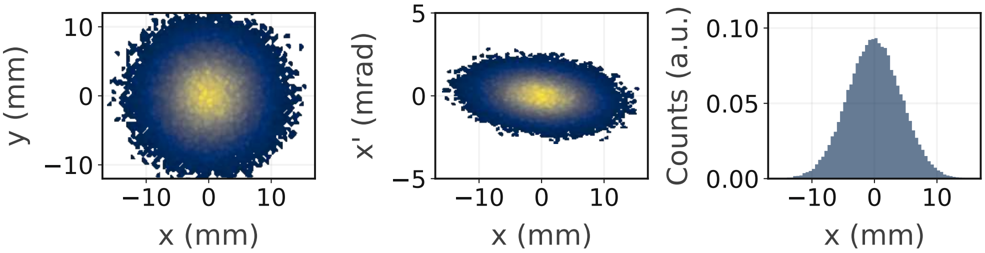

(b) Bivariate Normal distribution.

Figure 1.9: Examples for rms equivalent transverse distributions: illustration of the (x, y) and (x, x') spaces and the respective horizontal profiles. The parameters are similar to LHC-like emittances at PSB injection energy: $\epsilon_{x,\mathrm{n,rms}} = \epsilon_{y,\mathrm{n,rms}} = 2\,\mu\mathrm{m}$, $\beta_\mathrm{r} = 0.52$, $\beta_x = 5.7\,\mathrm{m}$, $\beta_y = 4.5\,\mathrm{m}$, $\alpha_x = 0.2\,\mathrm{rad}$, $\alpha_y = 0.2\,\mathrm{rad}$.

1.4.3 Evolution of Multi-Particle Distributions and Liouville's Theorem

In a linear machine, every particle of the distribution can be described by an ellipse with similar eccentricity and orientation (but different phase and action). The entire distribution is consequently characterised by the ellipse circumscribing all individual particle ellipses. In the presence of nonlinearities, however, different forces act on particles with different actions, which drives a redistribution of the particles and the area covered in phase space deviates from an ellipse. However, according to *Liouville's theorem* the volume occupied in $6D$ phase space can be distorted due to nonlinearities but does not change under the presence of only conservative forces (i.e. when the equations of motion can be derived from a Hamiltonian; compare [67, Chp. 2]).

1.4.4 Intensity and Beam Brightness

An important quantity in accelerator physics is the *beam brightness*, which is a measure for the beam density, i.e. *intensity* (number of particles) $N_{\mathrm{p}+}$ per emittance (beam size)

$$B = \frac{N_{\mathrm{p}+}}{0.5\left(\epsilon_x + \epsilon_y\right)}. \tag{1.44}$$

The intensities delivered from the PSB post-LS2 span a range $N_{\mathrm{p}+} \approx 10^{10}$ to $> 10^{13}$ p+ per ring. The beam intensity can be measured with *beam current transformers* (BCT, see [64]).

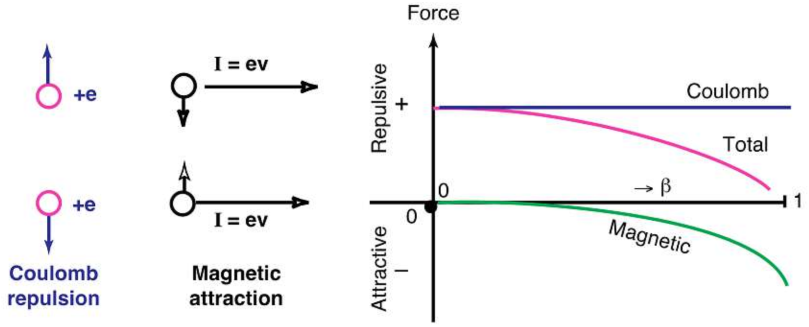

Figure 1.10: Coulomb forces between two point-like particles with equal charge $q_1 = q_2 = e$, moving on parallel trajectories with $v_1 = v_2 = v$ [68].

1.5 Collective Effects and Space Charge

So far, all of the discussed effects involve the individual motion of single particles in external guiding fields. Additionally, it is crucial to consider *collective effects*, which originate in the interaction of the particles with one another and the surroundings and therefore depend on the particle distribution. One of these effects, especially prominent in machines with low energy and high brightness, is *space charge*. *Direct space charge* describes the interaction of particles in a bunch with each other. *Indirect space charge* concerns the interaction of the charged particle beam with image charges and currents, which are induced by the beam distribution itself in the beam pipes. In this thesis, the discussion is restricted to direct space charge effects. This section summarises the impact of direct space charge on particle distributions and mitigation techniques. More details are given e.g. in [66–69].

1.5.1 Forces Between Two Point-Like Charges

In a particle beam, equally charged particles move on (approximate) parallel trajectories with similar velocities v, as illustrated schematically in Fig. 1.10. The particles with charge $q = e$ experience Coulomb repulsion due to the similar charge polarity, but magnetic attraction due to the parallel movement. The net force acting between the two particles with distance r in the lab frame acts in radial direction and can be derived as [67, see e.g.]

$$F_r = \frac{E_r}{\gamma_\mathrm{r}^2} = \frac{e}{4\pi\epsilon_0\gamma_\mathrm{r} r^2}, \tag{1.45}$$

with the vacuum permittivity ϵ_0. This expression is proportional to $\propto 1/\gamma_r^2$. The net force hence vanishes for relativistic energies with $v \longrightarrow c$, as the Coulomb repulsion and the magnetic attraction compensate each other (see Fig. 1.10). Space charge effects are therefore only relevant at low energies.

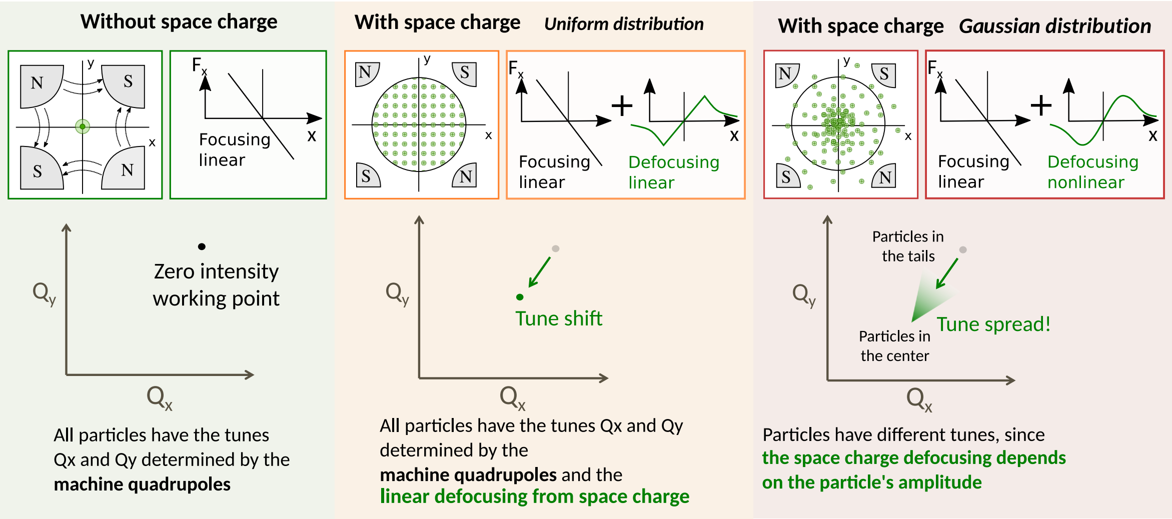

Figure 1.11: Tune footprints for different scenarios. Left: linear lattice (only dipoles and quadrupoles), without space change; center: K-V distribution in a linear lattice with space charge forces; right: bi-Gaussian distribution, yielding nonlinear space charge forces, in a linear lattice. Adapted from [67, 68].

1.5.2 Direct Space Charge Tune Spread

This Coulomb repulsion has a defocusing effect in both planes. Consequently, compared to a linear machine without space charge, in which the tune is given by the external quadrupole settings (Fig. 1.11, left), space charge causes a reduction of the particle tune (Fig. 1.11, centre and right). The net field that a test particle sees and the consequent tune reduction depends on the entire particle distribution and cannot be calculated analytically for real distributions. However, several approximations can be made, for example by using rms equivalent model distributions. The force on a particle in a K-V distribution (uniformly charged cylinder with radius a and constant line density $\lambda =$ const.) can be derived as (see e.g. [68])

$$F_x = \frac{\lambda e}{2\pi\epsilon_0\gamma_{\mathrm{r}}^2 a^2}x \tag{1.46}$$

$$F_y = \frac{\lambda e}{2\pi\epsilon_0\gamma_{\mathrm{r}}^2 a^2}y. \tag{1.47}$$

It is linear in x and y and can be compared to the defocusing effect of a quadrupole in both planes. The consequent tune reduction can be obtained by adding the space charge contribution as a perturbation term to the Hamiltonian or the equations of motion. For a K-V distribution, the perturbation term is a quadrupolar error and the tune shift

$$\Delta Q_{u,\mathrm{KV}} = -\frac{r_0 R}{e\beta_{\mathrm{r}}\gamma_{\mathrm{r}}^2}\frac{\lambda}{\epsilon_{u,\mathrm{n}}}, \quad r < a, \tag{1.48}$$

equal for all particles (Fig. 1.11, center). R denotes the machine radius and $r_0 = e^2/\left(4\pi\epsilon_0 m_0 c^2\right) = 1.54 \times 10^{-18}$ m the classical particle radius.

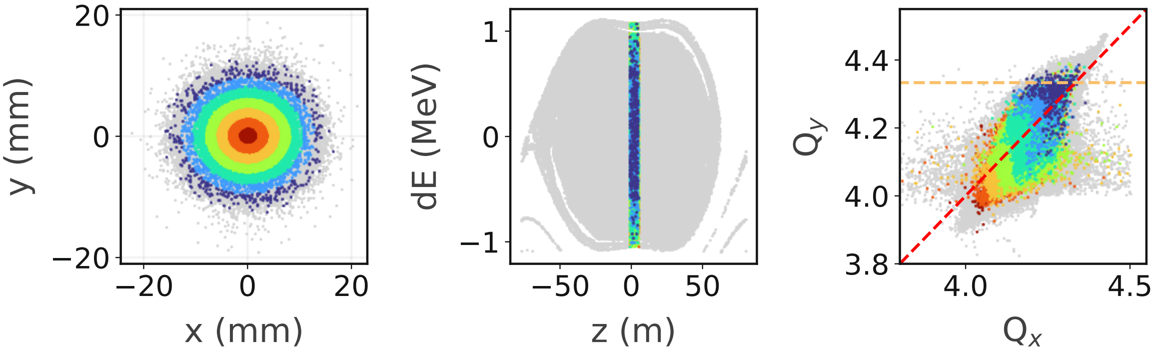

Figure 1.12: Transverse x-y (left), longitudinal ΔE-z (center) and tune distribution Q_x-Q_y (right) for an LHC-like beam in the PSB. Particles from a slice of the longitudinal distribution are highlighted and colour-coded according to the transverse radial component.

However, coasting beams with nonuniform transverse distribution (e.g. Gaussian) generate nonlinear forces and hence a different detuning for each particle (Fig. 1.11, right). This gives rise to a distribution of tunes rather than a tune shift, the *incoherent tune spread*. For small transverse amplitudes $r \ll \sigma_u$ in a Gaussian transverse distribution, one can linearise the force to obtain the detuning of particles close to the core as

$$\Delta Q_{u,\text{Gauss-max}} = \overset{\text{I}}{\boxed{-}}\,\frac{r_0 R}{e\,\underset{\text{II}}{\boxed{\beta_\mathrm{r}\gamma_\mathrm{r}^2}}}\,\underset{\text{III}}{\boxed{\frac{\lambda}{\epsilon_{u,\mathrm{n}}}}}\cdot\overset{\text{IV}}{\boxed{2}},\quad r \ll \sigma_u. \tag{1.49}$$

The following key points are highlighted:

I The detuning is always negative, i.e. direct space charge effects always defocus in both planes and reduce the betatron oscillation frequency.

II The space charge forces are dominant at low energy and vanish for $v \longrightarrow c$ due to the dependence $\Delta Q \propto 1/\beta_\mathrm{r}\gamma_\mathrm{r}^2$ (when expressed using ϵ_n).

III The space charge effects are directly proportional to the intensity (here given by the longitudinal line density λ) and indirectly to the transverse emittance. The detuning increases with the beam brightness.

IV The maximum detuning of a beam with Gaussian cross-section is approximately twice the tune shift of an rms equivalent K-V distribution. This can be explained by the increased charge density in the Gaussian beam core. In contrast to that, a K-V distribution gives rise to the smallest possible tune spread.

The simulated tune footprint for a bi-Gaussian LHC-like beam in the PSB beam is illustrated in Fig. 1.12 and is analysed in detail e.g. in [60, Chp. 4]. The particles are colour-coded according to the position in the bi-Gaussian transverse distribution (for a single slice from the longitudinal distribution at $z \approx 0\,\mathrm{m}$). The tune shift is the largest for particles in the beam centre (red) and the smallest for the tails (dark blue). For nonconstant longitudinal line densities $\lambda \neq$ const., as present in a real machine, each longitudinal slice at s experiences a different detuning depending on $\lambda(s)$.

1.5.3 Particle-In-Cell Simulations

Space charge is a collective effect and it is, therefore, necessary to compute the propagation of the entire particle ensemble rather than tracking individual particles.

In the CERN injector chain, pyORBIT [70] is used for space charge simulations. This is a python wrapper for the Particle-in-Cell (PIC) solver PTC-ORBIT [71]. The PIC method is a so-called *self-consistent method* and is based on the following concepts:

- The large number of real particles is represented by a smaller number of *macroparticles* with extrapolated properties, i.e. "particle clumps".
- Each of these macroparticles is propagated individually through the external guiding fields using a *tracking code*, here PTC [72].
- The propagation is regularly halted at *nodes*, at which the macroparticle distribution is mapped onto a *mesh* (grid) to obtain a local charge density estimate.
- At each node, a *field solver* solves Maxwell's equations to obtain the space charge field based on this meshed density estimate. In pyORBIT, the ORBIT code provides a 2.5D-Fast Fourier Transform (FFT) Poisson solver to estimate the nonlinear local space charge forces. These are subsequently applied as additional force kicks before propagating the particle distribution to the next node.

Such self-consistent methods hence derive the space charge field directly from the locally observed particle distribution. They are computationally expensive but do not require any approximation regarding particle distributions, in contrast to other techniques (e.g. *frozen* approach based on the Bassetti-Erskine formula [73]).

Using MADX-PTC [58] one can create a realistic machine model, which is subsequently used in pyORBIT. This enables the inclusion of time-varying fields, scattering effects of the stripping foil, apertures, edge effects, magnetic field and alignment errors.

1.5.4 Space Charge Driven Resonances and Emittance Exchange on the Montague Resonance

So far, machine imperfections and magnet nonlinearities have been introduced as the primary driving term for resonances. In addition to these external forces, resonances can be driven by the space charge potential itself: the distribution and hence space charge potential is modulated with the focusing properties of the machine. It is therefore periodic with the lattice structure and can drive single particle resonant effects. Assuming frozen space charge and a symmetric, bi-Gaussian beam, which is matched to the machine optics, these resonances can be derived by including the terms of the expanded space charge potential (compare [74])

$$
\begin{aligned}
V_{SC}(x,y) &= -\frac{\lambda r_0}{\beta_r^2\gamma_r^2}\int_0^\infty \frac{1-e^{-\frac{x^2}{2\sigma_x^2+t}-\frac{y^2}{2\sigma_y^2+t}}}{\sqrt{\left(2\sigma_x^2+t\right)\cdot\left(2\sigma_y^2+t\right)}}\,dt, \\
&= -\frac{\lambda r_0}{\beta_r^2\gamma_r^2}\Bigg(\left(\frac{x^2}{\sigma_x\left(\sigma_x+\sigma_y\right)}+\frac{y^2}{\sigma_y\left(\sigma_x+\sigma_y\right)}\right)- \\
&\qquad \left(\frac{(2\sigma_x+\sigma_y)x^4}{12\sigma_x^3\left(\sigma_x+\sigma_y\right)^2}+\frac{(2\sigma_x+\sigma_y)y^4}{12\sigma_y^3\left(\sigma_x+\sigma_y\right)^2}+\frac{x^2y^2}{2\sigma_x\sigma_y\left(\sigma_x+\sigma_y\right)^2}\right)+\ldots\Bigg)
\end{aligned}
\tag{1.50}
$$

as perturbation terms to the nonperturbed Hamiltonian [75] (see e.g. [76, Chp. 2.1] or [77] for more details). The pseudo-octupole term $V_{SC} \propto x^2y^2$ ($\propto J_x \cdot J_y$ after the Floquet transform) drives the 4th-order single particle difference resonance

$$2Q_x - 2Q_y = 0. \tag{1.51}$$

Particles close to $Q_x = Q_y$ interact with this so-called *Montague resonance* [75]. This results in a coupled motion between the two transverse planes characterised by an exchange between the actions J_x and J_y. This effect is particularly prominent for "flat beams", which have a small tune spread in one and a large tune spread in the other plane due to the unequal emittances. To avoid undesirable emittance exchange, the overlap of the tune spread with the coupling resonance is often avoided in operation by choosing unequal (split) tunes Q_y and Q_x.

As mentioned above, the derivation of this single particle resonant effect assumes frozen space charge for a symmetric, bi-Gaussian beam, which has constant longitudinal line density and is matched to the machine optics. Such a beam has unchanged charge distribution and no coherent beam movement. However, this image is hardly realistic, especially not directly after injection. A coherent motion, e.g. oscillation of an initially mismatched beam, drives time-varying forces, which can also excite the Montague resonance. It is not possible to approximate these effects using the frozen space charge approach. Self-consistent modelling, e.g. with a PIC code, is required. A detailed discussion of emittance exchange in anisotropic beams, which goes beyond the here presented treatment as a single particle resonance phenomenon, is given in [69].

1.5.5 Impact on Machine Performance and Mitigation

For large tune footprints, i.e. $\Delta Q \rightarrow 0.5$, it becomes not possible to avoid interaction of all detuned particles with strong resonances, mainly integer and half-integer, as illustrated schematically in Fig. 1.13 for $Q_x = 4.4$, $Q_y = 4.55$. Particles from the beam core that are excited by resonances are driven to the outside of the distribution, causing an emittance growth (case A in Fig. 1.13), beam brightness reduction and hence also reduction of the tune spread. This space charge-driven emittance growth takes place until the maximum detuning is reduced to a level, which avoids any further interaction of core particles with such resonances. Interaction of the distribution

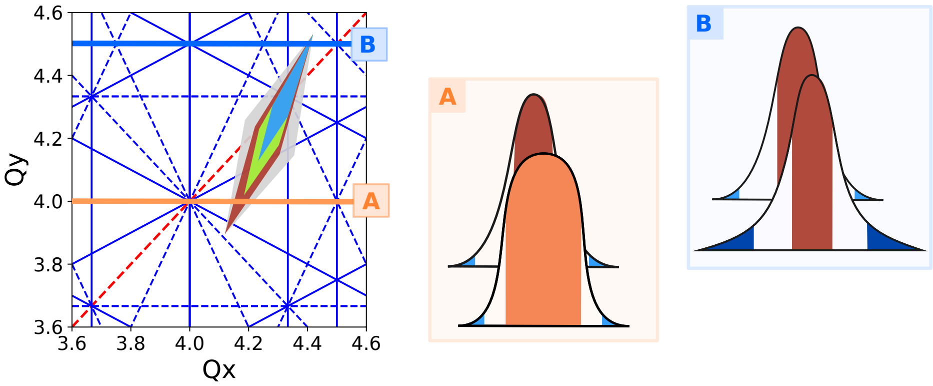

Figure 1.13: Interplay of a large tune footprint with resonances. The horizontal half-integer resonances are indicated in blue, and the integer resonances in orange. In this scenario, the beam core (red shaded area, same colour code as in Fig. 1.12) interacts with the integer resonances, causing emittance growth and a consequent brightness and tune spread reduction (case A). The particles in the tails (blue shaded area) interact with the half-integer resonances, the tails get populated and the particles are lost in the machine aperture.

tails (minimum detuning, close to the nominal WP) with strong resonances populates these tails further until particles are eventually lost in the machine aperture (case B in Fig. 1.13).

Overall, this explains the often quoted *space charge limit* of a synchrotron: $\Delta Q_{\mathrm{max}} \approx 0.5$ is considered to be the maximum acceptable detuning for providing a steady particle distribution without emittance growth and particle losses. Space charge is therefore a limiting factor when producing high brightness beams in low energy machines. However, Eq. (1.49) inspires several common mitigation techniques, which help to reduce the tune spread to a certain extent and push the delivered bream brightness, such as increased injection energy, smaller machine circumference, reduced line density or reduced transverse charge density. The latter is targeted by phase space painting, i.e. optimisation of the transverse distribution during the injection process. As discussed in Section 1.5.2, a minimised tune footprint could be theoretically obtained by generating a uniform transverse distribution.

1.6 Particle-Matter Interactions with Thin Scatterers such as Stripper Systems

Ion beams can be intercepted by a thin scatterer, such as a beam screen for measurements or a stripping foil in a CEI. The impacting ions undergo inelastic and elastic interactions with the electric field of the target atoms, which cause energy deposition in the target, distort the beam distribution and cause losses in the surrounding machine elements. Generally, the energy deposition in the target and the scattered distributions depend on several factors, such as beam energy, emittance, intensity and material properties of the target. The main particle-matter interaction mechanisms for low energy ion beams with a stripping foil are outlined below.

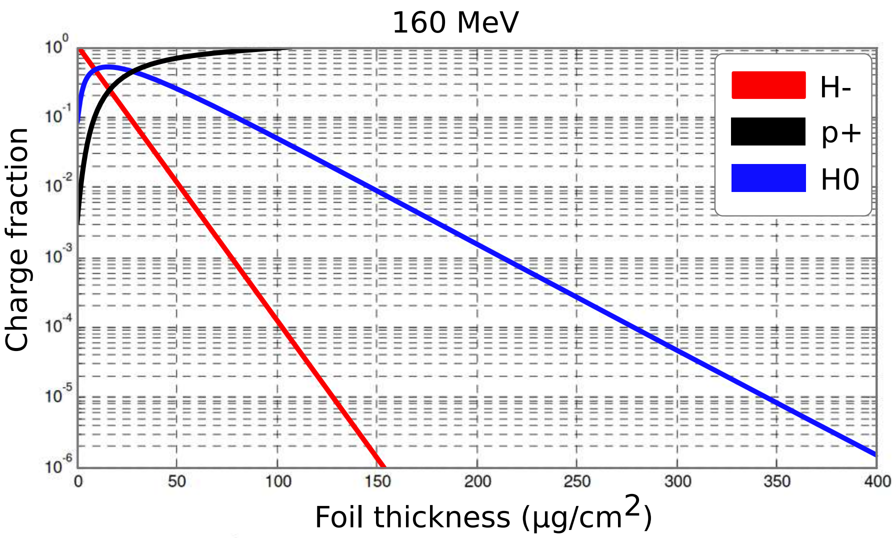

Figure 1.14: H$^-$, H^0 and p$^+$ yield as a function of stripping foil thickness for an 160 MeV H$^-$ beam impacting a carbon foil [78].

Electron stripping of the impacting H$^-$ beam: The electrons of the impacting H$^-$ beam are stripped in collisions with electrons or nuclei of the carbon foil. The probability of obtaining H$^-$, H^0 and p$^+$ when impacting a foil with thickness d with an H$^-$ beam can be computed using the cross-sections for one- and two-electron stripping. For the PSB stripping foil, this is done in [78] and illustrated in Fig. 1.14. The H$^-$, H^0 and p$^+$ yields depend on the foil thickness, the material and the energy of the impacting beam. The chosen foil thickness for a CEI must be large enough to achieve negligible probabilities of H^0/H$^-$ survival (blue and red lines in Fig. 1.14). In the PSB, a foil thickness of 200 µg cm^{-2} to provide a p+ yield of $> 99\,\%$.

Single and multiple Coulomb scattering: The impacting ions experience elastic scattering by the Coulomb interaction with the Carbon atoms of the foil, which is known as *Rutherford* or *Coulomb scattering*. Due to the lower mass of the incoming particles, energy transfer can usually be neglected in such collisions. Each single scattering event, however, adds a small angular deflection to the original particle trajectory. During the passage of a thin scatterer a particle experiences multiple such elastic small angle deflections. Simulation codes such as pyORBIT [70][†] or FLUKA [80, 81], repeat the single Coulomb scattering event multiple times during a foil passage, generating at each step a random scattering angle and random distance to the next scattering event.

The majority of the scattering events result in small scattering angles. The combined net deflection Θ from the original particle trajectory as a cumulative effect of multiple small scattering angles can be analytically approximated, which is known as *multiple Coulomb scattering*. The cumulative angle is normally distributed (central limit theorem; usually valid for more than

---

[†] In this thesis the *Simple Scattering Model* is applied, which is based on [79]. pyORBIT also provides a *Full Scattering Model*, which additionally simulates nuclear scattering events and energy loss. However, this model uses Moliere's Gaussian approximation for the multiple Coulomb scattering and is thus not applicable for low energy beams impacting thin stripping foil [39].

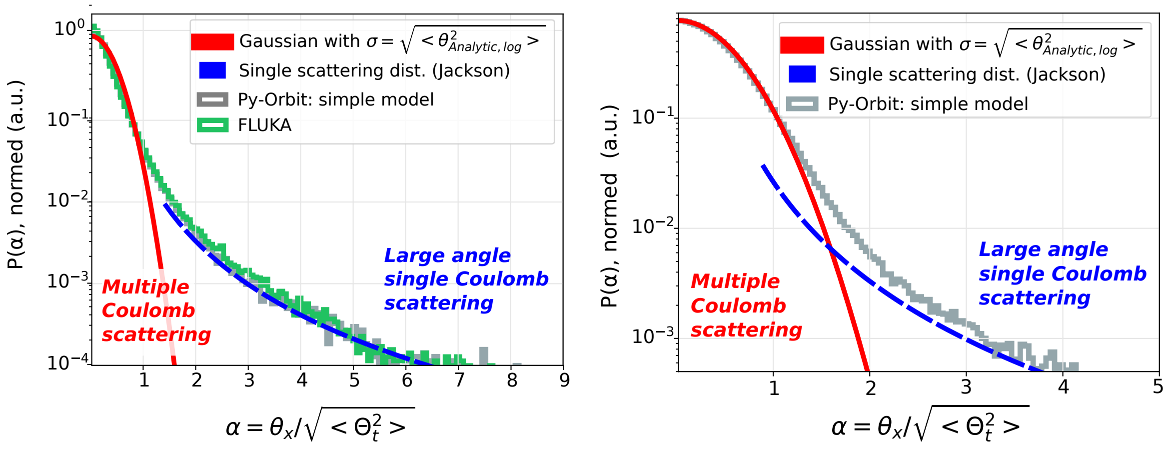

(a) d = 200 μg/cm^2. **(b)** d = 50 mg/cm^2.

Figure 1.15: Angular distributions of the scattering angles obtained for a 160 MeV H$^-$ beam impinging a carbon foil. The histograms (grey and green) show the simulated particle distribution after the respective foil passage. The multiple Coulomb Gaussian approximation with logarithmic correction is illustrated in red. The analytic approximation for the large angle single Coulomb scattering distribution is marked in blue (dashed).

20 scattering events [79]). The expected scattering angle $\sqrt{<\Theta^2_{\mathrm{MC}}>}$ (projected onto a plane, e.g. $u = x, y$) obtained when a particle beam with momentum p intercepts a target with length l_{target} is approximated by Moliere's formula [82] with logarithmic correction for thin targets [83]

$$\sqrt{<\Theta^2_{\mathrm{MC}}>} = \frac{13.6}{p\,[\mathrm{MeV}]\beta_{\mathrm{r}}c}\sqrt{\frac{l_{\mathrm{target}}}{L_{\mathrm{rad}}}} \cdot \left(1 + 0.038 \cdot \ln\frac{l_{\mathrm{target}}}{L_{\mathrm{rad}}}\right). \tag{1.52}$$

The radiation length $L_{\mathrm{rad}} = 19$ cm is specific for the target material, i.e. here carbon. In a CEI, the circulating beam crosses a stripping foil with thickness d multiple, i.e. N_{F}, times. The total 'target thickness´ is consequently $l_{\mathrm{target}} = N_{\mathrm{F}} \cdot d$.

This approximation is valid for the core of the resulting angular distribution but does not represent the tails. These are dominated by rare *large angle single Coulomb scattering* events due to small impact parameters, as analytically formulated in [84, Chp. 13]. Large angle scattering events cause beam loss, which is analysed in [78] for the PSB injection system and aperture.

The transition between the single and multiple Coulomb scattering distributions (*plural scattering*) depends on the thickness of the target and the beam energy. Figure 1.15 shows the expected distribution of scattering angles for parameters, which are similar to the PSB injection process: an 160 MeV H$^-$ pencil beam impinges a 200 μg cm^{-2} (Fig. 1.15a) or ≈ 50 mg cm^{-2} carbon foil (Fig. 1.15b). The latter is equivalent to ≈ 250 crossings of the PSB foil.

The distribution of the resulting scattering angles can be obtained using simulation codes, e.g. pyORBIT (grey in Fig. 1.15) or FLUKA (green) [85]. It can be seen, that the core of the simulated distribution can be approximated by Molière's formula with logarithmic correction (Eq. (1.52), red), whereas the tails follow the single Coulomb scattering distribution ([84, Chp. 13]; blue, dashed). It is evident, that with increasing foil passages (i.e. thicker equivalent target thickness), Molière's formula with logarithmic correction becomes more accurate for the entire distribution.

Nuclear scattering: Both, inelastic and elastic nuclear scattering yield particle loss due to large angle scattering. For the PSB, these losses are estimated to be $\mathcal{O}(10^{-5}\text{-}10^{-4})$ [78] and are not considered further in this thesis.

Foil heating and energy loss straggling: Inelastic collisions with the electrons of the target atoms result in energy loss of the particle beam and foil heating. In the PSB, the expected peak foil temperature during high-intensity beam production was estimated to be $\approx 650\,\mathrm{K}$ [78]. This is low compared to temperatures of $\approx 1500\,\mathrm{K}$, which are required in high power facilities such as spallation neutron sources. Foil heating is not expected to be problematic for the foil's lifetime or performance in the PSB. The average energy loss for a single foil passage in the PSB injection was estimated as $dE = 0.96\,\mathrm{keV}$, which was shown to be negligible in first order for the beam production in the PSB [78].

CHAPTER 2

The New PSB Injection System as Part of the LHC Injectors Upgrade

Connecting Linac4 to the PSB and the related increase in injection energy allows for doubled beam brightness, as required for HL-LHC [9], while maintaining the tune-spread induced by space charge as pre-LS2 ($\propto N_{\mathrm{p+}}/(\gamma_{\mathrm{r}}^2\beta_{\mathrm{r}}) \approx -0.5$). The charge exchange mechanism is further significant for reducing losses during the injection of high-intensity beams. Accumulating high intensities over multiple turns in a conventional multi-turn injection system, as done pre-LS2, produces high losses at the required septum (see [86] for more details). With the new CEI system, similar beams can be generated while keeping losses during the injection process within $< 1\,\%$ (a few percent along the cycle).

This section provides a brief introduction to both the Linac4 and the PSB and highlights the relevant machine parameters, with a particular focus on the new injection system and phase space painting.

2.1 Linac4

Figure 2.1 displays the 86 m long Linac4 [12] and its location on the CERN site. The first stage after the H^- source [12, Chp. 2.1], the radiofrequency quadrupole (RFQ) [12, Chp. 2.2], accelerates a pulse with $\approx$ 600 µs length to 3 MeV. The beam subsequently passes the chopper line [12, Chp. 2.3], which is described in more detail in Section 2.3.1. The following structures (i.e. a drift tube linac, a cell-coupled drift tube linac and Pi–mode structures [12, Chp. 2.5-2.7]) bring the then already bunched beam to the final energy of 160 MeV. A debuncher cavity [12, Chp. 2.8] is programmed pulse-per-pulse to modify the beam energy spread according to user-specific requests. The beam has a natural energy spread of 250 keV, which is altered operationally between $\approx$ 100-440 keV [87] by the debuncher cavity. Table 2.1 summarises the main Linac4 parameters, including the performance and settings during the first post-LS2 operational year (2021) [88].

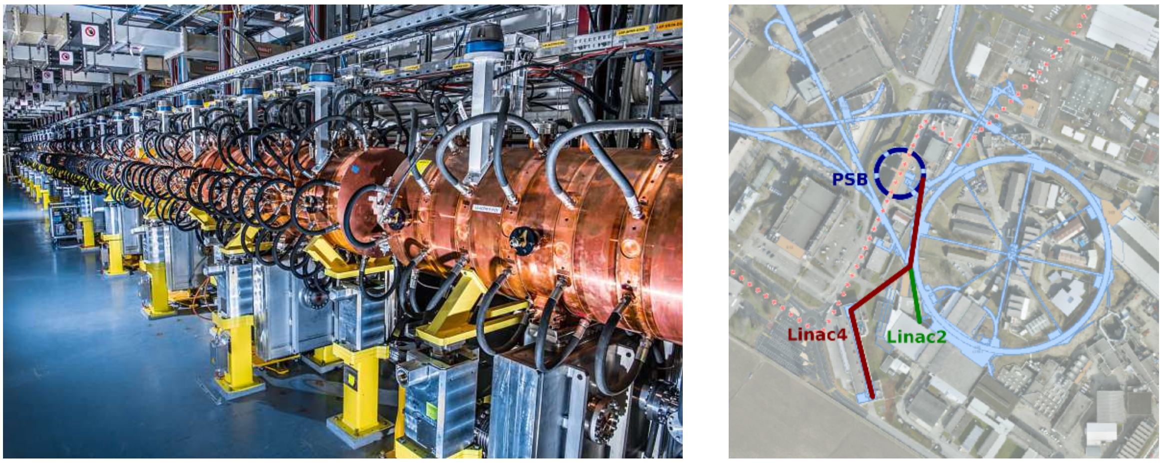

(a) Accelerating cavities of Linac4 [89].

(b) Satellite view of the CERN infrastructure.

Figure 2.1: CERN's newest accelerator Linac4 provides 160 MeV H⁻ ions.

Table 2.1: Linac4 parameters [12] and operational performance in 2021 [88, 90, 91].

Parameter	Unit	Value
Linac4 parameters		
Length	m	86
Ion species	-	H^-
Output energy	MeV	160.7
Bunch frequency	MHz	352.2
Maximum repetition rate (i.e. cycles / second)	Hz	2
Operational repetition rate (i.e. cycles / second)	Hz	0.83
User-specific settings 2021 (pulse-per-pulse)		
Chopping factor	-	0.3-0.7
Energy spread after debuncher cavity	keV	100, 280 and 440
Performance in 2021 [88]		
Natural energy spread before debuncher cavity	keV	250
Source current	mA	35
RFQ current	mA	28
Normalised rms emittance H / V	µm	<0.3 / 0.3
Shot-to-shot intensity fluctuations	%	< 2
Shot-to-shot energy fluctuations	keV	< 100
Shot-to-shot transverse position	mm	<1.5

2.2 Proton Synchrotron Booster

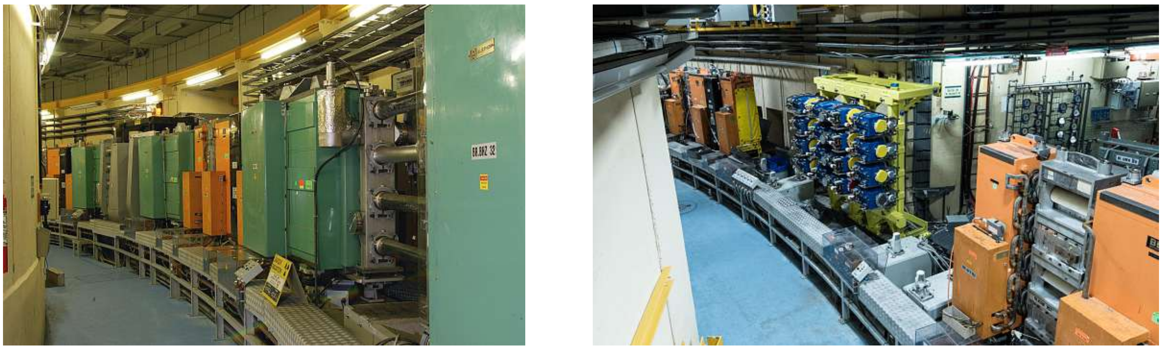

(a) The four PSB rings, with the main dipoles (green) and quadrupoles (orange) [92].

(b) The new PSB injection system during the installation phase in 2019, displaying the 16 BSW magnets (4 per ring) in blue [93].

Figure 2.2: The CERN PSB in its tunnel (a) before and (b) during the upgrades during LS2 (2019/2020).

2.2.1 Layout

The PSB has a circumference of 157 m with the unique property that it consists of four superposed rings to accelerate beams simultaneously (Fig. 2.2). It is divided into 16 equal sections, also called *periods* (labelled as P01-P16, Fig. 2.3), i.e. segments with similar lattice structure and symmetric optical properties. Each period comprises two main dipoles for horizontal bending, two focusing and one defocusing quadrupole. Dipole and multipole corrector magnets are installed in the straight sections between the main dipoles and quadrupoles for enhanced beam control. The main parameters are summarised in Table 2.2. Beam position (BPM) and beam loss monitors (BLM) are installed in each period, which enables the acquisition of the transverse position and the beam losses at the respective location (yellow scatter markers for BPM-1 to BPM-16 and green for the BLMs in Fig. 2.3). A more detailed layout is provided in [94, 95].

The entire PSB cycle lasts 1.2 s. In this thesis, time in ms relative to the start of the cycle (*C-time*) is used to refer to time instances within the cycle. The beam is injected at the cycle time 275 ms, which is labelled as C275. It takes 530 ms to accelerate beam from 160 MeV to 2 GeV. Extraction takes place at cycle time 805 ms (C805).

2.2.2 PSB History and Upgrades

The PSB was first inaugurated in 1972 to increase the PS injection energy by pre-accelerating a beam up to 800 MeV. Soon after, an energy upgrade increased the extraction energy to 1 GeV (1988). During that time, the only recipient of PSB beams was the PS. In 1992, the PSB also started to deliver beam to the ISOLDE facility. With the motivation to produce adequate beams

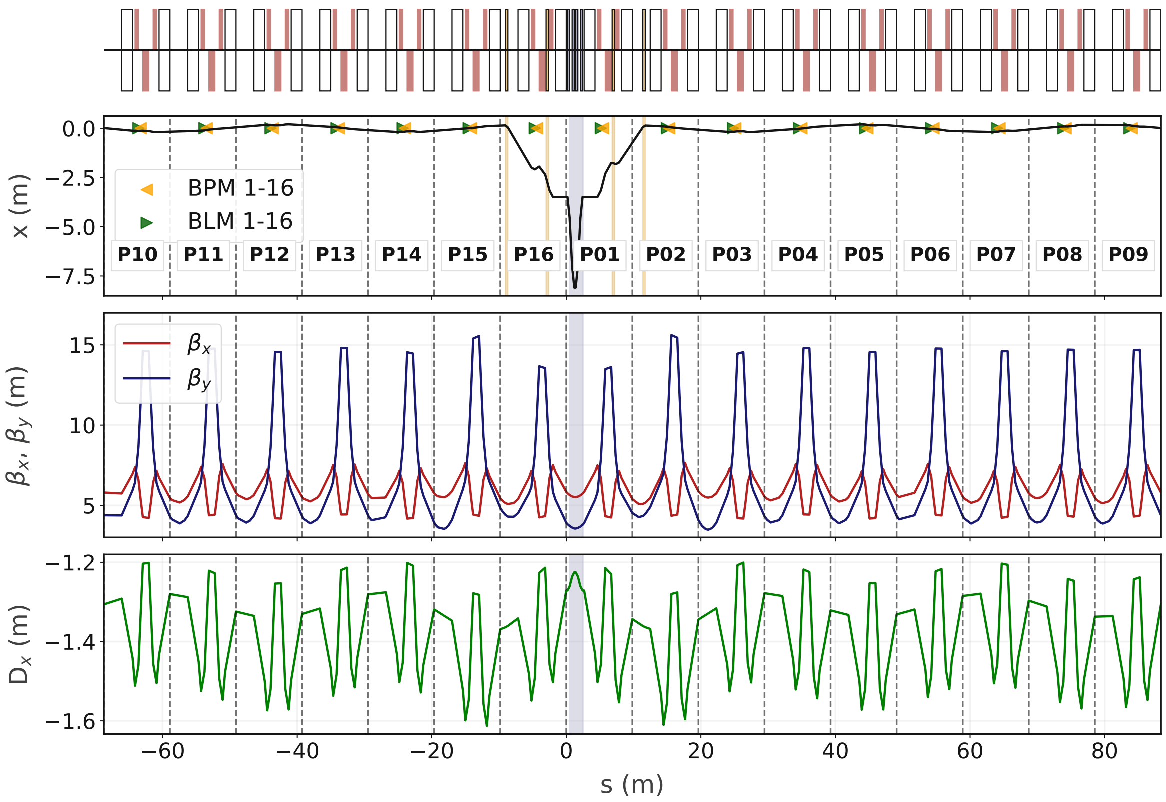

Figure 2.3: Optics and synoptic layout of the PSB. Top: synoptic layout, displaying the dipoles (white) and quadrupoles (red). Center and bottom: Twiss parameters for optics configurations as applied during the injection of fixed target beams ($Q_x = 4.22, Q_y = 4.45$). The 16 periods with similar lattice structures are separated by the dashed lines. The injection region in P01 is highlighted by the grey shaded region.

for the LHC era starting in 2008, the extraction energy of the PSB was increased another time to 1.4 GeV in 2000 [96]. The last major upgrades of the PSB, which were conducted in 2019 and 2020 as part of the LIU project, include among others:

- **Upgrades of the injection line (BI line) and injection period (see Section 2.3):** Apart from the installation of the new CEI system, significant modifications were also required in the transfer line between Linac4 and PSB (BI Line) due to the higher injection energy and the increased beam rigidity.
- **Upgrades of the PSB rings and the extraction lines:** The extraction energy is increased from 1.4 GeV to 2 GeV to reduce space charge effects during PS injection. The required modifications include a new power converter system, a new magnet powering scheme [10, Chp. 3.6] and the installation of a new wideband RF system based on Finemet® magnetic alloy [97, 98]. Additionally, modifications in the PSB extraction line were necessary to meet the requirements of the increased beam rigidity.

Table 2.2: PSB parameters before and after the LIU upgrades [10].

Parameter	Unit	Value	
Circumference	m	157.08	
Radius	m	25	
Rings	#	4	
Ion species	-	p+	
Bunches per ring at injection	#/ring	1	
Bunches per ring at extraction	#/ring	1 - 2	
Cycle length	s	1.2	
Typical tunes at injection	-	$Q_x \approx$ 4.1-4.4	
	-	$Q_y \approx$ 4.17-4.45	
	-	$Q_s \approx 0.001$	
		Pre-LS2	**Post-LS2**
Injection energy	MeV	50	160.7
Extraction energy	GeV	1.4	1.4 (ISOLDE) and 2.0 (PS)
β_r, γ_r at injection	-	0.31, 1.05	0.52, 1.17
β_r, γ_r at extraction to PS	-	0.92, 2.5	0.95, 3.13
β_r, γ_r at extraction to ISOLDE	-	0.92, 2.5	0.92, 2.5
Revolution frequency at injection	MHz	0.577	0.994
Revolution frequency at extraction	MHz	1.75	1.75 (ISOLDE) and 1.8 (PS)
Intensity per ring	p+/ring	0.5-1000 $\times 10^{10}$	0.5-1600 $\times 10^{10}$*
H: normalised emittance $\epsilon_{\mathrm{n},x}$	µm	≈1-15	≈0.5-10
V: normalised emittance $\epsilon_{\mathrm{n},y}$	µm	≈1-9	≈0.5-6
RF system harmonics	-	$h = 1, 2$ and 16	Multi-harmonic

* Final target. In 2021, operation with maximum $N_{\mathrm{p}+} = 1 \times 10^{13}$ p+.

2.3 The PSB Injection Process and Beam Transfer from Linac4

2.3.1 Linac4 Pulse Structure and Intensity Injected per Turn

The number of protons injected into each PSB ring depends on the current delivered from Linac4. In Linac4, it is possible to remove part of the pulse at 3 MeV using the chopper [12, Chp. 2.3]. This electrostatic kicker is located in the low energy segment of Linac4 and transmits only the segments of the Linac4 pulse, which are requested by the PSB. This facilitates to inject the beam directly into the PSB RF bucket and reduces losses during the beam transfer and injection process at 160 MeV. The *chopping factor* (CF) quantifies the fraction of the transmitted beam current $I(t)$ and is related to the intensity injected during each PSB turn by [99]

$$\frac{N_{p+}}{\text{PSB turn}} = \frac{1}{\text{proton charge}} \int_0^{t_\mathrm{rev}} I(t)dt = \frac{1}{1.6 \times 10^{-19}} \left(CF \cdot I_\mathrm{peak} \cdot t_\mathrm{rev,PSB}\right) . \tag{2.1}$$

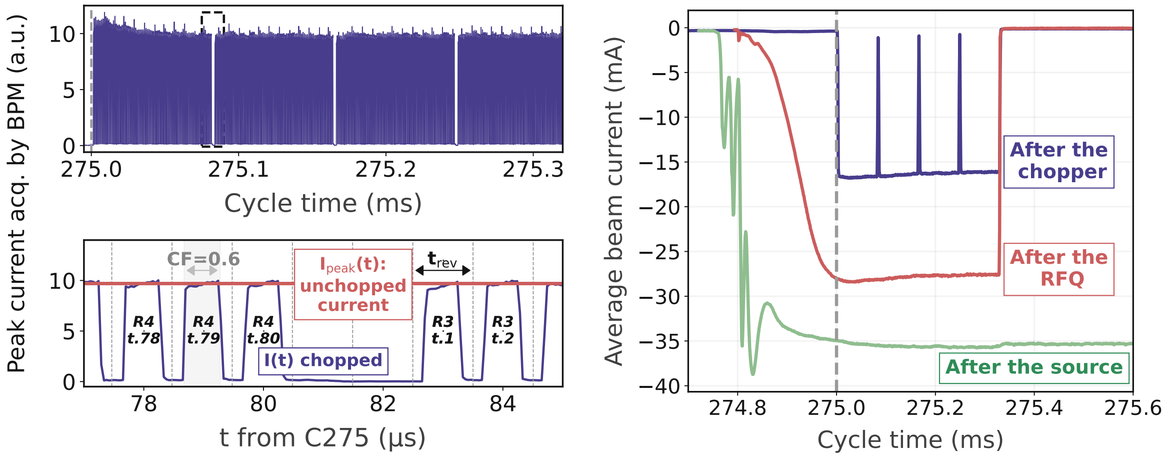

(a) The chopped beam intensity seen by a BPM in the transfer line (BI.BPM0, absolute values differ due to calibration). Bottom: enlarged view of the last and first bunches injected into R4 and R3, respectively.

(b) Measured average beam current after the source (green), the RFQ (red) and the chopper line (blue).

Figure 2.4: Linac4 current and beam chopping pattern measured for a high-intensity user, when injecting with $CF = 0.6$ over 80 turns into each PSB ring (ISOLDE in 2022; representative for the state in 2021).

I_{peak} is the peak current of the unchopped beam at the PSB injection ($I_{\text{peak}} = 26$ mA in 2021) and $t_{\text{rev}} = 1.006$ µs the PSB revolution time at injection energy. The CF is customised for each user, with typical values between 0.3-0.7. Figure 2.4a shows the current seen by the BPMs in the beam transfer to the PSB, which clearly features the chopped beam pattern (here for a high-intensity beam with injection over 80 turns into each ring and $CF = 0.6$). Figure 2.4b illustrates the respectively average current measured in Linac4 directly after the source (green, -35 mA), after the RFQ (red,-28 mA) and after the chopper (blue,-16.3 mA). The current after the chopper (blue) exhibits the pulse segments separated for the four rings.

2.3.2 The New Charge Exchange Injection System

The chopped beam is injected into the PSB via the new CEI. A schematic of the new injection system is described in the Introduction (Fig. B). The system comprises a carbon stripping foil and a horizontal orbit bump to deflect the circulating towards the injected beam. The closed orbit bump has a nominal amplitude of $\Delta x = -81$ mm at the foil and is created by two sets of magnets, the painting kicker (KSW, $\Delta x_{\text{KSW}} = -35$ mm bump, yellow in Fig. 2.1) and the injection chicane magnets (BSW, $\Delta x_{\text{BSW}} = -46$ mm bump, blue in Fig. 2.1).

Injection Chicane with H^0/H^- Dump

The injection chicane comprises four short rectangular dipole magnets in the injection region, each providing a 66 mrad deflection angle. The first BSW magnet (BSW1) acts as a magnetic septum, dividing the circulating beam's high-field region from the field-free region for the injected

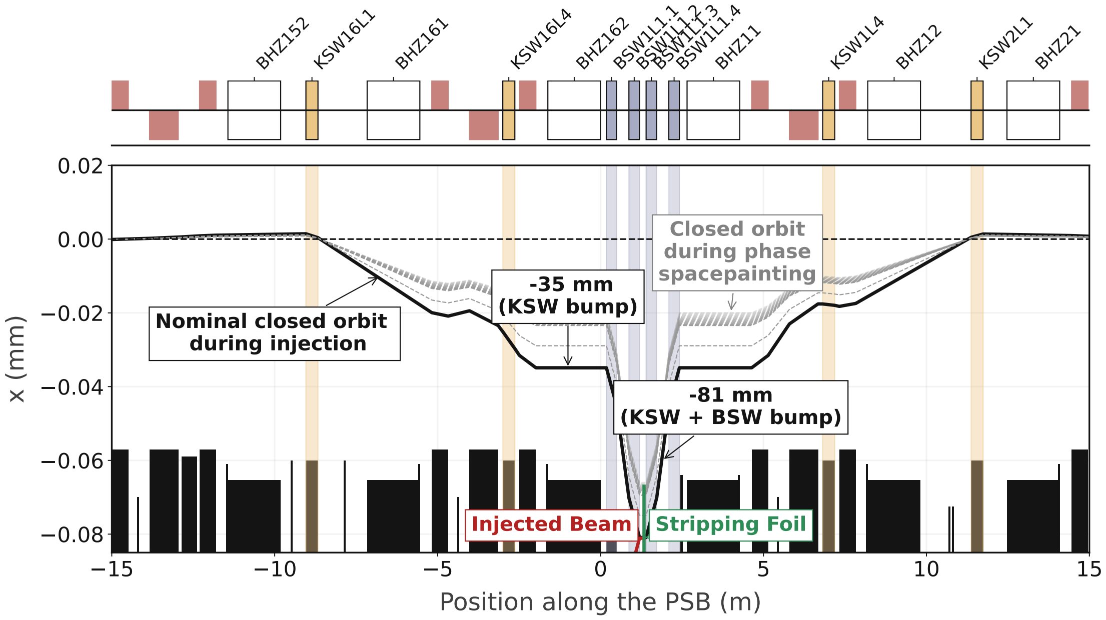

Figure 2.5: Horizontal orbit in P15-P02 during the injection process. The top displays the synoptic layout (white: main dipoles; red: focusing and defocusing quadrupoles, yellow: programmable painting kickers (KSW); blue: chicane magnets (BSW)), the half-aperture is indicated in black. The injection bump is generated by the KSWs (nominal deflection of -35 mm at the foil) and the BSWs (-46 mm at the foil). The KSW and hence the closed orbit decays during phase space painting (grey, dashed orbits). The injected beam is indicated in red.

H^- beam. BSW2 and BSW3 are identical to guarantee symmetry. BSW4 additionally contains the H^0/H^- dump for absorbing un- and partially stripped particles. The BSW bump amplitude of $A_{\mathrm{BSW}} = -\Delta x_{\mathrm{BSW}} = 46\,\mathrm{mm}$ is constant during the first 150 µs of the cycle (maximum time of the injection process) and decays subsequently within 5 ms. Spatial restrictions in the injection region required the magnets to be installed within 2.6 m straight section, limiting the system length of each magnet to 0.373 m (BSW1) and 0.380 m (BSW2-4) [100]. The edge focusing of these strong, short rectangular BSWs yields quadrupolar field perturbations in the vertical plane. Additionally, ramping down the magnet current generates eddy currents in the metallic chambers, which induce a sextupolar field component [41]. Both effects result in a vertical β-beating, which is compensated in operation using k-modulation, as described in [101].

Painting Bump and Phase Space Painting

The term *phase space painting* refers to the controlled tailoring of the (transverse) phase space distributions when injecting over multiple turns. Modulating the amplitude of the closed orbit bump during the injection process modifies the offset between the newly injected (red) and the already circulating beam (grey). Each new Linac4 bunch is hence injected with an average customised action $\langle J_x \rangle$, distributing the particles in phase space. The phase difference between the already circulating and the newly injected particles is given by the machine tune.

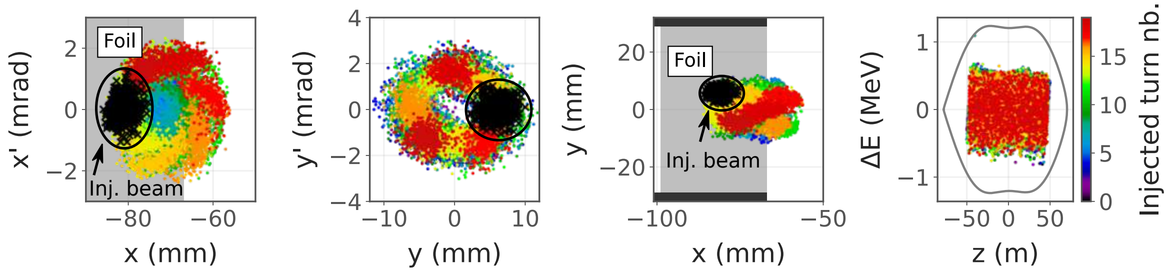

(a) With space charge: nonlinear forces immediately cause beam filamentation.

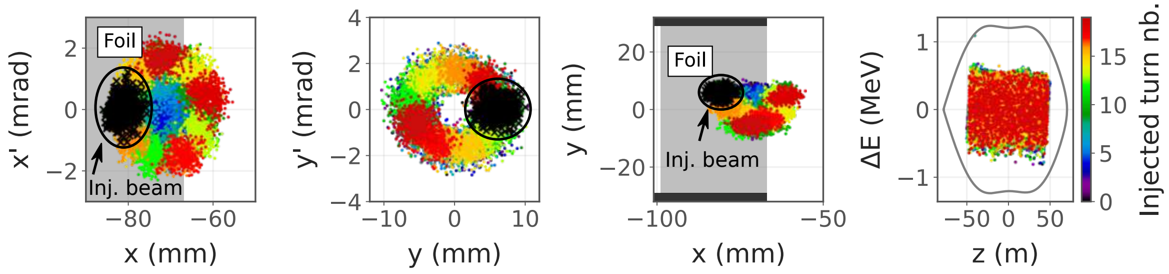

(b) Without space charge: Distinct area of each injected bunch in phase space.

Figure 2.6: Horizontal phase space painting in the PSB. For this illustration, a painting function (i.e. KSW field decay) as shown in Fig. 2.6 is applied with a vertical offset of $\Delta y = 6\,\mathrm{mm}$. The subfigures show the beam distribution in the different phase spaces at the location of the foil after 20 injected turns. The bunches injected between turn 1 and 20 are indicated by colour. The distribution of the newly injected particles is highlighted in black and enclosed by a circle. The stripping foil is indicated by the grey shaded area.

The PSB injection system employs horizontal phase space painting through customised programming of the KSW bump field decay. The vertical beam size can be tailored by defining a fixed offset Δy (or angle $\Delta y'$), using two corrector magnets at the end of the injection line. The horizontal orbit evolution during phase space painting for high-intensity beams is illustrated in Fig. 2.5 by the grey, dashed lines (plot one orbit every 5 µs). Figure 2.6 illustrates the painted phase space after 20 µs, when applying the painting function from Fig. 2.7a. The bunches injected during each turn are colour-coded. When comparing the phase space simulated with (Fig. 2.6a) and without space charge (Fig. 2.6b), one can see that the nonlinear space charge forces immediately cause beam filamentation.

In the long term, it is foreseen to also implement *longitudinal painting*, i.e. injecting each Linac4 bunch with different energy offsets. Longitudinal painting helps to fill the longitudinal bucket homogeneously and to reduce the peak line density λ. It was not operational in the PSB during commissioning and operation in 2021 and is therefore not considered further in this thesis. However, it will be essential to increase the intensity and brightness reach of the various PSB users in the future [60].

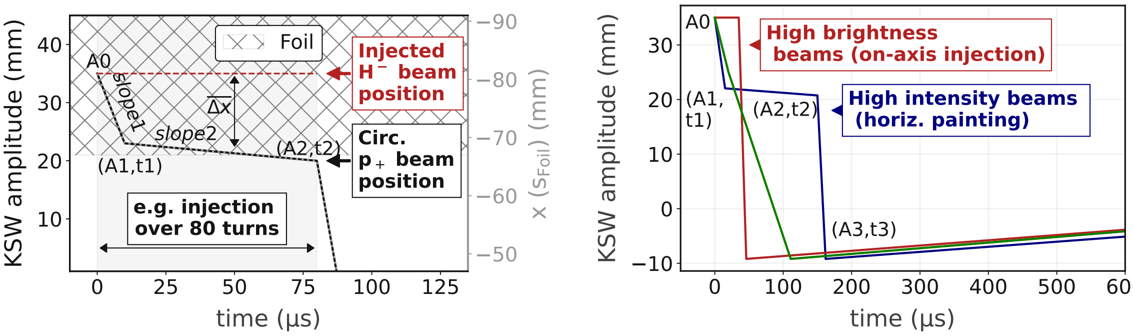

(a) Painting function (i.e. KSW amplitude) as applied for high-intensity fixed target beam. The right axis shows the resulting horizontal beam position of the circulating beam at the location at the foil (KSW + BSW bump).

(b) KSW decay for different users.

Figure 2.7: Programmable KSW amplitude decay during the injection process.

Characteristic of the KSW Magnet Field Decay

The painting kicker field modulation during injection is controlled by piece-wise linear functions. Figure 2.7a illustrates the time evolution of the closed orbit at the location of the stripping foil, for a generic KSW field decay as required for high-intensity beams. The field decay is defined by the time-current markers P_i at time t_i with the KSW bump amplitude $A_i = -\Delta x_{\mathrm{KSW,foil}}$. The maximum bump amplitude A_0 dictates the offset between the circulating and injected beam when injecting the first bunch. The horizontal phase space distribution and the resulting painted beam size are mainly tailored by setting slope 1 through setting the amplitude-marker pair A_1 and t_1. Slope 2 (A_2, t_2) controls the subsequent intensity accumulation. t_2 marks the end of the injection process and is set equal to number of PSB revolutions during beam accumulation (up to $t_2 = 150\,\mu\mathrm{s}$). After injection, the circulating beam is moved away as fast as possible from the foil for most beams to mitigate beam degradation and scattering losses due to additional foil crossings. The bump decays within $\approx 10\,\mu\mathrm{s}$ to $A_3 = -9.2\,\mathrm{mm}$, which is fixed for all waveform types. The bump decays to negative amplitudes to minimise the interaction of the beam with the stripping foil after the injection process, while the BSW is still at maximum amplitude. From there the amplitude finally decays to $A_4 = 0\,\mathrm{mm}$ within 1 ms, counteracting the decay of the injection chicane (which starts to decay after the injection process) during the same time interval. Based on user-specific definition of P_0, P_1 and P_2 the remaining markers P_3 and P_4 are computed automatically. The specified amplitude during the field decay is $< 1\,\%$.

The KSW magnet parameters can be found in [102]. New pulsed magnet current generators [103] were developed to provide the high flexibility and precision of the magnet current decay needed for phase space painting, which are described in more detail in Section 7.1.

Stripping Foil

The stripping foil in the PSB is made out of carbon (for reasons of thermal and mechanical stability, high sublimation temperature and radiation resistance) [104]. The thickness $d = 200\,\mu\mathrm{g\,cm^{-2}}$ is

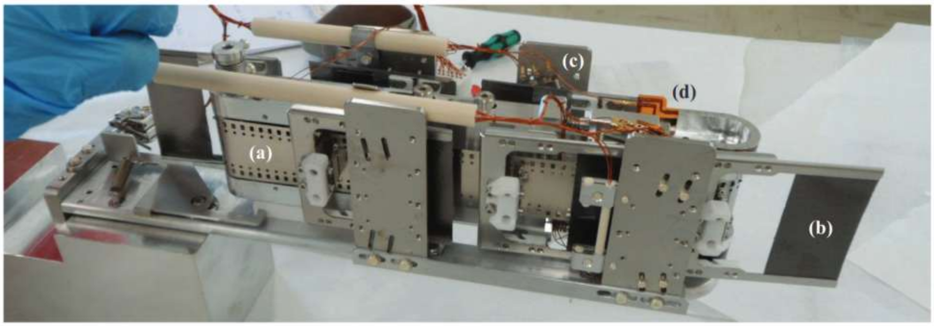

Figure 2.8: Stripping foil exchange mechanism, which is installed in each PSB ring. (a) Rotating stainless steel belt, (b) the holders with stripping foils, (c) ultra-high vacuum compatible microswitches, (d) membrane potentiometers to determine the precise position of the foil holder [104].

(a) Type 1: XCF-200 **(b)** Type 2: MLG-250 **(c)** Type 3: GSI-200

Figure 2.9: Different stripping foil types installed in the PSB in 2021.

driven by efforts to maximise the stripping efficiency ($> 98\,\%$) while minimising beam degradation due to foil scattering [78]. In 2018/2019 foils of different manufacturers were qualified regarding stripping efficiency and mechanical resistance in a test stand installed in the Linac4 transfer line [105, 106] and suitable foil types were subsequently installed in the PSB.

Each PSB ring houses a stripping foil exchange mechanism (Fig. 2.8) with 6 installed stripping foils. This mechanism enables fast foil exchange during operation without requiring any machine intervention and downtime. Table 2.3 lists the characteristics of the foils installed in the foil loaders in PSB in 2021.

Table 2.3: Characteristics of the stripping foils installed in the PSB in 2021.

Type	Thickness	Description
1 / XCF-200	$200\,\mu g\,cm^{-2}$	Arc evaporated amorphous Carbon [107]
2 / MLG-250	$240\,\mu g\,cm^{-2}$	Multilayer Graphene [108]
3 / GSI-200	$200\,\mu g\,cm^{-2}$	Arc evaporated amorphous Carbon [109]

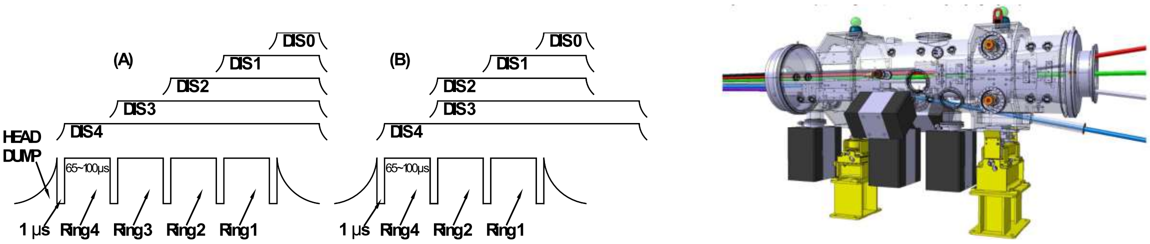

(a) Example for Linac4 pulse structures and the respective BI.DIS timings: (A) standard operation with 65–100 injected turns per ring, (B) operation with 0 injected turns for R3.

(b) The BI.SMV vacuum tank assembly. The beam is separated into four separate lines to inject beam into R4 (red), R3 (green, no kick), R2 (white) and R1 (blue).

Figure 2.10: Distribution kicker and septa to separate the beam into the four rings in the BI line [10].

2.3.3 Beam Transfer from L4 to PSB (BI Line) and Orthogonal Steering

The BI line is the transfer line between Linac4 and the PSB. A full layout of the BI line can be found in [110] and [10, Fig. 3.17].

Beam Separation Scheme in the BI Line

The BI line houses the beam separation scheme to distribute the Linac4 pulses into the respective PSB rings, which comprises vertical beam distribution kickers (BI.DIS) and vertical septum magnets (BI.SMV, see Fig. 2.10). The BI.DIS is a system of five pulsed ferrite core kickers, which produces the initial vertical kick to separate the time-resolved slices of the Linac4 pulse to different vertical positions at the entrance of the septa. The total kick required for the separation is produced by combining the waveforms of four individual BI.DIS modules. The trigger timings of the four modules relative to each other depend on the pulse length, which is to be injected into each PSB ring (see [10, Sec. 3.2.2.2]).

Matching and Orthogonal Steering

After being separated at the BI.SMV, the beam proceeds in four individual vacuum pipes. Each of these lines is controlled by individually powered magnets. Individually powered quadrupoles are used to match the injected beam optics to the circulating beam. Dipolar corrector magnets steer the beam to the PSB reference orbit to minimise injection errors and oscillations.

The last two corrector magnets upstream of the injection insertion are used to independently control the user-specific offset and angle between injected and circulating beam trajectory. This is referred to as *orthogonal steering* and is used when tailoring the respective distribution (mainly vertical, i.e. define Δy and $\Delta y'$).

CHAPTER 3

Injection Precision During the PS Booster Commissioning

In the ideal case, a particle beam is injected into a synchrotron with a *matched phase space distribution*. This means, that it is injected precisely onto the design trajectory and with the Twiss parameters, which are present in the synchrotron at the location of the injection system. However, injection imprecisions cause a *mismatch of the injected distribution*, which can result in unwanted emittance and/or halo growth. Such errors include steering errors, optics errors or multiple Coulomb scattering at the stripping foil.

It is important to note, that for the production of the operational beams in the PSB, such injection errors are only of secondary importance. The evolution of the operational transverse beam sizes is either driven by phase space painting or space charge effects. If a painted distribution is affected by systematic injection errors, the painting settings can be adapted to compensate for the mismatch. For high-brightness beam types, the space charge-driven emittance growth usually conceals mismatched-driven emittance and/or halo growth. To state an example: previous multi-particle simulation studies analysed the impact of injection offsets for the high-brightness LHC25 beams with $N_{\mathrm{p}+} = 3.52 \times 10^{12}\,\mathrm{p}+$ per ring, at a WP of $Q_x = 4.43$ and $Q_y = 4.60$ [60, Chp. 7.3]. These studies concluded, that for such intensities, no significant brightness and tail degradation is expected even for large steering offsets of $\Delta y < 2\,\mathrm{mm}$ and $\Delta x < 3\,\mathrm{mm}$. Operationally, injection errors are most relevant, but also not critical, for low-intensity, low-emittance beams, which are injected over a single PSB turn.

However, when discussing the painting schemes for the various beam types in Chapter 4, awareness of the expected error sources is an important input to improve the comparison between simulation and measurement results. As part of commissioning the new system, this chapter hence characterises the anticipated injection imprecisions. The studies are mainly performed for ring 3, as this is the ring used for the beam production studies in Chapter 4. The discussion focuses on steering errors and ripples (Section 3.2) and foil scattering-induced emittance growth (Section 3.3).

3.1 Impact of Injection Imprecisions in the PSB

A beam which is injected into a synchrotron with a mismatch regarding the design distribution, such as a transverse offset in Fig. 3.1, starts oscillating around the closed orbit. In a perfect machine with no nonlinearities and zero chromaticity, each particle (and hence the centroid of the injected beam) would proceed to perform linear betatron oscillations around the reference orbit. In a real machine, however, a spread of the individual particle tunes, which can occur due to e.g. nonlinearities in magnetic fields, chromaticity or space charge forces, causes a beam dilution in phase space. This process takes place until equilibrium is reached and the particles are equally distributed over all phases. The oscillation amplitude of the beam centre-of-mass decays and the emittance increases. This process is called *phase-mixing* or *filamentation* and is explained in more detail e.g. in [111].

The equilibrium distribution after filamentation is often non-Gaussian and depends not only on the mismatch but also on the mechanisms, which are dominant during phase-mixing. This decoherence process can be significantly affected by coherent and incoherent tune shifts due to direct and indirect space charge effects and their respective complex interplay with chromatic decoherence (see e.g. [112–114]). One of the occurring phenomena is the interaction of the single particle motion with the periodic space charge potential modulation, which is caused by the coherent oscillation of the mismatched beam. The periodic envelope modulation can cause resonant excitations of particles if their tune is close to the tune of the coherent oscillation, and hence drive halo build-up, as shown e.g. in [113, Chp. B]. Note that this excitation depends on both the chromatic and the space charge tune spread as the tune of the single particle $Q = Q_0 - \Delta Q_{\text{inc}} + \Delta Q_\xi$ is determined by the tune set by the quadrupoles (Q_0), the incoherent space charge (ΔQ_{inc}) and the chromatic tune shift (ΔQ_ξ).

Beams produced in the PSB span a wide range of brightnesses, longitudinal momentum spreads and WPs. Space charge forces, tune, momentum distribution and chromatic tune spread are specific for each beam type and consequently also the impact of injection errors. A brief example for how the same error (here $\Delta y = 3\,\text{mm}$, corresponding to $\approx 2\sigma_{y,\text{L4}}$) can result in different core and tail distributions for different intensities is provided in Fig. 3.1. The beam parameters correspond to different beams along the LHC brightness curve, which are injected on-axis over 1-33 turns (see Section 4.4 and Table 4.6 for more details and machine configurations). Figure 3.1 illustrates the normalised vertical phase space evolution for 1, 3 and 17 injected turns, with (coloured) and without (grey) steering errors. Figure 3.2 shows the tune footprints and vertical beam centroid oscillation for the respective cases.

Figure 3.1a: injecting $N_{\text{p+}} \approx 10 \times 10^{10}$ p+ over 1 turn *without including space charge* in simulations. Phase mixing is driven by the chromatic tune spread ($\xi_y = -14$ and $\Delta p/p_{\text{rms}} = 1.5 \times 10^{-3}$). Due to the different tunes, the particles redistribute equally over all phases while preserving the action. This results in the population of a torus in phase space with respective non-Gaussian tails.

Figure 3.1b: injecting $N_{\text{p+}} \approx 10 \times 10^{10}$ p+ over 1 turn *with space charge*. Space charge changes the dynamics drastically. The decoherence rate slows down and a large halo is

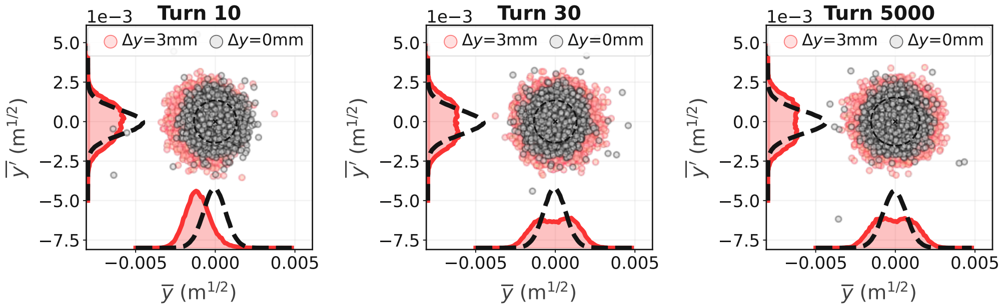

(a) 1 turn ($N_{\mathrm{p+}} = 10 \times 10^{10}$ p+) injected with $\Delta y = 3$ mm, simulated without space charge.

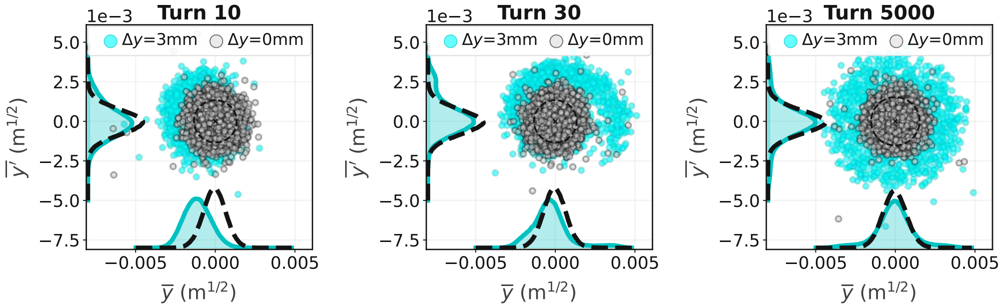

(b) 1 turn ($N_{\mathrm{p+}} = 10 \times 10^{10}$ p+) injected with $\Delta y = 3$ mm, simulated with space charge.

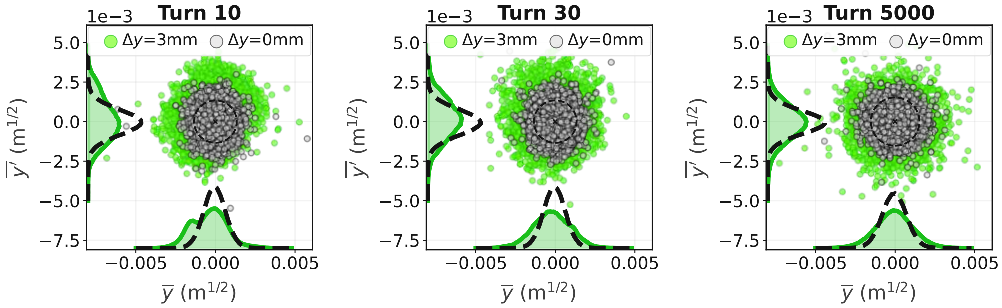

(c) 3 turns ($N_{\mathrm{p+}} = 30 \times 10^{10}$ p+) injected with $\Delta y = 3$ mm, simulated with space charge.

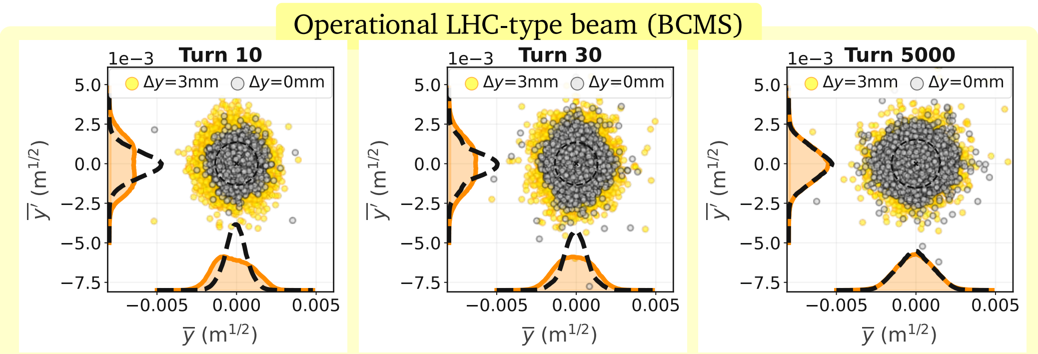

(d) 17 turns ($N_{\mathrm{p+}} = 170 \times 10^{10}$ p+) injected with $\Delta y = 3$ mm, simulated with space charge.

Figure 3.1: Simulated vertical filamentation when injecting LHC-like beams of different intensities with a vertical steering offset of $\Delta y = 3$ mm ($a_y \approx 2\sigma_{y,\mathrm{L4}}$) into the PSB. For each scenario, the normalised vertical phase space is shown after 10 (left), 30 (centre) or 5000 PSB turns (right).

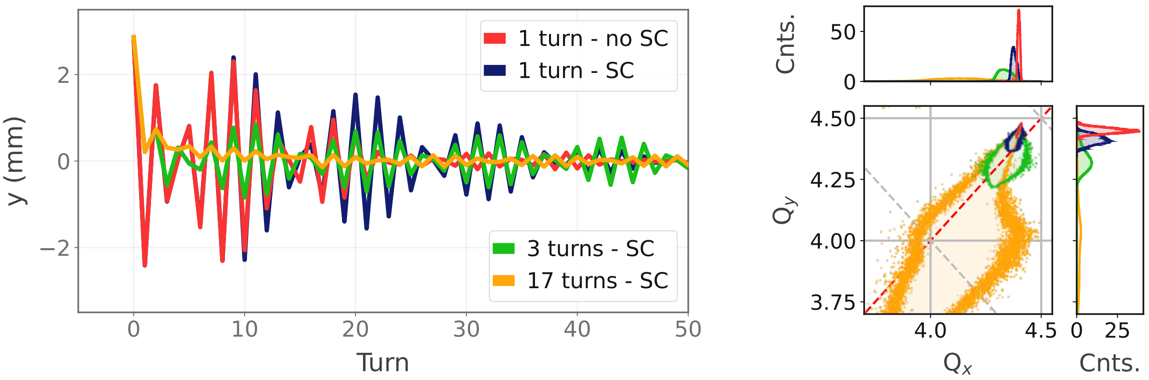

(a) Simulated position of vertical beam centroid after each turn.

(b) Tune footprints after 500 turns.

Figure 3.2: Vertical injection oscillations and tune footprints when injecting LHC-like beams of different intensities with a vertical steering offset of $\Delta y = 3\,\mathrm{mm}$ $(a_y \approx 2\sigma_{y,\mathrm{L4}})$ into the PSB (SC: space charge).

generated due to the interplay between coherent motion, chromatic and space charge detuning [113, 114]. The beam core of the filamented and the matched distribution are similar. However, the tails of the mismatched, filamented distribution are significantly enhanced.

Figure 3.1c: injecting $N_{\mathrm{p+}} \approx 30 \times 10^{10}$ p+ over 3 turns *with space charge*. The three mismatched bunches are injected with different vertical phases, as given by the vertical tune (here $Q_y = 4.45$). The beam is consequently more evenly distributed in phase space, which suppresses the coherent movement of the centre-of-mass and hence the resonant excitation and halo build-up. In this case, the steering offset causes growth of the beam core.

Figure 3.1d: injecting $N_{\mathrm{p+}} \approx 170 \times 10^{10}$ p+ over 17 turns *with space charge*. Out of the presented cases, this is the only operational scenario. It corresponds to the injection of BCMS beams for LHC (see Section 4.4). The high brigtness increases the incoherent tune spread to $\Delta Q_y \approx 0.8$ and $\Delta Q_x \approx 0.55$ at $Q_x = 4.4$, $Q_y = 4.45$. The emittance grows due to the interaction of particles in the beam core with the integer resonances. The space charge-driven is similar to the offset-driven emittance growth. The injection error does consequently not impact the final profile significantly.

Analytic Estimates For Emittance Growth Without Space Charge

Without space charge, it is possible to derive the maximum rms emittance growth due to injection imprecisions by considering the redistribution of the individual particle phases while keeping the action constant, as e.g. shown in [111]. The obtained equations are listed below. It should be noted that these analytical approximations have to be considered with caution if space charge is present. Space charge can alter both the rms emittance growth and the beam profiles, as shown schematically above. The rms emittance growth estimates do not necessarily represent the growth of the beam core. Here, these approximations are solely applied to assess the order of magnitude of the anticipated beam degradation.

Table 3.1: Maximum imprecisions*, which were considered and specified in previous PSB injection studies [60, 99, 115]. The analytical approximations for the consequent emittance growth assume $(\Delta p/p)_{\mathrm{rms}} = 1.5\times10^{-3}$ and $\epsilon_{0,\mathrm{n,rms}} = 0.3\,\mu\mathrm{m}$.

Variable	**Nominal optics at the foil (4.4 / 4.45)**	**Errors in the PSB for 15% β-beat**	**Errors of the injected beam**	$\Delta\epsilon_{\mathbf{n,rms}}$ **(µm)**
β_x (m)	5.5	4.7/5.8	3.8/7.2 (i.e. ±30%)	H: < 0.1
α_x (rad)	0	±0.15	±0.25	
β_y (m)	3.5	3/3.7	2.4/4.6 (i.e. ±30%)	V: < 0.1
α_y (rad)	0	±0.15	±0.25	
D_x (m)	-1.22	±0.1	-1.7/0.7 ($\Delta D_x = \pm0.5$)**	H: $\lesssim$0.1
D'_x (rad)	0	±0.015	0	
D_y (m)	0	0	±0.5**	V: $\lesssim$0.1
D'_y (rad)	0	0	0	
ΔE (keV)	0	0	100	H: < 0.05
x (mm)	0	±0.15	±2**	H: 0.5
x' (mrad)	0	±0.04	0	
y (mm)	0	0	±2**	V: 0.6
y' (mrad)	0	0	0	

* Conservative limits.

** The quoted offset represents a combination of Δu and $\Delta u'$; the dispersion a combination of ΔD and $\Delta D'$.

Steering errors are errors in the position or angle of the injected beam relative to the closed orbit trajectory, i.e. $u_1 \neq u_0$ and/or $u'_1 \neq u'_0$ $(u = x, y)$. u_1 labels the injected and u_0 the closed orbit parameters. The resulting growth of ϵ_{rms} can be derived as (ϵ refers to ϵ_{rms} in Eqs. (3.1) to (3.4))

$$\frac{\epsilon_{\mathrm{new}}}{\epsilon_0} = 1 + \frac{1}{2}\frac{\Delta u^2 + (\beta_0 \Delta u' + \alpha_0 \Delta u)^2}{\beta_0 \epsilon_0} = 1 + \frac{\Delta \bar{u}^2 + \Delta \bar{u}'^2}{2\epsilon_0}. \tag{3.1}$$

Similarly, optics mismatches, i.e. when $\alpha_1 \neq \alpha_0$ and/or $\beta_1 \neq \beta_0$ yield

$$\frac{\epsilon_{\mathrm{new}}}{\epsilon_0} = \frac{1}{2}\left(\frac{\beta_0}{\beta_1} + \frac{\beta_1}{\beta_0}\left(\alpha_0 - \alpha_1\frac{\beta_0}{\beta_1}\right)^2 + \frac{\beta_1}{\beta_0}\right), \tag{3.2}$$

dispersion mismatch ($D_1 \neq D_0$ and/or $D'_1 \neq D'_0$)

$$\frac{\epsilon_{\mathrm{new}}}{\epsilon_0} = 1 + \frac{1}{2}\frac{\Delta D^2 + (\beta \Delta D' + \alpha \Delta D)^2}{\beta \epsilon_0}\frac{\Delta p}{p}^2, \tag{3.3}$$

and energy mismatch

$$\frac{\epsilon_{\mathrm{new}}}{\epsilon_0} = 1 + \frac{1}{2}\frac{D^2}{\beta\epsilon_0}\frac{\Delta p}{p}^2. \tag{3.4}$$

Table 3.1 lists the maximum injection imprecisions, which were considered and specified in previous studies [60, 99, 115], and the analytic estimate for the consequent rms normalised emittance growth $\Delta\epsilon_{\mathrm{n,rms}}$. The quoted emittance growth corresponds to the maximum value obtained for the listed mismatch ranges.

The results highlight that steering errors are the largest anticipated source of beam degradation. Furthermore, studies performed within the framework of this thesis focus on the different painting schemes, which rely on the variation of the trajectory offsets. For these reasons, this chapter focuses on the characterisation of steering errors. The impact of optics, dispersion and energy mismatches are of second order and subject to further studies. However, it has to be noted for completeness that the strong edge effects of the distribution septum cause differences in optics and dispersion in the four transfer lines. Given the initial conditions from Linac4 [116] and the available matching quadrupoles in the transfer lines, it is challenging to match the optics and dispersion for all four transfer lines simultaneously. The optics and dispersion mismatch for other rings can exceed the values stated in Table 3.1. This is valid particularly for the transfer lines to R1 as the respective beam experiences the largest deflection by the septum. Nevertheless, as the beam production measurements performed in Chapter 4 focus on R3, optics errors are not further considered in this thesis.

3.2 Characterising Sources of Steering Errors and Ripples

Trajectory offsets of the injected beam are caused by quadrupole misalignments or errors and ripples in the bending fields of the PSB, Linac4 and the transfer line. To minimise these errors, the injected beam position is steered to the circulating beam with the steering program YASP [117]. This program observes the betatron oscillation of the injected beam around the reference orbit (see e.g. [111, Chp. 3.1]). The magnetic fields of the steering magnets required to minimise this oscillation are computed using model-based trajectory correction algorithms, such as MICADO [118] or Singular Value Decomposition (SVD) [119]. This steering is performed when injecting beam over a single turn. Ripples along the pulse cause a modulation of the transverse position when injecting over multiple turns and have to be therefore considered when quantifying the anticipated errors. However, it is highlighted again, that beams, which are injected over multiple turns are less sensitive to errors due to the larger beam size. In addition to systematic steering imprecisions, random errors occur on a shot-to-shot basis due to fluctuations in the BPM acquisition, the Linac4 and PSB trajectories.

This section describes the main anticipated sources for steering errors and ripples. To provide a quantification independent of the observation point, the error in the plane $u = x, y$ is expressed in units of beam sigma

$$\Delta a_u/\sigma_{u,\mathrm{L4}} = \sqrt{\frac{\gamma_u \cdot \Delta u^2 + 2 \cdot \alpha_u \Delta u \Delta u' + \beta_u \cdot \Delta u'^2}{\epsilon_u}}, \tag{3.5}$$

following the procedure from [120]. Here, the reference beam size is based on the matched Linac4 emittance $\epsilon_{0,\mathrm{n,rms}} = 0.3\,\mu\mathrm{m}$. The results are summarised in Tables 3.2 and 3.3.

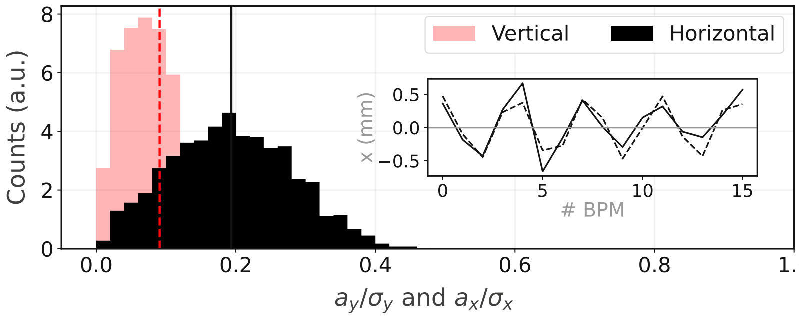

Figure 3.3: Random shot-to-shot trajectory fluctuations: horizontal (black) and vertical (red) distribution of the random injection errors in units of beam sigma with $\epsilon_0 = 0.3\,\mu\mathrm{m}$, observed over 2000 acquisitions. The dashed lines indicate the average reconstructed error. The inset axis show the measured remnant injection oscillations in the 16 BPMs of the PSB (solid) and the modelled oscillation based on the reconstructed error (dashed).

3.2.1 Description of Steering Error and Ripple Sources

Random Shot-to-Shot Trajectory Fluctuations (Vertical and Horizontal, Random)

Random errors occur on a shot-to-shot basis due to fluctuations of the BPM acquisition, the Linac4 and PSB trajectories. To quantify these errors, the injection oscillations are acquired 2000 times over ≈ 12 h. The average of all acquisitions is considered as reference steering and subtracted. For each shot, MAD-X [58] is used to determine the injection errors (x, x') and (y, y'), which reproduce the remnant oscillation. Figure 3.3 displays the distribution of reconstructed errors given in units of beam sigma. The average error is indicated by the dashed lines and subsequently listed as the expected random error: $a_x/\sigma_{x,\mathrm{L4}} = 0.2$ and $a_y/\sigma_{y,\mathrm{L4}} = 0.1$. For an LHC-like WP ($Q_x = 4.4, Q_y = 4.45$), this corresponds to offsets at the foil of $\Delta x = 0.3\,\mathrm{mm}$ and $\Delta y = 0.1\,\mathrm{mm}$, which is negligible and does not impact the beam production.

Steering Precision (Horizontal and Vertical, Systematic)

Such random shot-to-shot fluctuations limit, together with reconstruction and model errors, the achievable steering precision. In 2021 operation, injection oscillations could be reproducibly minimised to amplitudes $< \pm 0.5\,\mathrm{mm}$ in both planes. Using the machine model in [95, "PSB 2021: LHC-injection optics"], this corresponds to $a_x/\sigma_{x,\mathrm{L4}} \approx 0.3$ and $a_y/\sigma_{y,\mathrm{L4}} \approx 0.2$, which are subsequently considered as systematic steering errors.

Distribution Kicker Flat-Top Ripples (BI.DIS10, Vertical, Systematic)

The distribution kickers in the BI line produce the initial vertical kicks to separate the beam into the four PSB rings by combining the waveforms of four individual kicker modules (see Section 2.3.3). The trigger timings of the four modules relative to each other depend on the number of turns injected into each PSB ring, as illustrated in Fig. 3.4a (here injecting over 17 µs per ring, as done for operational BCMS beams). Each of the generators produces a current I_{DISi} with a reproducible

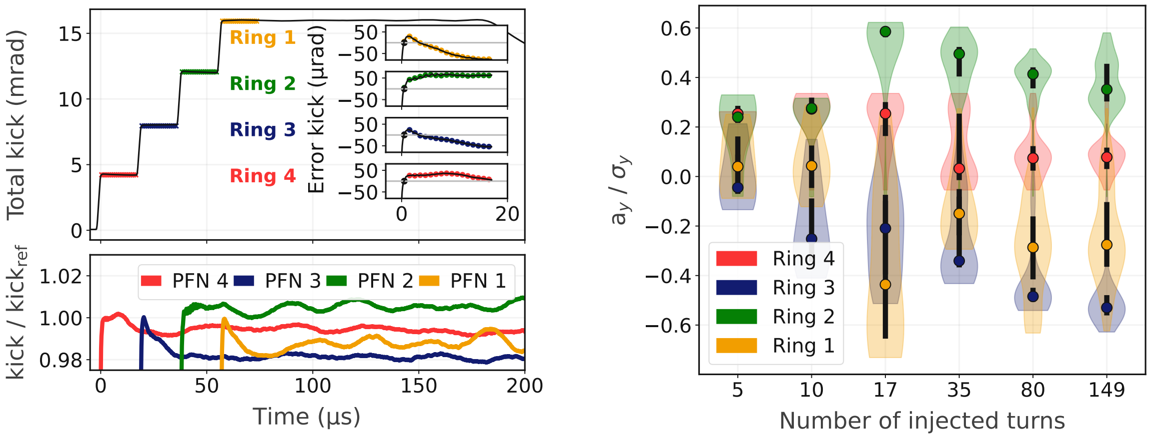

(a) Top: total kick of the four distribution kicker modules when injecting beam over 17 µs into each ring. The inset axes show the combined relative error due to ripples for each injected bunch. Bottom: enlarged view of the flat-top ripples of each individual module.

(b) Distribution of injection errors due to distribution kicker flat-top ripples for 5-150 injected turns (in units of beam sigma).

Figure 3.4: Distribution kicker flat-top ripples: schematic overview and impact on steering errors.

flat-top ripple, which is within the specifications of $\Delta I_{\mathrm{DISi}}/I_{\mathrm{DISi}} = \pm 1\,\%$ [121]. Figure 3.4a (bottom) shows the measured current of the four individual power converters when normalising it to the current after the rise time. This ripple causes a modulation of the vertical beam position along the injected pulse. The resulting total erroneous kick the beam experiences is a consequence of the superposition of the four kicker module flat-top ripples and hence specific for each injection configuration.

Steering is performed with the beam, which is injected over the first PSB turn (black scatter marker in Fig. 3.4a). The insets in Fig. 3.4a show the effective miskick of the subsequent bunches relative to this reference bunch, when injecting over 17 turns into each ring. The anticipated distribution of the injection offsets when injecting over 5-150 turns is summarised in Fig. 3.4b. The values are given in units of $\Delta a_y/\sigma_{y,\mathrm{L4}}$ and are estimated using $\beta_y = 44\,\mathrm{m}$ at the distribution kicker [95, "PSB 2021: LHC-injection optics"]. The resulting offsets are within $\pm 0.75\,\sigma_{y,\mathrm{L4}}$ in all rings, which corresponds to $\Delta y \approx \pm 1\,\mathrm{mm}$ at the injection foil. The average offsets when injecting over multiple turns are marked by the circles in Fig. 3.4b. The maximum average error modelled in all rings is listed in Table 3.3 as an indication of the expected systematic error contribution from the distributor.

Distribution Septum Flat-Top Ripples (BIr.SMV10, Vertical, Systematic)

The vertical distribution septum (see Section 2.3.3) also features a reproducible flat-top ripple, which can be approximated by a sine wave with 10 kHz oscillation frequency and a peak-to-peak amplitude of $< 0.025\,\%$, as specified in [122]. The beam going to ring 3, i.e the ring in which the beam production studies are performed, is not deflected and septa ripples are therefore not

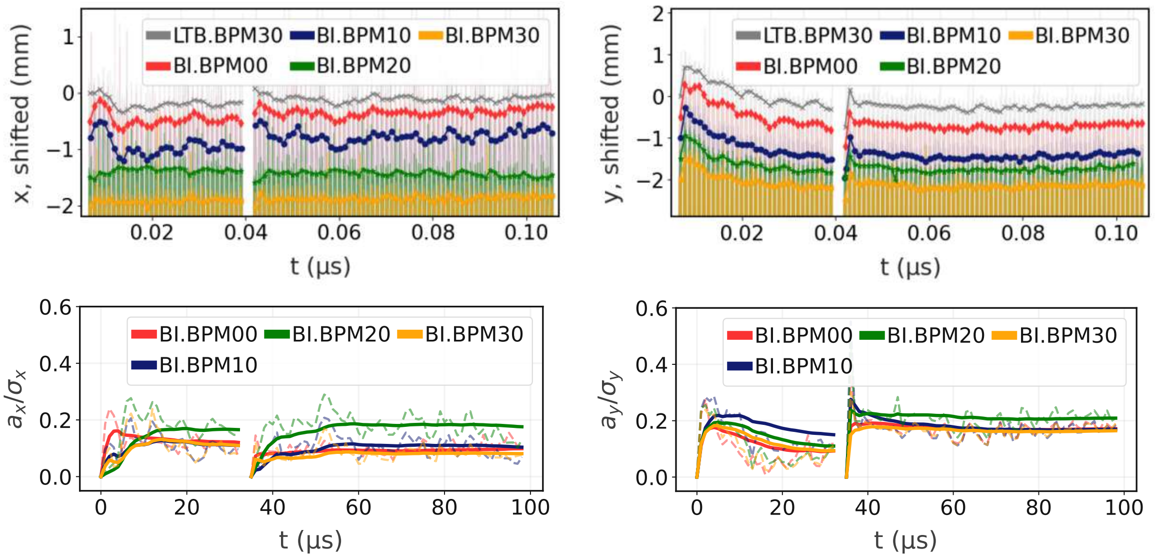

(a) Horizontal. **(b)** Vertical.

Figure 3.5: Trajectory modulation along the Linac4 pulse, observed with beam position monitors (BPMs) at the beginning of the BI-line, i.e. upstream of the distribution septa and kickers. Top: transverse position modulation along the part of the pulse, which is injected into R4 (over 33 turns) and R3 (over 64 turns, with $\Delta E_{\mathrm{rms}} = 250$ keV energy spread). Bottom: position error of each Linac4 bunch relative to the steering bunch, i.e. the beam injected over the first PSB turn in each ring. The error is reconstructed using the offset variation between LTB.BPM30 and the respective BI BPMs and the optics model of the transfer line. The dashed lines show the reconstructed offset of each individual bunch. The solid lines display the average steering offset when injecting beam over multiple turns.

further considered here[†].

Modulation of the Position Along the Linac4 Pulse (Horizontal and Vertical, Systematic)

Various sources in Linac4 already upstream of the beam distribution system can cause a systematic modulation of the position along the delivered Linac4 pulse. This modulation is partially corrected by an adaptive feed-forward system. Figure 3.5 (top) illustrates the horizontal and vertical ripples measured at several BPMs just before (LTB.BPM30) and at the beginning of the BI-line (BI.BPM00-30, upstream of the distributor and the septum), when injecting beam over 33 turns into R4 and over 64 turns into R3. As steering is performed in each ring using the beam, which is injected from Linac4 over the first PSB turn, it is of interest for injection precision studies to consider the position modulation relative to this reference bunch. The measured transverse positions and the modelled Twiss parameters [123, "PSB Injection - AD Stitched, optics for 100 kV debuncher voltage"] at

---

[†] The septa provide a kick of −163.7 mrad to bend the beam vertically into R1, −129.5 mrad into R2 and 129.5 mrad into R1. The effective error seen by the beam depends on the trigger timing between the septa and the distributors and is hence specific for different numbers of injected turns. However, the maximum anticipated error for ring 1, 2 and 4 is $\Delta a_y/\sigma_{y,\mathrm{L4}} \lessapprox 0.2$, which is operationally acceptable.

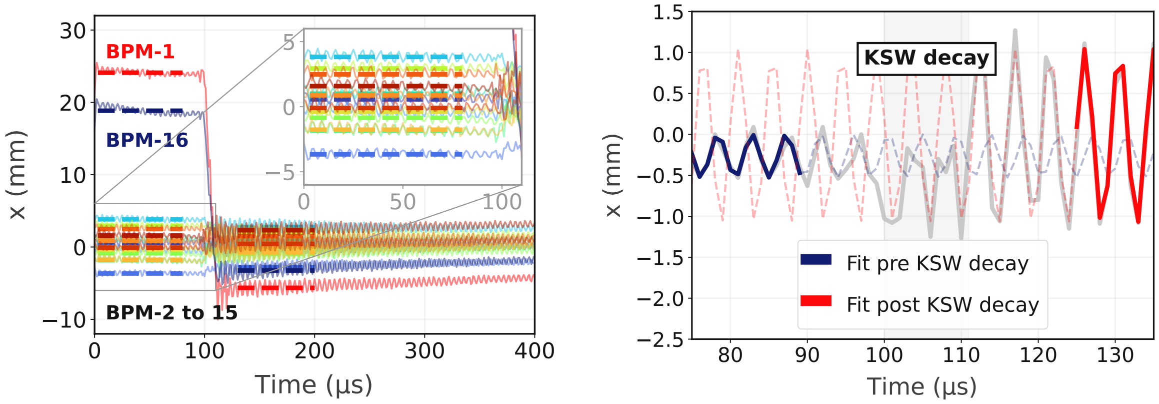

(a) Horizontal turn-by-turn BPM (BPM-1 to 16, ring 3) acquisitions during the KSW bump.

(b) Enlarged view of the BPM-10 TbT traces during the KSW decay. The fitted oscillations before and after the decay are shown in blue and red, respectively.

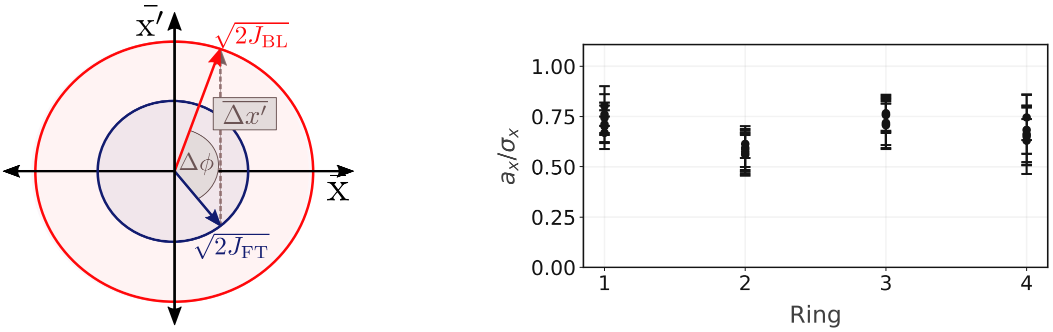

(c) Schematic of reconstructing the erroneous kick $\Delta x'$ in normalised phase space.

(d) Reconstructed error in all rings in units of beam sigma.

Figure 3.6: Quantification of the non-nominal kick introduced during the decay of the KSW bump in 2021 for $Q_x/Q_y = 4.22/4.39$.

the respective BPMs are used to reconstruct this error in units of beam sigma (using Eq. (1.24)). The results are illustrated in Fig. 3.5 (bottom) using the dashed lines. The solid lines indicate the cumulative average offset when injecting over t µs. This procedure is subject to uncertainties in the BPM acquisitions and the modelled optics during the commissioning phase. This can also be seen by the different results when reconstructing the same position modulation with different BPMs. The average standard error obtained over all acquisitions is $\sigma_{a_y/\sigma_y} \approx 0.022$. However, this approximation suffices to quote an expected average position error when injecting multiple bunches, as reported in Tables 3.2 and 3.3.

Mismatch During the KSW Decay (Horizontal, Systematic)

Another source of injection mismatch was identified during beam commissioning connected to the decay of the KSW bump. Figure 3.6a shows the horizontal turn-by-turn (TbT) beam position measurements at the 16 ring BPMs during the first 400 µs after injection. In this example, the KSW bump is programmed to decay after 100 µs. This decay is particularly prominent when looking at the BPMs, which are within the KSW bump (BPM1 and BPM16). These measurements reveal an erroneous horizontal kick, which occurs during the KSW decay (slope 3, here from 100-111 µs) and increases the horizontal oscillation amplitude. This observation suggests a discrepancy in the decay of the four KSW magnet currents, which is subject to future studies. As input for the painting studies, the erroneous kick is quantified here by comparing the action J_x and phase Φ_x directly before (τ_0 = 65-90 µs) and after the decay (τ_1 = 125-150 µs). These are determined from the measured oscillation using a sinusoidal fit (Fig. 3.6b)[†]

$$x_{\tau,\mathrm{osc}}(t) = \sqrt{2J_{x,\tau} \cdot \beta_{\mathrm{BPMi}}} \cdot \sin\left(2\pi \cdot \left(t \cdot Q_{x,\tau} - \phi_\tau\right)\right). \tag{3.6}$$

The erroneous kick can be derived in normalised coordinates using

$$\overline{\Delta x'}^2 = 2J_{x,1} + 2J_{x,0} - \sqrt{2J_{x,0}} \cdot \sqrt{2J_{x,1}} \cdot \cos\left(2\pi \cdot (\phi_0 - \phi_1)\right), \tag{3.7}$$

as displayed schematically in Fig. 3.6c. This reconstruction is performed in all rings, for all BPMs. For each acquired shot, the average and standard error for the 16 different BPMs are estimated and displayed in Fig. 3.6d. The individual lines correspond to multiple acquired shots. The estimated horizontal error in units of beam sigma is $a_x/\sigma_{x,\mathrm{L4}} \approx 0.7$.

Systematic Drifts and Shot-to-Shot Fluctuations due to External Influences on Linac4 and PSB Orbit Stability (Horizontal and Vertical)

The reported Linac4 trajectory stability was 1-3 mm peak to peak in 2021 [88, 90]. Systematic shot-to-shot variations are mainly attributed to magnetic stray fields of elements pulsing for neighbouring machines and transfer lines (e.g. the main magnets of the PS). Automated tools help to monitor and correct such errors [88] and are therefore excluded during the measurements of the beam production schemes presented in this thesis.

3.2.2 Summary of Expected Errors in Ring 3

Tables 3.2 and 3.3 summarise the identified horizontal and vertical average steering errors when injecting beams with different batch lengths. The systematic error sources are combined using a the root of the sum of squares. The resulting expected steering offsets are within the specified limits of $\Delta u \lessapprox 2$ mm and are hence not expected to impact the performance of the operational beams.

When injecting beam over a single turn, all systematic errors originating in the Linac4 and the BI line can be compensated by steering. The remaining error sources are the steering imprecision, shot-to-shot fluctuations (which are both negligible) and the systematic mismatch during the decay of the KSW in the horizontal plane. When injecting over multiple turns, the horizontal and vertical beam positions are modulated due to various error sources in Linac4 and the BI line. This trajectory modulation is especially prominent in the vertical plane. The resulting systematic errors

---

[†] Note that the commonly applied Fast Fourier Transform (FFT) analysis for estimating action and phase from TbT data is not applicable in this case due to the small number of signal sample points (here N = 25). The limited spectral resolution yields significant systematic errors.

Table 3.2: Main contributions to horizontal delivery imprecision into the PSB ($\sigma_{x,\mathrm{foil}} = 1.65\,\mathrm{mm}$).

Type	Error source	Unit	Injection over N turns/ring				
			N=1	**5**	**10**	**35**	**80**
Random	**Injection oscillation jitter**	$\sigma_{x,\mathrm{L4}}$	0.2	0.2	0.2	0.2	0.2
Systematic	**Steering precision**	$\sigma_{x,\mathrm{L4}}$	0.3	0.3	0.3	0.3	0.3
Systematic	**KSW decay**	$\sigma_{x,\mathrm{L4}}$	0.7	0.7	0.7	0.7	0.7
Systematic	**Drift along L4 pulse**	$\sigma_{x,\mathrm{L4}}$	0	0.15	0.15	0.15	0.15
Random	**Random error**	$\sigma_{x,\mathrm{L4}}$	0.2	0.2	0.2	0.2	0.2
Systematic	**Total syst. error (sum)**	$\sigma_{x,\mathrm{L4}}$	0.76	0.8	0.8	0.8	0.8

Table 3.3: Main contributions to vertical delivery imprecision into the PSB ($\sigma_{y,\mathrm{foil}} = 1.3\,\mathrm{mm}$).

Type	Error source	Unit	Injection over N turns/ring				
			N=1	**5**	**10**	**35**	**80**
Random	**Injection oscillation jitter**	$\sigma_{y,\mathrm{L4}}$	0.1	0.1	0.1	0.1	0.1
Systematic	**Steering precision**	$\sigma_{y,\mathrm{L4}}$	0.2	0.2	0.2	0.2	0.2
Systematic	**Distribution kicker**	$\sigma_{y,\mathrm{L4}}$	0	0.3	0.3	0.5	0.5
Systematic	**Drift along L4 pulse**	$\sigma_{y,\mathrm{L4}}$	0	0.3	0.2	0.2	0.2
Random	**Random error**	$\sigma_{y,\mathrm{L4}}$	0.1	0.1	0.1	0.1	0.1
Systematic	**Total syst. error (sum)**	$\sigma_{y,\mathrm{L4}}$	0.2	0.5	0.5	0.6	0.6

depend on the number of turns, over which beam is injected into each ring. Particular attention to these modulations has to be given when injecting high-brightness beams over 2-10 PSB turns, due to the small produced beam size but the large overshoot of the various power converter ripples.

The listed errors are worst-case estimates and more detailed studies considering different trigger timings, verified optics models and the phase advance between the different elements will give a more precise knowledge about the error distribution for future studies. Additionally, it is encouraged to complement to presented studies by systematically assessing the impact dispersion and optics mismatch, particularly for R1, R2 and R4.

3.3 Emittance Growth due to Multiple Coulomb Scattering at the Stripping Foil

Another source of emittance growth during the PSB injection process is multiple Coulomb scattering at the stripping foil (Section 2.3.2). The generated blow-up has a Gaussian characteristic and can

Table 3.4: Configurations for measuring the foil scattering-induced emittance growth.

Parameter	**Unit**	**Value**
Injected intensity	p+	1.5×10^{11}
Number of injected turns		3
Estimated (average) injection errors (see Section 3.2)		
Horizontal	mm	1-1.5
Vertical	mm	0.5-1
Injection painting settings		
Horizontal painting offset Δx	mm	0 (on-axis)
Vertical painting offset Δy	mm	0 (on-axis)
Number of foil crossings N_F	-	1-150
PSB settings		
Q_x/Q_y at injection (set)	-	4.17/4.23
β-beating correction	-	no
Q_x/Q_y at injection (modelled and measured)	-	4.17/4.25
Q_x/Q_y at extraction	-	4.17/4.23
Values for analytic approximations		
β_x at the foil (modelled at injection)	m	5.7 (±10 %)
β_y at the foil (modelled at injection)	m	4.0 (±10 %)
Thickness of the carbon stripping foil	$\mu\text{g}\,\text{cm}^{-2}$	200 (±10 %)
Expected incoherent tune spreads at injection		
$\lvert\Delta Q_{x,\max}\rvert / \lvert\Delta Q_{y,\max}\rvert$ for $N_t \lesssim 50$ turns	-	$\gtrsim 0.15$ / $\gtrsim 0.2$
$\lvert\Delta Q_{x,\max}\rvert / \lvert\Delta Q_{y,\max}\rvert$ for $N_t \gtrsim 50$ turns	-	$\lesssim 0.15$ /$\lesssim 0.2$

be analytically approximated through

$$\epsilon_{u,\text{new}} = \epsilon_{u,0} + \frac{\beta_{u,\text{foil}}}{2} < \Theta^2 > \tag{3.8}$$

in the respective plane $u = x, y$ (see e.g. [111]). The squared rms scattering angle $< \Theta^2 > \propto N_\text{F} \cdot d$ is defined in Eq. (1.52). Note that the emittance increase is proportional to the number of foil crossings N_F, the foil thickness d and the $\beta_{u,\text{foil}}$-function at the foil.

The flexibility to customise the number of foil crossings enables us to experimentally characterise the installed foils concerning scattering-induced emittance growth for the first time and assess their impact on beam degradation [124].

3.3.1 Methodology

Table 2.3 lists the three foil types used operationally in 2021. Two foils of each type are installed per ring. The different foils are characterised by measuring the beam emittance as a function of the

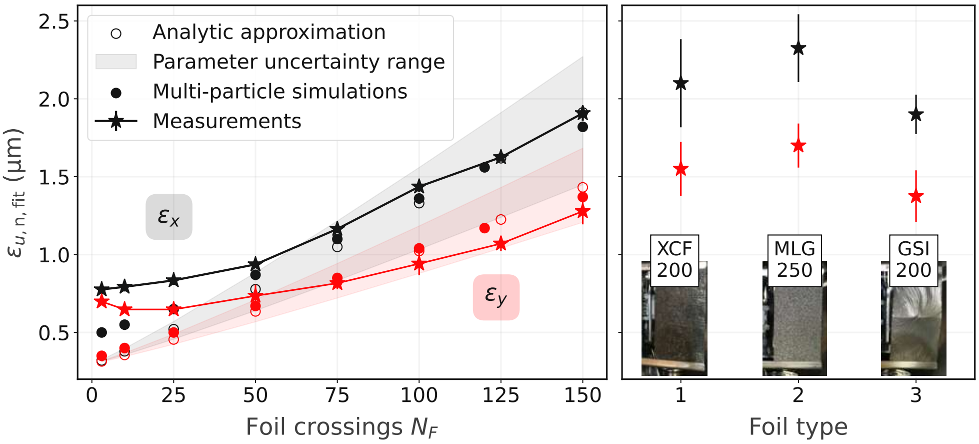

Figure 3.7: Emittance growth due to multiple Coulomb scattering at the PSB stripping foil. Left: transverse emittances for an increasing number of foil passages N_F (foil type 3). Right: transverse emittances obtained for different foil types in case of $N_\mathrm{F} = 150$ foil passages.

number of foil passages of the circulating beam, which are set to 1-150 crossings by programming the KSW decay accordingly.

The machine configurations and beam parameters are summarised in Table 3.4 and correspond to an INDIV-like beam set-up (see Section 4.5): beam with an intensity of $N_{\mathrm{p}+} = 1.5 \times 10^{11}$ p+ is injected on-axis over 3 PSB turns. The set WP ($Q_x = 4.17$, $Q_y = 4.23$) is constant over the cycle. The vertical β-beating, which is introduced during the first 5 ms due to the edge effects and eddy currents of the injection chicane magnets, is not corrected in these measurements. The resulting modelled and measured vertical tune at injection is, therefore, $Q_y = 4.25$ (compare [101]).

The beam profiles are measured using wire scan acquisitions at the end of the cycle (C795, i.e. at extraction energy). The emittances $\epsilon_{\mathrm{n,fit}}$ are retrieved by fitting a Gaussian function to the measured profile. Especially for multiple foil crossings one obtains Gaussian beam profiles without tails and hence $\epsilon_{\mathrm{n,fit}} \approx \epsilon_{\mathrm{n,rms}}$. The measured emittances are benchmarked with analytic estimates and multi-particle simulations. Analytically, the emittance growth (Eq. (3.8)) is computed using the scattering angle obtained from Molière's formalism with logarithmic correction for thin targets Eq. (1.52). In the PTC-pyOrbit [70] simulations, foil scattering is included through repeated single Coulomb scattering [79]. The rms width of the resulting distribution approaches Eq. (3.8) for multiple foil passages. The simulations are conducted for the first 5 ms of the cycle (up to C280). Based on the chosen WP evolution, no significant emittance degradation is expected between the acquisition times of the simulation (C280) and measurements (C795).

3.3.2 Results and Discussion

Figure 3.7 displays the emittance as a function of the number of foil crossings N_F for the GSI-200 foil (type 3, see Table 2.3). Good agreement is found between the analytical, simulation and measurement results for $N_\mathrm{F} > 30$-50. Both the anticipated linear dependence on the foil crossings and the magnitude of the horizontal and vertical emittance growth are well reproduced. For less than $N_\mathrm{F} < 30$-50 foil crossings, the measured are larger than the simulated emittances. This can be explained by emittance growth due to injection mismatches and/or space charge (compare Section 1.5.5). Space charge-driven emittance growth on the vertical integer resonances is also obtained in simulations for $N_\mathrm{F} < 30$ (black circles in Fig. 3.7). β-beating can explain discrepancies between measurements and simulations due to a change of optics at the foil compared to the simulated $\beta_x = 5.7\,\mathrm{m}$ and $\beta_y = 4\,\mathrm{m}$. Including ±10 % β-beating and a 10 % discrepancy in the foil thickness yields analytic parameter uncertainties as indicated by the shaded intervals in Fig. 3.7.

For future operational decisions, it is of interest to compare the different foil types regarding their scattering properties. Figure 3.7 (right) displays the respective emittance growth for $N_\mathrm{F} = 150$, averaged for multiple foils of the same type (four foils per type in ring 2 and 3). The blow-up generated for all foils is consistent with the model and within specifications. The smallest emittance growth is obtained with the GSI-200 foil (type 3), followed by the XCF-200 (type 1). The multilayer graphene foil MLG-250 yields the largest emittance increase. This foil has a thickness of $250\,\mathrm{\mu g\,cm^{-2}}$, but is stated to correspond to carbon with a thickness of $200\,\mathrm{\mu g\,cm^{-2}}$ [108]. For $N_\mathrm{F} = 150$, the difference between the emittance growth induced by GSI-200 and MLG-250 is $0.4\,\mathrm{\mu m}$ in the horizontal and $0.3\,\mathrm{\mu m}$ in the vertical plane.

3.4 Conclusion and Outlook

Characterising the main sources of injection imprecision is an essential part of beam commissioning and input for subsequent beam production studies, particularly for low-intensity and low-emittance beams.

During the PSB injection into ring 3, steering errors and ripples are the main sources of brightness degradation. The main error in the horizontal plane is a mismatch, which occurs during the KSW decay. The vertical steering imprecision is dominated by reproducible ripples of the beam distribution system and the position modulation along the L4 pulse. The quantified errors are within specifications and are therefore not expected to impact the performance of the operational beams. However, the estimated values will be used as input when comparing simulations and measurement results in Chapter 4.

Another source of beam degradation in a CEI system is foil scattering-induced emittance growth. A first experimental assessment verifies that all installed foils are within specifications and produce an emittance growth as anticipated from simulations. No significant scattering-induced beam degradation is expected for any foil type when producing high-brightness LHC-type beams (see Section 4.4). Follow-up studies beyond the commissioning period are encouraged to further improve the comparison with the theoretical models. A key component will be correcting the β-beating induced by the injection chicane to increase the certainty of β_u at the foil.

CHAPTER 4

Transverse Emittance Tailoring with the New PSB H$^-$ Injection System

The flexibility to apply transverse phase space painting during the PSB injection process paves the way for delivering more customised beam distributions to the various users. At the same time, the new system requires a fundamental redesign of the injection schemes compared to the pre-LS2 operation with the conventional multiturn injection.

This chapter outlines selected simulation and measurement results for commissioning the painting schemes and tailoring the requested beam distributions. The presented studies focus on high-intensity beams for the ISOLDE facility (Section 4.3), high-brightness beams for the HL-LHC era (Section 4.4) and LHC Single Bunch Beams (Section 4.5). The challenges posed to achieve and push beyond the specified brightness and intensity targets are highlighted. Automatically adapting the developed painting schemes based on beam instrumentation feedback and changing user requests will become a key aspect for increasing the operational efficiency in the future. The concepts introduced in this chapter form a basis for the development of respective numerical optimisation frameworks, which are further discussed in Chapter 6.

4.1 Target Beam Characteristics

4.1.1 Objective and Investigated Beam Types

The first objective for commissioning the beam production schemes with the new CEI system and hence the primary purpose of these studies is to reproduce the pre-LS2 beam performance for all beam types. The respective parameter set is outlined in Table 4.1. It should be noted, that selected target values differ from pre-LS2 specifications, as they are adapted to the new beam production schemes in the entire injector chain and the upgraded PSB (new aperture bottlenecks). For all beam types, the **aim is to achieve the listed brightness targets while limiting the losses to a few per cent**. Tailoring these target emittances is achieved by customising the KSW modulation functions and the vertical offset Δy of the injected beam (compare Section 2.3.2 and Fig. 2.7). For the scope of this chapter, the various beam types are categorised regarding beam requirements and transverse painting strategies:

Table 4.1: Target beam characteristics at extraction for the various PSB users in 2021: the respective pre-LS2 values are listed for comparison if the specifications differ.

Beam type	N_{p+} **/ ring (10^{10} p+)**	$\epsilon_{x,n,fit}$ **(µm)**	$\epsilon_{y,n,fit}$ **(µm)**	ϵ_{long} **(eVs)**	**Harm. number at injection**
LHC single bunch	**0.5-12**	**0.8-2.5**	**0.8-2.5**	**0.2-0.3**	**1**
LHCPROBE	0.5-2	0.8	0.8	0.2	1
LHCINDIV	2-12	<2	<1.5	0.3	1
LHCINDIV_VDM	10	~2.5	~2.5	0.3	1
LHC Beams	**40-340**	**0.6-2**	**0.6-2**	**0.9-1.3**	**1, 1+2**
2018: LHC 25ns DB_A/B	165	~2	~2	1.3	1
2018: LHC 50ns DB_A/B	~80	~1.5	~1	1.3	1
2018: BCMS 25ns DB_A/B	85	<1.1	<1.2	0.9	1
2018: LHC 8b4e_BCS	45-60	~0.6	~0.6	~0.82	1
2018: LHC 8b4e DB_A/B	~165	~2	~2	1.3	1
2021: HL-LHC	342	<1.7	<1.7	1.5 (-3)	1+2
2021: BCMS	171	<1.36	<1.36	1.5 (-3)	1+2
Fixed target beams	**50-1000**	**0.6-2**	**0.6-2**	**0.9-1.3**	**1, 1+2**
Antiproton Decelerator					
2018: AD	400±50	9	5	<1.3	1+2
2021: AD	400±50	<9	<5	<1.3	1+2
East Area					
EAST	50-67	<1.5	<1.5	<1.3	1
SPS fixed target beams					
2018: SFTPRO_MTE	600	~6-8	~5-6	1.3	1+2
2021: SFTPRO_MTE	<600	<10	2.5-3	1.3	1+2
n_TOF					
2018: TOF	850	11	9	1.7	1+2
2021: TOF	850	<10*	<6*	2.5	1+2
ISOLDE					
2018: NORMGPS/HRS	900	<15	<8	<1.8	1+2
2021: NORMGPS/HRS	900	<10	<6	<2.2**	1+2
STAGISO 1.4GeV	~200/350	<10	<6	<1.8	1+2

* In 2021 established beam sizes after injection and long-term target beam sizes at extraction [91].

** Agreement on new, relaxed longitudinal beam specifications during the 2021 beam commissioning [91].

Section 4.3 - **Fixed target beams:** The fixed target experiments request different intensities and transverse emittances, which are tailored by customised horizontal painting and vertical injection offsets. For several high-intensity users efforts aim to increase the delivered intensity per cycle while minimising losses (e.g. towards $N_{\mathrm{p+}} > 1 \times 10^{13}$ p+ per ring for ISOLDE users).

Section 4.4 - **LHC high-brightness beams**: An on-axis injection in both planes is foreseen as a baseline, meaning that no transverse painting is applied. Injection studies during beam commissioning focus on minimising emittance degradation due to injection errors, such as the imprecisions discussed in Chapter 3.

Section 4.5 - **LHC single bunch beams**: In selected cases, LHC requests single bunch beams with low intensity but blown-up Gaussian transverse profiles. The produced emittances should be similar to those of high-brightness LHC beams. The requested characteristics are established by combining emittance growth from transverse offsets and multiple passages through the stripping foil.

4.2 Methodology for Comparing Multi-Particle Simulations with Measurements

Measurements of the painting schemes are performed for the various users as part of the post-LS2 commissioning. The measurements are compared to multi-particle simulations using the PTC-pyORBIT simulation framework of the upgraded PSB [125] with the 2021 aperture model [95]. The simulations are performed for the first 5-30 ms of the cycle, using similar machine configurations as in operation. Scattering at the stripping foil is incorporated using the *simple scattering model* of pyORBIT, which repeats a single Coulomb scattering event multiple times during a foil passage. The simulation model also includes optics perturbations, which are introduced during the first 5 ms by the injection chicane (edge effects and eddy currents during the decay). For selected users, if explicitly mentioned, the octupole and sextupole strengths of the multipole correctors are set to reproduce the resonances as observed in the PSB ring 3 in 2021 [126].

These simulations serve as a guideline to interpret the experimental observations. The expected injection errors as identified in Chapter 3 are listed for all studies and used to explain discrepancies between simulations and measurements. If explicitly mentioned, these errors are included in the simulations by adapting the painting accordingly.

When qualitatively comparing simulated and measured profiles, the simulated betatronic distributions $f_{\beta,\mathrm{sim}}(u)$ are transformed to the configurations of the measurements with

$$\tilde{f}_{\mathrm{sim}}(u) = f_{\beta,\mathrm{sim}}(u) \cdot \sqrt{\frac{(\beta_{\mathrm{r}}\gamma_{\mathrm{r}})_{\mathrm{sim}} \cdot \beta_{u,\mathrm{WS}}}{(\beta_{\mathrm{r}}\gamma_{\mathrm{r}})_{\mathrm{meas}} \cdot \beta_{u,\mathrm{sim}}}} + D_{\mathrm{WS}} \cdot g_{\mathrm{dpp,\ meas}}, \tag{4.1}$$

considering the optics functions at the location of the simulation results $\beta_{u,\mathrm{sim}}$ and the wire scanner ($\beta_{u,\mathrm{WS}}$, $D_{u,\mathrm{WS}}$), the respective relativistic factors $\beta_{\mathrm{r}}\gamma_{\mathrm{r}}$ and the momentum distribution measured at the C-time of the measurement $g_{\mathrm{dpp,\ meas}}$.

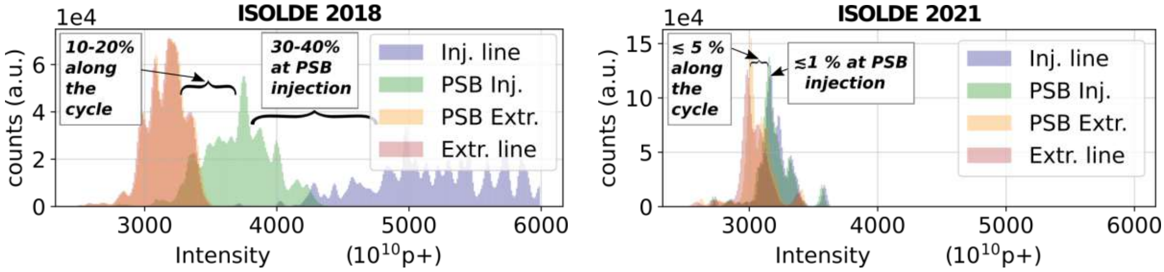

(a) Pre-LS2: conventional 50 MeV multiturn injection.

(b) Post-LS2: 160 MeV CEI system.

Figure 4.1: Intensities measured in the PSB and transfer lines for ISOLDE beams before (2018) and after the upgrade (2021): the distributions show all cycles recorded over an entire operational year. The intensities are measured in the injection line (blue), in the PSB after the injection process (green), in the PSB before the extraction process (yellow) and in the transfer line to the ISOLDE facility (red).

4.3 High-Intensity Fixed Target Beams

This section discusses phase space painting schemes for fixed target beams using the example of high-intensity ISOLDE users. The ISOLDE beam facility [1] requests a high current on the target, which will eventually require the PSB to push the delivered intensity from the currently operational $N_{\mathrm{p+}} = 0.8\text{-}1 \times 10^{13}$ to 1.6×10^{13} p+ per ring [10]. Reducing the charge density during beam accumulation through phase space painting is crucial for minimising the space charge detuning and the consequent emittance growth and/or losses due to interaction of the detuned protons with betatronic resonances (compare Section 1.5.5).

4.3.1 Targets and Restrictions for the ISOLDE Beam Production

Pre-LS2, injecting ISOLDE beams with the conventional multiturn injection caused 30-40 % losses, predominantly during injection at the septum but also during RF capture and along the cycle. These losses are evident in the histograms in Fig. 4.1a, which display the combined intensities recorded in all four PSB rings and the transfer lines over the entire 2018 run ($N_{\mathrm{p+}} = 0.8\text{-}1 \times 10^{13}$ p+ per ring). Figure 4.1b shows that the aim to provide similar intensities as pre-LS2 with the new CEI system, while keeping losses in the PSB globally to a few per cent, was achieved in 2021.

This section compares simulations and measurements to study the impact of different injection painting settings on the loss rates and transverse profiles. The studies focus on the operational intensities of $0.8\text{-}0.9 \times 10^{13}$ p+ per ring, injected over 80 turns. The general parameters applied during these studies are listed in Table 4.2 and motivated by loss reduction studies [127]. Figure 4.2a shows the intensity measured along the cycle for such machine configurations and different paintings. It can be seen, that the intensity evolution is dominated by two loss mechanisms, which

Table 4.2: Target characteristics and general machine configurations for producing high-intensity ISOLDE beams in post-LS2 painting studies (2021).

Parameter	**Unit**	**Value**
Target		
Target emittances $\epsilon_{x,\mathrm{n}}$ / $\epsilon_{y,\mathrm{n}}$	µm / µm	<10 / <6
Intensity per ring (2021)	p+	$0.8\text{-}1.0 \times 10^{13}$
Intensity per ring (long term target)	p+	1.6×10^{13}
Maximum losses along the cycle	%	5-10
Linac4 settings (machine development studies 2021)		
Number of injected turns	-	80-90
Injected intensity	p+	$0.8\text{-}0.9 \times 10^{13}$
Energy spread of injected beam dE_{rms}	keV	280
Chopped bunch length	µs	0.6
PSB settings		
Harmonic of RF bucket at injection (voltage program as in Fig. B.1a)	-	2
Q_x/Q_y at injection (set tune)	-	4.22/4.36
β-beating correction enabled	-	no
Q_x/Q_y at injection (modelled tune)	-	4.22/4.38
Q_x/Q_y at injection (measured tune)	-	4.22/4.39
Q_x/Q_y at extraction	-	4.17/4.23

are both affected by the originally tailored transverse distribution[†]:

- Aperture limitations during the injection and extraction process cause losses of $< 1\,\%$.
- The majority of the losses, i.e. $\gtrsim$ 2-3 %, are caused along the cycle by trapping of particles in the tune spread tail on strong resonances. Figure 4.2b shows the respective simulated tune spreads after 25 ms. Due to the high beam brightness as well as the resonances present in the machine, it is not possible to place the full footprint in a tune space free of resonances [91, 127]. The WP is chosen as $Q_x = 4.22$ and $Q_y = 4.36$[‡] to cross only the 4th-order resonances, $4Q_y = 17$ and $2Q_x + 2Q_y = 17$ (green in Fig. 4.2b) and the 3rd-order skew resonance, $3Q_y = 13$ (yellow, dashed) during the tune ramp. Further, the energy spread of the injected beam was reduced from the originally foreseen $dE_{\mathrm{rms}} = 440\,\mathrm{keV}$ to 280 keV. This reduces the losses, which occur due to periodic resonance crossing in the presence of space charge

---

[†] Loss mechanisms which are not sensitive to the transverse painting settings are not further included in this section. However, these losses are either not dominant for operational ISOLDE beams (e.g. large angle Single Coulomb scattering at the stripping foil causing $< \mathcal{O}(0.1)\,\%$ losses or longitudinal out-of-bucket losses) or mitigated by adequate operational settings (e.g. transverse instabilities cured by WP choice and transverse feedback).

[‡] Note that the vertical β-beating introduced by the chicane is not corrected in these studies, causing $Q_y = 4.39$ during the injection process.

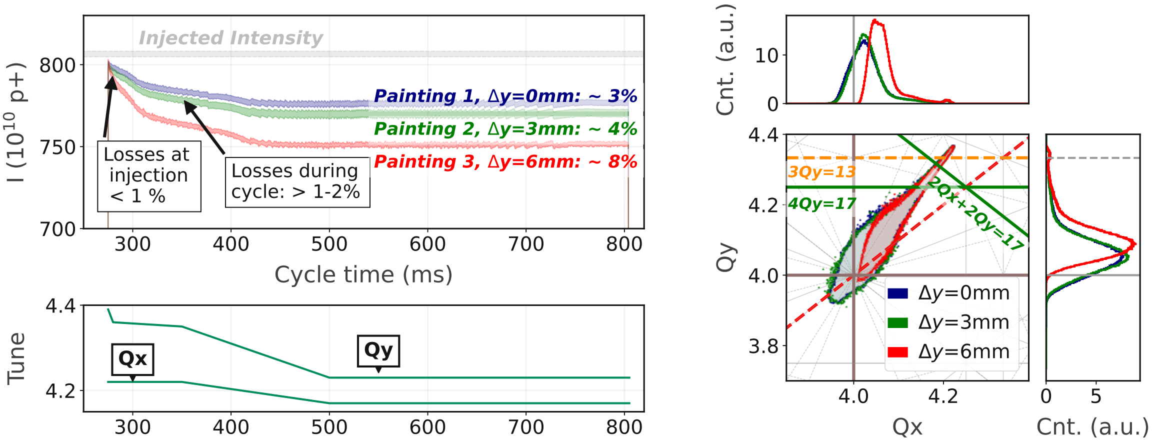

(a) Top: measured intensity along the cycle (1σ error bar, injection: C275, extraction: C805). The injected intensity is indicated by the grey bar. Bottom: modelled tune evolution when setting $Q_x = 4.22, Q_y = 4.36$ at C275. The vertical tune at C275 is $Q_y \approx 4.39$ due to the uncorrected β-beating induced by the injection chicane.

(b) Simulated tune spread after 25 ms for the different paintings. Experimentally observed 3rd and 4th-order resonances (2021), which are crossed by the tune footprint, are indicated in yellow and green.

Figure 4.2: Intensity evolution along the PSB cycle for different injection paintings at $Q_x = 4.22, Q_y = 4.36$: applying a vertical offset has a significant effect on the observed loss rates (KSW: $A_0 = 35\,\text{mm}$, $t_1 = 10\,\mu\text{s}$, $t_2 = 80\,\mu\text{s}$, $A_1 = A_2 = 20\,\text{mm}$).

as shown in literature [128].

The aim when optimising the painting is thus to establish a beam cross-section within the aperture limitations while minimising the space charge forces. The latter aims not only to reduce the footprint but to limit the interaction of both the tune spread core and tails with strong resonances for a given WP (Fig. 4.2b) [129].

It has to be noted that general machine optimisation studies [59, 91, 127], including resonance compensation, correction of the β-beating introduced by the injection chicane, WP settings and tuning of the longitudinal distribution, are continuously ongoing. However, the painting concepts, which will be discussed in this section are transferable to evolving machine configurations or intensities when respectively adapting the painting functions.

The studies performed at the operational WP and intensity will be complemented by selected painting studies with reduced intensity at $Q_x = 4.14$ and $Q_y = 4.22$, i.e. a WP below the mentioned 3rd and 4th-order resonances. These tests aim to verify loss patterns due to exceeding beam sizes and transverse distributions without the influence of the mentioned resonances.

Aperture Considerations and Expected Loss Maps

The main goal for the ISOLDE beam production is the reduction of losses. The delivered transverse emittances are not a design parameter per se but rather a consequence of this loss optimisation and beam size limitations in the machine. To enable a correlation of painted beam sizes and loss levels in the subsequent studies, the main anticipated aperture bottlenecks in the machine are introduced in this segment.

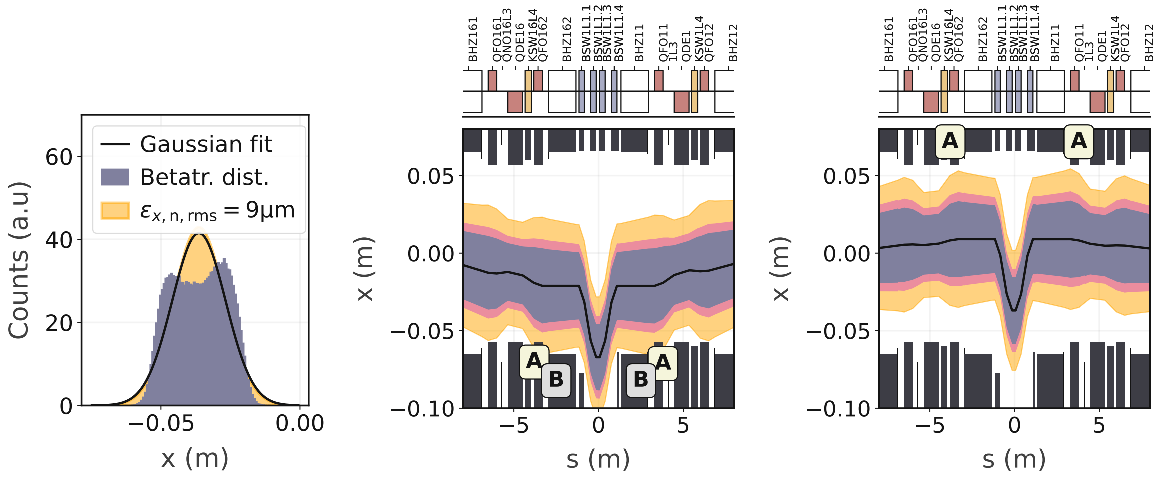

(a) Profile at $t = 100\,\mu\mathrm{s}$. **(b)** $t = 100\,\mu\mathrm{s}$; $A_{\mathrm{KSW}} = 21.5$ mm. **(c)** $t = 120\,\mu\mathrm{s}$; $A_{\mathrm{KSW}} = -9$ mm.

Figure 4.3: Horizontal beam envelope in the injection region when injecting high-intensity fixed target beams with $\epsilon_{x,\mathrm{n,rms}} = 9\,\mu\mathrm{m}$. The black line indicates the closed orbit, which is created by the KSW and BSW orbit bumps. Yellow: Gaussian horizontal distribution with a margin for orbit and alignment errors; blue: simulated distribution; pink: simulated distribution with a margin for orbit and alignment errors. The anticipated aperture bottlenecks are (A) the focusing quadrupoles and (B) the beam scrapers of main dipoles within the bump.

Horizontally, the acceptance is limited in the injection region during the painting process. The vertical limit is the upgraded recombination septum in the extraction line. Previous studies analysed the acceptance of the PSB based on Gaussian beam distributions to guide the design phase of the LIU upgrade. These conservative estimates yield maximum allowed normalised 1σ emittances of $\epsilon_{x,\mathrm{n,max}} = 9\,\mu\mathrm{m}$ [46] and $\epsilon_{y,\mathrm{n,max}} = 6\,\mu\mathrm{m}$ [130] in order to fit the beam into the horizontal $4\sigma_{x,\mathrm{max}}$ and vertical $2.5\sigma_{y,\mathrm{max}}$ acceptance, respectively. A new absorber system comprising a movable and a fixed mask was consequently installed during LS2 in P08 based on these estimates. The fixed mask (TSAB8L4) features per design an acceptance of $4\sigma_{x,\mathrm{max}}$ and $3.5\sigma_{y,\mathrm{max}}$ at injection energy. When inserting the movable mask (TSAA8L4), the acceptance is reduced to $3.5\sigma_{x,\mathrm{max}}$ and $2.5\sigma_{y,\mathrm{max}}$ [131].

Figure 4.3 visualises the simulated horizontal beam envelope during the injection process, when painting a beam with $\epsilon_{x,\mathrm{n,\,rms}} = 9\,\mu\mathrm{m}$ and $\epsilon_{y,\mathrm{n,\,rms}} = 6\,\mu\mathrm{m}^{\dagger}$. This plot shows, that the horizontally painted distribution can feature strongly under-populated tails. The envelope is thus smaller than for a Gaussian beam with similar $\epsilon_{\mathrm{n,rms}}$ (yellow), which is computed using

$$Env_u = 3 \cdot \sqrt{\beta_u \epsilon_u} + D_u \cdot dp/p_{\mathrm{max}} + x_{\mathrm{err,tot}},$$

with the 2021 optics model [95, "psb/2021/scenarios/isolde/0_injection"]. The total transverse error $x_{\mathrm{err,tot}}$ combines mechanical alignment ($\Delta x_{\mathrm{mech}} = 1$ mm) and orbit errors ($\Delta x_{\mathrm{orb}} = 5\,\mathrm{mm} \cdot \sqrt{\beta_u/\beta_{u,\mathrm{max}}}$).

[†] Injection of $N_{\mathrm{p+}} = 1.15 \times 10^{13}$ p+ per ring over 100 turns with $I_{\mathrm{L4}} = 25$ mA, $CF = 0.7$, $dE_{\mathrm{rms}} = 440$ keV. Painting with $A_0 = 35$ mm, $A_1 = A2 = 21.5$ mm $t_1 = 10\,\mu\mathrm{s}$, $\Delta y = 7$ mm at $Q_x = 4.22$, $Q_y = 4.45$.

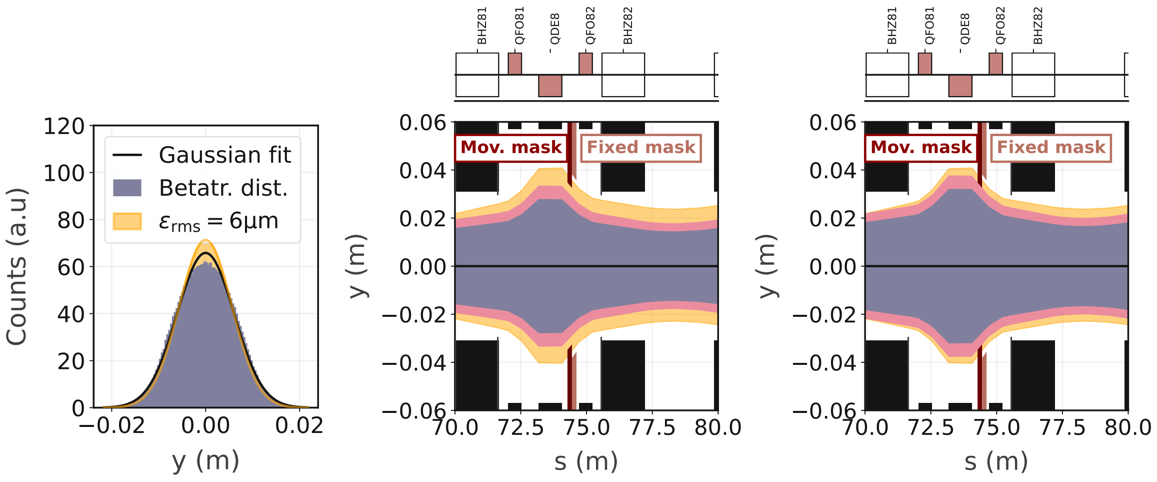

(a) Profile at $t = 5$ ms.

(b) $t = 1$ ms.

(c) $t = 5$ ms.

Figure 4.4: Vertical profile and beam envelope at the location of the mask (P08) during the first 5 ms of the high-intensity fixed target beam production with $\epsilon_{y,\mathrm{n,rms}} = 6\,\mu\mathrm{m}$. The black line indicates the closed orbit. The aperture limitations of the moveable and fixed mask are indicated in red and pink, respectively. Yellow: Gaussian vertical distribution with a margin for orbit and alignment errors; blue: simulated distribution; pink: simulated distribution with a margin for orbit and alignment errors.

The 3σ Gaussian reference envelope (yellow) is compared in Fig. 4.3 with envelopes containing 99.7 % of the simulated beam distributions, without (blue) and with (pink) orbit and alignment errors. In the multi-particle simulations, the distribution is retrieved at each turn at the location of the injection foil. The respective 6D distribution is consequently linearly mapped along the PSB using Eq. (1.24) to produce the envelopes plotted in Fig. 4.3.

The large amplitude of the KSW bump during beam accumulation, $A_{\mathrm{KSW}} \approx$ 18-25 mm, limits the aperture at the elements within the bump over a few tens of turns. The main bottlenecks are observed in the focusing quadrupoles BR.QFO11 and BR.QFO162 up- and downstream of the injection region (Fig. 4.3, A) as well as the beam scrapers of the main dipoles in P01 and P16, BR.SPSCRAP11 and BR.STSCRAP162 (Fig. 4.3, B). After the end of beam accumulation the KSW decays to negative amplitudes for a few hundred turns ($A_{\mathrm{KSW}} \approx -9$ to 0 mm, Fig. 4.3c). During this time, the same elements limit the acceptance, but on the other side of the machine axis.

The vertical acceptance bottleneck is the newly installed beam absorber in P08. Figure 4.4 illustrates the vertical beam envelope in P08 after 1 ms and 5 ms. The vertical profiles are closer to a Gaussian distribution than in the horizontal plane and hence the limit of $\epsilon_{y,\mathrm{n,rms}} \approx 6\,\mu\mathrm{m}$ more accurate.

Additionally to the non-Gaussian characteristic, it should be noted that painting can produce beams with a quasi rectangular x-y cross-section while the apertures of some elements are circular or elliptical. When discussing different painting schemes below, emphasis will therefore be put on the evolution of the x-y cross-section at the location of the bottlenecks.

The simulated cumulative loss map (Fig. 4.5a) and temporal loss evolution (Fig. 4.5b) confirm that, after the initial horizontal beam loss related to the injection process, the majority of the

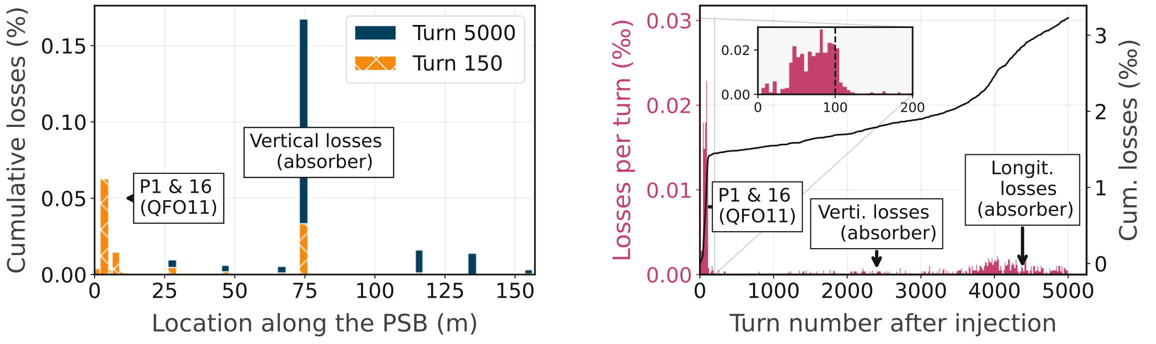

(a) Cumulative losses along the machine. The losses during the injection process concentrate in the injection region (orange). The subsequent losses along the cycle are recorded at the absorber (blue, after 5 ms).

(b) Loss evolution (left axis) during the first 5 ms. The cumulative losses are illustrated using the right axis.

Figure 4.5: Simulated loss locations and evolution for high-intensity beams: results for a beam with $N_{\mathrm{p+}} = 1.15 \times 10^{13}$ p+ per ring, injected over 100 turns with $I_{\mathrm{L4}} = 25$ mA, $CF = 0.7$, $dE_{\mathrm{rms}} = 440$ keV. Painting with $A_0 = 35$ mm, $A_1 = A2 = 21.5$ mm $t_1 = 10$ µs, $\Delta y = 7$ mm at $Q_x = 4.22$, $Q_y = 4.45$.

simulated losses are expected vertically at the absorber. Potential longitudinal off-bucket particles are lost at the horizontal aperture of the absorber after a few ms.

4.3.2 Painting Scenarios

When discussing the impact of painting setting variations on the resulting beam and loss distributions, both during injection and along the cycle, it is essential to highlight the different effects, which contribute to the transverse beam evolution during the first milliseconds. These effects mainly include emittance growth purely defined by the applied painting actions, beam core and/or halo growth caused by the interaction with (mainly integer) resonances or emittance exchange due to interaction with the space charge-driven Montague resonance $2Q_x - 2Q_y = 0$, Eq. (1.51).

This section exemplifies the dynamics for different painting scenarios using multi-particle simulations. The machine configurations correspond to operational settings, as listed in Table 4.2, i.e. $N_{\mathrm{p+}} \approx 0.8 \times 10^{13}$ p+ injected over 80 turns at $Q_x = 4.22$ and $Q_y = 4.36$. The examined painting settings are summarised in Table 4.3 and Fig. 4.6 and are chosen to produce comparable transverse profiles and rms emittances after 25 ms despite triggering different growth mechanisms. Exceptions are *cases B* and *E*, which are produced with extreme painting settings and only presented for illustrative purposes. The evolutions of the phase spaces, profiles, envelopes and tune spreads are illustrated in Figs. 4.7 to 4.10. Intermediate paintings can result in a combination of the presented examples.

A. *Painting-driven emittance evolution in both planes* (Fig. 4.7): This scenario has been targeted in all previous phase space painting studies for the PSB injection system [44–48]. It aims at fully defining the beam distribution through the painting settings rather than the interaction of the beam core with the integer resonances. Minimising the incoherent tune spread to avoid the

Table 4.3: Transverse painting parameters for *cases A to E* and the corresponding simulation results (KSW set to $A_0 = 35$ mm, $t_1 = 10\,\mu$s in all cases).

Case	A_1 (mm)	A_2 (mm)	Δy (mm)	$\epsilon_{x,\mathrm{n,rms}}$ at 25 ms (µm)	$\epsilon_{y,\mathrm{n,rms}}$ at 25 ms (µm)	x-y cross-section at injection	Losses after 200 µs (%)	Losses after 5 ms (%)
A	21	21	6	≈8.6	≈4.3	Rectangular	0.13	0.26
B	29	29	0	≈9	≈5.8	Ellipse	0.2	1.25
C	23	23	0	≈9	≈4.3	Ellipse	0.14	0.2
D	27	15	0	≈8.9	≈4	Ellipse	0.08	0.12
E	16	16	11	≈17.6	≈9.2	Rectangular	1	2.5

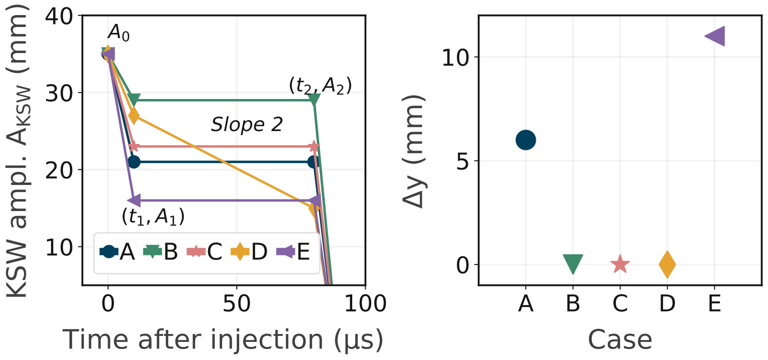

Figure 4.6: Transverse painting parameters for the examples presented in *case A to E*.

integer resonances (here $\Delta Q_x \lessapprox 0.2$ and $\Delta Q_y \lessapprox 0.4$) requires painting sufficiently large beam sizes in both planes. The phase spaces painted in this example feature a hollow characteristic during the injection process (Fig. 4.7a), which filaments to a more uniform distribution during the first milliseconds. Horizontally, this structure can be optimised by variation of t_1, A_1 and A_2 to target a more uniform distribution already during painting.

The large actions, with which the bunches are injected in both planes create a quasi rectangular x-y cross-section during beam accumulation (red scatter markers Fig. 4.7a). The red contours in Fig. 4.7c show, that this cross-section reduces the vertical acceptance in the elliptical aperture of the beam scrapers SPSCRAP11 and STSCRAP162 at the end of beam accumulation. Furthermore, these particles experience a small detuning in both planes and are prone to particle trapping at the mentioned 3rd and 4th-order resonances during the tune ramp (yellow and green in Fig. 4.7a).

B. *Space charge-driven emittance evolution in both planes* (Fig. 4.8): This case is only listed for academic purposes and is not considered a realistic operational scenario. Failing to reduce the charge density when painting insufficiently large beam sizes causes incoherent tune spreads of $\Delta Q_x \approx 1$, $\Delta Q_y \approx 1$ after injection. Both the beam core and the tails interact with strong resonances in the entire tune space, particularly the integer resonances, which results in an uncontrolled blow-up of the emittance, halo formation and losses at the beginning of the cycle.

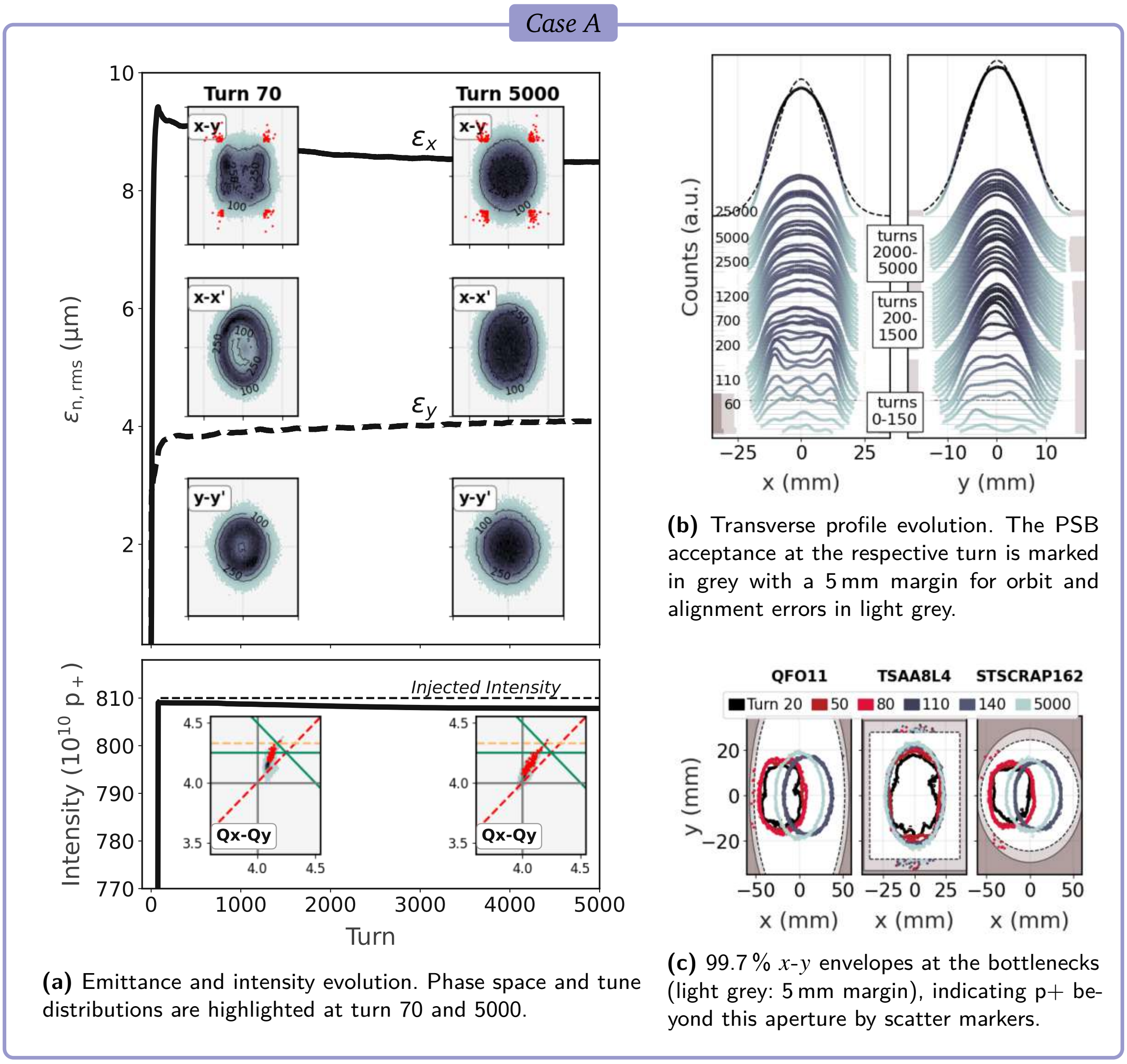

(a) Emittance and intensity evolution. Phase space and tune distributions are highlighted at turn 70 and 5000.

(b) Transverse profile evolution. The PSB acceptance at the respective turn is marked in grey with a 5 mm margin for orbit and alignment errors in light grey.

(c) 99.7 % x-y envelopes at the bottlenecks (light grey: 5 mm margin), indicating p+ beyond this aperture by scatter markers.

Figure 4.7: Transverse dynamics during the first 5 ms for *case A* (painting-driven emittance growth).

Note that in the operational tune regime of the PSB, with both tunes being close to 4, the integer resonances are strong as $4Q_x = 16$ and $4Q_y = 16$ are systematic resonances of even order and can hence be driven by space charge [76, 132].

In addition to losses due to excitation on resonances, such paintings also produce higher loss rates due to acceptance limitations during the injection process, as listed in Table 4.3. The space charge-driven growth of the horizontal halo occurs already during beam accumulation, while the amplitude of the KSW bump is at high values (red envelope in Fig. 4.8c with $A_{\mathrm{KSW}} = 29\,\mathrm{mm}$).

Case B

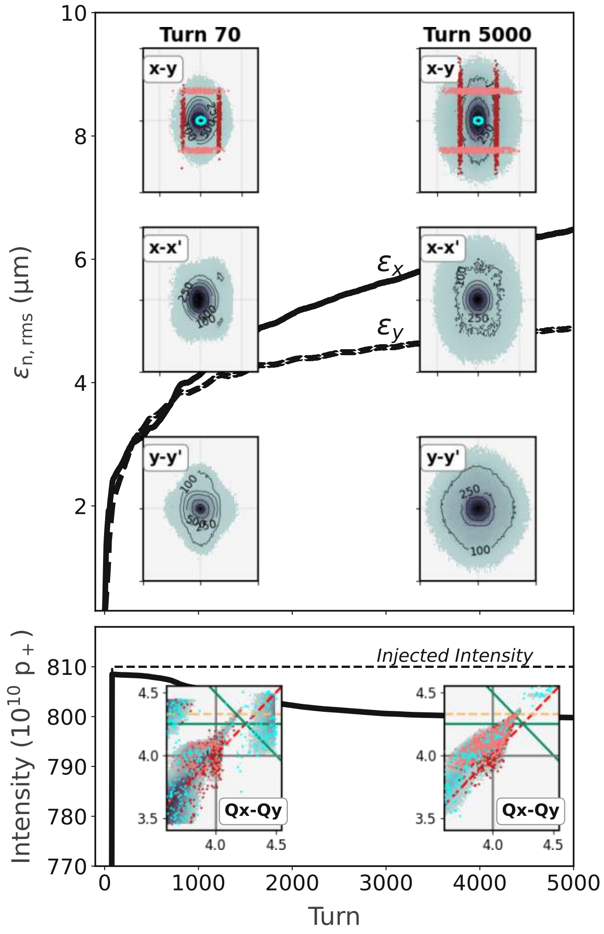

(a) Emittance and intensity evolution. Phase space and tune distributions are highlighted at turn 70 and 5000.

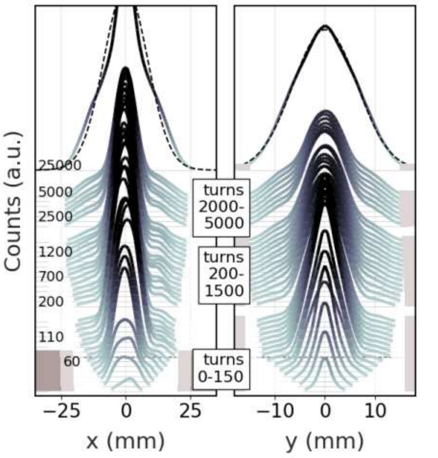

(b) Transverse profile evolution. The PSB acceptance at the respective turn is marked in grey with a 5 mm margin for orbit and alignment errors in light grey.

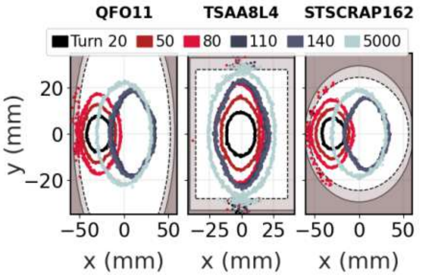

(c) 99.7 % x-y envelopes at the bottlenecks (light grey: 5 mm margin), indicating p+ beyond this aperture by scatter markers.

Figure 4.8: Transverse dynamics during the first 5 ms for *case B* (space charge-driven emittance growth).

C. *Coupling-driven emittance evolution* (Fig. 4.9): Painting an initially flat beam aims at avoiding the rectangular characteristic of the transverse distribution, which is obtained in *case A*. Injecting vertically on-axis ($\Delta y \approx 0$) results in a large vertical tune spread, the interaction of the beam core with the vertical integer resonances and a consequent space charge-dominated emittance growth in the vertical plane. In the horizontal plane, however, a large painting offset $\overline{\Delta}_{x\,\mathrm{SI2}}$ is applied, aiming for painting-driven horizontal emittance growth. The horizontal tune spread is minimised and interaction with the horizontal integer resonances is avoided.

Such paintings can be strongly impacted by the interaction with the space charge-driven Montague resonance, which is indicated by the red, dashed line in Fig. 4.9a. The initially painted flat x-y cross-section is still recognisable at turn 30 in Fig. 4.9a. Increasing the intensity during

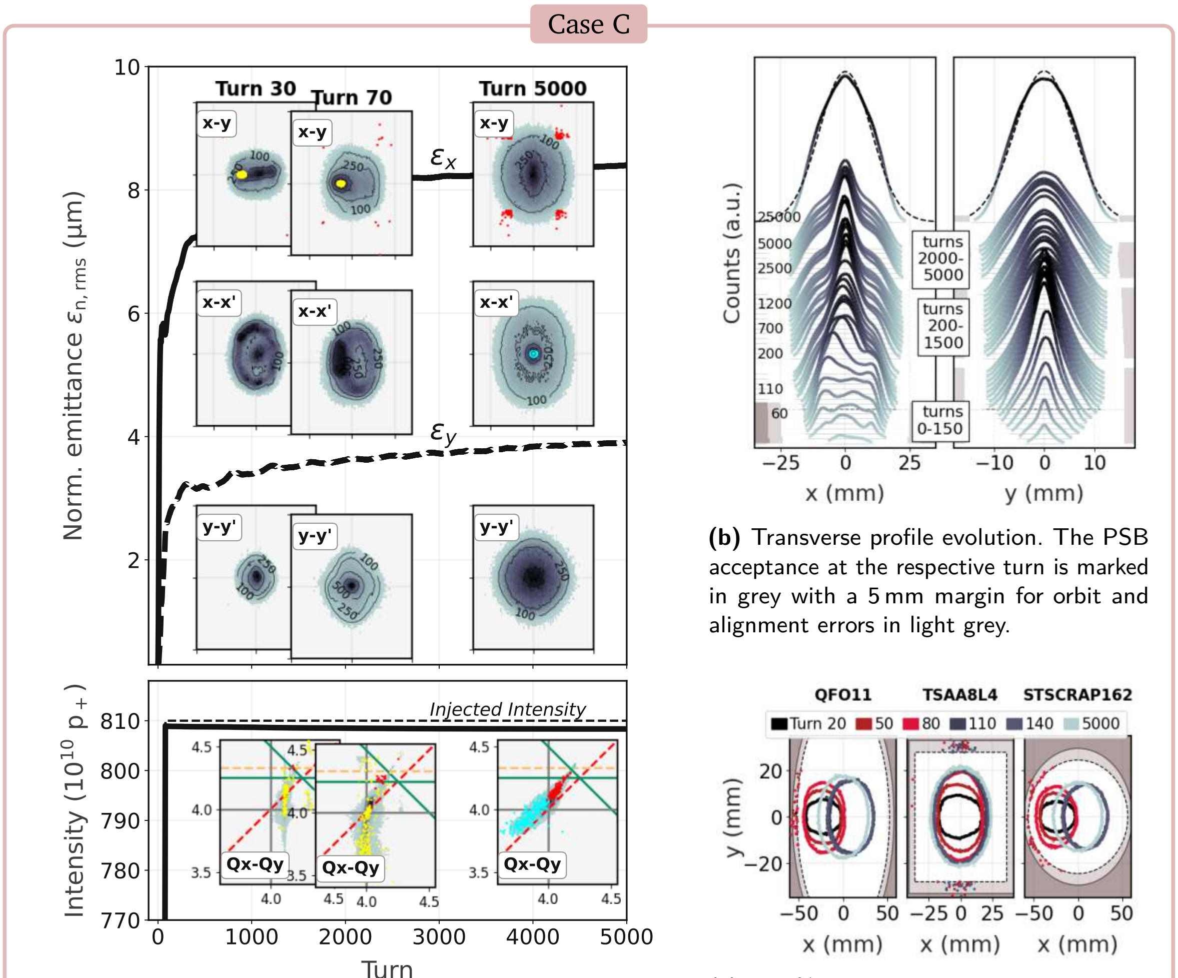

(a) Emittance and intensity evolution. Phase space and tune distributions are highlighted at turn 30, 70 and 5000.

(b) Transverse profile evolution. The PSB acceptance at the respective turn is marked in grey with a 5 mm margin for orbit and alignment errors in light grey.

(c) 99.7 % x-y envelopes at the bottlenecks (light grey: 5 mm margin), indicating p+ beyond this aperture by scatter markers.

Figure 4.9: Transverse dynamics during the first 5 ms for *case C* (coupling-driven emittance growth).

beam accumulation results in faster growth of the vertical compared to the horizontal tune spread during the first 100 turns. This drives not only vertical emittance growth at the vertical integer resonances but also emittance exchange at the Montague resonance. Transverse coupling already starts during beam accumulation (i.e. around turn 30), transferring horizontal to vertical action. The horizontal tune spread can consequently increase beyond $\Delta Q_x > 0.2$, despite the large painting settings. Particles congregate close to the horizontal integer resonances already during beam accumulation, causing newly injected particles to be piled up at the same location in the horizontal phase space. The increased local charge density is indicated by the yellow scatter markers at turn 30 and 70 in Fig. 4.9a.

Coupling at the Montague resonance continues to drive a transfer from horizontal to vertical

Case D

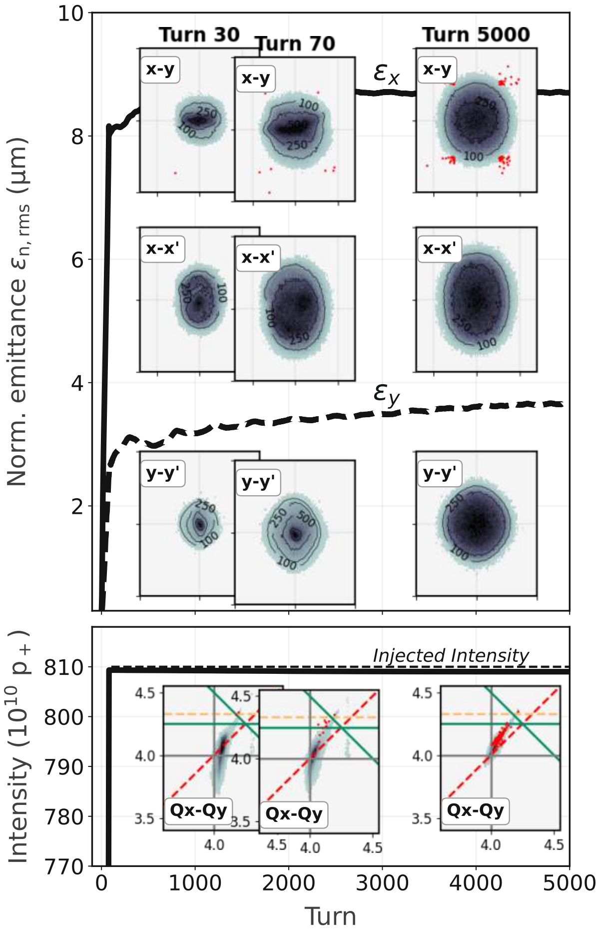

(a) Emittance and intensity evolution. Phase space and tune distributions are highlighted at turn 30, 70 and 5000.

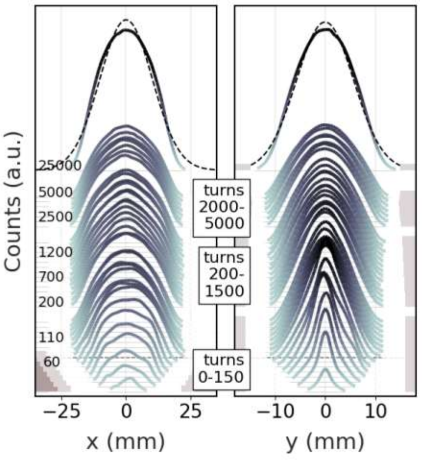

(b) Transverse profile evolution. The PSB acceptance at the respective turn is marked in grey with a 5 mm margin for orbit and alignment errors in light grey.

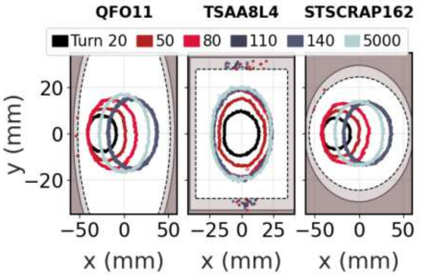

(c) 99.7 % x-y beam envelope at the bottlenecks. A 5 mm margin for orbit errors is marked in light grey. p+ beyond this aperture are highlighted by scatter markers.

Figure 4.10: Transverse dynamics during the first 5 ms for *case D*.

action, also after injection. This forms a high-density island in the horizontal plane, which is marked in cyan at turn 5000 in Fig. 4.9a (compare [33]).

Adapting the horizontal painting, mainly the amplitude and/or the gradient of *slope-2*, changes the ratio of vertical and horizontal tune spread and consequently the extent of coupling. It is enhanced for paintings with constant KSW amplitude during beam accumulation, i.e. $A_1 \gtrsim A_2$, as most particles are injected at similar densities, causing equivalent horizontal detunings and probabilities for action transfer to the vertical plane.

However, no significant implication of this coupling-driven beam evolution is identified for the operational performance, i.e. the loss rates and the resulting beam profiles after > 30 ms. The

Case E

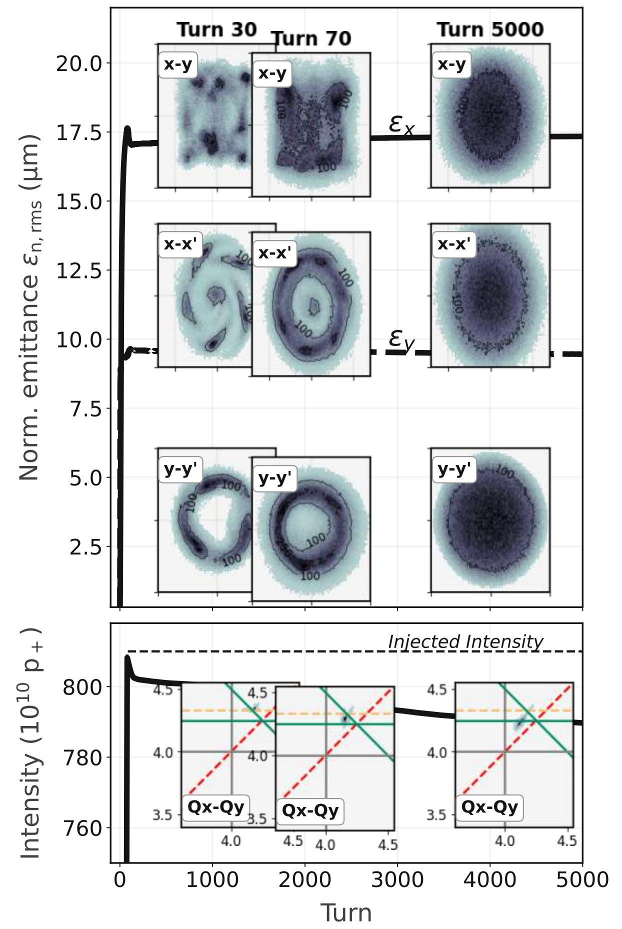

(a) Emittance and intensity evolution. Phase space and tune distributions are highlighted at turn 30, 70 and 5000.

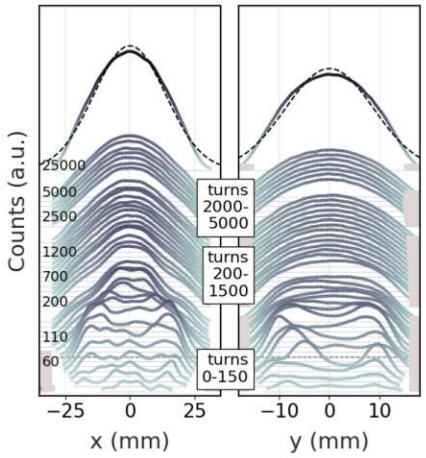

(b) Transverse profile evolution. The PSB acceptance at the respective turn is marked in grey with a 5 mm margin for orbit and alignment errors in light grey.

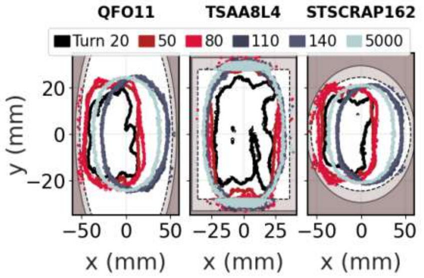

(c) Evolution of 99.7 % x-y envelopes at the bottlenecks (grey). 5 mm margin for errors is indicated in light grey and p+ beyond this aperture by scatter markers.

Figure 4.11: Transverse dynamics during the first 5 ms for *case E*.

rectangular characteristic of the x-y cross-section is successfully avoided. Compared to *case A*, the acceptance during painting increases. At the same time, the accumulation of particles in the vicinity of the resonances during the tune ramp decreases while providing similar emittances and envelopes as in *case A*.

D. *Painting-driven in the horizontal and space charge-driven evolution in the vertical plane* (Fig. 4.10): This case aims at painting a flat beam, as in *C*, while minimising the creation of high-density islands due to emittance exchange. As in *case C*, the beam is injected vertically on-axis. Horizontally, however, the painted action is gradually increased during beam accumulation by setting $A_1 \gg A_2$. This allows spreading the ratio $\Delta Q_x / \Delta Q_y \approx$ const. during beam accumulation and reduces the number of particles trapped at the Montague resonance. The phase spaces and profiles (Fig. 4.10) show that such painting results in a more uniform distribution already after injection. Out of all investigated cases, this painting yields the largest acceptance during the injection process, as indicated by the acceptance in the profile plot Fig. 4.10b, and the smallest loss rates during and after injection as listed in Table 4.3. Alternatively to varying *slope-2*, modifying t_1 or setting $A_2 \lessapprox A_1$, respectively, can also reduce the interaction with the Montague resonance.

E. *Exceeding paintings, hollow beams and filamentation-driven beam evolution* (Fig. 4.11): This scenario is listed to complement the other cases and is not realistic in operation. The beam is injected with exceeding actions in the horizontal and vertical plane, larger than in *case A*. The painted beam distribution is extremely hollow and asymmetric. For such extreme painting cases, the transverse beam evolution can be driven by beam filamentation. As described in Chapter 3, this beam dilution in phase space is affected by the coherent beam oscillation, the incoherent space charge and the chromatic tune spread. Such a scenario is illustrated in Fig. 4.11, which shows the redistribution of the particles in horizontal phase space during the first 200 µs. In the presented case, the profile after filamentation has a more triangular characteristic, instead of the more uniform horizontal distribution achieved through painting in e.g. *case A*.

4.3.3 Methodology for Measurements

During the post-LS2 commissioning, it was possible for the first time to experimentally assess these painting schemes in the PSB and demonstrate the discussed impact on loss rates and transverse beam distributions. The measurements aim to probe the entire range from *controlled, painting-driven emittance growth* to *uncontrolled SC driven emittance growth* (*cases A to E*) by varying the painting settings Δy, A_1 and A_2.

Painting Settings

In all measurements, A_0 is set to match the design position of the injected beam and minimise injection oscillations. *Slope-2* is characterised in this chapter using the average offset of the orbit to the newly injected beam

$$\overline{\Delta x}_{\mathrm{Sl2}} = A_0 - \frac{A_1 + A_2}{2} \tag{4.2}$$

and the gradient

$$k_{\mathrm{Sl2}} = \frac{A_2 - A_1}{t_2 - t_1}. \tag{4.3}$$

Applying optimisation algorithms in Chapter 6 will demonstrate that the sensitivity to variations in A_0 and t_1 is comparatively small. A_0 and t_1 are therefore left constant in the studies presented in this section.

Beam Observables

The painting settings will be evaluated regarding several beam loss, intensity and beam size observables:

- **Loss fractions:** The operationally relevant figure of merit and objective to minimise is the total loss fraction, which is obtained using the intensity measured in the transfer line and the PSB ring. The intensity is acquired using beam current transformers (BCT). The fraction of particles, which is lost at injection and in the cycle up to a specified C-time t is defined as

  $$L_t = \frac{N_{\mathrm{p+,INJ}} - N_{\mathrm{p+,BR},t}}{N_{\mathrm{p+,INJ}}}, \tag{4.4}$$

  with $N_{\mathrm{p+,INJ}}$ being the intensity of the H$^-$ beam measured in the BI line (indicated in grey in Fig. 4.2a) and $N_{\mathrm{p+,BR},t}$ the intensity, which is observed with the ring BCT at the cycle time t. The total loss fraction along the entire cycle is labelled as L_{C805} and is computed using the intensity measured with the ring BCT just before extraction, i.e. at C805. L_{C275} describes the losses, which occur during the injection process and the first ms of the cycle and is estimated using the acquisition of the ring BCT after injection, i.e. at C275.

- **Loss distribution:** The BLMs in the injection region, the ring and the extraction line are used to obtain spatial loss distributions (see Fig. 2.3). These loss patterns are analysed to verify the modelled bottlenecks for different painting settings.

- **Transverse beam profiles:** The transverse distributions are measured with the newly installed LIU wire scanner [133]. Measurements are mainly performed close to the end of the cycle (C770). Acquiring the profiles at the PSB extraction energy minimises distortions of the profiles due to multiple Coulomb scattering at the wire. Further, acquisitions just before the extraction process enable an analysis of the acceptance limitations in the extraction line. Additionally, measurements in the first half of the cycle aim at evaluating the profiles during the tune ramp (Fig. 4.2a, bottom), particularly at C350 in the vertical plane. Acquisitions at earlier cycle times are discarded, as the profile degradation by multiple Coulomb scattering at the wire increases with decreasing energy. This scattering distortion is more prominent in the horizontal than the vertical plane due to the larger beam size, Horizontal reference measurements during the tune ramp are therefore conducted only at C400. The emittances are computed in first approximation based on Eq. (1.41). The momentum distribution at the cycle time of the wire scan is reconstructed using longitudinal tomography [134] (Fig. B.2). The betatronic transverse beam sizes are reconstructed using the standard Gaussian subtraction of the dispersive contribution Eq. (1.40), despite the betatronic and longitudinal profiles being non-Gaussian. However, the error, which is consequently introduced, is accepted as these first emittance acquisitions mainly aim to identify space charge and painting-driven regimes and conduct a verification of the expected beam sizes and bottlenecks. Still, to reduce the error the focus is put on horizontal measurements at C770, due to the more Gaussian momentum distribution and the smaller energy spread (compare Fig. B.2).

  The intensity in the tails is integrated to correlate the loss patterns in the ring and transfer lines to the transverse distributions. The cut-off thresholds u_{thres} for this integration

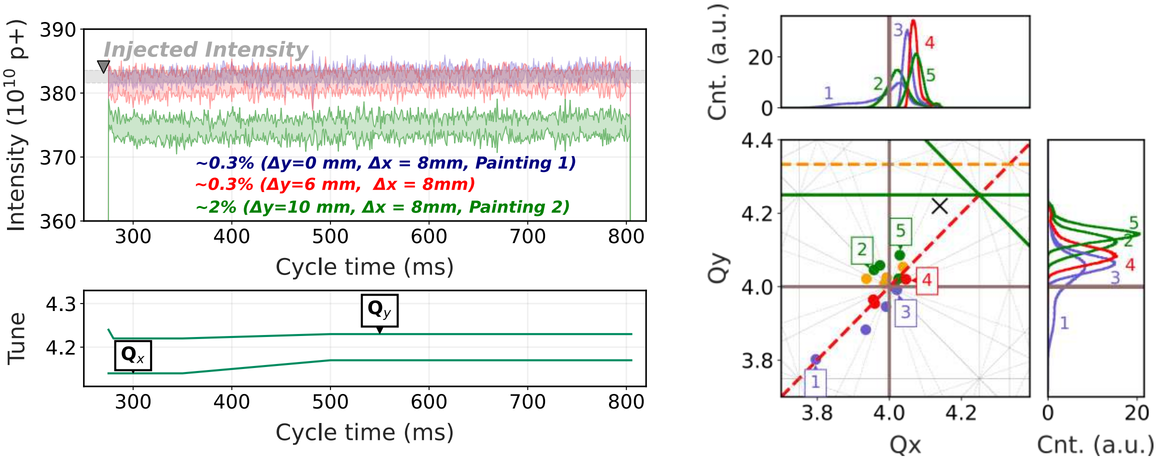

(a) Top: measured intensity along the cycle (1σ error bar, injection: C275, extraction: C805). The injected intensity is indicated by the grey bar. Bottom: modelled tune evolution. The vertical tune at C275 is $Q_y \approx 4.24$ due to the uncorrected β-beating induced by the injection chicane.

(b) Simulated maximum tune shifts after 5 ms for different paintings (x: bare tune). Experimentally observed 3rd and 4th-order resonances (yellow and green) are avoided at this working point.

Figure 4.12: Impact of different injection painting settings on intensity evolution and tune spread for $Q_x = 4.14, Q_y = 4.22$ and $N_{\mathrm{p+}} = 380 \times 10^{10}$ p+ per ring.

$N_{\mathrm{p+}}$ $(u > u_{\mathrm{thres}})$ are chosen based on the acceptance limitations discussed in Section 4.3.1: $x_{\mathrm{thres}} = 3\sigma_{x,\mathrm{ref},\beta}$ in the horizontal and $y_{\mathrm{thres}} = 2.3\sigma_{y,\mathrm{ref},\beta}$ in the vertical plane. $\sigma_{u,\mathrm{ref},\beta}$ refers to the betatronic beam size for the respective reference emittances $\epsilon_{x,\mathrm{n,ref}} = 10\,\mu\mathrm{m}$ and $\epsilon_{y,\mathrm{n,fref}} = 6\,\mu\mathrm{m}$.

Simulation Settings

Comparative simulations are performed with the inclusion of several machine errors. Firstly, the multipole strengths as listed in Table 4.5 [126] are included to drive the relevant 3rd and 4th-order resonances, which were observed in ring 3 in 2021 [59]. Secondly, the painting is corrected for observed injection errors: the injection imprecisions studies presented in Section 3.2.2 (Table 3.2) conclude that a horizontal error of 1-1.5 mm is expected in measurements, mainly due to the mismatch during the KSW decay. The effective average offset during painting $\overline{\Delta x}_{\mathrm{SI2}}$ is consequently larger than set experimentally. To account for this mismatch, 1 mm is added to $\overline{\Delta x}_{\mathrm{SI2}}$ in simulations. This means, that measurements with $A_{1,\mathrm{sim}}$, $A_{2,\mathrm{sim}}$ are compared to simulations with $A_{1,\mathrm{meas}} - 1$ mm and $A_{2,\mathrm{meas}} - 1$ mm. The values stated in the thesis correspond to the experimentally set amplitudes $A_{1,\mathrm{meas}}$, $A_{2,\mathrm{meas}}$.

4.3.4 Measurements at $Q_x = 4.14, Q_y = 4.22$

As introduced above, for the operational WP ($Q_x = 4.22, Q_y = 4.36$) and intensity ($N_{\mathrm{p+}} = 0.8\text{-}0.9 \times 10^{13}$ p+ per ring) the majority of the losses are expected to occur along the cycle by trapping of particles in the tails on strong resonances. Before focusing on these operational

Table 4.4: Parameters for phase space painting studies at $Q_x = 4.14, Q_y = 4.22$.

Parameter	**Unit**	**Values**
Number of injected turns	-	38
Intensity per ring	p+	0.38×10^{13}
Movable mask state	-	inserted
Estimated (average) injection errors (see Section 3.2)		
Horizontal	mm	1-1.5
Vertical	mm	0.5-1
Injection painting settings		
H: KSW - t_1 (length of slope-1; painting)	µs	10
H: KSW - A_0 (bump amplitude)	mm	35
H: KSW - A_1 (amplitude end of slope-1)	mm	19-27
H: KSW - A_2 (amplitude end of beam accumulation)	mm	as A_1
V: orthogonal steering - Δy	mm	0-10
PSB settings		
Harmonic of RF bucket at injection (voltage program as in Fig. B.1a)	-	2
Q_x/Q_y at injection (set tune)	-	4.14/4.22
β-beating correction	-	no
Q_x/Q_y at injection (modelled tune)	-	4.14/4.24
Q_x/Q_y at injection (measured tune)	-	4.14/4.24
Q_x/Q_y at extraction	-	4.17/4.23

parameters, selected studies at a WP below the observed resonances are presented, i.e. when setting $Q_x = 4.14$ and $Q_y = 4.22$ ($Q_y = 4.24$ during the injection process due to the β-beating introduced by the injection chicane). These measurements simplify the comparison between expected loss levels in simulations and measurements because the losses occur predominantly due to beam size limitations within the first 1 ms, as evident in Fig. 4.12. Further, the transverse profiles are not affected by the tail population due to interaction with the observed 3rd and 4th-order resonances.

To facilitate investigation of the painting-driven emittance growth regime also at this lower WP the incoherent tune spread is reduced by injecting a reduced intensity of $N_{\mathrm{p+}} = 380 \times 10^{10}$ p+ per ring over 38 turns. The respective parameter set is listed in Table 4.4. The vertical and horizontal offsets are varied between Δy = 0-10 mm and $\overline{\Delta x_{\mathrm{SI2}}}$ = 8-16 mm, respectively.

Results and Discussion

Figure 4.12 displays the intensity evolution along the cycle as well as the simulated maximum tune shifts after 5 ms for different painting settings, which are colour-coded by the applied vertical offset Δy. All losses occur during the injection process and the first ms in the PSB, no further

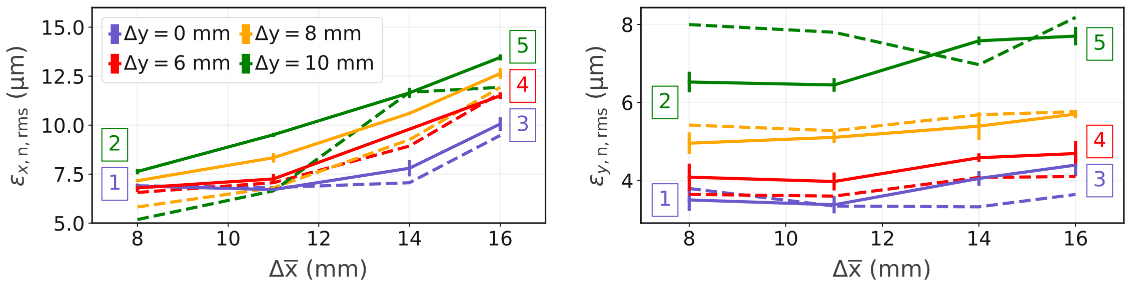

(a) Transverse emittances for different horizontal paintings (x-axis) and vertical offsets (colours). The measured emittances at C770 (solid) are compared to respective simulation results at C280 (dashed).

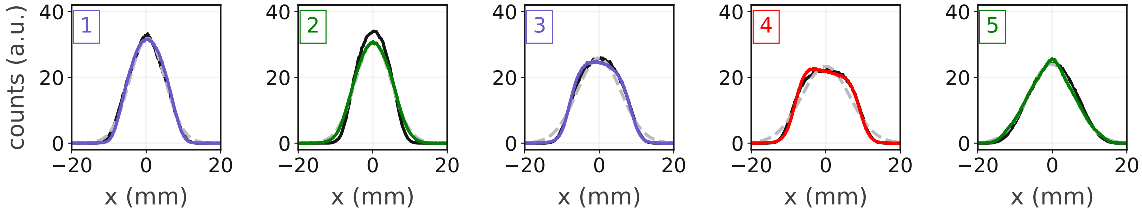

(b) Horizontal profiles (colour: measurement; black: simulations, grey, dashed: Gaussian fit to measured profile).

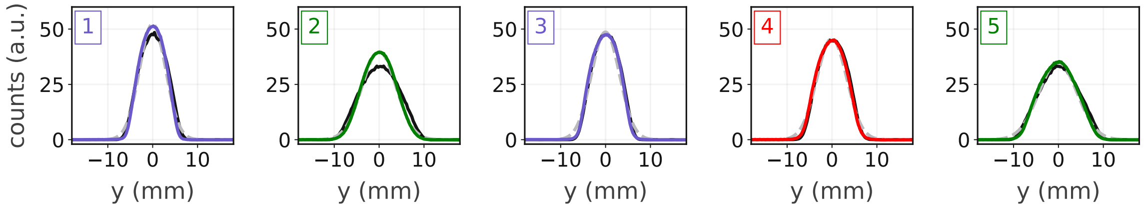

(c) Vertical profiles (colour: measurement; black: simulations, grey, dashed: Gaussian fit to measured profile).

Figure 4.13: Impact of different injection painting settings on transverse emittances and profiles at $Q_x = 4.14, Q_y = 4.22$ ($N_{p+} = 380 \times 10^{10}$ p+ per ring).

losses are observed along the cycle. Figure 4.13a illustrates the measured (solid lines, C770) and simulated (dashed lines, C300) rms emittances for the respective injection settings. The measured rms emittances are within $\epsilon_{y,\mathrm{n,rms}} \approx$ 7-14 µm in the horizontal and $\epsilon_{x,\mathrm{n,rms}} \approx$ 3.5-8 µm in the vertical plane. The transition from space charge to painting dominated emittance increase can be recognised in Fig. 4.13a at $\overline{\Delta x}_{\mathrm{SI2}} \gtrapprox$ 10-12 mm, starting from which the horizontal beam size increases with increasing horizontal offset. Vertically, this transition is observed for $\Delta y \gtrapprox$ 6 mm. The profiles are plotted for selected examples, i.e. the marked paintings 1-5, to compare the measured (coloured; Gaussian fit in grey, dashed lines) with the scaled, simulated (black) profile. Overall, for most paintings, a good agreement is found between simulated and measured beam profiles and emittances. The following agreements and disagreements are highlighted:

Painting 1: Δy = 0 mm and $\overline{\Delta x}_{\mathrm{SI2}}$ = 8 mm, as in *case B*. The simulated and measured beam profiles are in agreement. Both feature an increased beam core size and underpopulated tails, as expected for space charge-driven emittance growth due to the interaction of the beam core with the integer resonances.

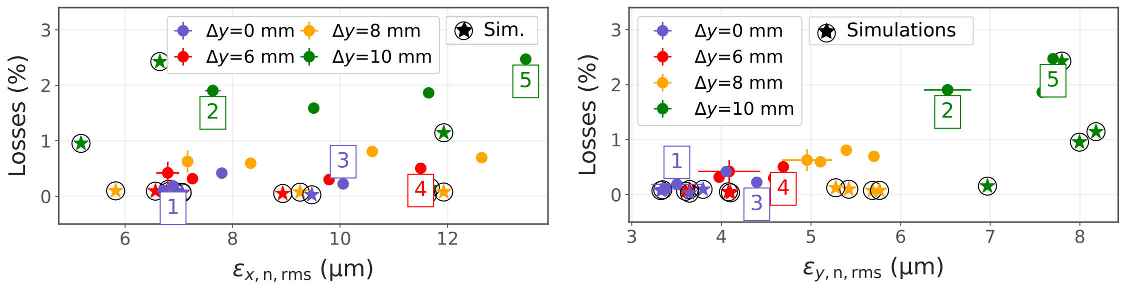

Figure 4.14: Correlation between transverse beam sizes and loss rates at $Q_x = 4.14, Q_y = 4.22$ ($N_{\mathrm{p+}} = 380 \times 10^{10}$ p+ per ring), in simulations (circles) and measurements (stars). The scatter markers are colour-coded by the vertical offset.

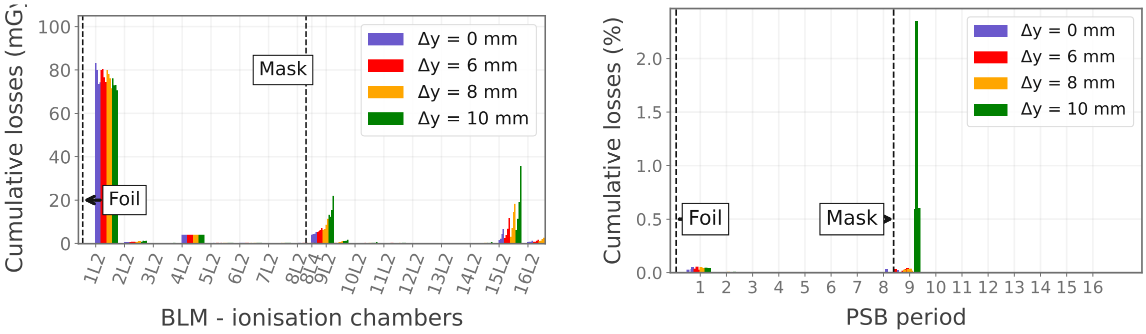

(a) Measured loss map.

(b) Simulated loss map.

Figure 4.15: Loss maps for different paintings at $Q_x = 4.14, Q_y = 4.22$ ($N_{\mathrm{p+}} = 380 \times 10^{10}$ p+ per ring). The losses for the 16 probed painting are recorded at each beam loss monitor (measurements) and in each PSB period (simulations). The results are displayed using the bar plot, where each bar corresponds to one painting setting, colour-coded by the vertical offset.

Painting 2: Δy = 10 mm and $\overline{\Delta x}_{\mathrm{SI2}}$ = 8 mm. This case causes painting-driven emittance growth in the vertical and space charge-driven growth in the horizontal plane. For such paintings, the disagreement between simulated and measured profiles and emittances is largest, i.e. $\Delta\epsilon_{u,\mathrm{n,rms}} \approx 2$ µm. The horizontal beam size is underestimated in simulations, whereas the vertical beam size is overestimated.

Painting 3: Δy = 0 mm and $\overline{\Delta x}_{\mathrm{SI2}}$ = 16 mm, as in *case C*. Applying large paintings in the horizontal plane but $\Delta y = 0$ causes an overlap of the tune spread with the Montague resonance and hence emittance transfer from the horizontal to the vertical plane. This is evident in the vertical beam size, which is $\Delta\epsilon_{y,\mathrm{n,rms}} \approx 1$ µm larger compared to painting (1) in measurements. The horizontal profile exhibits the more uniform characteristic as tailored by the applied painting.

Painting 4: Δy = 6 mm and $\overline{\Delta x}_{\mathrm{SI2}}$ = 16 mm, as in *case A*. Applying also a large vertical offset causes painting-driven emittance growth in both planes. The horizontal emittance is

≈ 2 µm larger compared to painting (3), due to the mitigated emittance transfer from the horizontal to the vertical plane.

Painting 5: $\Delta y = 10\,\mathrm{mm}$ and $\overline{\Delta x}_{\mathrm{SI2}} = 16\,\mathrm{mm}$, as in *case E*. Applying extreme painting offsets in both planes creates a hollow, asymmetric distribution. The beam evolution of the transverse distribution is dominated by the interplay of chromatic and space charge effects during filamentation. The resulting distribution has a triangular shape both in measurements and simulations.

Figure 4.14 displays the correlation of the horizontal (left) and vertical (right) beam size with the measured loss rates L_{C805} for the different paintings. The measurements are colour-coded by the vertical offset Δy. The plots additionally display the simulated losses after 30 ms using the star-markers in the respective colour. The measured losses are within 0-2.5 % and the simulated losses within 0-1 % for all probed paintings. The comparison of the losses to the transverse emittances shows that the losses increase with increasing vertical beam size, both in measurements and simulations, but do not correlate with the horizontal beam size. The majority of the losses are, therefore, attributed to the vertical acceptance limit. Losses significantly increase for $\epsilon_{y,\mathrm{n,rms}} \gtrapprox 6\,\mu\mathrm{m}$, as expected from the aperture studies. For all paintings, the majority of the losses are measured at the loss monitor in P01, rather than at the beam loss monitor downstream of the mask. In simulations, however, the vertical losses are recorded at the mask. Orbit and alignment errors are not included in the simulations, which can explain that the measured bottleneck is observed in P16-P01 instead of at the mask. The losses, which are measured in BLM15 occur during the extraction process and are therefore not expected to occur in simulations.

4.3.5 Measurements for the Operational Working Point ($Q_x = 4.22, Q_y = 4.36$)

The presented painting observations at a WP below the 3rd and 4th-order resonances facilitated an analysis of the *losses due to acceptance limitations and exceeding beam sizes*. These studies are now expanded by measurements at operational intensities and at the operational WP. Here, the focus is put on investigating the impact of the painting on the *losses, which occur along the cycle due to the particles in the tails being trapped on strong resonances*. The general machine configurations and measurement parameters are listed in Table 4.2 and Table 4.5, respectively. For these settings, two painting regimes are probed:

Scan 1: sensitivity to Δy and $\overline{\Delta x}_{\mathrm{SI2}}$ for $k_{\mathrm{SI2}} = 0\,\mathrm{mm/\mu s}$.

Scan 2: sensitivity to k_{SI2} and $\overline{\Delta x}_{\mathrm{SI2}}$ for constant $\Delta y = 0\,\mathrm{mm}$ (vertical on-axis injection).

Impact of Painting on Transverse Beam Distributions

Similar to the studies presented above, Fig. 4.16 compares the measured and simulated emittances for different combinations of Δy and $\overline{\Delta x}_{\mathrm{SI2}}$ (*Scan 1* in Table 4.5). Whereas the general sensitivity of the emittance to painting variations agrees between measurements and simulations, numerical differences up to $\Delta\epsilon_{x,\mathrm{n,rms}} = 2\,\mu\mathrm{m}$ are observed in the horizontal plane. Generally larger emittances are simulated than measured. This difference can be caused by various systematic errors

Table 4.5: Phase space painting studies with operational ISOLDE beams.

	Parameter	Unit	Scan 1	Scan 2
	Ring	-	3	
	Movable mask state	-	inserted	
	Number of injected turns	-	80	
	Injected intensity	p+	805×10^{10}	840×10^{10}
	Estimated (average) injection errors (see Section 3.2)			
	Horizontal	mm	1-1.5	
	Vertical	mm	0.5-1	
	Input to reconst. the resonances identified in [59] (before) after compen. in sim.			
	Octupoles: k_3 ONO4L1	m^{-4}	3.51 (14.04)	
	Octupoles: k_3 ONO12L1	m^{-4}	1.8 (15.85)	
	Skew sextupoles: $k_{2,S}$ XSK2L4	m^{-3}	0.0012 (0.0077)	
	Skew sextupoles: $k_{2,S}$ XSK6L4	m^{-3}	0.002 (-0.0162)	
Painting	H: KSW - A_0	mm	35	
	H: KSW - t_1 (length of slope-1; painting)	µs	10	18
	H: KSW - t_2 (end of beam accumulation)	µs	80	80
	H: KSW - A_1 (amplitude end of slope-1)	mm	30 to 21	30 to 13
	H: KSW - A_2 (amplitude end of beam accum.)	mm	as A_1	A_1 to A_1-11
	V: orthogonal steering - Δy	mm	0-6	0
	H: KSW - gradient of slope-2 k_{Sl2}	mm/µs	0	0 to -0.2
	H: KSW - average offset of slope-2 $\overline{\Delta x}_{\mathrm{Sl2}}$	mm	5-15	5-22
Results	**Emittance measurements during the tune ramp, i.e. at C350 (V) and C400 (H)**			
	Momentum spread dp/p_{rms}	10^{-3}	$\approx 1.27 \pm 0.01$	$\approx 1.27 \pm 0.01$
	H: emittance, Gaussian fit $\epsilon_{x,\mathrm{n,fit}}$	µm	≈ 9-14	≈ 10-21
	V: emittance, Gaussian fit $\epsilon_{y,\mathrm{n,fit}}$	µm	≈ 6	≈ 5.5-8
	H: emittance, rms $\epsilon_{x,\mathrm{n,rms}}$	µm	≈ 7.5-10.5	≈ 8-15
	V: emittance, rms $\epsilon_{y,\mathrm{n,rms}}$	µm	≈ 4.5-5.5	≈ 4-6.5
	Emittance measurements before extraction, i.e. at C770 (H and V)			
	Momentum spread dp/p_{rms}	10^{-3}	$\approx 1.1 \pm 0.06$	$\approx 1.1 \pm 0.06$
	H: emittance, Gaussian fit $\epsilon_{x,\mathrm{n,fit}}$	µm	≈ 9-14	≈ 9-20
	V: emittance, Gaussian fit $\epsilon_{y,\mathrm{n,fit}}$	µm	≈ 6	≈ 5.8-7.4
	H: emittance, rms $\epsilon_{x,\mathrm{n,rms}}$	µm	≈ 7.5-10.5	≈ 7.5-15
	V: emittance, rms $\epsilon_{y,\mathrm{n,rms}}$	µm	≈ 4.5-5.5	≈ 4.8-6.5
	Total loss fraction L_{C805}	%	2.6-7.5	2.5-16

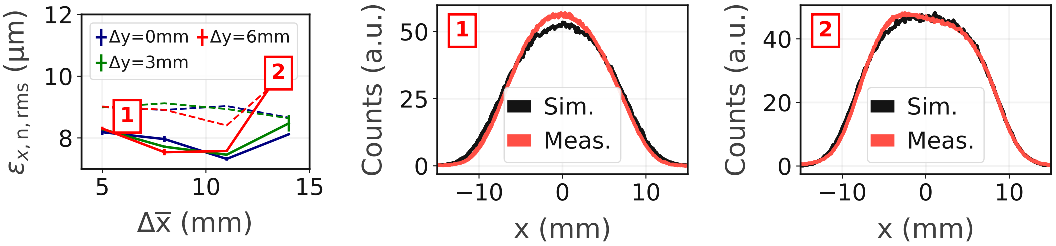

(a) Horizontal beam sizes and profiles.

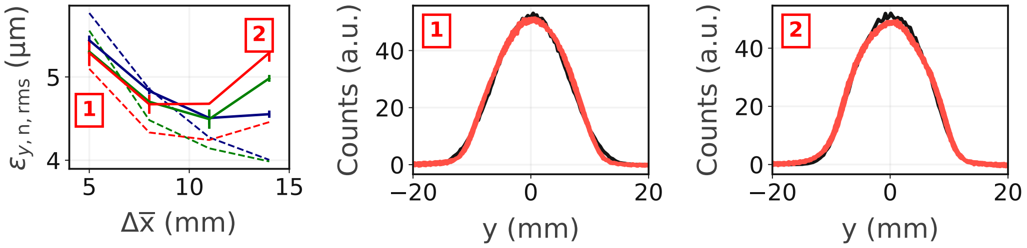

(b) Vertical beam sizes and profiles.

Figure 4.16: Transverse emittances and profiles for different injection painting settings (Scan 1 , Table 4.5) at $Q_x = 4.22, Q_y = 4.36$ ($N_{\mathrm{p}+} = 810 \times 10^{10}$ p+ per ring). Left: simulated (dashed) and measured (solid) transverse emittances. Emittances obtained for different vertical offsets $\Delta y = 0, 3, 6$ mm are plotted in different colours. Centre and right: simulated and measured profiles for two selected settings, which are representative for space charge (1: $\Delta y = 6$ mm, $\overline{\Delta x}_{\mathrm{SI2}} = 5$ mm) and painting-driven emittance growth (2: $\Delta y = 6$ mm, $\overline{\Delta x}_{\mathrm{SI2}} = 21$ mm) in the horizontal plane, respectively.

(mainly errors in the β-function at the wire scanner, scattering at the wire scanner and errors when subtracting the dispersive contribution). Reducing these errors to improve the emittance measurements for the painted ISOLDE beams goes beyond the stage of beam commissioning and is subject to further studies.

For large vertical offsets ($\Delta y = 6$ mm, red curves in Fig. 4.16, left) the transition from space charge to painting-driven emittance growth in the horizontal plane is observed at $\overline{\Delta x}_{\mathrm{SI2}} = 8$-$11$ mm, both in measurements and simulations. The characteristic of the measured profiles for painting (marker 2) and space charge-driven (marker 1) emittance growth is again well reproduced in the simulations.

The sensitivity of the vertical emittance to the horizontal painting due to emittance transfer is evident both in the simulations (dashed) and the measurements (solid). Here, this can account for vertical emittance variations up to $\Delta\epsilon_{y,\mathrm{n,rms}} \approx 1$ µm, despite constant vertical offsets. Especially for small horizontal paintings, the impact of the horizontal painting on $\epsilon_{y,\mathrm{n,rms}}$ is larger than the effect of applying vertical offsets $\Delta y = 0$-6 mm. This is again an indication of the sensitivity to the space charge-driven coupling resonance in these machine configurations.

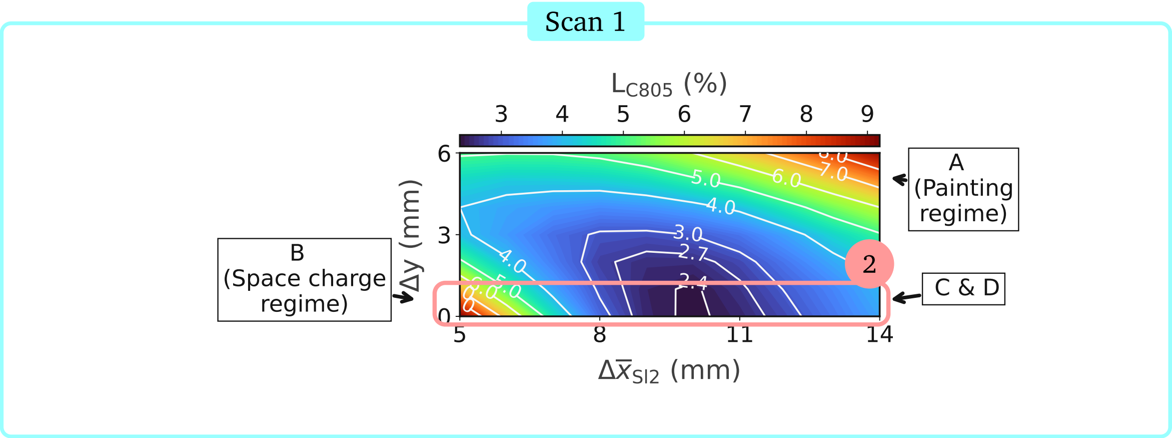

Figure 4.17: Total loss fraction L_{C805} for different horizontal and vertical injection painting settings at $Q_x = 4.22, Q_y = 4.36$, with $N_{\mathrm{p+}} = 810 \times 10^{10}$ p+ per ring.

Impact of Painting on Loss Patterns

The most relevant observable for ISOLDE beam production is the total loss fraction L_{C805}, which is illustrated in Fig. 4.17 for different horizontal and vertical paintings (*Scan 1*). For the probed paintings, the total loss fractions range from ≈ 2.6 to ≈ 9 %. It can be seen, that for small horizontal paintings (*case B:* space charge-driven blow-up of ϵ_x) losses decrease when applying vertical offsets $\Delta y > 0$ mm, which reduces the charge density in the vertical plane. On the other hand, in the case of large horizontal paintings (*case A,C,D,E:* painting dominated blow-up of ϵ_x) losses increase with increasing Δy. In this experiment, a minimal total loss fraction $L_{805,\,\mathrm{min}} \approx 2.6 \pm 0.2$ % is obtained for a vertical on-axis injection ($\Delta y = 0$ mm) and a horizontal painting at the transition from space charge to painting dominated regime ($\Delta\overline{x}_{\mathrm{SI2}} = 11$ mm).

These results demonstrate a significant sensitivity of the losses, which occur during the tune ramp, on the applied vertical offset. This motivates a more detailed look at the vertical tail population for the different painting settings. Figure 4.18 compares the scaled, simulated (C300) and measured (C350) tail population for selected, extreme painting cases. Additionally, the simulated tune footprints, emittance and intensity evolution are shown for reference. The profiles are compared to a Gaussian reference distribution for $\epsilon_{y,\mathrm{n}} = 5\,\mu\mathrm{m}$. The respective residuals are plotted to accentuate the tail population. The following observations are highlighted:

- The paintings, which result in high loss fractions, feature a higher density of particles in the vertical tails, in both the simulations and measurements[†]. These particles experience a smaller tune shift and are hence more likely to be trapped at the observed 3rd and 4th-order resonances.

- It has to be noted that the measured high loss rates, which are observed during the tune ramp for the different paintings could not be reproduced in the current simulation set-up

---

[†] As the wire crosses the beam in Fig. 4.18 from right to left, the right side of the profile (y = 5 to 10 mm) is considered less affected by distortions due to multiple Coulomb scattering.

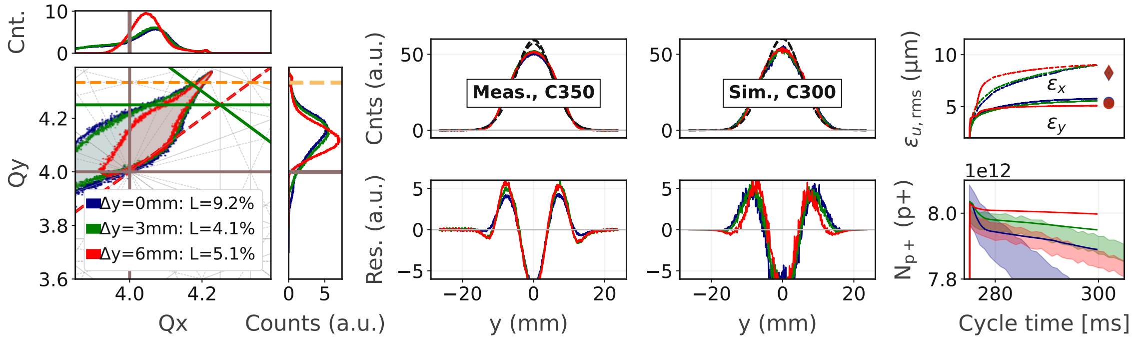

(a) $\overline{\Delta x}_{\mathrm{SI2}} = 5$ mm.

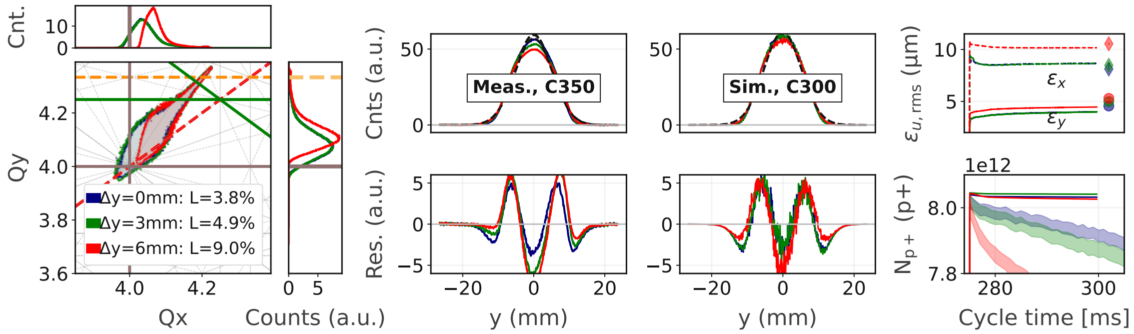

(b) $\overline{\Delta x}_{\mathrm{SI2}} = 14$ mm.

Figure 4.18: Comparative multi-particle simulation results for selected painting settings (*Scan 1*) at $Q_x = 4.22, Q_y = 4.36$ ($N_{\mathrm{p+}} = 810 \times 10^{10}$ p+ per ring). Left: simulated tune footprints at C300. Resonances observed 2021 in the PSB and relevant for this WP are highlighted in green (4th) and dashed, yellow (3rd-order skew resonances). The legend lists the measured total loss fractions L_{C805} for the respective case. Centre: measured (C350) and simulated (C300) vertical profiles and residuals, compared to a Gaussian with $\epsilon_{y,\mathrm{n}} = 5$ μm (black, dashed). Right: simulated rms emittance and intensity evolution up to C300. The emittances measured at C350 (V) and C770 (H) are displayed with scatter markers.

(Fig. 4.18, right). However, attempting to reproduce these losses in simulations by e.g. reviewing the strength of the included multipole errors goes beyond the commissioning period and the scope of this thesis. In this context, it should also be noted that the resonances are characterised experimentally at injection energy, whereas most of the losses occur at higher energies [126].

Scan 2 in Fig. 4.19 follows up on these results by varying $\overline{\Delta x}_{\mathrm{SI2}}$ and k_{SI2} to investigate the paintings with a vertical on-axis injection in more detail (flat paintings, *cases B, C and D*). It is evident, that whereas $\overline{\Delta x}_{\mathrm{SI2}}$ clearly affects the loss rates, the impact of the gradient k_{SI2} is negligible in first order. The KSW waveforms for the different cases are illustrated in Figs. 4.19a and 4.19b and colour-coded by the losses.

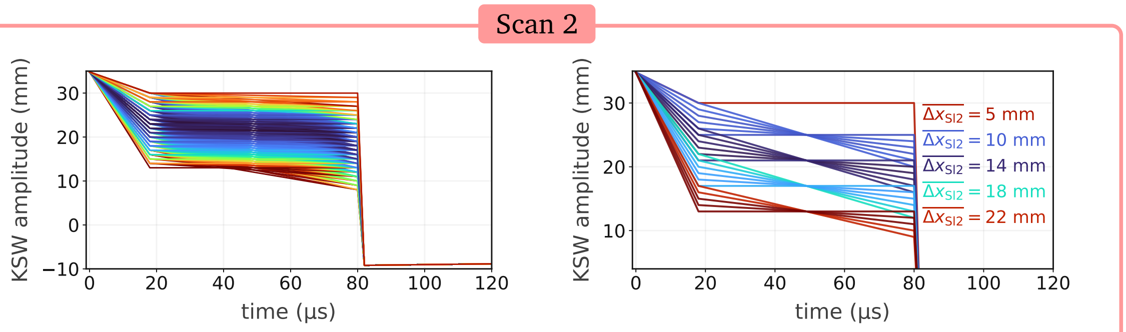

(a) Scanned KSW functions, colour-coded by resulting $L_{\rm C805}$.

(b) Subset of scanned KSW functions for constant $\overline{\Delta x}_{\rm SI2}$ but different slopes.

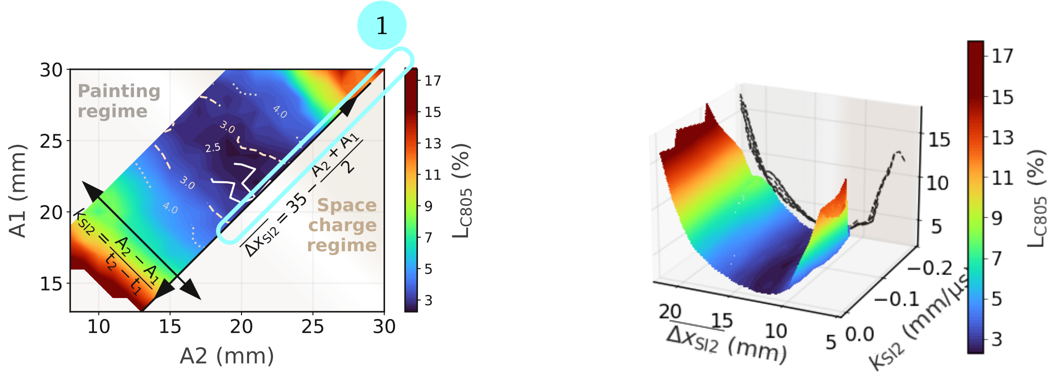

(c) Losses as function of A_1 and A_2.

(d) Rotated view: losses as function of $\overline{\Delta x}_{\rm SI2}$ and $k_{\rm SI2}$.

Figure 4.19: Impact of different horizontal injection painting settings (A_1 and A_2) on the total loss fraction at $Q_x = 4.22, Q_y = 4.36$ ($N_{\rm p+} = 840 \times 10^{10}$ p+ per ring). The respective KSW settings are illustrated at the top.

Correlation Between Loss Patterns and Beam Profiles for Different Paintings

For the operational WP, the cumulative loss distribution in the PSB ring (Fig. 4.20) is as anticipated in simulations (Fig. 4.5a), with the majority of the dose recorded in the BLMs downstream of the mask (i.e. BLM-8L4 and BLM-9L2). In the future, it would be interesting to combine multiple loss and current measurements to optimise not only the total loss rate but also the temporal and spatial loss distribution. This motivates a comparison of the various transverse beam size and loss metrics for different $\overline{\Delta x}_{\rm SI2}$. The presented results are averaged over all $k_{\rm SI2}$ ($\Delta y = 0$ mm, *scan 2*), as illustrated in Fig. 4.19d. The full response surfaces similar to Fig. 4.19d are displayed for all quantities in Appendix B.2.

Firstly, Fig. 4.21 provides a comparison between the total loss fraction, vertical beam size and the vertical tail population. On the one hand, it shows a significant impact of the horizontal painting on the vertical emittance, causing variations up to $\Delta\epsilon_{y,\rm n,fit} \approx 2$ µm. On the other hand, it is evident that the loss fraction one obtains for different paintings correlates with the vertical

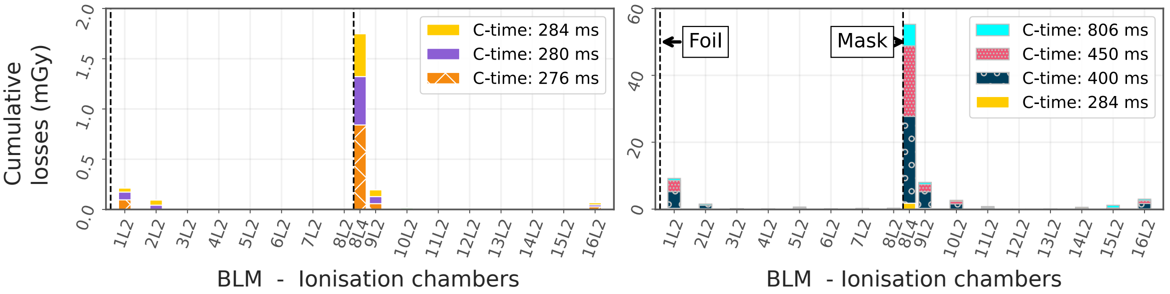

Figure 4.20: Loss patterns measured in the PSB during the production of high-intensity ISOLDE beams: during the first 2-10 ms (left) and along the entire cycle (right). The losses are acquired with the ionisation chamber BLMs in each PSB period.

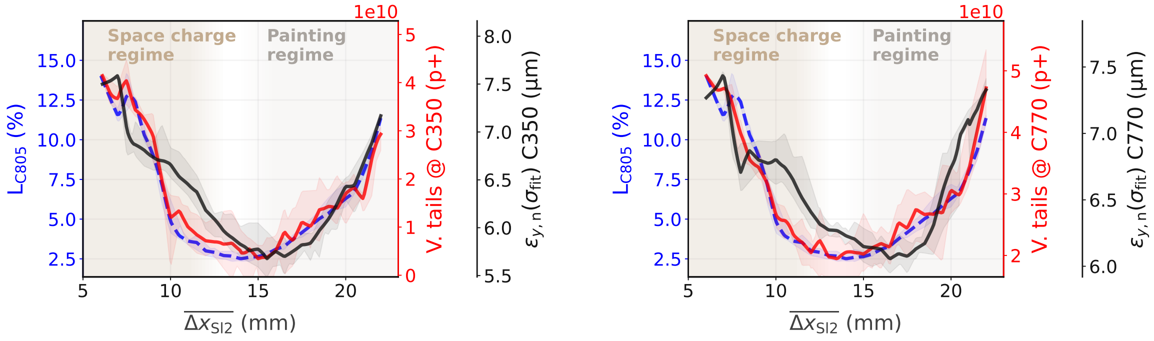

(a) Profiles measured at C350.

(b) Profiles measured at C770.

Figure 4.21: Sensitivity of the total loss fraction (left axis), the integrated vertical tail population (right axis) and the vertical emittance (Gaussian fit; right axis) to horizontal paintings with $\overline{\Delta x}_{\mathrm{SI2}}$.

tail population rather than the emittance. The minimum $\epsilon_{y,\mathrm{n,fit}}$ does not correspond to solutions with minimised losses. This trend is already observed in the measurements performed during the tune ramp (C350), but is even more pronounced in the profiles acquired before extraction (C770, Fig. 4.21b).

Figure 4.22a shows a similar analysis for the horizontal plane. Here, the evolution of the horizontal tail population and emittances are comparable, which is also a result of the large variation in horizontal beam sizes and the generally underpopulated horizontal tails. The balance between mitigating space charge effects and painting an increased beam envelope when increasing the $\overline{\Delta x}_{\mathrm{SI2}}$ is located at $\overline{\Delta x}_{\mathrm{SI2}} \approx 15\,\mathrm{mm}$. Unlike the vertical plane, the horizontal beam size does not correlate with the total loss fraction over the entire range of painting settings. While the losses and the vertical beam size increase significantly in the space charge regime, the horizontal emittance does not increase to the same relative extent. This is consistent with the expectation that the losses occur in the vertical plane.

Figure 4.22b compares the horizontal beam size and the losses recorded during the injection process at a BLM, which is installed in the injection region (BLM.1L2.2). These results show a clear increase in losses when reducing the horizontal offset $\overline{\Delta x}_{\mathrm{SI2}}$ during painting, as expected

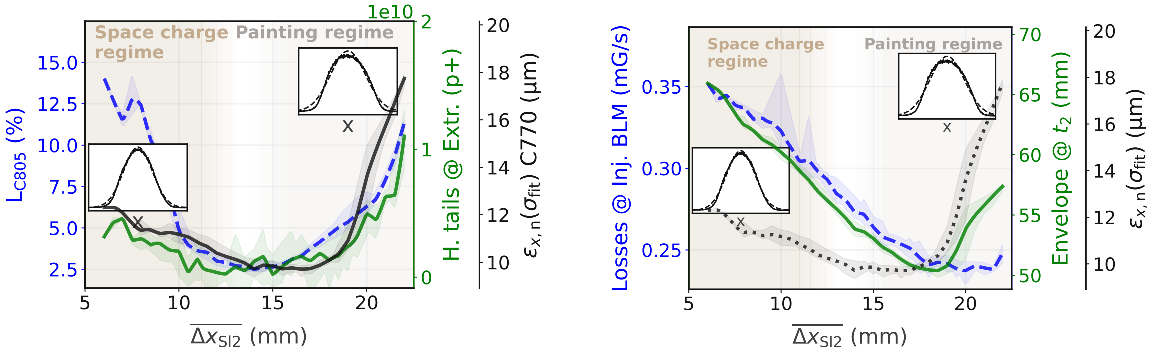

(a) Total loss fraction (left), horiz. emittance and tail population (right).

(b) Losses in the injection region (BLM.1L1.2, left), horiz. emittance and the envelope at the quadrupole in P01 during beam accumulation, approximated by $A_{\mathrm{KSW}} + 2\sigma_{x,\beta}$ (right).

Figure 4.22: Sensitivity of the total loss fraction, losses in the injection region and the horizontal profiles to horizontal paintings at $Q_x = 4.22, Q_y = 4.36$ ($N_{\mathrm{p+}} = 840 \times 10^{10}$ p+ per ring).

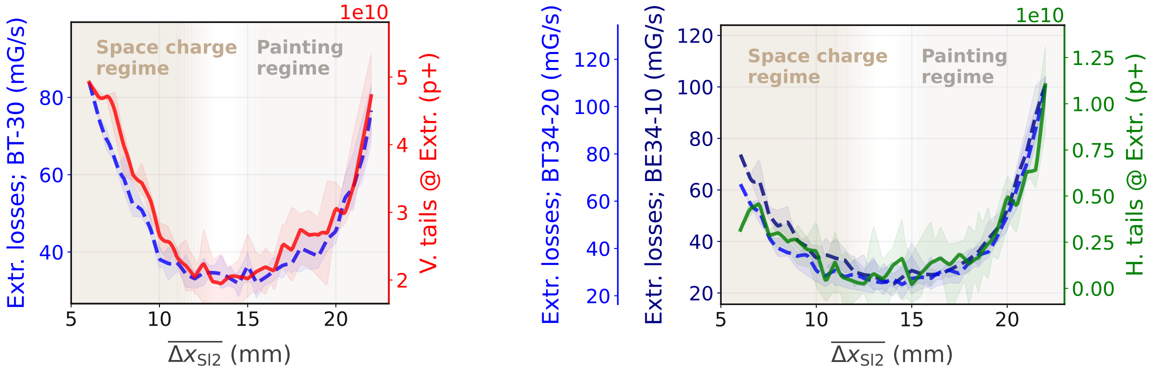

(a) Losses observed in the BLM downstream of the recombination septum (left) and vertical tail population (right).

(b) Losses observed directly after the extraction upstream of the recombination septum (left) and horizontal tail population (right).

Figure 4.23: Sensitivity of losses in the extraction line (left axes) and the transverse tail populations (right axes) to horizontal paintings at $Q_x = 4.22, Q_y = 4.36$ ($N_{\mathrm{p+}} = 840 \times 10^{10}$ p+ per ring).

from simulation results (injection losses in *case B*). The losses increase linearly with decreasing $\overline{\Delta x}_{\mathrm{SI2}}$ due to the large amplitude of the KSW bump and the related reduced horizontal acceptance during beam accumulation.

Finally, Fig. 4.23 compares the dose rates measured in the extraction and recombination line to the transverse tail populations at extraction. It can be seen, that for the employed machine configurations, the minimum loss fraction along the PSB cycle coincides with the minimum losses in the extraction line. The dose rates recorded by the BLM downstream of the recombination septum, i.e. the anticipated vertical bottleneck (BT.BLM-30) correlate with the vertical tail population. The dose rates in the BLMs directly after the extraction, upstream of the recombination septum

(BE.BLM34-10 and BT.BLM34-20) correlate with the horizontal tail population, hinting at the presence of a horizontal acceptance limitation.

4.3.6 Conclusion and Outlook for High-Intensity Beam Production Studies

The new PSB CEI facilitates tailoring of the transverse phase space distribution during injection of high-intensity fixed target beams. The impact of different transverse painting programs for ISOLDE beam production is discussed using multi-particle simulations and validated by first experimental results during beam commissioning.

These results confirm, that in the present operational configuration, most of the losses are obtained as expected along the cycle due to excitation of the transverse tails by betatronic resonances rather than aperture limitations during the injection process. The losses are within the budgets of $< 1\,\%$ during the injection process and $< 5\text{-}10\,\%$ along the cycle. The results demonstrate that the painting settings significantly affect both the losses along the cycle and during the injection process.

It is empirically shown, that it is not beneficial to paint large transverse emittances in both planes (and hence paint a quasi rectangular distribution), as the reduced initial tune spread both horizontally and vertically results in more particles being trapped on the observed 3rd and 4th-order resonances. Minimised losses are obtained when programming a horizontal painting, which balances space charge and painting-driven horizontal emittance growth while injecting vertically on-axis.

Another important result is, that the losses recorded at the aperture bottlenecks during the injection and extraction process can be successfully correlated to the transverse tail population in the respective plane.

The painting functions, which are configured to produce the requested beam characteristic, may need to be adapted when changing the operating conditions such as injected intensity, WP, energy spread or resonance compensation This sensitivity of the optimised injection settings to varying operational conditions makes automatic tuning of injection settings attractive. The results presented in this section serve as a basis for developing an automated optimisation setup in Chapter 6.

4.4 LHC High Brightness Beams

The aim of the LIU upgrade was to double the maximum brightness of the LHC beams. The LHC beams produced in the PSB span different intensities. The main operational beam types are the BCMS beams with 1.7×10^{12} p+ per ring, which request emittances within $\epsilon_{x,y,n} < 1.5\,\mu\text{m}$ and the LHC25 beams with 3.52×10^{12} p+ per ring and emittances within $\epsilon_{x,y,\text{n}} < 2\,\mu\text{m}$.

The machine configurations applied during commissioning in 2021 are listed in Table 4.6 [90]. The WP is set to $Q_x = 4.4$ and $Q_y = 4.43$ (similar to pre-LS2) to maximise the beam brightness. The WP allows staying below the half-integer resonance to be less sensitive to machine imperfections [90, 101]. The energy spread of the Linac4 beam is set to $\Delta E_\text{rms} = 440\,\text{keV}$. The double

Table 4.6: Target characteristics, configurations and injection parameter settings for producing LHC beams during post-LS2 beam commissioning (2021).

Parameter	**Unit**	**Baseline value**
Target		
Target emittances $\epsilon_{x,\mathrm{n}}$ / $\epsilon_{y,\mathrm{n}}$	µm	LHC25: < 2; BCMS: < 1.5
Target intensity	10^{12} p+	LHC25: 3.52; BCMS: 1.7
Linac4 settings		
Number of injected turns	-	LHC25: 35; BCMS: 17
Energy spread of injected beam dE_{rms}	keV	440
Chopped bunch length	µs	0.7
Estimated (avg.) inj. errors (see Section 3.2)		
Horizontal	mm	1-1.5
Vertical	mm	0.5-1
Injection painting settings		
H: constant KSW amplitude: $A_0 = A_1 = A_2$	mm	35 (i.e. on-axis)
H: $t_1 = t_2$ = number of injected turns	µs	LHC25: 35; BCMS: 17
V: orthogonal steering, Δy	mm	0 (i.e. on-axis)
PSB settings		
Harmonic of RF bucket at injection (voltage program as in Fig. B.1b)	-	2
Q_x/Q_y at injection (set)	-	4.4/4.43
β-beating correction	-	no
Q_x/Q_y at injection (measured)	-	4.4/4.46
Q_x/Q_y at extraction	-	4.17/4.23

harmonic bucket at injection is designed to minimise the longitudinal line density and hence the space charge detuning at the beginning of the cycle [135]. When implementing the correction of the vertical β-beating induced by the injection chicane and respectively adapting the WP [101], the produced beams met the LIU brightness targets already in 2021, as shown in [90, 101].

The Linac4 beam is injected into the PSB over up to 35 turns. The baseline injection procedure is to not apply any painting, but to inject the beam on-axis both horizontally and vertically. Several studies indicate that in certain machine configurations, e.g. when injecting with smaller energy spread, applying injection paintings or offsets of $\Delta u \approx$ 1-2 mm can be beneficial for increasing the brightness [136]. However, this is considered a beyond-baseline injection procedure and is to be investigated in more detail in further studies. As most relevant for the commissioning period, this section focuses on characterising the impact of injection errors on brightness degradation and tail population in measurements.

4.4.1 Impact of Steering Errors on Brightness Curve

The general assessment of injection imperfections in Chapter 3 identified steering errors and field ripples as the main potential sources of brightness degradation during the PSB injection process. Optics mismatches and emittance growth due to foil scattering play a less pronounced role and are hence not taken into account in this section.

Previous multi-particle simulation studies analysed the impact of injection offsets mainly for LHC25 beams with $N_{\mathrm{p+}} = 3.52\times10^{12}$ p+ per ring, e.g. [60, Chp. 7.3]. It was shown in simulations that for such intensities, no significant brightness and tail degradation is expected for injection errors of $\Delta y < 2$ mm and $\Delta x < 3$ mm. The studies were performed at a WP of $Q_x = 4.43$ and $Q_y = 4.60$.

However, injection errors mainly affect LHC beams with lower intensities, e.g. BCMS, due to the smaller space charge-driven emittance growth. This section provides a first experimental assessment of the beam degradation due to injection errors, not only for the maximum but for various intensities along the LHC brightness curve. The results are related to the discussion on beam filamentation in Section 3.1, which showed that the same error can result in different core and tail distributions depending on the beam intensity.

Methodology

The impact of steering errors on the LHC brightness curve is experimentally assessed for machine configurations as listed in Table 4.6. Prior to the measurements, the injection oscillations are minimised to $< \pm 0.5$ mm, as described in Appendix B.1.1. The order of magnitude of the remnant injection errors is characterised in Chapter 3 and listed in Table 4.6.

During the measurements, the beam is injected into the PSB with additional, programmed steering errors. The applied errors are Δx = 0-4 mm and Δy = 0-3 mm, which corresponds to $\Delta a = 0, 0.65, 1.3$ and $1.95\,\sigma_u$ in units of beam sigma. The respective emittances are estimated from the measured profiles using a Gaussian fit. The dispersive contribution to the beam size is removed with the standard Gaussian subtraction (Eq. (1.40)). The tails are quantified using a q-Gaussian fit (see Appendix A.2). It should be noted, that in these measurements, the horizontal q-factor is obtained from the horizontal profile without prior deconvolution of the dispersive contribution. The absolute value of the horizontal q-factor does hence not describe solely the betatronic horizontal tails. However, these tests aim to compare the relative impact of the different steering errors, which is still reflected by the relative change of the q-factor.

Results and Discussion

Figure 4.24a illustrates the measured impact of injection errors on the brightness curve. The LIU brightness target is indicated by the black line for different intensities. When injecting low intensities over a few turns, the theoretically achievable brightness is limited by the injected emittance $\epsilon_{x,\mathrm{n}} \approx \epsilon_{y,\mathrm{n}} \approx 0.3\,\mu$m and foil scattering.

The blue curve represents the measurements of an on-axis injection without additionally applied steering offsets. For low intensities, the average emittance lies $\Delta\epsilon_{(x+y)/2,\mathrm{n}} \approx 0.5\,\mu$m above the

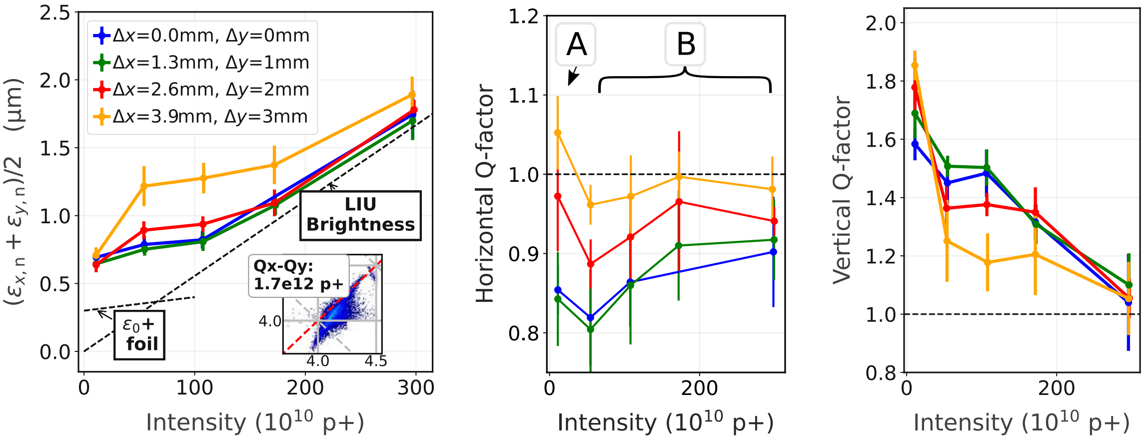

(a) Brightness curve with steering errors. **(b)** Horizontal q-factor. **(c)** Vertical q-factor.

Figure 4.24: Impact of injection errors on the LHC brightness curve. The emittance is obtained using a Gaussian fit of the beam core. The transverse tails are quantified using the q-factor. Note that the horizontal q-factor is computed without deconvoluting the dispersive contribution.

injected emittances. This 'emittance plateau' can be partially caused by the systematic injection errors presented in Tables 3.2 and 3.3, particularly the mismatch during the KSW decay.

The green, yellow and red lines show the brightness curve, measured when applying additional horizontal and vertical steering offsets. Figures 4.24b and 4.24c show the respective q-factors in the horizontal and vertical plane. The following observations are highlighted:

A **Low intensity (injection over a single turn):** Injecting $N_{\mathrm{p+}} \approx 10 \times 10^{10}$ p+ per ring over a single turn yields an average transverse beam size of $(\epsilon_{x,\mathrm{n}} + \epsilon_{y,\mathrm{n}})/2 \approx 0.6$ µm.

Applying additional steering errors does not increase the measured beam core size (Fig. 4.24a) but rather the beam halo. The increase of the transverse tail population is represented by the q-factor, which increases by 20 % in both planes when applying maximum injection errors (yellow in Figs. 4.24b and 4.24c).

B **Injection of higher intensities over multiple turns:** When injecting higher intensities over multiple turns, the applied steering errors cause growth of the beam core rather than the halo, as also discussed in Section 3.1.

No significant emittance increase is obtained for errors of $\Delta x, y \approx 1$ mm (green curve). For medium intensities of $N_{\mathrm{p+}} \lessapprox 1 \times 10^{12}$ p+ per ring, the emittance starts to increase for injection errors larger than $\Delta x, y \approx 2$ mm (red curve). For operational intensities (BCMS and HL-LHC beams, $N_{\mathrm{p+}} > 1.7 \times 10^{12}$ p+ per ring) only extreme errors in the range of $\Delta x > 2.5$ mm and $\Delta y > 2$ mm cause a measurable emittance growth.

For all errors, the q-factor is smaller compared to *case A* in both planes due to the increased blow-up of the beam core. It is interesting to note, that the vertical q-factor decreases for larger steering offsets (due to the larger emittance), whereas the horizontal q-factor increases.

4.4.2 Conclusion and Outlook for High-Brightness LHC Beams

The presented injection studies concerning the production of high-brightness LHC beams focus on assessing the sensitivity of the LHC brightness curve to injection imprecisions. For non-operational, low-intensity beams (i.e. injection over a single turn), injection errors cause an increase in the beam halo rather than the beam core. For medium and large intensity ranges, errors cause an increase in the beam core size, which is represented by an 'emittance plateau' in the brightness curve. Beams with operational intensities are not sensitive to realistic steering errors, as space charge becomes the dominant source for emittance growth. For both BCMS and HL-LHC only extreme errors in the range of $\Delta x > 2.5\,\mathrm{mm}$ and $\Delta y > 2\,\mathrm{mm}$ cause a measurable emittance growth. Note that these steering offsets are applied in addition to the systematic injection errors caused by injection imprecisions, which are discussed and quantified in Chapter 3.

4.5 LHC Single Bunch Beams

LHC and SPS regularly request low intensity ($2\text{-}12 \times 10^{10}$ p+), single bunch beams, which are used for example prior to filling the LHC, for commissioning or machine development studies. The transverse characteristics of these beams are already established in the PSB (Table 4.1).

The *LHCPROBE* or *Pilot* are low intensity and small emittance beams ($< 0.8\,\mu\mathrm{m}$). *LHC Individual Bunch Physics Beams* (LHCINDIV), on the other hand, are beams which have a transverse emittances similar to LHC beams (1-2 µm), but significantly lower intensities, i.e. $2\text{-}12 \times 10^{10}$ p+ per ring. A particular variant of the LHCINDIV beam is the LHCINDIV_VDM beam, which is provided for the *Van der Meer scan* [137] in the LHC. This method calibrates the luminosity in colliders by measuring the collision rate while sweeping the two colliding beams transversely across each other. It requires hence a beam with large emittance, moderate intensity and a specifically Gaussian beam profile [138].

This section reviews proposed beam production procedures using the new CEI and identifies related challenges. The injection schemes are required to

- facilitate flexible and reproducible tailoring of the wide range of transverse emittances despite the low brightness and
- assure Gaussian transverse profiles, particularly for LHCINDIV_VDM beams.

4.5.1 PILOT/PROBE

To produce the small emittance LHCPROBE and Pilot beams a single turn ($\approx 5.5 \times 10^{10}$ p+ per ring) is injected on-axis into the PSB. The intensity is subsequently fine-tuned using longitudinal shaving [135]. The achievable smallest transverse emittance mainly depends on the respective Linac4 parameters. Imprecisions during the injection process, such as residual steering errors, shot-to-shot fluctuations or optics mismatch, can further deteriorate the transverse beam characteristics. While, in this case, mismatches do not increase the size of the beam core ϵ_{fit} significantly, they contribute to intensely populated transverse tails, as discussed in Chapter 3.

Table 4.7: Target characteristics, configurations and injection painting settings for producing LHCINDIV beams during post-LS2 beam commissioning (2021).

Parameter	Unit	Baseline value
Target		
Emittance $\epsilon_{x,\mathrm{n}}$ / $\epsilon_{y,\mathrm{n}}$	µm / µm	1-2 / 1-2
Injected intensity	p+	1.5×10^{11}
Linac4 settings		
Number of injected turns		3
Energy spread of injected beam dE_{rms}	keV	100
Chopped bunch length	µs	0.333
Estimated (average) injection errors (see Section 3.2)		
Horizontal	mm	1.-1.5
Vertical (injection over 1 turn, PILOT)	mm	< 0.5
Vertical (injection over 3 turns, LHCINDIV)	mm	0.5-1
Injection painting settings		
Number of foil passages N_{F}	-	50-150
KSW: decay at $t_1 = t_2$	µs	as N_{F}
V: orthogonal Steering Δy	mm	0-4
H: orthogonal Steering Δx (or $\equiv A_0 = A_1 = A_2 = 35 - \Delta x$)	mm	0-3
PSB settings during beam measurements		
Harmonic of RF bucket at injection (voltage program as in Fig. B.1c)	-	1
Q_x/Q_y at injection (set)	-	4.17/4.23
β-beating correction	-	no
Q_x/Q_y at injection (measured)	-	4.17/4.25
Q_x/Q_y at extraction	-	4.17/4.23
Modelled parameters for analytic approximations		
β_x / β_y at the foil during injection	m	5.7 / 4.0(±10 %)
α_x / α_y at the foil during injection	rad	0 / 0
Thickness of the carbon stripping foil	$\mu\mathrm{g\,cm}^{-2}$	200 (±10 %)
Foil parameters during measurements		
Installed foil type during measurements	-	GSI-200 (slot 6)
Approximate operational age of the foil	months	5

4.5.2 LHCINDIV and LHCINDIV_VDM

Pre-LS2 the production scheme for LHCINDIV and LHCINDIV_VDM beams (hereinafter collectively referred to as INDIV) relied on injecting similar intensities as for nominal LHC beams from Linac2 into the PSB, i.e. 150-180 $\times 10^{10}$ p+ per ring over 1.8-2.5 turns. The beam size was consequently established by space charge-induced emittance growth, as for the nominal LHC beams. Most of the beam was subsequently lost close to injection energy through a slow RF capture. The intensity was fine-tuned with longitudinal shaving, the emittance with transverse shaving (compare [138]).

With the new injection system, the aim is to tailor these beams without injecting and subsequently losing this exceeding intensity. Low intensities $N_{\mathrm{p+}} = 5.5\text{-}16.5 \times 10^{10}$ p+ per ring, i.e. less than 10 % of the intensities from pre-LS2, are injected over 1-3 turns. As pre-LS2, the intensity is then fine-tuned to 2-12 $\times 10^{10}$ p+ per ring through longitudinal shaving. The smaller intensity and increased injection energy lower the incoherent space charge tune footprint. Relying, as pre-LS2, on the integer resonances to produce emittances with ≈ 2 µm would require WPs close to the integer tunes. However, the emittance evolution with the WP is remarkably nonlinear, as shown in simulations in [139]. Small tune fluctuations could cause large variations in the transverse emittances, which would pose a challenge for reproducibility.

Emittance and Profile Tailoring Using Injection Offsets and Foil Scattering

The new CEI system allows to establish the transverse characteristics through manipulating the injection settings instead: the emittances are tailored in a controlled way using a combination of injection mismatches and multiple Coulomb scattering at the stripping foil (see Sections 1.6 and 3.3). The related injection configurations are accordingly the number of foil crossings N_F and the transverse offsets Δu ($u = x, y$) between the injected beam position and the closed orbit at the stripping foil. The analytic approximations Eqs. (3.1) and (3.8), which are based on phase-mixing without space charge effects, are combined to provide an estimate for the anticipated upper limit of the rms emittance growth (not necessarily ϵ_fit of the beam core, see Section 3.1)

$$\epsilon_{u,\mathrm{n}} \approx \epsilon_{u,\mathrm{n},0} + w_\mathrm{scat} \cdot \frac{\gamma_\mathrm{r}\beta_\mathrm{r}}{2} \langle \Theta^2 \rangle_\mathrm{ref} \cdot N_\mathrm{F} \cdot d \cdot \beta_u + w_\mathrm{off} \left(\frac{\gamma_\mathrm{r}\beta_\mathrm{r}}{2} \right) \cdot \frac{\Delta u^2}{\beta_u}. \tag{4.5}$$

$\epsilon_{u,\mathrm{n},0} \approx 0.3$ µm is the emittance of the injected beam and d the foil thickness. $\langle \Theta^2 \rangle_\mathrm{ref}$ is the linearised squared rms scattering angle per unit length, if $\langle \Theta^2 \rangle_\mathrm{ref} \cdot N_\mathrm{F} \cdot d$ is the total squared scattering angle for N_F passages of a foil with thickness d. w_scat and w_off are the weights for combining the two contributions. Here, we assume $w_\mathrm{off}, w_\mathrm{scat} = 1$. Equation (4.5) is further based on the assumption that $\alpha_{u,\mathrm{foil}} \approx 0$, as expected for nominal machine configurations.

The injection offsets drive a blow-up, which is proportional to $\propto 1/\beta_u$. The scattering-induced emittance growth, however, is proportional to $\propto \beta_u$. Figure 4.25 illustrates the expected emittance growth for different combinations of N_F, β_u and Δu. The β-functions for the range of operationally employed WPs are indicated by the grey shaded intervals. These estimates show, that extreme offsets between $\Delta u \approx$ 4-6 mm would be required to increase the injected emittance of $\epsilon_{x,y,\mathrm{rms}} \approx$ 0.3 µm to the requested ≈ 2 µm by merely applying injection paintings or offsets. However, the multi-particle simulations presented in Fig. 4.26a demonstrate, that such offsets can lead to

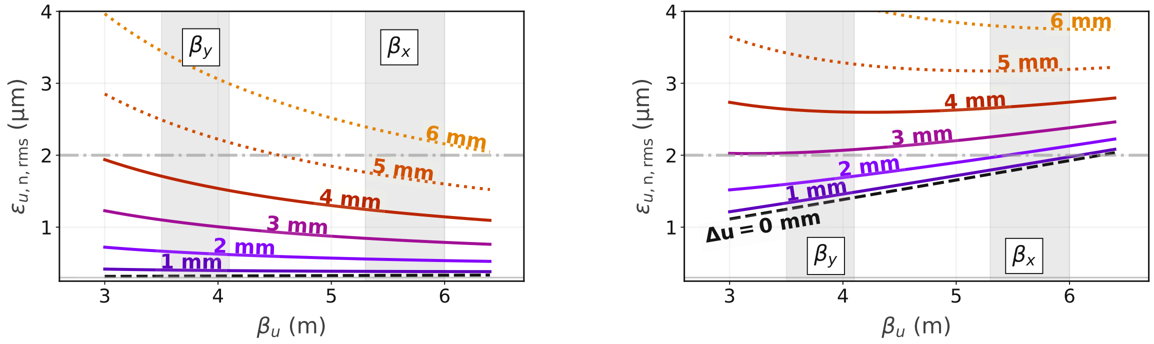

(a) N_F = 5 foil passages.

(b) N_F = 150 foil passages.

Figure 4.25: Analytic approximations for tailoring the transverse characteristic of LHCINDIV beams using a combination of foil scattering and steering offsets; Eq. (4.5).

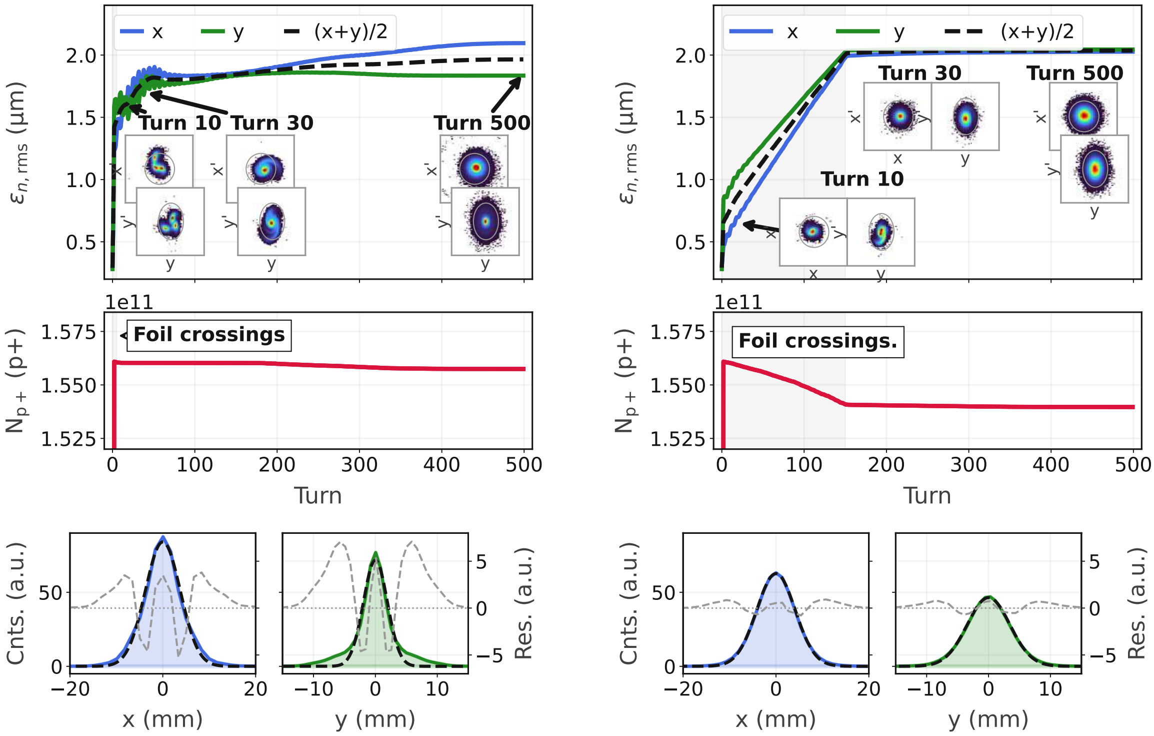

(a) N_F = 5 foil crossings, Δx = 7 mm and Δy = 4.5 mm.

(b) N_F = 150 crossings, Δx = 2.5 mm and Δy = 3 mm.

Figure 4.26: Multi-particle simulations for tailoring LHCINDIV beams during the PSB injection using (a) only injection offsets and (b) a combination of injection offsets and foil crossings. Top: transverse emittance, intensity and phase space evolution during the first 500 turns (0.5 ms); bottom: transverse beam profiles after 0.5 ms compared to the Gaussian fits (black). The residuals are plotted in grey (right axis).

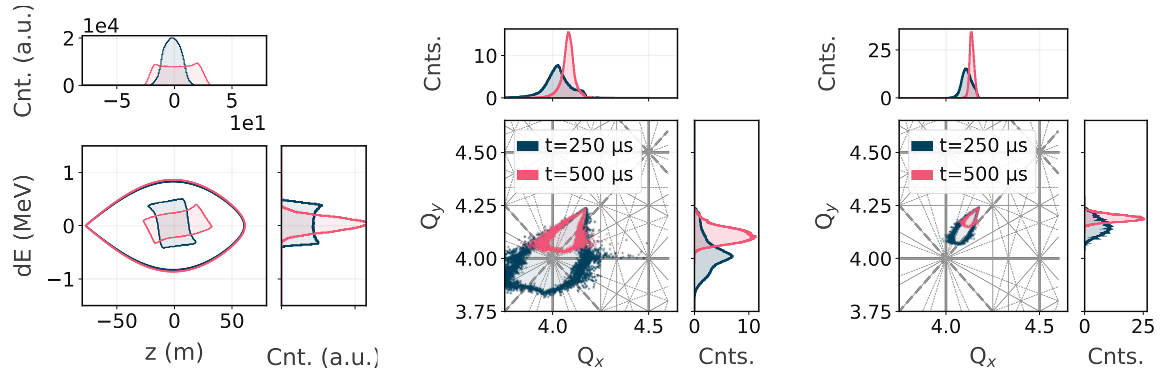

(a) Longitudinal phase space and separatrix during filamentation.

(b) Tune diagram for $N_\mathrm{F} = 5$ foil crossings ($\Delta x = \Delta y = 0$ mm).

(c) Tune diagram for $N_\mathrm{F} = 150$ crossings ($\Delta x = \Delta y = 0$ mm).

Figure 4.27: Longitudinal phase space and tune footprints when injecting LHCINDIV beams with different injection parameters: the time instances during longitudinal filamentation, at which the simulated line density is largest (blue) and smallest (pink) are highlighted.

unacceptable tails after filamentation, while the Gaussian core maintains an insufficient emittance of $\epsilon_{x,y,\mathrm{fit}} \lessapprox 1\,\mu\mathrm{m}$.

To guarantee a Gaussian profile, the majority of the requested emittance blow-up is instead established through multiple Coulomb scattering (Fig. 4.26b). The resulting emittance growth is proportional to N_F and β_u and hence larger in the horizontal than in the vertical plane. Transverse offsets of $\Delta u \approx$ 0-4 mm can be subsequently applied to the injected beam to provide the remaining emittance growth and fine-tune the target emittance in both planes. To state an example, the emittance target of $\approx 2\,\mu\mathrm{m}$ in both planes is achieved in simulations when applying for example $N_\mathrm{F} = 150$ foil crossings, $\Delta x = 2.5$ mm and $\Delta y = 3$ mm.

Passing through the stripping foil multiple times causes beam loss due to large angle single Coulomb scattering, inelastic and elastic nuclear scattering. The respective particles are lost mainly in the vicinity of the injection region. The loss level is in first order proportional to the number of foil hits. For 150 foil passages, loss fractions of $\approx$ 1-1.5% are expected, which corresponds to $\mathcal{O}(10^9)$ p+ per ring (Fig. 4.26b). These loss rates are negligible compared to losses, which occur when injecting high-intensity beams, i.e. $\mathcal{O}(10^{11})$ p+ per ring.

The operational WP for the INDIV production is set to $Q_x = 4.17$, $Q_y = 4.23$ to avoid interaction with the $2Q_x + 2Q_y = 17$ resonance (compare Fig. 1.6). Figure 4.27c demonstrates that one avoids interaction with major resonances for the baseline injection configurations, i.e. $N_\mathrm{F} =$ 100-150 foil crossings. The line density varies significantly during longitudinal filamentation [135]. The consequent maximum and the minimum incoherent tune spread differ by a factor of ≈ 2 and are observed after ≈ 250 and ≈ 500 turns, respectively. $|\Delta Q_{u,\mathrm{max}}|$ during this process depends on the beam brightness, which has been priorly established through foil scattering, as illustrated in Fig. 4.27c for $\approx 1.5 \times 10^{11}$ p+ injected over 3 turns.

4.5.3 Measurements

Motivation and Methodology

The proposed injection procedure is validated experimentally during beam commissioning, with machine configurations as listed in Table 4.7. This study is performed for injection over only 1 turn ($N_{\mathrm{p+}} = 0.5 \times 10^{11}$ p+, as Pilot) and 3 turns ($N_{\mathrm{p+}} = 1.5 \times 10^{11}$ p+, as LHCINDIV). The measurements focus on applying a vertical rather than a horizontal steering offset. This ensures that the entire beam intercepts the stripping foil in each foil passage, also when applying large offsets. One can consequently equate the assumed foil hits per proton with the number of foil crossings $N_{\mathrm{hits}} \approx N_{\mathrm{F}}$, independent of the applied injection offsets.

The transverse beam profiles are acquired using wire scan measurements at two cycle times (C290, 25 ms after injection and C770, 35 ms before extraction). However, the characteristic of the results does not significantly differ for these two time instances. To simplify the presentation of the results, only the measurements at C770 are listed in this section.

The size of the beam core is quantified using ϵ_{fit}. Different figures of merit have been considered for quantifying the tail population. A q-Gaussian fails to fit light tails with large amplitudes when analysing simulation results for extreme offsets. In these tests, the tails are therefore simply quantified using the ratio of the rms beam size $\sigma_{u,\mathrm{rms}}$ and the beam size obtained when performing a Gaussian fit of the beam core $\sigma_{u,\mathrm{fit}}$. For each configuration, the results are averaged over 3 acquisitions.

Results

$N_{\mathrm{p+}} = 0.5 \times 10^{11}$ p+, injected over 1 turn, (Fig. 4.28): The results demonstrate a general agreement between the measurements (solid) and the simulations (dashed). All steering offsets Δy only increase the vertical tail population but not ϵ_{fit} (see Chapter 3). The ratio $\sigma_{\mathrm{rms}}/\sigma_{\mathrm{fit}}$, which is used to quantify the tails, decreases with the number of foil crossings due to the increasing σ_{fit}. The absolute value of this ratio mainly differs between measurements and simulations for extreme offsets ($\Delta y = 6$ mm; yellow in Fig. 4.28). Such paintings yield light tails with large amplitudes in simulations, which are difficult to detect experimentally.

It should be noted, that when not passing the foil multiple times ($N_{\mathrm{F}} = 5$), the profiles feature tails also when not applying any offset, i.e. $\Delta y = \Delta x = 0$ mm. This is indicated by the ratio $\sigma_{\mathrm{rms}}/\sigma_{\mathrm{fit}} > 1$ in this case. An example profile is shown in blue in Fig. 4.28b. These tails are assumed to be caused by a combination of Linac4 tails and injection mismatches (Fig. 3.6). For $N_{\mathrm{F}} \gtrsim 50$ these tails vanish due to the blown-up beam core (grey in Fig. 4.28b).

$N_{\mathrm{p+}} = 1.5 \times 10^{11}$ p+, injected over 3 turns, (Fig. 4.29): Figure 4.29 depicts a similar agreement between simulations and measurements when injecting 1.5×10^{11} p+ over 3 turns (LHCINDIV). It can be seen, that for all N_{F}, injecting with an offset Δy causes mainly emittance growth but not a halo formation. As discussed in Chapter 3, this is likely to be attributed to the more even distribution of the 3 mismatched bunches in phase space and the consequently reduced coherent oscillation. The results show, that applying offsets in addition to configuring N_{F} allows us to flexibly fine-tune $\epsilon_{y,\mathrm{fit}}$ independent of $\epsilon_{x,\mathrm{fit}}$ over the operational range, without generating

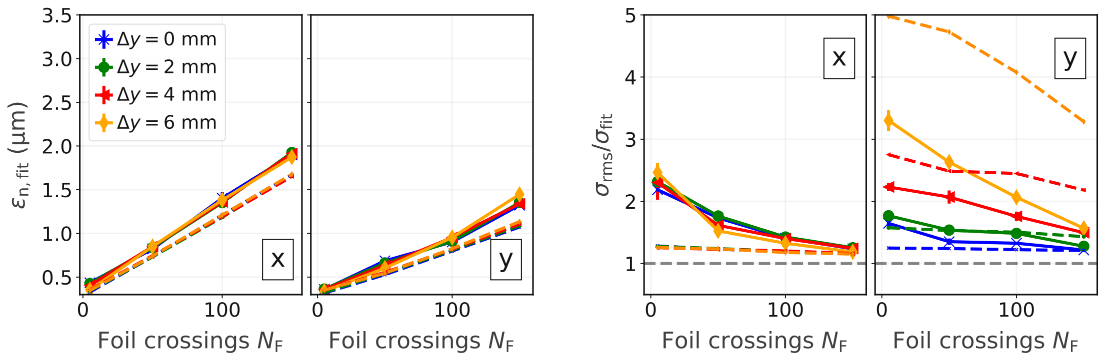

(a) Left: emittance obtained through a Gaussian fit. Right: $\sigma_{\mathrm{rms}}/\sigma_{\mathrm{fit}}$ as a measure for the tails. The profiles are measured before extraction (C770, solid) and simulated up to C290 (dotted).

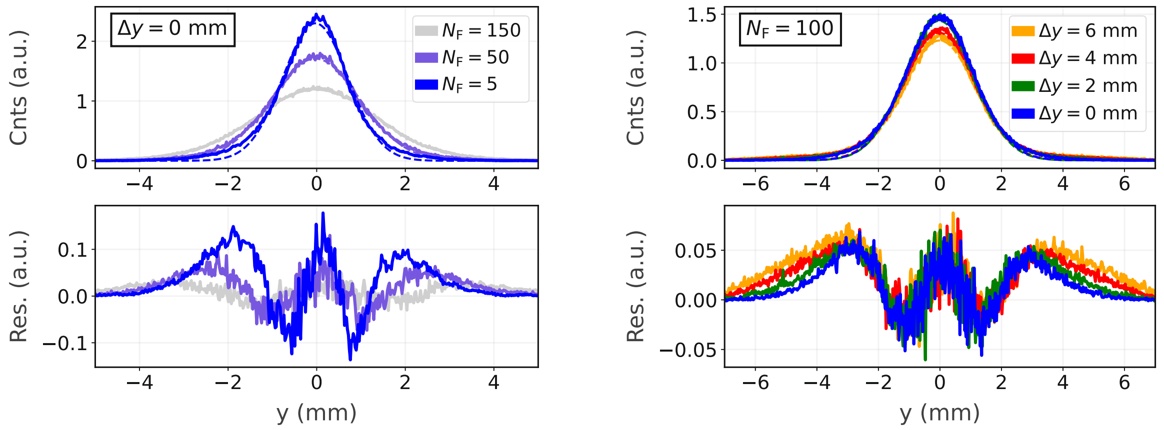

(b) Vertical profile measurements (solid), Gaussian fits (dashed) and residuals (bottom) for $\Delta y = 0$ mm and different N_{F}.

(c) Vertical profile measurements (solid), Gaussian fits (dashed) and residuals (bottom) for $N_{\mathrm{F}} = 100$ foil crossings and different offsets Δy.

Figure 4.28: Transverse LHCINDIV beam characteristics for different PSB injection settings: $N_{\mathrm{p+}} = 0.5 \times 10^{11}$ p+ injected over 1 turn.

major tails. The remaining light tails are not only affected by the injection offsets but also by the interplay of the tune spread, which itself depends on the painting settings Δu and N_{F}, with the integer and the coupling resonances. It is not possible anymore to make the simple statement that applying a larger offset increases the tail population.

It should be noted, that a small number of foil crossings (here $N_{\mathrm{F}} = 5$) and small offsets ($\Delta y = $ 0-2 mm) result in interaction of the beam core with the integer resonances in these measurements (compare Fig. 4.27b). The affected data samples are excluded, as indicated by the grey shaded area in Fig. 4.29.

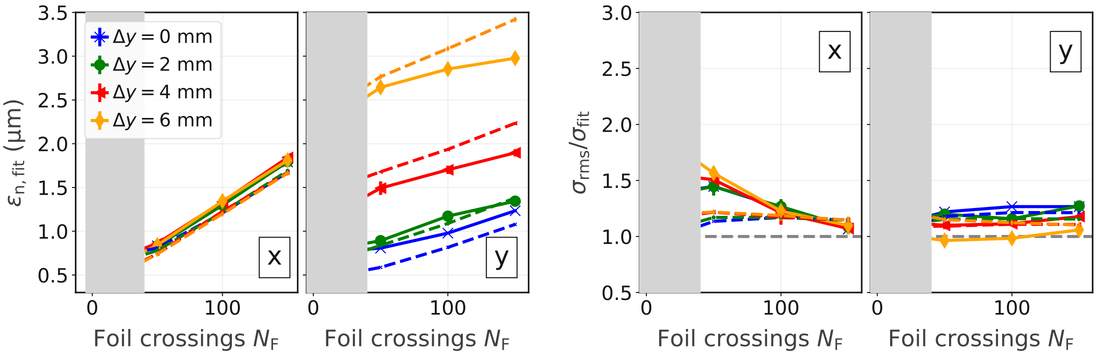

Figure 4.29: Transverse LHCINDIV beam characteristics for different PSB injection settings: $N_{\rm p+} = 1.5 \times 10^{11}$ p+ injected over 3 turns. Left: emittance obtained through a Gaussian fit. Right: $\sigma_{\rm rms}/\sigma_{\rm fit}$ as a measure for the tails. The profiles are measured before extraction (C770, solid) and simulated up to C290 (dotted).

4.5.4 Conclusion and Outlook for LHC Single Bunch Beams

A new procedure to tailor the transverse characteristics of the LHC Single Bunch beams with the new PSB CEI is proposed using multi-particle simulations and verified through measurements. It is demonstrated that beams can be delivered over the entire requested emittance range (0.8-2.5 µm) by controlling the number of foil crossings in combination with transverse injection offsets. The stochastic nature of the foil scattering induced emittance growth yields relatively Gaussian beam profiles in the transverse plane, also for non-Gaussian input distributions.

The delivered Pilot beam emittances of $\epsilon_{u,\rm fit} \approx 0.4$-$0.5$ µm (if not blown-up on purpose with additional foil crossings) are well within specifications of $\epsilon_{u,\rm fit} < 0.8$ µm. Steering errors or shot-to-shot fluctuations will not significantly impact the measured $\epsilon_{\rm fit}$ but only the tail population.

For LHCINDIV and LHCINDIV_VDM beams, simulations and measurements demonstrate that it is possible to flexibly fine-tune the requested transverse emittances, without generating major tails. To state an example, an LHCINDIV beam with $\epsilon_{u,\rm fit} \approx 2$ µm could be operationally tailored using $N_{\rm F} = 150$ foil passages, $\Delta x = 0$ mm and $\Delta y = 4$ mm.

It has to be noted that using this production scheme alone, it is not possible to produce beam profiles with underpopulated tails compared to a Gaussian. In case of such a requirement, e.g. due to additional tail generation along the injector chain, options are to remove tails using transverse shaving or set the WP closer to the integer stop-band.

4.6 Conclusion and Outlook

This chapter presents simulation and measurement results for tailoring the transverse beam distributions as requested by the various CERN users during the PSB injection process.

For high-intensity fixed target beams the objective is to minimise the overall loss rates. Simulation and measurement results show that in the present operational configuration, most of the losses are obtained as expected along the cycle due to excitation of the transverse tails by betatronic resonances rather than aperture limitations during the injection process. The losses are within the budgets of $< 1\,\%$ during the injection process and $< 5\text{-}10\,\%$ along the cycle. The results demonstrate that the painting settings significantly affect both the losses along the cycle and during the injection process. It is empirically shown, that it is not beneficial to paint large transverse emittances in both planes (and hence paint a quasi rectangular distribution), as the reduced initial tune spread both horizontally and vertically results in more particles being trapped on the observed 3$^{\text{rd}}$ and 4$^{\text{th}}$-order resonances. Minimised losses are obtained when programming a horizontal painting to balance space charge and painting-driven horizontal emittance growth, while injecting vertically on-axis.

For high-brightness LHC beams, an analysis of the sensitivity of the brightness curves to injection errors is provided to identify acceptable error margins for different intensities. For both BCMS and HL-LHC only extreme errors in the range of $\Delta x > 2.5\,\text{mm}$ and $\Delta y > 2\,\text{mm}$ cause a measurable emittance growth.

LHCINDIV beams are produced using a new injection scheme. The requested transverse beam sizes and Gaussian profiles are tailored using controlled foil-induced emittance growth in combination with steering offsets. It is demonstrated in both simulations and measurements that one can flexibly fine-tune the requested transverse emittance range by adjusting the offset and the number of foil crossings, without generating major tails.

For most users, the required painting functions are sensitive to varying operational conditions and may have to be adapted in operation. Investigating solutions towards efficiently, reliably and automatically adapting the injection settings online based on beam instrumentation feedback will be a key aspect for pushing the operational performance of the PSB and is discussed in Part II.

Part II

Machine Learning and Numerical Optimisation Techniques for Improving the Performance of the PSB Injection System

CHAPTER 5

Theoretical Background on Numerical Optimisation and Machine Learning

The availability of large data sets and computing power is causing a paradigm shift towards data-driven approaches for modelling and controlling complex systems. Also in engineering and industrial processes, such as particle accelerator technologies, numerical optimisation and machine learning (ML) techniques are increasingly employed. This chapter gives a brief introduction to the main concepts of supervised learning (Section 5.1) and numerical optimisation (Section 5.2), which are subsequently applied in Chapters 6 and 7 to enhance the performance of the new PSB injection system.

5.1 Supervised Learning Methods

An extensive introduction to ML techniques and its three main subfields (supervised, unsupervised or reinforcement learning) can be found e.g. in [140–143]. The studies presented in the Chapters 6 and 7 are based on *supervised algorithms*, which are statistical methods for creating a data-driven model $\hat{f}(\mathbf{x}) : \mathbb{R}^n \rightarrow \mathbb{R}^m$

$$\hat{\mathbf{y}} = \hat{f}(\mathbf{x}) \tag{5.1}$$

to predict the output $\mathbf{y} \in \mathbb{R}^m$ of a relation

$$\mathbf{y} = f(\mathbf{x}), \tag{5.2}$$

which is difficult or impossible to model using analytic or numerical computations. $\mathbf{x} \in \mathbb{R}^n$ are the input variables, also called *features*. During the learning phase, the model is trained using a set of labelled training data $(\mathbf{x}_{\text{train}}, \mathbf{y}_{\text{train}})$ with known in- and outputs. The parameters of the model are adapted to minimise the error between predicted $\hat{\mathbf{y}}$ and labelled, known outputs $\mathbf{y}_{\text{gt}}$. The latter is also referred to as *ground truth* and is the target one aims to predict with the supervised machine learning algorithm. The error is quantified by the *loss or cost function*

$$\mathcal{L}(\hat{\mathbf{y}}_{\text{train}}, \mathbf{y}_{\text{train,gt}}). \tag{5.3}$$

The model structure can be altered by model-specific parameters, so-called *hyperparameters*. A labelled validation data set $\mathbf{x}_{\text{val}}, \mathbf{y}_{\text{val}}$, which is not used during the training step, is used to assess

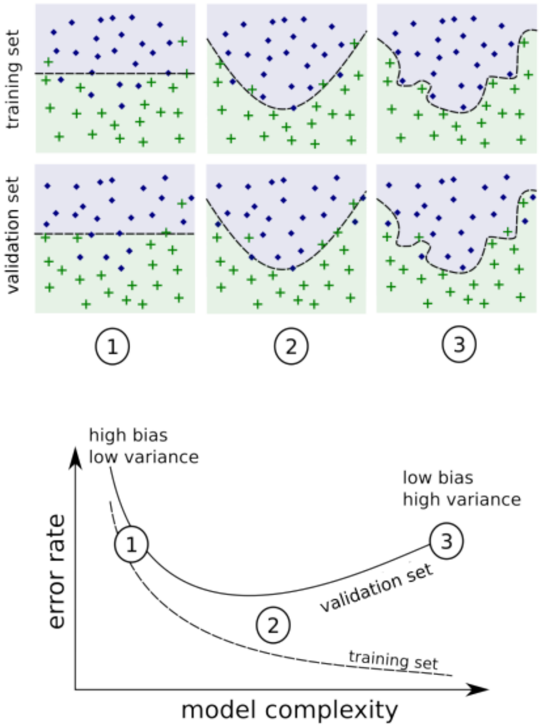

Figure 5.1: Variance-bias tradeoff for different model complexities. The blue and green data points correspond to classes 0 and 1, respectively. The top row shows the training data samples and the estimated decision boundaries for different model complexities. The centre row illustrates how unseen test data samples will be classified based on the trained decision boundaries. The bottom plot displays the training (dashed) and validation (solid) loss as a function of the model complexities.

the performance of the model and to tune hyperparameters. In the end, the performance of the final learned model is quantified using a test set $\mathbf{x}_{\text{test}}, \mathbf{y}_{\text{test}}$, which is independent of the training and validation sets. The final model can be applied to predict the output of unlabeled, new data samples.

There are a variety of widely distributed algorithms for supervised learning, such as *support-vector machines, artificial neural networks* or *random forests*. The methods can be applied in a similar way as classification or regression models. The main difference is that in classifiers y_i is a categorical variable (mostly $y_i \in \{0, 1\}$ or $y_i \in \{-1, 1\}$), whereas regression models predict $y_i \in \mathbb{R}$. This thesis applies artificial neural networks and random forests, which are briefly explained in the following subsections.

5.1.1 Model Complexity, Bias and Variance

Regulating the model complexity is a key task in creating any ML model. It can be tuned using a set of architecture parameters (hyperparameters), which are specific to the respective algorithm.

The model must be sufficiently complex to correctly map the characteristics of the data space (e.g. nonlinear decision boundaries) while being general enough to mitigate overfitting to the training dataset. The related prediction errors are described by the *bias* and *variance*. The *bias*

$$\mathrm{Bias}\left(\hat{f}(\mathbf{x})\right) = \mathbb{E}[\hat{f}(\mathbf{x}) - f(\mathbf{x})] \tag{5.4}$$

describes the systematic difference between the predicted outputs $\hat{f}(\mathbf{X})$ and the ground truths $f(\mathbf{X})$ [140, 141]. It increases with decreasing model complexity (e.g. a linear decision boundary for a nonlinear problem), as the model fails to map the data distribution correctly. The *variance*

$$\mathrm{Var}\left(\hat{f}(\mathbf{x})\right) = \mathbb{E}[\hat{f}(\mathbf{x})^2] - \mathbb{E}[\hat{f}(\mathbf{x})]^2 \tag{5.5}$$

describes the deviation of the test error when training the model with different training sets. It increases with increasing model complexity (e.g. a high-order polynomial decision boundary) due to overfitting. A model aims at keeping the variance small to facilitate generalisation to unseen datasets.

Minimising the overall error by balancing the two error contributions is known as *variance-bias tradeoff* (Fig. 5.1, see e.g. [140, Chp. 5.5.2]). Figure 5.1 (bottom) schematically displays a common evolution of training and validation error for increasing model complexity. It can be seen, why it is essential to assess the model performance using independent datasets, which are not used for training. The error estimated using the validation dataset is the smallest for specific model complexity, beyond which it can increase due to overfitting to the training dataset.

Many machine learning methods use randomly selected subsets of the training dataset during each training iteration and keep the remaining samples to compute the validation error (e.g. mini-batch gradient descent in ANN, out-of-bag error for random forests).

5.1.2 Neural Networks and Deep Learning

One of the most prominent classes of ML algorithms are *artificial neural networks* (ANN) with the subfield of deep learning (see [144] for a broad introduction). The name refers to the fact that these networks are based on the connection of many "neurons", which are inspired by signal processing and learning in human brains. Original proposals for such methods go back to the 1940s, often also known under different names (e.g. *cybernetics* in the 1940s-1960s and *connectionism* in the 1980s-1990s) [144, Chp. 1.2.1]. However, the field stagnated due to lacking computing hardware and access to sufficient training data. This changed in the last two decades, causing deep learning to celebrate a resurgence since the early 2000s with an increased number of real-world applications. Main advances were driven by the fields of speech and image classification, in which ANNs solved problems conventional algorithms had failed at. The increasing dataset sizes facilitated increased model sizes and complexities and consequently improved prediction accuracy. A historical overview of the development and the impact of ANNs is given for example in [144, Chp. 1].

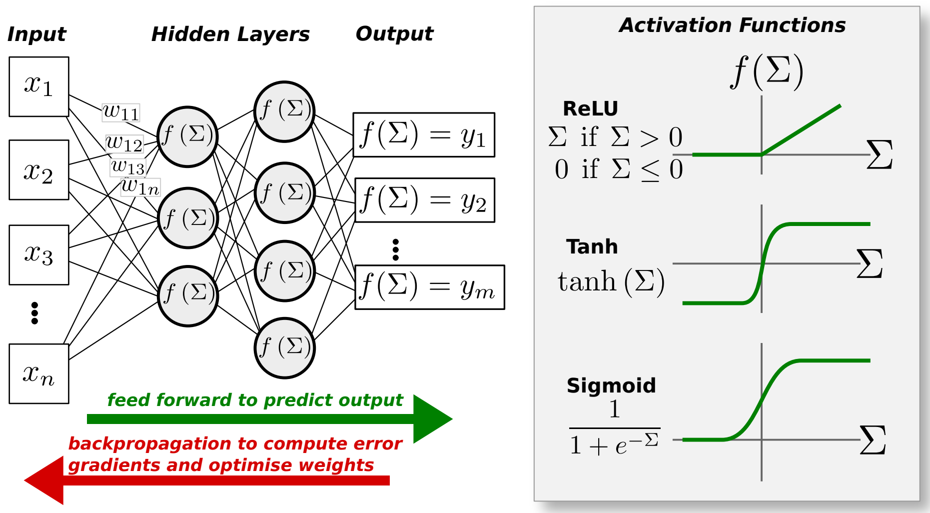

Figure 5.2: Schematic of a multilayer perceptron (MLP) with two hidden layers (left) and examples for common activation functions (right).

Multilayer Perceptrons

The most conventional architectures are deep feedforward networks, also known as *multilayer perceptrons* (MLP) [144, Chp. 6]. An example is illustrated in Fig. 5.2. The input features are fed to a network of connected processing nodes, which are structured in one or multiple hidden layers (here $k = 2$). Each neuron transforms the input it obtains using a custom (mostly nonlinear) activation function. The outputs of the different neurons are linearly combined using customisable weights and fed as input to the neurons of subsequent hidden layers. Multiple such layers can be combined to eventually predict the output values $\hat{\mathbf{y}}$. This process can be written as

$$\hat{\mathbf{y}} = f_k\left(\boldsymbol{w_k}\ldots, f_2\left(\boldsymbol{w_2}, f_1\left(\boldsymbol{w_1}, \mathbf{x}\right)\right)\right). \tag{5.6}$$

The main concepts of any neural network are as follows:

- **Weights:** The matrix $\boldsymbol{w}_j$ contains the weights of the connection between the neurons from the (j-1)-th to the j-th layer.
- **Hidden units and activation function:** The response of a neuron (also called *hidden unit*) to inputs is defined by the *activation function* $f(\cdot)$, which is usually nonlinear. Typical activation functions are rectifier linear unit (ReLU), hyperbolic tangent (tanh) or logistic sigmoid functions, as illustrated in Fig. 5.2 (right). See [144, Chp. 6.3] for details.
- **Cost (loss) function:** The prediction accuracy, i.e. the deviation of the predicted solution from the ground truth, is quantified by a *loss function* $\mathcal{L}(\mathbf{y}_{\text{pred}}, \mathbf{y}_{\text{gt}})$. A standard loss function used for regression problems is the Mean Squared Error [144, Chp. 6.2.1].
- **Gradient-based learning, backpropagation and learning rate:** During the training process, the weights of the ANN are adjusted to minimise the loss function $\mathcal{L}$ and hence optimise

the function approximation. This is done by combining the concept of *backpropagation* [144, Chp. 6.5] with an optimisation algorithm, such as *stochastic gradient descent* [144, Chp. 8]. Backpropagation uses the partial derivatives $\frac{\partial \mathcal{L}}{\partial w_{ij}}$ to assess the impact of the individual weights on the total prediction error. The optimisation algorithm subsequently updates the weights during each training step to minimise the error. The *learning rate* is a hyperparameter, which defines the step size of the optimisation algorithm. Setting a learning rate, which is suitable for the problem, is fundamental for efficient training of an accurate network.

- **Regularisation:** Creating a complex network with multiple layers allows to model complex relations. However, such networks are prone to overfitting. Regularisation techniques are required to minimise the model variance [144, Chp. 7]. One option is to add a regularisation term to the loss function

$$\mathcal{L} = \mathcal{L}_{\text{pred}} + \mathcal{L}_{\text{reg}}, \tag{5.7}$$

which drives the weights closer to the origin. A common choice is the L^2-regularisation [144, Chp. 7.1.1]

$$\mathcal{L}_{\text{reg}} = \lambda \cdot \sum_i w_i^2, \tag{5.8}$$

also known as *weight decay* with the weighting factor λ. A complementary approach is to include so-called *dropout layers* [145] after selected hidden layers. These dropout layers set weights between two neurons to 0 and hence deactivate this connection on a random basis [144, Chp. 7.12].

- **Model architecture:** A key aspect to solving a problem using ANNs is selecting a suitable model architecture, such as the number of neurons, hidden layers and the activation functions of the MLP. [144, Chp. 6.4] summarises the motives behind choosing deep networks with multiple layers, which often outperform shallow networks with wider layers. However, ANN architectures can be creatively expanded and the way to connect the different units can be altered. Modern models often go beyond the "vanilla", fully connected MLP and for example skip or repeat certain connections. Specific network structures are optimised for problems related to time series prediction (e.g. *long short term memory* or *recurrent neural networks*) or image recognition (*convolutional neural networks*).

The universal function theorem [146] states, that any function can be approximated using a vanilla MLP. Evidently, this is a theoretical result. Estimating the required network structure and training the weights is a nontrivial task for many real-world applications and requires a large amount of training data [144, Chp. 6.4.1].

5.1.3 Random Forests as Example for Ensemble Methods

Another prominent supervised learning method is *random forest regression and classification* [147]. A random forest is an ensemble method based on binary decision trees. Decision trees belong to the most trivial classifiers and split the feature space based on a sequence of binary decisions, each carried out considering a subset of descriptors (see Fig. 5.3). At each node, the data is split into two subsets, according to a criterion which is found to separate the samples in the best

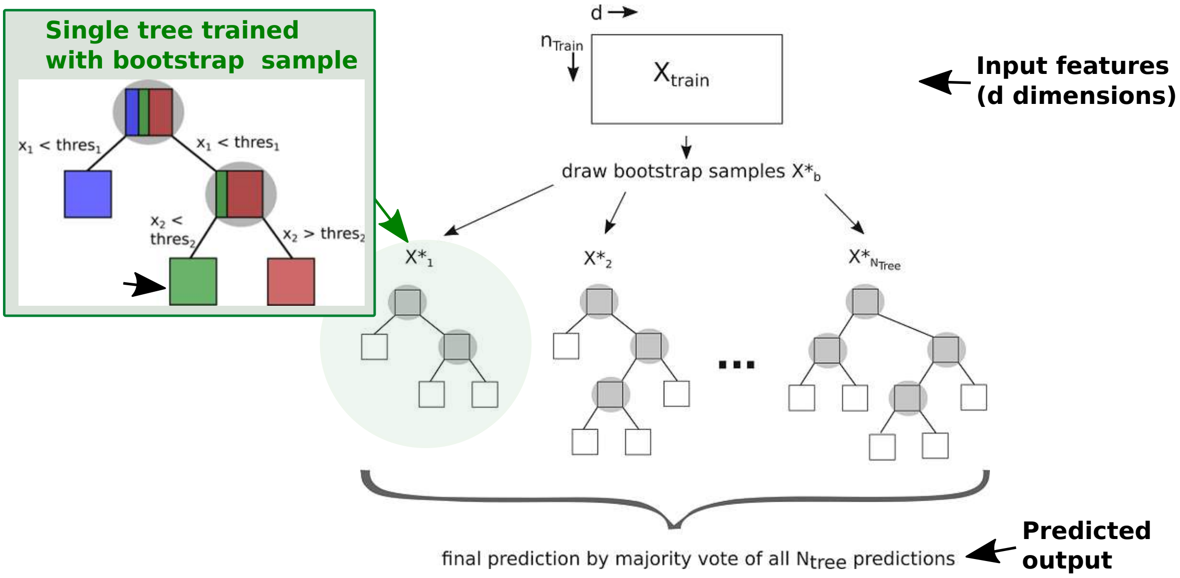

Figure 5.3: Simplified illustration of a random forest classifier or regressor consisting of N_T trees.

possible way. With every decision the tree grows deeper and the purity of the nodes increases. The growing process is finished when a termination criterium is met, such as all the samples in a node belonging to the same class. This terminal node is also called *leaf*. Decision trees are "weak" classifiers. They exhibit low bias (if they are grown sufficiently deep) because with each node the model can be adapted better to the training data. However, they also exhibit high variance as fully grown trees overfit by design. The idea behind ensemble methods is to combine several weak models with low bias but high variance, such as decision trees, into an ensemble to create an improved overall model. Each of the weak models is trained using a different subset which is drawn with replacement from the training dataset (also known as *bootstrap sampling*).

The remaining data samples, which are not used to train this specific tree, are called *out-of-bag samples* $\mathbf{x}_\mathrm{oob}$ and are used as a validation set to estimate the prediction error.

Combining multiple weak models, which are trained with different bootstrap samples, is called *bootstrap aggregation* or *bagging* [148]. The variance of each tree is assumed to be σ^2 and the positive pairwise correlation $\rho\left(\hat{\mathbf{y}}_\text{Tr-A}, \hat{\mathbf{y}}_\text{Tr-B}\right) = \rho$ of tree A and B. The variance of the mean of N_T

trees with variance σ^2 is then[†]

$$\begin{aligned}
\mathrm{Var}\left[\frac{1}{N_\mathrm{T}}\sum_{b=1}^{N_\mathrm{T}}\hat{f}(\mathbf{x}_{\mathrm{oob},b})\right] &= \frac{1}{N_\mathrm{T}^2}\mathrm{Var}\left[\sum_{b=1}^{N_\mathrm{T}}\hat{f}(\mathbf{x}_{\mathrm{oob},b})\right] = \\
&= \frac{1}{N_\mathrm{T}^2}\left(\sum_{b=1}^{N_\mathrm{T}}\mathrm{Var}\left(\hat{f}(\mathbf{x}_{\mathrm{oob},b}),\hat{f}(\mathbf{x}_{\mathrm{oob},b})\right)\right) + \\
&\quad\frac{1}{N_\mathrm{T}^2}\left(\sum_{b1=1}^{N_\mathrm{T}}\sum_{b2\neq b1;b2=1}^{N_\mathrm{T}}\mathrm{Var}\left(\hat{f}(\mathbf{x}_{\mathrm{oob},b1}),\hat{f}(\mathbf{x}_{\mathrm{oob},b2})\right)\right) \\
&= \frac{1}{N_\mathrm{T}^2}\left(N_\mathrm{T}\cdot\sigma^2 + N_\mathrm{T}\cdot(N_\mathrm{T}-1)\rho\sigma^2\right) = \sigma^2\rho + \frac{1-\rho}{N_\mathrm{T}}\sigma^2.
\end{aligned} \tag{5.9}$$

Equation (5.9) demonstrates that the variance decreases with increasing N_T. Furthermore, it has to be emphasised that if ρ is not negligibly small (much smaller than 1), the first term in Eq. (5.9) limits the effect of averaging the predictions of the tree ensemble. It is therefore essential to minimise the positive pairwise correlation ρ of the decision trees. See [140, Chp. 9.2], [149] and [140, Chp. 16] for more details on decision trees and ensemble learning, respectively.

Random forests are such bagged tree ensembles with one additional tweak to reduce the correlation of the individual trees: the splitting conditions on each node are trained using only a randomly selected subset $m < d$ instead of all d features. Thus, different splitting conditions are found for each node, resulting in differing trees and minimised pairwise correlation ρ. The main model hyperparameters are

- the number of trees N_T, which needs to be sufficiently large to decrease the model variance (see [140, Chp. 5.2]),
- the number of variables $m \leq d$, which are randomly selected at each node to train the respective splitting decision (see [140, Chp. 5.3., 5.4.1]),
- the parameters defining the depth and hence the bias of each tree (e.g. the maximum depth of a tree, the minimum number of samples per final node or the required purity per node, see e.g. [149]).

Random forests have evolved to one of the state of the art ML methods, which handle nonlinear data, for both classification and regression and are nowadays applied in various fields. Significant advantages are the robustness concerning the hyperparameter settings, high-dimensional dataspaces and insensitivity to data-scaling and missing data points. Random forests can therefore be applied in a wide range of applications without extensive hyperparameter tuning or data preprocessing. However, as the separation of the parameter space is based on comparing the

---

[†]

$$\rho\left(\hat{\mathbf{y}}_{\text{Tr-A}},\hat{\mathbf{y}}_{\text{Tr-B}}\right) = \frac{\mathrm{cov}\left(\hat{\mathbf{y}}_{\text{Tr-A}},\hat{\mathbf{y}}_{\text{Tr-B}}\right)}{\sigma^2_{\text{Tr-A}}\sigma^2_{\text{Tr-B}}}$$

If $\sigma^2_{\text{Tr-A}} = \sigma^2_{\text{Tr-B}} = \sigma^2$ and $\rho\left(\hat{\mathbf{y}}_{\text{Tr-A}},\hat{\mathbf{y}}_{\text{Tr-B}}\right) = \rho$, it follows that $\mathrm{cov}\left(\hat{\mathbf{y}}_{\text{Tr-A}},\hat{\mathbf{y}}_{\text{Tr-B}}\right) = \rho\sigma^2$.

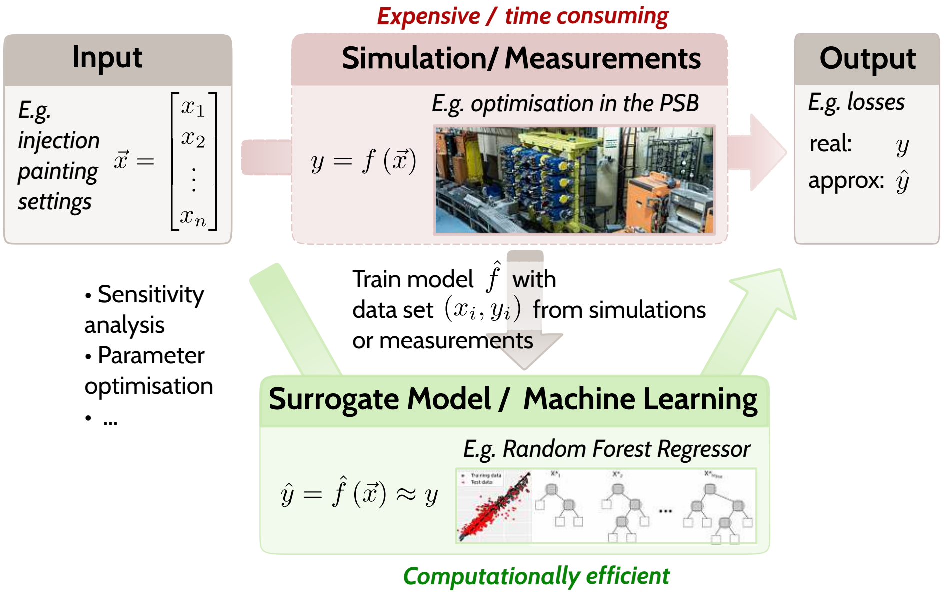

Figure 5.4: Surrogate models as substitutes for expensive measurement or simulation results.

feature values, random forests used for regression, i.e. random forest Regressors (RFR) cannot extrapolate beyond unseen training data. Furthermore, the performance decreases for imbalanced or skewed datasets.

5.1.4 Surrogate Models Based on Supervised Learning Methods

A complex system, such as the loss response to the transverse injection painting, is often expensive and time-consuming to evaluate. A surrogate model $\hat{f}$ (also called emulator, approximation model or response surface model, see Fig. 5.4) approximates the input/output behaviour of the complex system $y = f(\mathbf{x})$ by $\hat{y} = \hat{f}(\mathbf{x}) \approx y$. It is faster and cheaper to evaluate than the original system and is therefore used as a substitute in time-consuming studies, e.g. sensitivity studies, parameter optimisation or algorithm performance assessment. Supervised machine learning algorithms, such as RFR or ANN, are commonly used for developing such surrogate models.

5.2 Numerical Online Optimisation of Particle Accelerators

The other method applied to optimise the performance of the new injection system is *numerical optimisation*. An optimisation problem $\mathcal{P}$ can be generally formulated as

$$\mathcal{P}: \quad \min_{\mathbf{x}} \quad f_0(\mathbf{x}) : \mathbb{R}^n \to \mathbb{R}^m \tag{5.10)a}$$

$$\text{subject to} \quad c_i(\mathbf{x}) \leq 0. \tag{5.10)b}$$

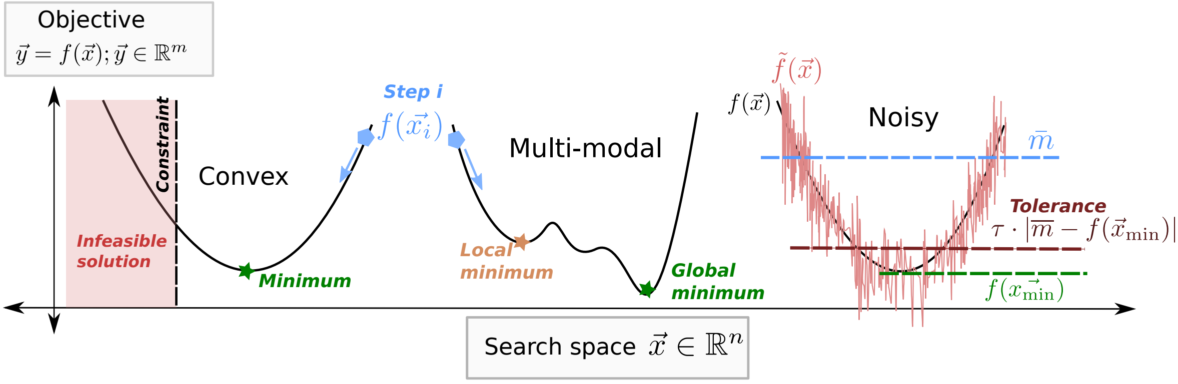

Figure 5.5: Schematic of numerical optimisation problems, with convex (left), nonconvex (centre) and noisy (right) objective functions. Constraints can restrict the search space to feasible solutions.

The aim is to efficiently estimate the n-dimensional parameter set $\mathbf{x} \in \mathbb{R}^n$ (*feature vector*), which minimises the *objective function(s)* $f_0(\mathbf{x}) \in \mathbb{R}^m$, while respecting any *constraints* c_i on the allowed parameter range (Fig. 5.5). Such problems exist in many variations and differ e.g. in dimensionality or characteristic of the objective function. An extensive introduction can be found in [150]. There is no single optimisation method that performs best on all kinds of problems ("*there is no free lunch*" theorem [151]). To select a suitable method for solving a specific task $\mathcal{P}$, it is necessary to first comprehend the problem characteristic. Common criteria to classify the type of an optimisation problem are as follows:

- **Black-box versus model-based:** Most complex industrial and laboratory settings aim at optimising a problem in which the underlying function cannot be accessed directly. There is no analytical model of the objective and/or the constraints available, only the observed output. Such tasks are known as *black-box* (BB) problems. The lack of a model makes the application of derivatives during the optimisation process challenging. Derivatives would need to first be computed using multiple function evaluation, which is often not feasible in real-life applications as they aim at solving a problem as efficiently as possible. Solving BB problems therefore mostly relies on derivative-free optimisation methods. Optimising injection painting functions without an analytic formula, using loss measurements as a response, is such a BB problem.

- **Dimensionality of the feature space, single-objective and multi-objective optimisation:** The dimensionality of the problem is given by the number of input and output features. A single-objective problem aims at optimising a single output variable $y \in \mathbb{R}$. Multi-objective optimisation targets the simultaneous optimisation of multiple output variables $\mathbf{y} \in \mathbb{R}^m$.

- **Continuous versus discrete:** This distinction refers to the characteristic of the search space, i.e. if the variables which are to be optimised are discrete or continuous.

- **Convex versus nonconvex (multi-modal):** The response of the objective to the feature combinations, i.e. the *response surface* is convex if the objectives and constraints are convex functions of the features. A convex problem has a single minimum, whereas nonconvex functions feature multiple local minima (see Fig. 5.5, centre).

- **Unconstrained versus constrained:** Industrial and real-life optimisation problems are often constrained, which means that system properties such as hardware limitations restrict the search space of the feature variables (see Fig. 5.5, left). *Feature bounds*

$$c_i(\mathbf{x}) : a \leq x_i \leq b \tag{5.11}$$

are constraints, which only depend on a single decision variable. Such bounds are often supported internally by algorithms such as most methods of the scipy-optimization package [152]. *Constraints* on the other hand are limitations on combinations of the decision variables. These are generally included in optimisation environments by the penalty method. In case the optimiser proposes a solution $\mathbf{x}_{\text{req.}}$, which violates any of the constraints, it is corrected to $\mathbf{x}_{\text{req.}} \rightarrow \mathbf{x}_{\text{set}}$ to comply with the accepted feature domain. The objective function is then evaluated for the corrected feature vector, but expanded by a penalty term $g(\mathbf{x}_{\text{req.}}, \mathbf{x}_{\text{set}})$ to include information about the constraint violation

$$f(\mathbf{x}_{\text{req.}}) = f_0(\mathbf{x}_{\text{set}}) + \xi \cdot g(\mathbf{x}_{\text{req.}}, \mathbf{x}_{\text{set}}) \tag{5.12}$$

with a tunable penalty factor ξ.

- **Cost of sample evaluation:** An important property of an optimisation problem and criterium for selecting suitable algorithms is the cost of a function evaluation, i.e. the computation or acquisition time.

- **Noisy versus noise-free:** In a noisy optimisation problem the objective function is disturbed by simulation or measurement noise, e.g. for additive and normally distributed noise

$$\widetilde{f_0}(\mathbf{x}) = \mathcal{N}\left(f_0, \sigma_n^2\right). \tag{5.13}$$

$\widetilde{f_0}(\mathbf{x})$ is the noisy and $f_0(\mathbf{x})$ the bare objective function, as illustrated in Fig. 5.5 (right). The noise amplitude σ_n can be quantified using the noise level α, which sets the noise in ratio to the expected range of the explored objective function [153], i.e.

$$\sigma_n = \alpha \cdot |\overline{m} - f(\mathbf{x}_{\min})|, \tag{5.14}$$

where $f(\mathbf{x}_{\min})$ is the (approximate or expected) minimised objective and $\overline{m}$ the expectation value over $n_{\text{expl.}}$ randomly sampled values

$$\overline{m} = \frac{\sum_{j=1}^{n_{\text{expl.}}} \widetilde{f}(\mathbf{x}_j)}{n_{\text{expl.}}}. \tag{5.15}$$

5.2.1 Performance Metrics for Assessing Optimisation Algorithms

Optimisation algorithms aim at solving a problem in as few steps as possible (*sample efficiency*) and/or finding the minimum as accurately and reliably as possible. The performance of different algorithms has to be therefore compared using criteria for efficiency, success rate and reliability, as summarised in [154, Chp. 4], [155].

The *incumbent solution* $\mathbf{x}^*$ is the best solution seen up to a certain step, i.e. the solution which has resulted in the smallest (noisy) objective evaluation $\widetilde{f}(\mathbf{x}^*)$. As the absolute function minimum is normally not known, the solutions are usually classified as *successful* if the found objective falls within a certain range. Similar as for the noise level, this range can be specified based on the tolerance τ, which describes the fraction of the expected objective range $|\overline{m} - f(\mathbf{x}_{\text{min}})|$, i.e.

$$\text{succesful if} \quad f(\mathbf{x}^*) < \tau \cdot |\overline{m} - f(\mathbf{x}_{\text{min}})| \,. \tag{5.16}$$

5.2.2 Derivative-Free Numerical Optimisation Algorithms

The phase space painting optimisation relies on derivative-free (DF) optimisation algorithms due to the expensive and noisy function evaluation. Such methods work without gradient estimation and are dealt with extensively in the literature, e.g. [156–158]†. There are various ways of categorising DF optimisation methods.

Local versus Global Optimisers

One distinction is made between algorithms searching for global optima of a multi-modal function (global optimisers, GO) and local optimisers (LO). For finding a global solution, the optimiser needs to balance *exploitation*, i.e. intensifying the search in regions with known small objective values, and *exploration*, i.e. searching in regions that have not been explored before [161]. If the initial sampling points are chosen appropriately, LO can still find the global minimum to sufficient accuracy and can be more efficient than GO due to the focus on exploitation. To avoid stagnation in a local optimum, hybrid solvers combine the efficient exploitation of a local solver with stochastic, global exploration steps, which are triggered when the local solver stagnates [161].

Model-Based versus Direct-Search Methods

Another way to categorise optimisation methods is the distinction between *model-based* and *direct-search methods* [156, 159, 162]. Broadly speaking, direct-search methods directly compare the evaluated sample points with each other to determine appropriate candidate points for the subsequent iterations. Contrary, model-based methods consider the objective to be locally smooth and approximate it locally by a surrogate model, which can be created through e.g. interpolation or regression. The selection of the next candidate point is based on this model rather than the direct sample acquisitions. One class of model-based algorithms is called *trust-region method* [163], which

---

[†] The terms *derivative-free optimisation*, *derivative-free algorithms* and *BB optimisation* are inconsistently used in literature, as discussed in [159, 160]. Contrary to the here applied terminology, several resources reserve the term *derivative-free optimisation* for deterministic algorithms, for which mathematical convergence to a critical point can be proven and a stopping criterion established [156].

assumes that a model is valid within a certain neighbourhood (*trust-region*) of the current solution. The algorithm searches for a minimum within this neighbourhood to propose a subsequent candidate point. Depending on the obtained objective reduction, this point can be accepted or rejected, and the trust-region radius increased or decreased for the subsequent steps.

5.2.3 Selected Optimisation Algorithms

Several local and global optimisation algorithms will be investigated in Chapter 6 for optimising the injection painting and are briefly introduced below. The algorithms are selected based on operational availability [164] or recommendations from literature for related applications, e.g. [165–168].

Local Optimisers

- **Nelder-Mead (NM),** published initially in 1965 by John Nelder and Roger Mead [169], is a widely popular algorithm and is often referred to as *simplex search*. It is a direct-search method that evaluates the objective on the vertices, i.e. the corner points, of a simplex (the generalisation of a triangle in the 2-dimensional space, i.e. n+1 affinely independent points in the n-dimensional search space). Based on the difference between these acquisitions, the constructed simplex is contracted, expanded or reflected in the next iteration. The original algorithm becomes inefficient for high-dimensional problems. Gao *et. al.* [170] proposed *Adaptive Nelder-Mead* (ANM), an extension in which the algorithm parameters for expansion, contraction, and shrinking are adapted to the dimensionality of the problem.

- **Powell**, also called *conjugate direction method*, is an adaption of *Powell's method* [119, 171], one of the earliest DF optimisers. A bi-directional search minimises the objective along each direction of a set of conjugate search vectors. The obtained minimum along each line is the starting point for the search along a new, conjugate search vector. The directions of the search vectors are updated during the minimisation process.

- **COBYLA** (Constrained Optimisation BY Linear Approximation) is a model-based trust-region method, which uses linear interpolation of the vertices of a simplex for local function approximation [172–174]. Of the listed methods, only COBYLA facilitates the definition of constraints and not only feature bounds.

- **pyBOBYQA** [165, 175] is an adaptation of Powell's Bound Optimisation BY Quadratic Approximation (BOBYQA [176]) algorithm. It is a trust-region method similar to COBYLA. The main difference is that it employs a quadratic instead of a linear function for the local surrogate model. A trust-region step then proposes the following candidate point based on this model.

Global Optimisers

- **pyBOBYQA with multiple restart mechanisms:** The local pyBOBYQA solver can be expanded to a hybrid solver by including a mechanism, which forces multiple restarts in order

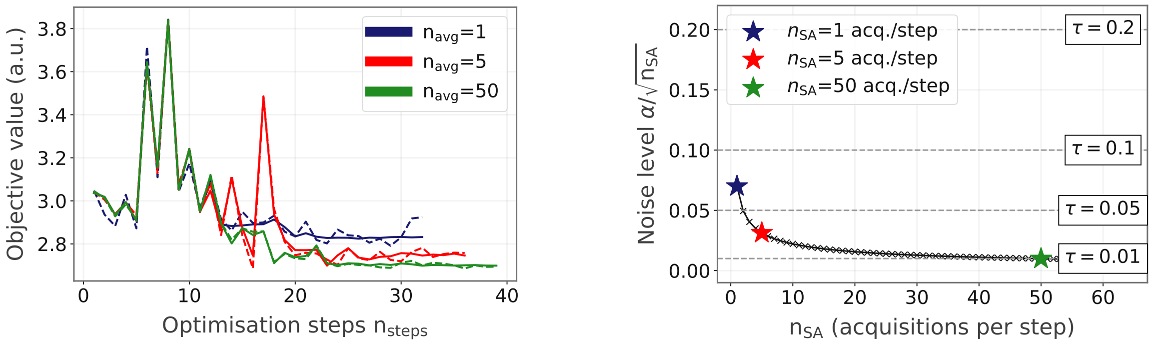

(a) pyBOBYQA without restart for different resampling. Dashed: sample average of noise objective; solid: noise-free objective value.

(b) Decreasing noise level with increasing resampling rate. Reliable convergence to a solution with accuracy τ requires a noise level $\alpha \ll \tau$.

Figure 5.6: Optimisation of noisy objective functions with $\alpha = 0.07$ for different resampling rates $n_{\mathrm{SA}} = 1, 5$ and 50 acquisitions per step.

to escape local minima [175] and stagnation due to noisy observations [165]. In this work, this variant is referred to as pyBOBYQA-noise-global.

- **Surrogate-based optimisation (SBO):** Using all of the already acquired data points, SBO constructs a global, not just a local, surrogate model to resemble the BB function. This surrogate model is then used to select subsequent candidate points, which either aim at improving the model or estimating the minimum. The model is constantly being updated and retrained with the newly acquired samples. SBO is a broad topic, with many different potential methods for creating the surrogate (e.g. radial basis functions, Gaussian processes, random forests), initial sampling strategies and methods for searching for new candidate points. Instructive introductions can be found e.g. in [177, Chp. 10] and [178]. A common SBO is Bayesian Optimisation [179], which usually uses Gaussian processes for the surrogate model.

5.2.4 Noise Reduction Techniques

In the presence of noise, many DF methods are prone to stagnation at incorrect solutions, despite not relying on derivative information, as illustrated in red in Fig. 5.6a. Different strategies for solving such noisy problems have been proposed and studied in the literature.

1. Many methods focus on reducing the noise level by *statistical resampling*, i.e. acquiring the noisy objective function $\widetilde{f}_j(\mathbf{x}_i)$ multiple times with n_{SA} acquisitions per step. In each step, the sample average

$$\overline{\widetilde{f}(\mathbf{x_i})} = \frac{\sum\limits_{j=0}^{n_{\mathrm{SA},i}} \widetilde{f}_j(\mathbf{x}_i)}{n_{\mathrm{SA},i}} \tag{5.17}$$

is used to approximate the noise-free objective $f(\mathbf{x_i})$. Figure 5.6 (yellow and blue) shows how increasing n_{SA} decreases the noise level to $\alpha/\sqrt{n_{\mathrm{SA}}}$ and increases the accuracy of the found solution. In general, to reliably guarantee convergence to a certain tolerance level τ, the effective noise level after statistical resampling needs to be $\alpha/\sqrt{n_{\mathrm{SA}}} \ll \tau$.

2. Other, often complementary, approaches adjust the algorithms themselves to decrease their sensitivity to noise. This is often done for model-based methods. In a noise-free setting, such methods use interpolation to create the local (mostly linear or quadratic) model. In the presence of noise, one can increase the robustness by replacing the local interpolation model with a local regression model [165]. However, creating the regression model requires an increased number of optimisation steps compared to the interpolation model.

3. Yet another approach is to combine the local solver with a restart mechanism, which is triggered when stagnation is detected. This strategy can be compared to the restarts, which hybrid solvers trigger for finding a global minimum. Different studies demonstrate that this can be a cheap option to enhance the robustness and can perform superiorly compared to sampling and regression techniques [165].

Generally, when optimising an expensive, noisy objective function, one has to balance between the number of exploration/exploitation steps n_{steps} and the resampling rate n_{SA} [165, 180] to minimise the total number of acquisitions n_{acq}

$$n_{\mathrm{acq}} = \sum_{i=0}^{n_{\mathrm{steps}}} n_{\mathrm{SA},i} \overset{n_{\mathrm{SA}}=\mathrm{const.}}{\longrightarrow} n_{\mathrm{SA}} \cdot n_{\mathrm{steps}}. \tag{5.18}$$

- Large n_{steps} facilitates a wider exploration of the parameter space. The individual acquisitions have a higher noise level.
- Large n_{SA} reduces the noise level of each acquisition. However, depending on the noise level, this can require many acquisitions per optimisation step, hence fewer total optimisation steps are feasible.

Various resources (e.g. [181]) explore different strategies for adapting $n_{\mathrm{SA}}(i)$ at each optimisation step depending on the algorithm progress.

To provide an example, Fig. 5.7 illustrates the convergence behaviour of pyBOBYQA, a trust-region method, in a noisy environment. In Fig. 5.7b, pyBOBYQA is applied in its default configuration as a local solver (without a restart mechanism). A high sampling rate $n_{\mathrm{SA}} = 40$ acquisitions per step is used to reduce the noise level. In Fig. 5.7a on the other hand, the extension pyBOBYQA-noise-global is used, which replaces the local interpolation with a regression model and triggers restart in case of stagnation. In this case, a lower sampling rate ($n_{\mathrm{SA}} = 40$ acquisitions per step) is applied. The optimiser takes more steps in the second scenario, because of the regression model and the multiple restarts. The total number of acquisitions required to find the function minimum, however, is similar due to the different sampling rates.

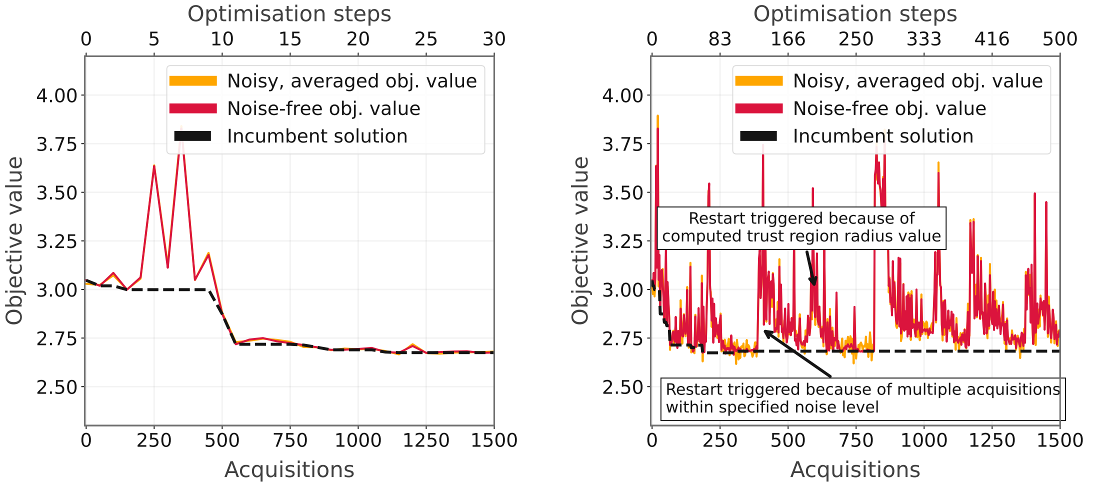

(a) pyBOBYQA without restarts (global=False, noise=False, $n_{\mathrm{SA}} = 40$ acq./step).

(b) pyBOBYQA with restarts (global=True, noise=True, $n_{\mathrm{SA}} = 3$ acq./step).

Figure 5.7: Strategies for optimising noisy problems: (A) shows the progress of a local trust-region solver with high statistical resampling rate $n_{\mathrm{SA}} = 40$ acq./step. In (B), an adaptation to the trust-region method for noisy objectives is used, which employs a local regression model and restart mechanism. The resampling rate $n_{\mathrm{SA}} = 3$ acq./step, however, is lower than in (A). The illustrations compare the noisy objective (orange, averaged over n_{SA} acquisitions per step), the noise-free objective (pink) and the incumbent solution (black). The number of optimisation steps (top axis) is lower in (A). The number of function acquisitions (bottom axis) required to find the function minimum is similar in both cases.

CHAPTER 6

Towards Injection Painting Using Derivative-Free Optimisation Algorithms

Numerical optimisation algorithms are increasingly employed to enhance the operational and commissioning efficiency of particle accelerators. Online optimisation based on beam instrumentation feedback is often a noisy, expensive to evaluate BB problem, which requires the application of efficient DF methods. An example of such an optimisation problem is tailoring the transverse beam distributions during the PSB injection process. A reliable framework to tune the painting functions based on pulse per pulse modulation user requests will become a key aspect for improving operational performance.

This chapter discusses the characteristics of the injection optimisation task to identify suitable optimisation strategies (Section 6.1) and experimentally demonstrate the feasibility of automated injection painting (Section 6.2). The data samples, which are acquired during the first beam tests are used to train a surrogate model using supervised ML algorithms (Section 6.3). This surrogate model facilitates systematic studies for a more in-depth comparison of the algorithm's reliability and efficiency without using physical resources (i.e. beam time on the accelerator). The respective results serve as a guideline for future PSB injection optimisations or similar applications in particle accelerator operation (Section 6.5).

6.1 Problem Characteristic of the Painting Optimisation

The loss rates, which are obtained during high-intensity beam production, are the consequence of a complex interplay of space charge effects, machine errors and beam size limitations. The studies presented in Section 4.3 showed, that the loss rates are significantly affected by the transverse injection painting settings. Here, we aim to develop a framework (Fig. 6.1), which automates the optimisation of the injection configurations. Such a system will help to achieve an efficient beam set-up and minimise losses during operation. Similar to many other optimisation applications in accelerator control, which are based on beam instrumentation feedback, this is a *multi-dimensional, constrained, single-objective, continuous, noisy, expensive to evaluate, nonconvex, DF, BB optimisation problem*:

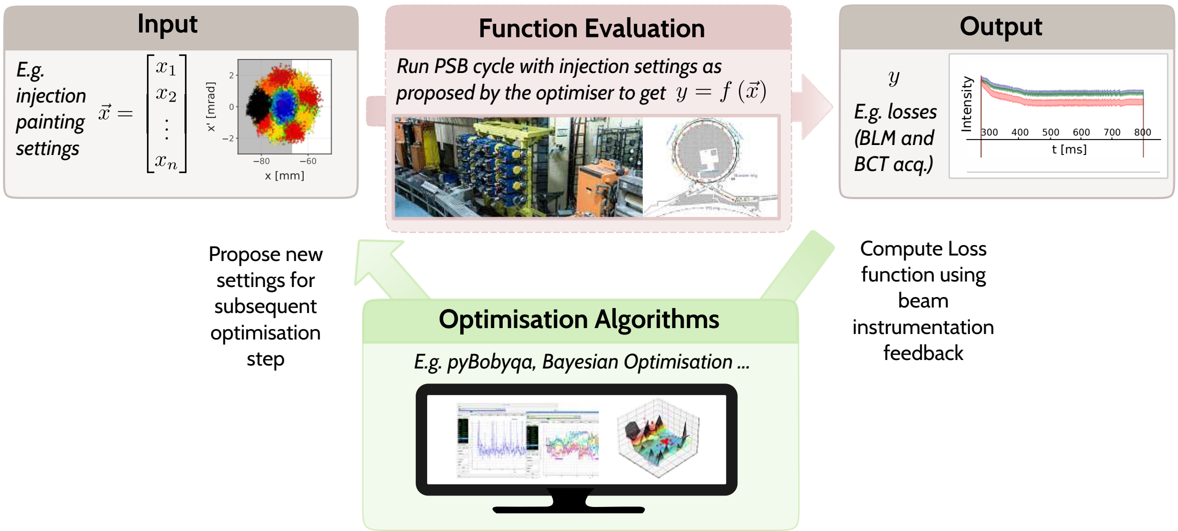

Figure 6.1: Application of numerical optimisation algorithms for tuning the PSB injection painting settings.

Input Features

The variables to be optimised are the injection settings, which control the phase space painting in the horizontal and vertical plane (see Fig. 2.7 and Section 2.3.2). The studies presented in this thesis aim at simultaneous optimisation of all 5 available painting parameters. Depending on the target distribution, it can be of advantage to reduce the dimensionality of the feature space and conduct the optimisation on a (transformed) subset $\hat{\mathbf{x}} = h(\mathbf{x}) \in \mathcal{R}^d$ with $d < 5$. For high intensity ISOLDE beams, this can mean for example optimising A_1, while keeping t_1, Δy, k_{SI2} and A_0 constant (based on the insights obtained in Section 4.3.5). However, this chapter aims at providing a general guideline for tuning the painting schemes in case of novel user requests. The search space is therefore not priorly restricted.

Objective Function

The objective function is continuous and is computed using beam instrumentation feedback, e.g. BCT and BLM readings. The loss function is here defined by the total loss fraction $f_0(\mathbf{x}) = L_{\mathrm{C805}}$ (see Eq. (4.4)). Depending on the requirements, future implementations may expand this loss function to facilitate solving multiple objectives, such as various intensity, loss and profile measurements, at once.

It should be noted, that the results presented in Section 4.3 indicate that the objective function is essentially convex over a wide range of the parameter space. However, given the dimensionality and the complexity of the problem (interplay of different loss mechanisms, coupling between horizontal and vertical planes, ...), the existence of local minima within the search space cannot be excluded. The objective function is therefore assumed to be multi-modal and not convex.

One of the fundamental challenges of this optimisation problem is the high noise level, as illustrated in Fig. 6.2. The correlation between the intensity measured in the injection line and the ring (Fig. 6.2b) shows that the majority of the noise can be attributed to shot-to-shot

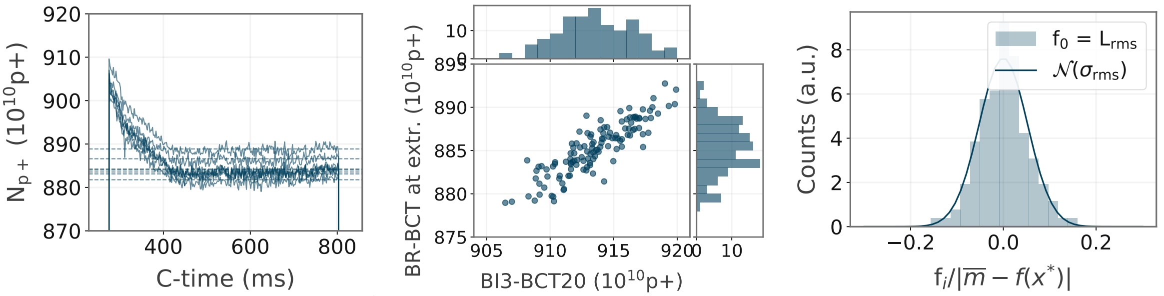

(a) Shot-to-shot variation of the intensity along the cycle. The dashed line indicates the average intensity before extraction (from C700-C800).

(b) Correlation between the intensity measured in the injection line (BI-BCT20) and at the end of the cycle (BR-BCT, C700-C800).

(c) Relative error distribution of L_{C805}, featuring a noise level of $\alpha \approx 0.07$.

Figure 6.2: Noise characteristic of the objective function (L_{C805}) for automated phase space painting (ISOLDE beam type, operational configurations as listed in Table 6.1).

jitters rather than measurement noise. The noise is considered to be additive and normally distributed (Eq. (5.13)). For an injected intensity of $N_{\text{p+,INJ}} = 0.9 \times 10^{13}$ p+ in ring 3, the noise level is estimated in measurements as $\alpha \approx 0.07$ (see Eq. (5.14)). Figure 6.2c shows the resulting Gaussian noise distribution of the objective[†].

Evaluation Cost and Sample Efficiency

A new acquisition with beam can be expected every 5-60 s in the PSB. This high evaluation cost of the objective function makes sample efficiency a key aspect when assessing the operational applicability of different algorithms.

Bounds and Constraints

Constraints arise from hardware limits of the KSW generator or user-specific operational boundaries (e.g. see Table C.1 for a list of the restrictions, which are to be considered for the ISOLDE painting optimisation). The constraints are included in the loss function using a single penalty term, which is computed through the integrated difference between the amplitude of the invalid, requested KSW decay $A_{\text{KSW, req.}}(t)$ and the set waveform $A_{\text{KSW, set}}(t)$

$$f(\mathbf{x}) = f_0(\mathbf{x}) + \xi_p \cdot p^2 \tag{6.1a}$$

$$\text{with} \;\; p = \int_0^{t_2} \left|(A_{\text{KSW, req.}}(t) - A_{\text{KSW, set}}(t)\right| \, dt. \tag{6.1b}$$

[†] Here, $\overline{m}$ and consequently α (Eq. (5.14)) are computed using the exploration steps of the pyBOBYQA algorithm with $\rho_{\text{beg}} = 0.5$.

Table 6.1: Phase space painting for ISOLDE beams with numerical optimisation algorithms: machine configurations and results.

Parameter	Unit	Set 1	Set 2	Set 3	Set 4
Ring	-	2	3	3	3
Number of injected turns	-	90	90	100	110
Injected intensity	10^{10} p+	920	910	1012	1115
Result: minimised L_{C805}	%	3.9	2.4	3	4.5

6.2 First Results With Online Painting Optimisation

Generic beam tests are performed on the machine to generally assess the feasibility of automatically optimising the PSB injection painting. The majority of these tests focus on optimising the painting when injecting ISOLDE-type beams with $N_{p+} = 0.9 \times 10^{13}$ p+ per ring, with machine settings similar as in the studies presented in Section 4.3 (Tables 4.1 and 4.5). The optimisation is performed using the Generic Optimisation Frontend and Framework (GeOFF) from the CERN operations group [164]. The results of these experiments help to characterise the general convergence behaviour, identify challenges and probe the structure of the data space. These first tests are performed using a selection of the algorithms listed in Section 5.2.3 with settings as listed in Table 6.2.

Figure 6.3 illustrates the convergence behaviour, which is observed in the PSB for different algorithms and resampling rates. The painting functions, which are set during the various optimisation runs in ring 3 are displayed in Fig. 6.4a and are colour-coded by the resulting losses, which range from $< 2.5\,\%$ (blue) to ≈ 4 to $> 15\,\%$ (red). The optimised painting settings for the different machine configurations, such as rings and intensities, are extracted and compared in Fig. 6.4b. The following observations can be summarised from these first tests:

- All of the tested algorithms manage to reduce the losses along the cycle to $< 2.8\,\%$ within 30-100 steps. This corresponds to $\approx$ 300-500 acquisitions, considering the different statistical resampling rates.

- Considering the applied hyperparameters, the local solvers Powell's Method and COBYLA terminate after around 30 steps, before being able to converge to the function minimum. pyBOBYQA-noise-global on the other hand continues the search due to the implemented restart mechanism and finds painting settings with lower loss rates of $\approx 2.5\,\%$.

- When comparing the function minima, which are found for the various operational conditions, it is evident that the minimised loss rates differ in the different rings (e.g. 2.3 % in ring 3 compared to 4 % in ring 2, see Table 6.1). This is expected due to differences in errors and resonance compensation in the four rings. However, the characteristic of the optimised painting configurations stays similar for different rings and intensities.

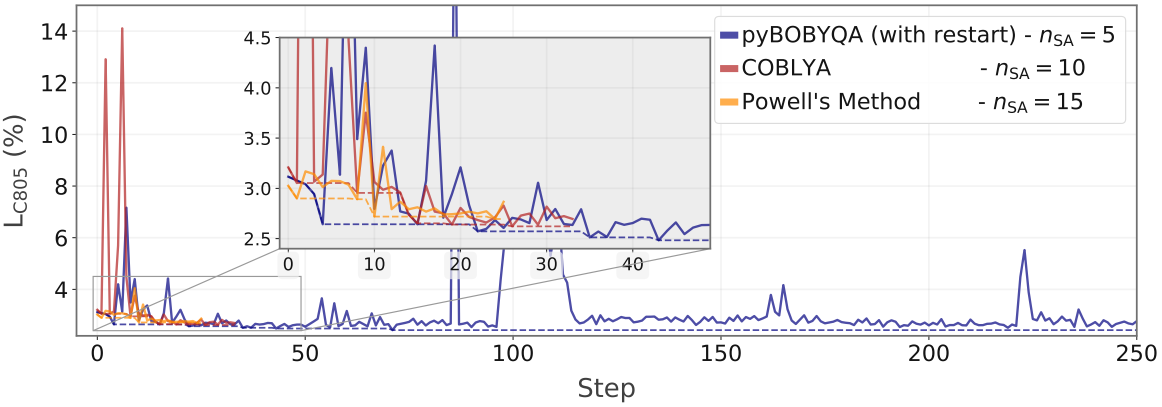

Figure 6.3: Online optimisation of the ISOLDE painting: convergence behaviour for selected algorithms and configurations. The incumbent solutions are marked by dashed lines.

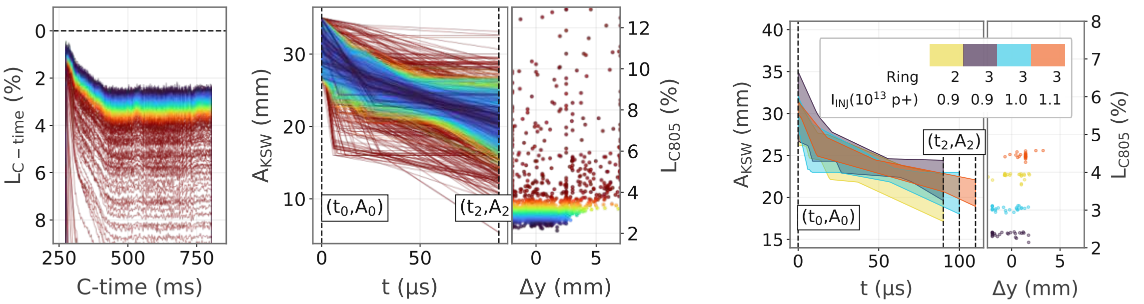

(a) Loss evolution along the cycle (left) for different KSW decays (centre) and Δy (right), which are set by the optimiser. The settings are colour-coded by the resulting objective L_{C805} ($N_{p+,INJ} = 0.9 \cdot 10^{13}$p+, R3).

(b) Span of optimised injection settings for different machine configurations.

Figure 6.4: Actor (injection settings) and objective data (L_{C805}) for online optimisation of the ISOLDE painting. The data sets are acquired in the PSB over multiple optimisation attempts with different operational configurations.

- The jitter in the convergence plot highlights the high noise level of the objective function, despite the already applied statistical resampling.

Whereas these first results show, that loss optimisation is feasible with different algorithms, they also raise questions about estimating the ideal sampling rates, algorithms and hyperparameters to find the minimum in as few steps as possible.

6.3 Surrogate Model for Offline Performance Tests

Conducting systematic tests on the machine to address these questions is infeasible because of limited beam time and drifts in the machine's performance, which occur due to external factors

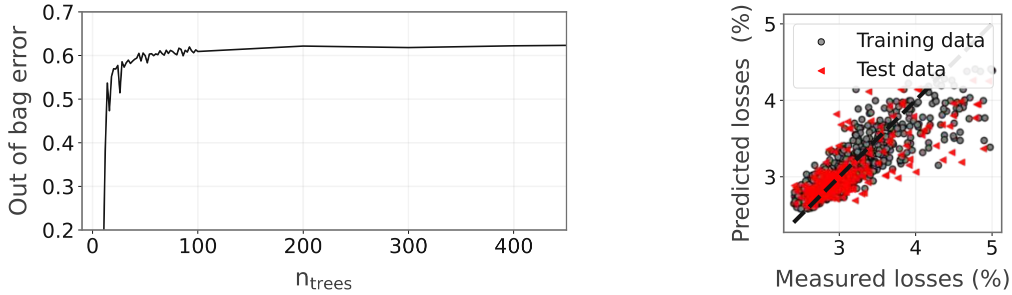

(a) Out-of-bag error (OOB) for an increasing number of trees. The final model is trained using N_T = 300 trees.

(b) Predicted versus measured objective function, for the training (grey) and test data (red).

Figure 6.5: Performance evaluation of the surrogate model created by the random forest regressor (using 300 trees, a minimum number of 6 samples per leaf and 3 out of 5 features per split).

when measuring over multiple days. The data samples, which are acquired during the first beam tests are therefore used to train a surrogate model using a RFR [147], which is described in more detail in Section 5.1.3. This choice is based on several criteria. Firstly, the RFR handles nonlinear data, as required for modelling the PSB injection dynamics. As an ensemble method, it is generally more robust to overfitting, noisy datasets, missing data or feature scales. Last but not least, a major advantage is its insensitivity to hyperparameter settings. The reliable and straightforward implementation of this algorithm makes the presented approach generalisable to other optimisation applications in controlling large-scale industrial or scientific facilities.

Specifics of the Training Data Set and Model Parameters

The training dataset[†] is obtained from the first online optimisation attempts and is therefore highly imbalanced, with the majority of the samples being acquired at low objective values between $L_{\mathrm{C805}} \approx 2.5$-5 %. Even though RFR are comparably robust to outliers, the data acquisitions with high losses $L_{\mathrm{C805}} > 5\,\%$ can distort the prediction in the vicinity of the minimum. These samples are therefore removed before training the model. The parameters for training the RFR ($n_T = 300$ trees, minimum 6 samples per leaf, 4 out of 5 features per split) are tuned to reduce the model variance rather than decrease the bias. While this mitigates overfitting and the introduction of artificial local minima, the increased bias results in a systematic prediction inaccuracy especially for data samples with relatively large and small objective values (see Fig. 6.5b). However, apart from such deviations for extreme objective values, the modelled data space is sufficiently close to the real data space to allow employing this model for offline tests. Finally, additive Gaussian noise with $\alpha = 0.07$ is added to the surrogate model to mimic the real optimisation environment, based on the noise estimates presented in Section 6.1,

---

[†] The training data set consists of 1800 samples and is split into 85 % training and 15 % test data samples.

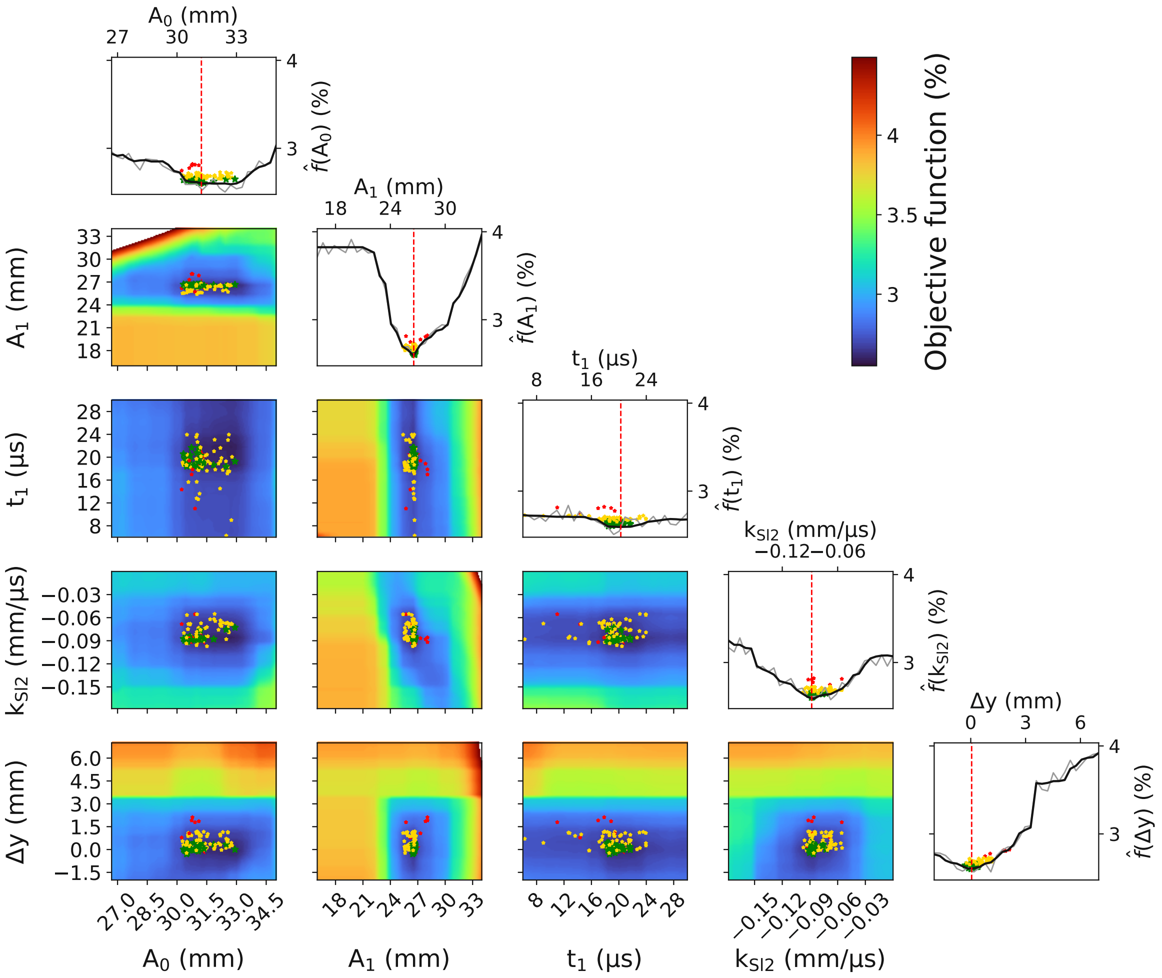

Figure 6.6: Response surfaces of the noise-free surrogate model, illustrating a 1- and 2-dimensional parameter variation around a proposed solution. Exemplary solutions obtained when running the optimiser (here pyBOBYQA without restarts) multiple times with different starting points are indicated by the scatter markers and colour-coded by the classified level of accuracy, i.e. green for high-accuracy solutions $f(\mathbf{x}) < 2.65\,\%$, yellow for low-accuracy solutions $f(\mathbf{x}) < 2.73\,\%$ and red for noncleared samples with $f(\mathbf{x}) > 2.73\,\%$. Plotting script modified from [182].

Assessing the Characteristic of the Response Surface using the Surrogate Model

The surrogate model (Fig. 6.6) further assists in comprehending the structure of the data space. Figure 6.6 shows the noise-free response surface, which is obtained from the surrogate model for a 1D and 2D parameter variation around the approximated function minimum [182]. In each subplot, one or two features are varied, while the remaining features are kept at the values of the incumbent solution. In agreement with the results presented in Section 4.3.5, the response surfaces clearly show the flat characteristic of the minimum, the increasing losses with increased vertical offset Δy, the convex dependence on the combination of A_1 and k_{SI2} and the comparably small impact of A_0 and t_1. The flat minimum is a major challenge for finding efficient optimisation routines and is relevant for tuning the optimiser's hyperparameters.

6.4 Testing Methodology and Performance Metrics

The surrogate model is subsequently used to systematically assess the performance of different algorithms offline, using a procedure as outlined below.

6.4.1 Assessed Optimisation Algorithms and Configurations

The investigated algorithms belong to the most common local and global single-objective, DF, nonlinear, nonconvex methods and are listed in Table 6.2 (see Section 5.2.3 for a brief introduction). These algorithms have been considered because of operational availability [164] or recommendations from literature for related applications, e.g. [165–168]. Evidently, there are numerous other eligible algorithms, which can be explored operationally in future studies, as listed e.g. in [159].

Table 6.2 references the utilised algorithmic implementations and lists the applied configurations, which are obtained from a rough hyperparameter tuning. The major alterations to the default parameters are as follows:

- **Algorithmic implementations:** Several local DF methods require an initial search range or step size parameter, which defines the search space exploration during the initialisation phase before the algorithm exploits a (local) minimum. This range is set using the initial trust-region radius ρ_{beg} for pyBOBYQA and COBYLA, initial step size for Powell's Method and initial simplex size for Nelder-Mead. In our case, the highest performance is achieved with a large initial search range, such as approximately 25 % of the feature range ($\rho_{\text{beg}} = 0.5$ for $x_i = [-1, 1]$).

  When applying the pyBOBYQA adaptation for noisy applications (pyBOBYQA-noise [165]), the expected additive noise amplitude $\sigma_n/\sqrt{n_{\text{SA}}}$ should be explicitly specified. This activates a restart mechanism once the last n_k objective values (i.e. the samples used for the local regression model) are within this noise level [165].

  pySOT [183] is a state-of-the-art surrogate optimisation package. It is selected as a representative for SBO due to reported good performance for noisy, expensive BB problems [165]. Parameters as configured in [165] are used without further tuning, i.e. a radial basis surrogate model with a DYCORS search strategy [184] and a latin hypercube sampling. SBO is a broad topic with a wide range of different solvers, surrogate modelling and sampling strategies. A dedicated study to explore such solvers in detail goes beyond the scope of this thesis but is strongly encouraged.

- **Termination criteria:** Optimisation processes, especially for global solvers, are often terminated because of reaching a pre-defined number of maximum function calls. This budget is set to 10^4 objective evaluations for the offline tests using the surrogate model (including

Table 6.2: Overview of the derivative-free numerical optimisation algorithms, which are applied in the PSB injection painting optimisation environment.

Algorithm	Impl.	Type	Hyperparameters and options
pyBOBYQA	[165] *v1.3*	Trust region (quadratic approximation)	Initial trust-region radius $\rho_{\text{beg}} = 0.5$
COBYLA	[152] *v1.8.0*	Trust region (linear approximation)	Initial trust-region radius $\rho_{\text{beg}} = 0.5$
Powell's Method	[152] *v1.8.0*	Direct search (bi-directional line search)	
Adaptive Nelder-Mead	[152] *v1.8.0*	Direct search (simplex based pattern search)	Initial simplex with step-size $h_j = 0.4$ for feature bounds of $(-1, 1)$
pyBOBYQA with restart	[165, 175] *v1.3*	Trust region (quadratic approximation) with restart mechanism	Initial trust-region radius $\rho_{\text{beg}} = 0.5$, *noise*- and *global*-flag enabled, *additive_noise_level*= $\sigma_n / \sqrt{n_{\text{SA}}}$
pySOT	[183] *v0.3.3*	Surrogate optimisation	Radial basis function surrogate, DYCORS [184] strategy, initial design of $2 \cdot d + 1$ latin hypercube points

statistical resampling) to avoid premature termination of an algorithm. Nevertheless, the study aims to identify solvers and configurations, which achieve a sufficient objective reduction as efficiently as possible. Therefore particular attention is given to the performance, which the optimisers achieve within $n_{\text{acquisitions}} \lessapprox 300$ acquisitions.

Local model-based and direct-search methods base the termination criteria additionally on a tolerance parameter tol. It describes the minimum distance in feature space between two subsequent function evaluations (or minimum trust-region radius ρ_{end}) and triggers termination once it is reached. To prevent early termination, which would distort the comparison of local solvers, small tolerance levels of $\mathcal{O}(10^{-4})$ are chosen for all local solvers. However, it should be noted that for operational purposes, a minimum tolerance/trust-region radius of $\rho_{\text{end}} = 0.005$ proved to be suitable.

6.4.2 Test Data and Performance Metrics

Each algorithm is tested for the same set of $N_s = 100$ randomly generated start configurations, as recommended in [154, Chp. 3-4]. These initial settings are uniformly sampled from a 20 % vicinity around the centre of the feature range and reflect for example user-dependant changes in feature bound settings and shifts in the response surface due to varying machine configurations.

The performance of the algorithms is compared using criteria for efficiency and reliability [154, Chp. 4], [155].

Measuring Reliability

Following the studies presented in [155], the reliability is measured using the *clearance rate*

$$CR = \frac{n_{\text{succ.}}(\tau)}{N_s}. \tag{6.2}$$

This quantity describes the proportion of cases $n_{\text{succ.}}$ in which the algorithm converges to an acceptable solution. The acceptable solutions are defined by the tolerance τ (see Eq. (5.16)). Note that for tests on the surrogate model, the noise-free objective value $f(\mathbf{x}^*)$ of the incumbent solution is known and is hence considered for assessing the success in Eq. (5.16).

To account for the flat characteristic of the function minimum, it is of interest to distinguish solutions with high and low accuracy. Converging to the region of the flat minimum, but not necessarily the optimum value within this region, is considered as *low-accuracy solution* and given by the tolerance $\tau = 0.2$, which corresponds to solutions with $f(\mathbf{x}) < 2.73\,\%$. *High-accuracy solutions* are expected to converge to the vicinity of the global optimum (green markers in Fig. 6.6), given by $\tau = 0.1$ and hence $f(\mathbf{x}) < 2.65\,\%$. These regimes are illustrated in Fig. 6.6 by yellow and green markers, respectively. The red markers indicate unaccepted solutions.

Measuring Efficiency

The efficiency is measured by the required number of function evaluations (i.e. number of PSB cycles) needed to reach a specific clearance rate CR. To simplify the comparison, statistical resampling with a constant resampling rate n_{SA} is considered. The number of required function evaluations is consequently determined by Eq. (5.18).

Reporting the Results Using Data Profiles

The tradeoff between efficiency and reliability can be illustrated using data profiles [185], which display the clearance rate CR as a function of the number of function evaluations, as shown in Fig. 6.7a. The area under the curve (AUC)

$$AUC = \frac{1}{n_{\text{aq,max}}} \int_1^{n_{\text{aq,max}}} CR(n_{\text{acq}}) \cdot dn_{\text{acq}} \tag{6.3}$$

is used to compare the data profiles quantitatively. For the here presented analysis a maximum of $n_{\text{aq,max}} = 5000$ objective evaluations is considered for computing the AUC. When comparing multiple optimisation methods (Fig. 6.7a), the best performing resampling rate n_{SA} (i.e. with the highest AUC) is considered for each method.

6.5 Offline Tests Using the Surrogate Model

Figure 6.7a compares the performance of the different algorithms using data profiles. For each algorithm, the statistical resampling rate n_{SA}, which gives the highest AUC is considered in this comparison. The sensitivity of the AUC on the statistical resampling rate is portrayed in Fig. 6.7b for the individual methods. The corresponding data profiles are presented in Appendix C for reference.

Low-Accuracy Solutions ($\tau = 0.2$)

It can be seen that for low-accuracy solutions all presented methods manage to reach a $CR > 0.8$ within $n_{\mathrm{acq}} < 1000$ steps. The best performance is achieved using the local solver ANM, which achieves $CR > 0.95$ within $n_{\mathrm{acq}} \approx 150$ steps. The global solvers pyBOBYQA-noise-global and pySOT approach $CR > 0.95$ within $n_{\mathrm{acq}} \approx 400$ and 800 steps, respectively. These three methods are less sensitive to noise and do not require a large statistical resampling rate. The highest AUC is consequently obtained for $n_{\mathrm{SA}} = 3\text{-}5$ acquisitions per step. This resampling rate is mainly required to reduce the noise level to $\alpha / \sqrt{n_{\mathrm{SA}}} \ll \tau$.

The local optimisers pyBOBYQA, Powell's Method and COBYLA only achieve a clearance rate of $CR = 0.8\text{-}0.9$, and this within $n_{\mathrm{acq}} = 1000$ acquisitions. For pyBOBYQA and COBYLA, the low sample efficiency can be attributed to the high $n_{\mathrm{SA}} = 30\text{-}50$ acq./step, which is required because of the low robustness to noise. For Powell's method, on the other hand, the best performance is still achieved with a low resampling rate ($n_{\mathrm{SA}} = 5$ acq./step). In this case, the low sample efficiency can be ascribed to the larger number of n_{step} during the initial search in each direction. However, from a practical point of view, it should be noted that the efficiency of Powell's method strongly depends on the configured initial directions, especially when targeting low-accuracy solutions. There is potential to increase the efficiency of Powell's method by including prior information about the feature space in the initial directions, e.g. select the directions of highest feature importance, i.e. Δy and A_1, as first search directions x_1 and x_2.

High-Accuracy Solutions ($\tau = 0.1$)

For high-accuracy solutions, only the global solvers (pySOT and pyBOBYQA-noise-global) as well as the local heuristic ANM achieve a clearance rate of $CR > 0.7$. However, converging to these solutions takes up to $n_{\mathrm{acq}} \rightarrow 2500$ acquisitions. The impact of the noise level on the performance is similar as for low accuracy solutions. The main difference is that the optimum number of acquisitions per step is shifted towards higher values for all algorithms. This is consistent with the fact, that one can only expect to reliably solve the problem to an accuracy $\tau \gg \sigma_n / \sqrt{\mathrm{n_{SA}}}$.

Summary of Results and Equivalent Machine Time

Overall, it is observed that ANM outperforms the other tested methods if the aim is not to find the global minimum but rather to quickly achieve an acceptable reduction in the objective

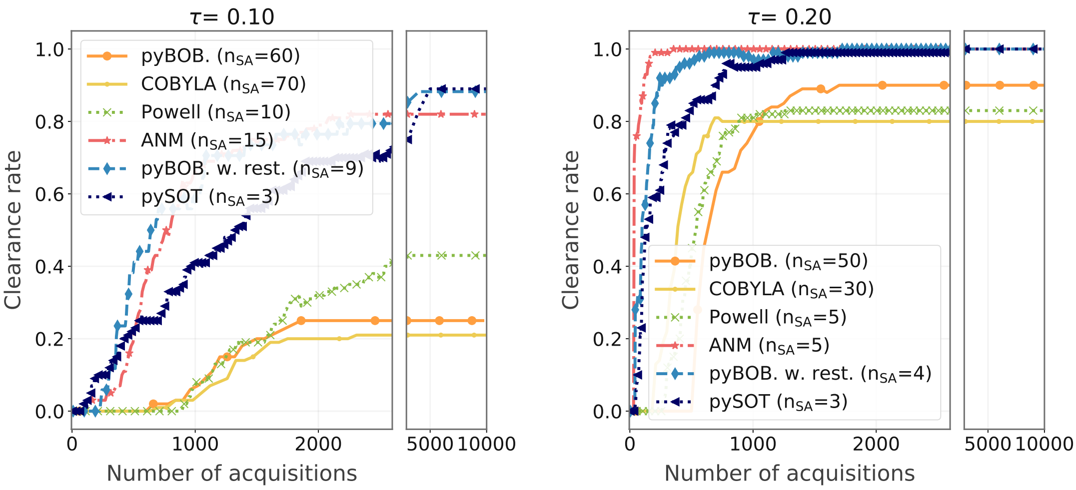

(a) Data profiles for comparing the performance of the different algorithms. For each algorithm, the statistical resampling rate, which yields the highest area under the curve (AUC) is applied.

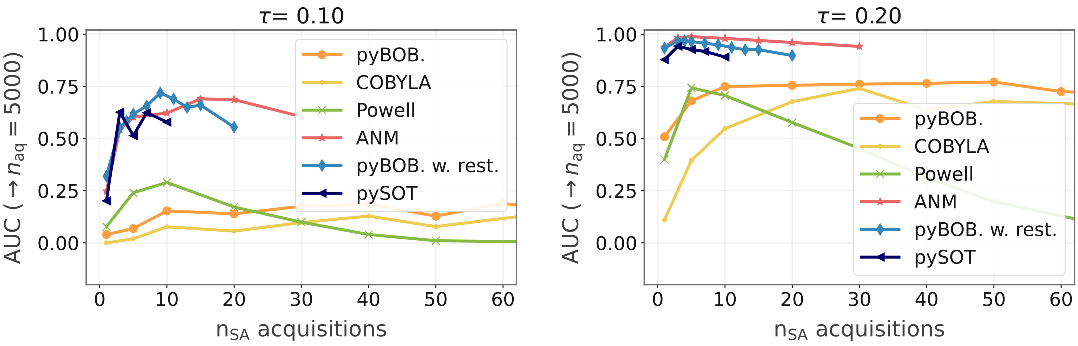

(b) Impact of the statistical resampling rate on the area under the curve (AUC) for the different algorithms.

Figure 6.7: Comparing the performance of different optimisation algorithms on the surrogate model: high (left) and low-accuracy solutions (right).

function, e.g. here find low-accuracy solutions with $\tau \approx 0.1$-0.2. This is also repeatedly reported in literature e.g. [119]. The quick improvement in the first steps is also attributable to the fact, that in the majority of the cases only one or two objective evaluations are required for each algorithmic iteration, which is the evaluation of a new simplex in case of ANM. The here presented results demonstrate again, why ANM is widely used in many engineering problems when to aim is to provide a quick, acceptable reduction of the objective. However, the hyperparameter tuning showed, that it is essential to start the optimisation with an initial simplex, which covers a wide range of the parameter space, e.g. with a simplex length of ≈ 20% of the feature range in this application. This requirement is particularly attributed to the flat minimum.

The performance of pyBOBYQA-noise-global is generally very comparable with ANM. However, to increase its efficiency it is beneficiary to explicitly set a noise level, which triggers a restart in case of stagnation due to noise. Further, for low-accuracy solutions, pyBOBYQA-noise-global loses to ANM because of the longer initialisation phase. For 5 dimensions the initialisation phase of pyBOBYQA-noise-global takes 21 steps. This corresponds to $n_{\mathrm{acq}} = 84$ acquisitions when acquiring 4 samples per step. Reducing the statistical resampling rate during this initialisation phase will yield a significant improvement in efficiency.

The surrogate-based optimiser pySOT achieves a similar CR as pyBOBYQA-noise-global for both low and high accuracy. However, in the applied configuration it requires approximately twice the number of function evaluations. Still, as the hyperparameters are set purely based on literature [175], without further fine-tuning, this is a promising result and motivates further investigation of SBO methods. These solvers become of particular interest, considering that a model can be pre-trained with priorly acquired results or surrogate models. This can reduce the initialisation phase significantly.

Tables 6.3 and 6.4 summarise the results for low and high-accuracy solutions, listing the AUC and the number of acquisitions n_{acq}, which are required to clear the problem with $CR > 0.95$ and $CR < 0.7$, respectively. Based on the assumption that one acquisition (i.e. a new PSB cycle and measurement) is obtained every 30 s, the number of acquisitions is converted to an equivalent machine time. This indicates, that also for such a low cycle rate, low-accuracy solutions can be achieved within 1 h, whereas high-accuracy solutions can be achieved within one shift, e.g. overnight.

Table 6.3: Performance summary for different optimisers when targeting low-accuracy solutions. The *equivalent time* $t_{\mathrm{eq.}}$ corresponds to the machine time required for n_{acq} steps assuming one acquisition (PSB cycle) every 30 s.

Optimiser	**AUC**	**n_{SA}**	**$n_{aq.}$ CR>0.9**	**$t_{eq.}$ (h)**	**Potential improvements**
ANM	0.99	5	150	1.3	Adaptive n_{SA}
pyBOB.-noise-glob.	0.97	4	400	3.3	Adaptive n_{SA}
pySOT	0.94	3	780	6.5	Adaptive n_{SA}, pre-learned model
pyBOBYQA	0.77	50	-	-	
COBYLA	0.74	5	-	-	
Powell	0.74	30	-	-	Choose initial search directions

Table 6.4: Performance summary for different optimisers when targeting high-accuracy solutions. The *equivalent time* $t_{\mathrm{eq.}}$ corresponds to the machine time required for n_{acq} steps assuming one acquisition (PSB cycle) every 30 s.

Optimiser	AUC	$\mathbf{n_{SA}}$	$\mathbf{n_{aq.}}$ CR>0.7	$\mathbf{t_{eq.}}$ (h)	Potential improvements
pyBOB.-noise-glob.	0.72	9	1070	9	Adaptive $\mathrm{n_{SA}}$
ANM	0.70	15	1185	10	Adaptive $\mathrm{n_{SA}}$
pySOT	0.63	3	2350	20	Adaptive $\mathrm{n_{SA}}$, pre-learned model
pyBOBYQA	0.29	10	-	-	
COBYLA	0.19	60	-	-	
Powell	0.16	70		-	Choose initial search directions

6.6 Conclusion and Outlook

Automating the transverse painting optimisation at the PSB injection based on user request and beam instrumentation feedback is fundamental for increasing operational efficiency and performance. Such a system can be for example employed to minimise beam loss during high-intensity beam production. As a proof of concept, different derivative-free optimisation algorithms are applied in the PSB. An acceptable loss reduction is achieved within a few hundred objective evaluations. As in most laboratory and industrial optimisation applications, the major challenges turn out to be the high noise level and the expensive function evaluations. In order to guarantee convergence to acceptable solutions, we either require the selected algorithm to be robust to noise (e.g. SBO, pyBOBYQA with extension for noisy applications, ANM) or reduce the noise level through statistical resampling. The data samples, which are acquired during the first experimental optimisation runs, are used to train a data-driven surrogate mode. This proved to be an efficient way of improving and assessing the performance of various algorithms and settings offline, without the need for physical resources like beam time. These tests clearly show that balancing noise reduction (resampling) with enhanced noise exploration (increased number of steps) is crucial for maximising efficiency and is specific to each solver.

The results presented in this chapter could be used to assess the feasibility of implementing a model-free controller in operation, for example using reinforcement learning or extremum-seeking controllers. This would allow maintaining the objective minimum, which has been previously found using the above-described methods instead of going through the full optimisation process again.

CHAPTER 7

Deep Learning for Electronic Circuit Parameterisation of the Painting Kicker Magnets

The in-house KSW generator design allows for programming the wide range of user-specific KSW field decays. This programmable field decay provides high operational flexibility but results in complex generator parameterisation. Numerous input parameters such as switching delays, capacitor voltages and amplifier analogue input voltages have a nonlinear effect on the output current and make an analytical description of the full electrical circuit difficult. A PD (proportional and derivative) feedback loop and a linear power amplifier are currently used in operation to achieve the required current precision of ±1 % for controlling the phase space painting schemes for the various users.

The complex parameterisation and the demand to reliably generate user-specific piece-wise linear waveforms with 1 % precision on a pulse per pulse basis make the KSW generator an interesting test bench to investigate control concepts based on supervised ML algorithms. An overview of data-driven methods to control dynamic systems can be found in [142]. In the long term, such methods could pave the way to e.g. substitute the implementation of a feedback loop or even be a generic way to solve similar tasks. At its core, parameterising the KSW is an inverse problem, which aims at identifying system parameters based on the observed system response. Solving such problems using deep learning [186] has gained much attention recently, also profiting from the advances in novel *physics-guided* (PGNN,[187]) or *physics-informed neural networks* (PINN, [188]).

This chapter investigates the feasibility of modelling and controlling the circuit parameterisation using supervised learning techniques as an alternative solution to the control based on a feedback loop. Section 7.1 provides an introduction to the generator layout and lists the hardware parameters, which are to be controlled. Section 7.2 outlines the investigated model structures, which are trained in Section 7.3 and assessed in Section 7.4.

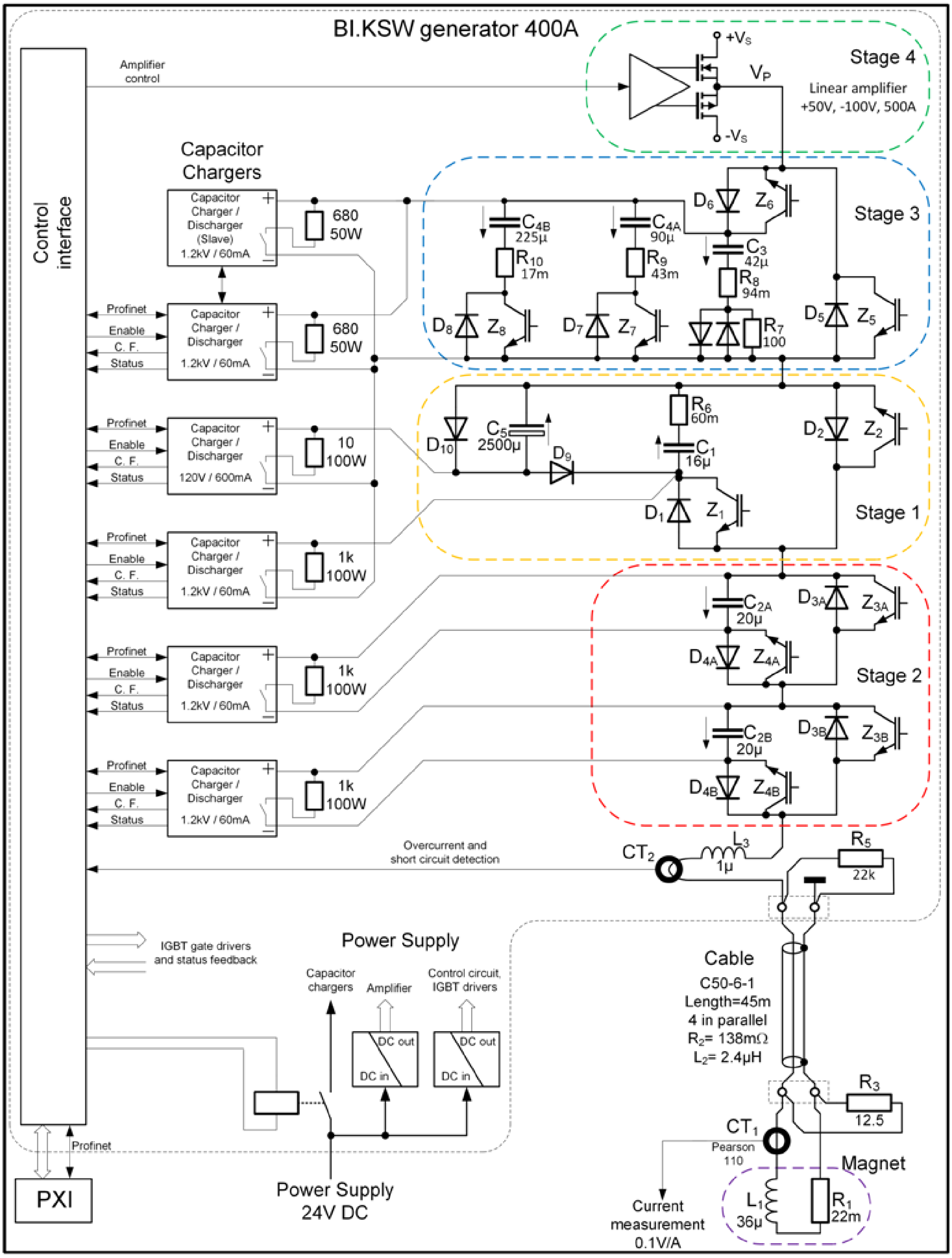

Figure 7.1: Schematic of the 400 A KSW generator: the coloured boxes highlight the four generator stages, which are switched on and off to create the custom current slopes highlighted in Fig. 7.2 [103].

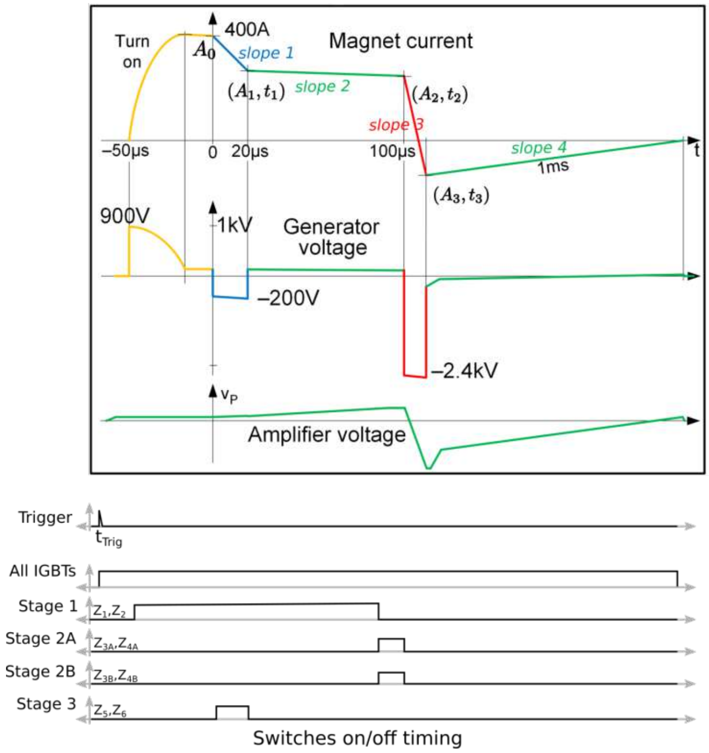

Figure 7.2: KSW magnet current, generator voltage waveform, amplifier input voltage and IGBT switch times for an ISOLDE-type painting function [103].

7.1 KSW Generator Layout and Control

The KSW pulse generator consists of four stages with pre-charged high voltage capacitors C_i (Fig. 7.1), as described in detail in [103]. The stages are connected in series and are successively switched to the magnet in order to generate the required painting kicker magnet current I_{KSW} (Fig. 7.2). All descriptions in this chapter focus on the generation of an ISOLDE-like waveform, but similar concepts are valid for other waveform types.

- **Stage 1** is active during the initial current rise (*turn-on*) and current decays *slope 1* and *slope 2*. It comprises two capacitors, which generate a positive output voltage, C_1 for *turn-on* and C_5 for the flat-top and the flat current segment between I_1 and I_2 (*slope 2*).

- **Stage 2** generates a negative output voltage to create the fast current decay during *slope 3*. It consists of two switching stages in series with the capacitors C_{2a} and C_{2b}.

- **Stage 3** is switched on to obtain the current decay during *slope 1*. The required negative output voltage is generated by the pre-charged capacitor C_3. C_3 alone is sufficient to generate

Table 7.1: KSW generator control parameters to be predicted by the machine learning model.

	Value	Unit	Stage	Remark	Predict
Capacitor voltages	V_{C1}	V	1	Turn-on	yes
	V_{C2a}	V	2	Slope 3	yes
	V_{C2b}	V	2	Slope 3, same as V_{C2b}	no
	V_{C3}	V	3	Slope 1	yes
	V_{C5}	V	1	Flat-top, slope 1 and 2	yes
Bits	c_{4a}	-	3	Change stage 3 capacitance	no
	c_{4b}	-	3	Change stage 3 capacitance	no
IGBT timings	$t_{\mathrm{R},1}$	µs	1	t_2, beginning slope 3	yes
	$t_{\mathrm{R},2}$	µs	2	Turn-on	yes
	$t_{\mathrm{R},3}$	µs	3	t_0, beginning slope 1	yes
	$t_{\mathrm{LEN},1}$	µs	1	t_3, end slope 3	yes
	$t_{\mathrm{LEN},2}$	µs	2	t_2, end slope 2	yes
	$t_{\mathrm{LEN},3}$	µs	3	t_1, end slope 1	yes
Lin. Ampl.	$\mathbf{t}_{\mathrm{LA}}$	µs	4	Entire waveform	yes
	$\mathbf{V}_{\mathrm{LA}}$	µs	4	Entire waveform	yes

slope 1 with a fast current decay

$$(\Delta i/\Delta t)_1 = -\frac{I_{0,\mathrm{KSW}} - I_{1,\mathrm{KSW}}}{I_{0,\mathrm{KSW}} \cdot t_{1,\mathrm{KSW}}} \tag{7.1}$$

and short duration. The maximum charging voltage, in this case, is 1.2 kV. To provide a *slope 1* with longer duration but lower $\Delta i/\Delta t_1$, additional capacitors C_{4a} and C_{4b} can be connected in parallel to C_3. In this case, the charging voltage is limited to 500V. The bits c_{4a}, c_{4b} control the connection of these additional capacitors and are set depending on the requested $\Delta i/\Delta t_1$.

- **Stage 4** consists of a linear power amplifier. The applied analogue amplifier input voltage is set as a series of time-amplitude markers (here 15 points $P_{\mathrm{LA}_i} = (t_{\mathrm{LA},i}, V_{\mathrm{LA},i})$ with i = 1-15) to correct for nonlinearities in the output current ($\mathbf{v}_P$, green in Fig. 7.2).

Depending on the time markers t_i of the requested current waveform, IGBT switches are programmed to activate the respective stages $s = 1$ to 3 by setting the rising edge $t_{\mathrm{R},s}$ and the length $t_{\mathrm{LEN},s}$ of the control signal (bottom in Fig. 7.2). The required timings orient on the respective time instances t_i, but need to be advanced by a time shift $\Delta t \approx O$ (µs) to account for delays of IGBT and gate drivers.

The programmable features are summarised in Table 7.1, i.e. IGBT switch timings, capacitor charging voltages, control bits for defining the capacitance of *stage 3* and the amplifier input voltage array. The dynamics of such a system can be mathematically formalised using state space theory [189, 190] as

$$\frac{d\mathbf{x}}{dt}(t) = \mathbf{A} \cdot \mathbf{x}(t) + \mathbf{B} \cdot \mathbf{u}(t). \tag{7.2}$$

$\mathbf{x}$ is the state vector and describes the system state at time t (i.e. here the magnet currents). The input $\mathbf{u}(t)$ is the driving term of the system at time t (i.e. here the piecewise linear sum of the generator forward voltage and the amplifier voltage). The system matrix $\mathbf{A}$ defines the dynamic behaviour. It depends on the inductors, capacitors and resistors of the stages, which are active to produce the respective slope. $\mathbf{B}$ is the control matrix Solving these equations to define the required amplifier and capacitor voltages is a complex task. Further, the dynamics cannot be modelled using this formalism during the transition between the individual stages, due to IGBT switching losses and related fast voltage drops. Initial attempts to identify the required circuit parameters for a specific waveform are presented in [189]. However, the pressing need for an accurate current and linearity control eventually motivated the implementation of an analogue feedback loop based on a PD controller [103] instead.

7.2 Machine Learning Model Overview

An alternative approach to the control using the feedback loop could be to estimate the required circuit parameters using an ML model. Ideally, such a model predicts the parameters, which are required to produce the linear current decay, as requested by the user. Given the constraint of linearity, the target waveform for operational applications is fully defined by the 8 time-amplitude markers $(A_0, A_1, A_2, A_3, t_1, t_2, t_3, t_4)$. However, the majority of the hardware parameterisations and hence also the training data samples, result in nonlinear current evolutions (mainly slope 2 and 3). The input to the ML model is therefore the entire waveform $I_{\mathrm{KSW}}(t)$ as a time series and not just the 8 time-amplitude markers (red box in Fig. 7.3). The waveform can be parameterised by n features through various preprocessing techniques to reduce the dimensionality of the input feature space. The overall model $\hat{f}$

$$\hat{f} : \mathbb{R}^n \rightarrow \mathbb{R}^m \tag{7.3}$$

subsequently aims at mapping these n inputs to $m = 40$ output features (4 capacitor voltages, 6 switch timings and 15×2 time-amplitude coordinate pairs for the amplifier waveform, green box in Fig. 7.3 and Table 7.1). Part of the predicted output, i.e. the amplifier input voltage, can be alternatively formulated as time series.

The ideal charging voltages produce a waveform close to, but not exactly, the linear target waveform, also without feeding an analogue input voltage to the amplifier. The amplifier voltage subsequently solely corrects for nonlinearities and remaining errors. It is therefore of interest, to model the generator dynamics without the amplifier voltage as the first proof of concept. Two networks are trained to solve the forward and inverse problems for operating the generator without the amplifier input voltage.

- **Step I** predicts the hardware parameters for a given input waveform (without analogue amplifier input voltage).

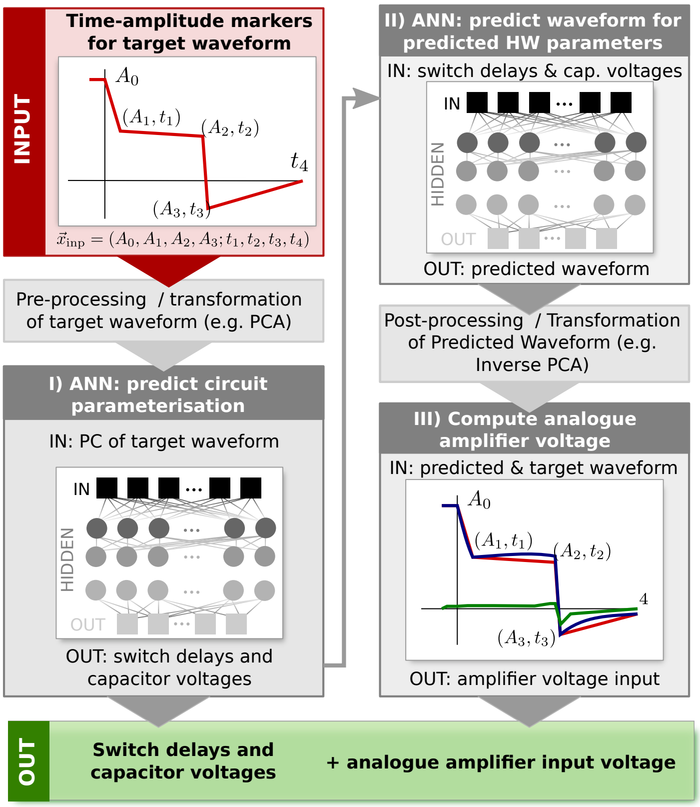

Figure 7.3: Artificial neural networks for predicting the circuit parameterisation of the KSW generators.

As the amplifier input voltage is missing in this model, it will not be possible to predict a hardware parameterisation, which generates a piece-wise linear current decay. However, the predicted parameterisation is supposed to produce a waveform close to the linear target waveform.

- **Step II** predicts the output waveform, which is expected for a given circuit parameterisation.

In the overall picture, Step II can be applied to predict the waveform, which is expected to be produced by the predicted hardware parameters. Assuming that the accuracies of the models in step 1 and 2 are sufficient, the difference between the nonlinear predicted and the linear target waveform could subsequently be used in

- **Step III**, to predict the analogue waveform required to correct the discrepancies and nonlinearities.

The first tests, which are presented in this chapter focus on creating models for steps I and II. In the long term, efforts will aim at combining steps I to III into a single model. However, the proposed modular approach is chosen here to simplify these first studies. Additionally, modelling the contribution of the generator forward and the amplifier voltage independently can simplify the application of underlying partial differential equations based on Eq. (7.2) when using PINNs in future studies.

Finally, it should be noted that training data samples with close to ideal hardware parameters are sparse. Extrapolating the predicted hardware parameters to these unseen regions is expected to be one of the major challenges of training an accurate ML model.

7.3 Methodology

The main model parameters of both models for step I and II are summarised in Tables 7.2 and 7.3. The respective design choices are motivated in the following subsections. The pyTorch [191] and scikit-learn [192] libraries are used for creating the model and preprocessing the data, respectively.

7.3.1 Training Data, Input and Output Feature Space

The labelled training and test data are acquired by pulsing a test generator [103] with different circuit control parameters. The pulse cycle takes 1.2 s, which enables the acquisition of large amounts of training data in reasonable time periods, i.e. 72000 samples within 24 hours. The here presented first feasibility tests are performed using a comparably small data set of 4000 samples, which is divided into 10 % test and 90 % training data.

The models are trained for ISOLDE-type waveforms with a fixed configuration of stage 3 ($c_{4a} = 1$ and $c_{4a} = 1$). Setting the capacitance for a specific waveform through the control bits is a design choice. The required parameters, the resulting dynamics and hence also the ANN weights change with altered *stage 3* capacitance. The trained models are therefore limited to KSW operation with similar stage 3 capacitance. However, the same concepts can eventually be applied to train models for different control bit configurations.

7.3.2 Data Preprocessing

Examples for the acquired waveforms (without amplifier voltage) are illustrated in Fig. 7.4a. Beam is here injected at $t = 0$ µs. The rising edge of the current waveform (turn-on, $t < 0$ µs) is not specified by the operationally requested waveform. The first step of preprocessing is therefore the extraction of the time period, in which the KSW current decay is specified by the user request (Fig. 7.4b). The subsequent preprocessing step aims at reducing the dimensionality of this cut waveform. This can be achieved through several techniques, such as wavelet and Fourier transform or dimensionality reduction using convolutional neural input layers (see [142, Chp. 5] for an overview). Because of its simplicity, the dimensionality reduction is performed in this study using a principal components analysis (PCA) [193] based on the implementation in [191, 194]. The first 30 principal components (PC) yield a good reconstruction of the original waveform, as illustrated in Fig. 7.4c. Using less PCs results in a misrepresentation of the sharp transitions between the individual slopes. Higher-order PCs solely reproduce the noise of the acquired current and do not provide additional information. Performing the PCA reduces the dimensionality of the input feature space in model 1 and output features space in model 2 from 800 time steps to $n = 30$ PCs. The PCs and hardware features are subsequently standardised before being fed to the MLPs.

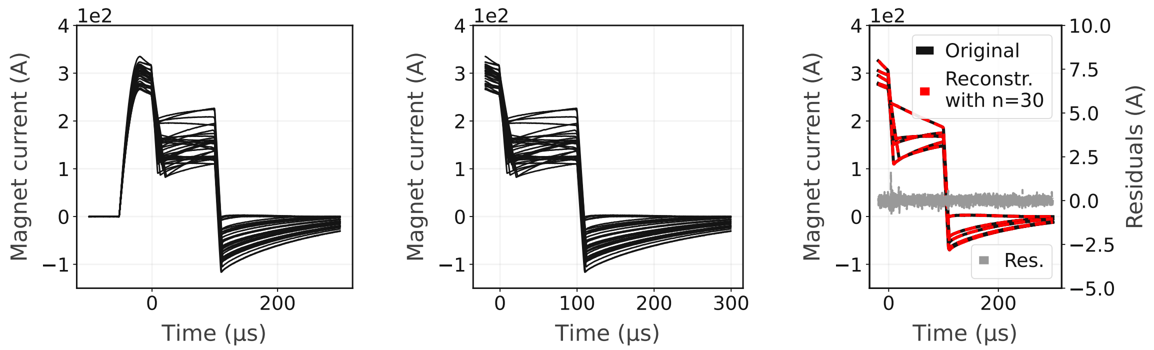

(a) Examples of original acquisitions (features: $d = 800$ time steps).

(b) Constraining the region of interest (features: $d = 635$ time steps).

(c) Projection to first $n_{\mathrm{PCA}} = 30$ PCs (features: $d = 30$ PCs).

Figure 7.4: Preprocessing steps prior to creating a machine learning model of the KSW generator control: d refers to the dimensionality of the feature space after the respective preprocessing step.

7.3.3 Model Architecture and Loss Function

Fully connected MLPs are chosen as initial architectures for both models, as outlined in Tables 7.2 and 7.3. The number of hidden layers and units are estimated on a trial-and-error basis and are subject to optimisation in further studies. The leaky-ReLU [195], which was originally introduced to mitigate performance limitations due to dying neurons in case of poor weight initialisation or data normalisation, is implemented as activation function. A batch normalisation layer [196] is included prior to every nonlinear operation (i.e. leaky ReLU activation) to accelerate and stabilise the training process. Two dropout layers with a dropout rate of 50 % are included to avoid overfitting the training data. Training is performed using backpropagation and the AdamW optimiser [197]. The applied learning rates (Tables 7.2 and 7.3) are empirically estimated.

For both models, the error between the prediction $\mathbf{y}$ and the ground truth y_{gt} over N samples is quantified using the Mean Squared Error

$$\mathcal{L}_{\mathrm{m1}} = \frac{\sum_{j}^{N} \left(\sum_{i}^{m=10} (y_i - y_{i,\mathrm{gt}})^2 \right)}{N} + \lambda \cdot \mathcal{L}_{\mathrm{reg}}, \tag{7.4}$$

as it is a generic loss function for regression problems. $\mathcal{L}_{\mathrm{reg}}$ with $\lambda = 0.1$ is the L^2-regularisation term (Eq. (5.8)), which is included to mitigate overfitting. When predicting the waveform in model 2, an additional term is added to the loss function based on the difference between the original $I_{\mathrm{gt}}(t)$ and the reconstructed current waveform $I(t)$

$$\mathcal{L}_{\mathrm{m2}} = \eta_1 \cdot \frac{\sum_{j}^{N} \left(\sum_{i}^{m=30} (y_i - y_{i,\mathrm{gt}})^2 \right)}{N} + \eta_2 \cdot \frac{\sum_{j}^{N} \left(\sum_{t}^{n_t} (I_t - I_{t,\mathrm{gt}})^2 \right)}{N} + \lambda \cdot \mathcal{L}_{\mathrm{reg}}. \tag{7.5}$$

The custom weights are chosen as $\eta_1 = 750$ and $\eta_2 = 1$ to balance both error contributions.

Table 7.2: Network architecture and training parameters for predicting the hardware parameters from the target waveform (step I).

Operation	Dimensions
Input	30
Dense-1	-
Batch Norm.-1	500
Leaky ReLU-1 (0.01)	500
Dense-2	-
Batch Norm.-2	500
Leaky ReLU-2 (0.01)	500
Dropout-2 (50 %)	500
Dense-3	-
Batch Norm.-3	500
Leaky ReLU-3 (0.01)	500
Dropout-3 (50 %)	500
Dense-4	-
Batch Norm.-4	300
Leaky ReLU-4 (0.01)	300
Dense-5	-
Output	10

- Input: PCs of target waveform
- Output: circuit parameters
- Learning rate: 5×10^{-5}
- Batch size: 400
- Epochs: 500

Table 7.3: Network architecture and training parameters for predicting the current waveform generated by the given hardware parameters (step II).

Operation	Dimensions
Input	10
Dense-1	-
Batch Norm.-1	1000
Leaky ReLU-1 (0.01)	1000
Dense-2	-
Batch Norm.-2	1000
Leaky ReLU-2 (0.01)	1000
Dropout-2 (50 %)	1000
Dense-3	-
Batch Norm.-3	1000
Leaky ReLU-3 (0.01)	1000
Dropout-3 (50 %)	1000
Dense-4	-
Batch Norm.-4	500
Leaky ReLU-4 (0.01)	500
Dense-5	-
Output	30

- Input: circuit parameters
- Output: PCs of predicted waveform
- Learning rate: 5×10^{-5}
- Batch size: 400
- Epochs: 700

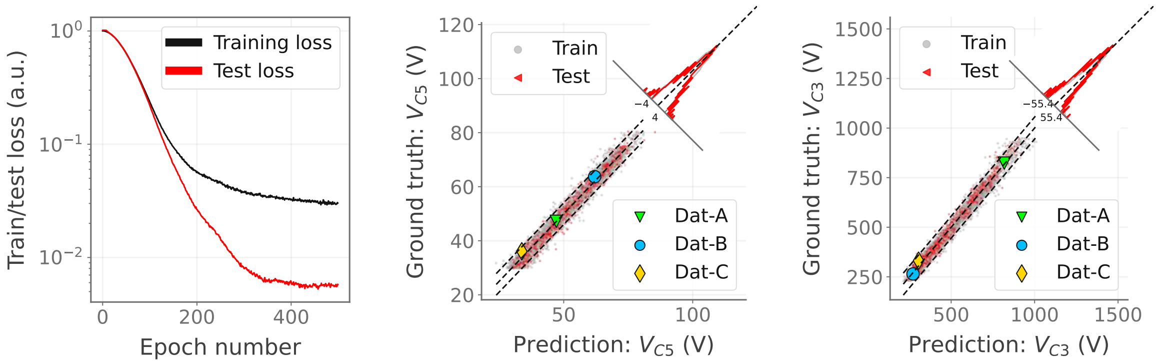

(a) Training (black) and test error (red) per training epoch.

(b) Predicted vs. real charging voltage V_{C5} (*flat-top*, *slope 1* and *2*).

(c) Predicted vs. real charging voltage V_{C3} (*slope 1*).

Figure 7.5: Step I: predicting the hardware parameters from a given current decay. The scatter markers Dat-A to C (green, blue, yellow) indicate selected samples, which are illustrated in Fig. 7.7 as examples. The dashed lines represent ±7 % of the prediction range.

7.4 Results and Discussion

7.4.1 Step I: Predicting the Hardware Parameters

The performance of the inverse model, i.e. predicting the hardware parameters from a given current decay, is displayed in Fig. 7.5. The validation error stagnates after approximately 400 epochs (Fig. 7.5a)[†], with an approximate CPU clock time of 1 s per epoch[‡]. Figures 7.5b and 7.5c illustrate the difference between selected real and predicted output features, i.e. the hardware parameters which are to be determined. The illustrated examples are representative of the remaining features. The residual errors are within ±7 % of the parameter range $(y_{i,\mathrm{gt,max}} - y_{i,\mathrm{gt,min}})$ for all variables i, which is indicated by the black, dashed lines in Figs. 7.5b and 7.5c.

7.4.2 Step II: Predicting the Waveform From Hardware Parameters

Figure 7.6 illustrates the performance of the forward model, i.e. predicting the current decay, which is generated by given hardware parameters. The validation error stagnates after approximately 500 epochs (Fig. 7.6a). The difference between the real and the predicted output variables of the MLP, i.e. the 30 first, standardised PCs, is shown in Fig. 7.6b. As expected, the prediction accuracy is highest for the first PCs, which have the largest impact on reconstructing the waveform. Figure 7.6c displays the reconstructed and the original current decay for the samples, which are indicated by the scatter markers in Figs. 7.5b and 7.5c. The residual errors of the reconstructed

---

[†] The training loss is larger than the validation loss during training due to the regularisation terms and dropout layers, which alter the loss function during training but not validation.

[‡] Estimated using *time.process_time()* of [198].

current decay are for the majority of the cases within ±3 % The reconstruction error is largest at the transition between the individual switching stages (t_0, t_1, t_2, t_3).

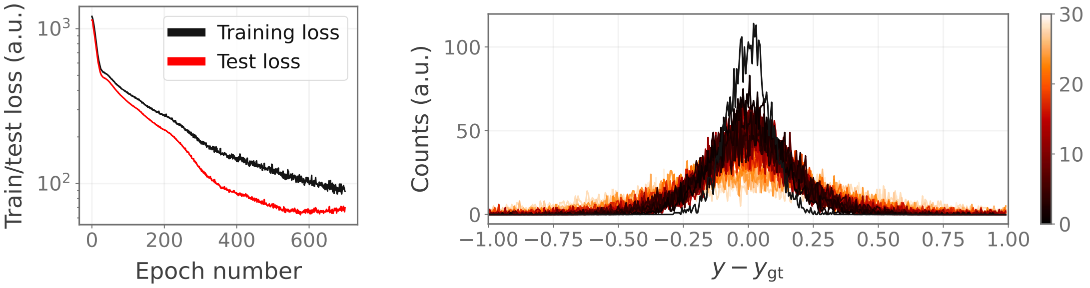

(a) Training (black) and test error (red) per training epoch.

(b) Difference between predicted and real, scaled PCs, colour-coded by the number i of the PC).

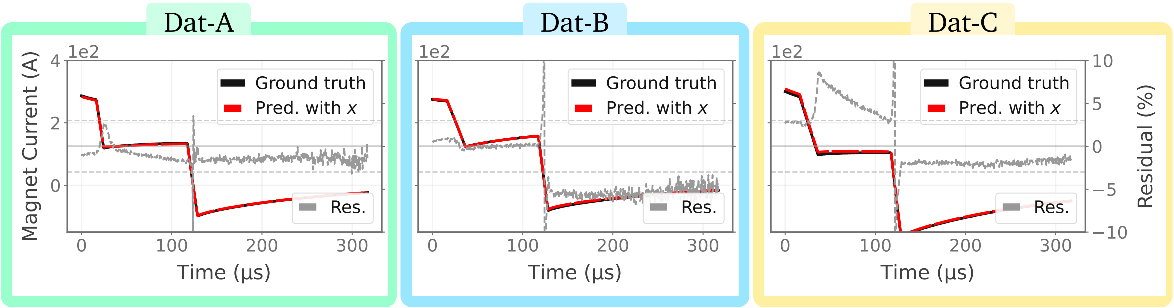

(c) Reconstructed (red) versus original (black) current decays for selected samples (Dat-A to Dat-C). The residuals (grey) are illustrated using the right axis.

Figure 7.6: Step II: predicting the output current produced by given hardware parameters.

7.4.3 Combination of Step I and II: Forward and Inverse Prediction

Finally, step I and II are combined to reconstruct the current decay based on the predicted instead of the measured hardware parameters. The results are illustrated in Fig. 7.7 for the test samples Dat-A to Dat-C. Note that the residuals are illustrated using a different scale than in Fig. 7.6c. For Dat-A (green), the accuracy is similar to predicting the waveform from the original hardware parameters. Dat-B (blue) and Dat-C (yellow) are selected as examples of cases in which the combination of step I and II causes significantly larger errors than predicting the waveform directly from the original hardware parameters. The respective samples are highlighted by scatter markers in Figs. 7.5b and 7.5c. It is evident, that the error for predicting the hardware parameters is the smallest for Dat-A (green), and approaches ±7 % of the parameter (here voltage) range for Dat-B and Dat-C. Reducing the prediction error of Step I will therefore be a key step to increasing the accuracy of such a combined model.

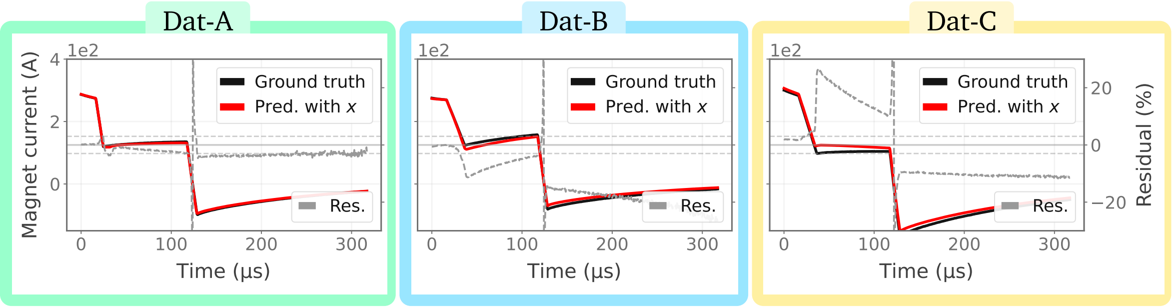

Figure 7.7: Step I+II: predicting the current decay, which is expected from the predicted hardware parameters. Reconstructed (red) versus original (black) current decays for Dat-A to Dat-C. The residuals (grey) are illustrated using the right axis.

7.5 Conclusion and Outlook

First ML models were developed to investigate a generator circuit parameterisation using supervised learning methods. These first approaches target predictions of both the forward (predict dynamical behaviour, i.e. current output) and the inverse problem (predict system parameters, i.e. charging voltages and switching times). Both models apply a PCA to reduce the dimensionality of the current waveform and standard MLPs for the prediction.

The results show, that even such simple models with relatively small data sets allow us to model the system dynamics in both directions. However, the remaining prediction errors are still too large to make this model operationally relevant. Future studies based on these first models will use larger training datasets and aim at systematically investigating techniques to increase the model accuracy, including the preprocessing and scaling steps.

Regarding the ANN itself, including system information via the state-space representation through PINNs is a promising approach. Such networks can be related to modelling the current waveforms using recurrent or long short-term memory neural networks. However, a key challenge for such approaches based on time series will be the correct identification and distinction of the individual stages. The system properties and hence the differential equations change when switching the stages on and off, which depends on the set switching times. Finding a way to automatically map these time intervals to different PINNs and connecting ANN nodes for the time series prediction accordingly is not trivial. The second open challenge is to model the analogue amplifier input voltage, which is required to correct nonlinearities in the output waveform. In addition to applying PINNs, acquiring suitable training data with different amplifier input voltage will be a key aspect of training a respective model. We propose to increase the number of relevant training samples using an optimisation algorithm or reinforcement learning during training data acquisition.

Chapter 8

Conclusion and Outlook

The new PSB H$^-$ charge exchange injection system was commissioned in winter 2020/2021 and is now used to tailor the transverse phase space distributions of the various beam types at CERN. The requirement to flexibly and reliably produce beams over the requested wide range of brightness targets comes at the cost of an increased complexity when defining the suitable injection painting schemes and required hardware settings.

Part I

Part I of this thesis is concerned with defining and optimising the phase space painting schemes, which are required for tailoring the different user-specific beam distributions. Self-consistent space charge simulations of the injection process were performed to study the beam evolution and loss distributions during and after the injection process. Injection painting schemes were proposed based on these simulation studies and implemented during beam commissioning. The experimental results were subsequently used to validate the simulation results and fine-tune the injection configurations, which are now used operationally in the PSB. The beam production studies presented in this thesis focus on three beam types: high-intensity fixed target beams, high-brightness HL-LHC beams and LHC single bunch beams.

Phase space painting is particularly relevant for reducing the losses during the production of high-intensity fixed target beams. Simulations and measurements showed that in 2021 most losses were obtained along the cycle due to the excitation of the transverse tails by betatronic resonances. The minority of the losses were attributed to acceptance limits of the machine. The losses of the operational beams were within the budgets of $< 1\,\%$ during the injection process (aperture bottlenecks) and $< 5\text{-}10\,\%$ along the cycle (resonances).

It was experimentally demonstrated that the chosen transverse painting schemes affected both the losses along the cycle and during the injection process, causing variations in the total loss rate from 2 to $> 15\%$ in operation. The proposed optimised painting functions for a given working point aimed not only at reducing the incoherent tune spread and fitting the beam into the machine acceptance but also at compromising the interaction of the tune spread core and tails with strong resonances. The results showed that aiming at painting-driven emittance growth in both planes was not beneficial. The increased number of particles with large transverse actions and hence smaller detuning increased the loss rates due to excitation by betatronic resonances during the tune ramp. The losses could be minimised when targeting the transition from space charge to the painting-driven emittance growth in the horizontal while injecting on-axis in the vertical plane.

Thoroughly benchmarking the simulation results with measurements goes beyond the commissioning period. The results presented in this thesis motivate studies in several aspects (e.g. deconvoluting the horizontal betatronic and dispersive beam size, correcting the measurements for wire-scattering induced emittance growth or facilitating beam size measurements shortly after injection). Solving these issues will impact the quality of the measurement results and make phase space painting in the PSB an exciting field for beam physics research in the coming years.

In 2021, LHC beams were injected into the PSB without painting, i.e. on-axis. The respective injection studies focused on assessing the beam degradation due to injection imprecisions, such as foil scattering or steering errors. The impact of steering errors on emittance growth and halo formation for different intensities along the LHC brightness curve was estimated in simulations and measurements. It was shown, that LHC beams with operational intensities (HL-LHC with $N_{\mathrm{p+}} = 3.53 \times 10^{12}$ p+/bunch and BCMS with $N_{\mathrm{p+}} = 1.72 \times 10^{12}$ p+/bunch) were not disturbed significantly by steering errors of $\Delta x, y \lessapprox 2\,\mathrm{mm}$. Additionally, the installed stripping foils were assessed concerning emittance growth due to multiple Coulomb scattering. As all foils were within specifications, producing an emittance growth as anticipated from simulations. Consequently, no significant scattering-induced beam degradation is expected for the high-brightness LHC-type beam production.

A new injection scheme was proposed for producing LHC single bunch beams: the requested transverse beam sizes and Gaussian profiles could be tailored using a combination of emittance growth due to foil scattering and steering offsets. It was demonstrated in both simulations and measurements that it was possible to flexibly fine-tune the requested transverse emittance range without generating significant tails by adjusting the steering offset and the number of foil crossings. The stochastic nature of the foil scattering-induced emittance growth yields beam profiles close to a Gaussian distribution in the transverse plane, also for non-Gaussian input distributions.

Part II

The proposed painting functions for the various users are sensitive to changes in the operational conditions or user requests. Finding solutions to efficiently and reliably adapt the injection settings and the related hardware parameters based on pulse-per-pulse beam instrumentation feedback will push the operational performance of the PSB in the coming years. Part II therefore investigates automation methods to increase the efficiency, reliability and stability of the new injection system.

One promising approach for increasing operational efficiency is to automate the injection painting set-up using derivative-free numerical optimisation algorithms. A respective framework was developed and applied for tailoring the high-intensity fixed target beam distributions. The first tests successfully demonstrated the feasibility but also identified the challenges, which must be overcome to make such a system operationally applicable. The objective function features a high noise level, a flat minimum and is expensive to evaluate. Conducting systematic tests with different algorithms on the machine to address these issues is infeasible because of limited beam time and machine drifts in when measuring over multiple days. Therefore, a supervised machine learning algorithm was used to train a data-driven surrogate model. This model allowed tuning the optimiser's hyperparameters and performing systematic studies offline without needing physical resources like beam time. The random forest regressor proved to be a robust method for creating such a model and is recommended to be applied for similar applications. The surrogate model was used to compare the performance of several derivative-free algorithms. The results showed that choosing appropriate noise reduction strategies and resampling rates is specific for each solver and crucial for maximising efficiency. Out of the tested algorithms, acceptable optimisation reliability, accuracy and efficiency were obtained with the solvers pyBOBYQA (with extension for noisy applications), adaptive Nelder Mead and the surrogate-based optimiser pySOT. With these solvers, optimising the injection painting based on beam instrumentation feedback is feasible within several tens to a few hundred function evaluations (PSB cycles), also when allowing the variation of all 5 injection painting parameters. Even higher efficiency can be achieved when only optimising a subset of the painting settings. The results presented in this thesis and the developed surrogate model can be used to assess the feasibility of implementing a model-free controller, such as reinforcement learning or extremum-seeking controllers. This would allow maintaining the objective minimum, which was previously found using the numerical optimisation algorithm, instead of going through the entire optimisation process again.

The custom magnet current decays for phase space painting are generated by a complex pulse generator. The magnet current is controlled by programming numerous input parameters, such as capacitor loading voltages, IGBT switch times and amplifier input voltages. All parameters have a nonlinear effect on the magnet current, which makes the generator control using an analytical description of the full electronic circuit complicated. A proportional and derivative feedback loop is therefore used in operation to provide current waveforms with the required precision. This thesis investigates the feasibility of using a control based on a supervised learning model as an alternative to the control based on a feedback loop. Using a simplified generator configuration for these first tests, it was demonstrated that multilayer perceptrons were able to replicate the dynamics in both directions, i.e predicting the hardware parameters to generate a specific output current and vice versa. The presented models did not achieve the prediction accuracy required for operational application but are a foundation for further improvement using advanced deep learning techniques (e.g. physics-guided or informed neural networks or time series prediction). A promising factor for creating more accurate and reliable models in future studies is that a large amount of training data is easily obtainable by pulsing the generator with different input parameters. However, whereas such datasets contain many samples with general parameters, they lack data points with the operational target parameterisation. This problem can be overcome in the future by using an optimisation algorithm or reinforcement learning when acquiring the training data.

Overall, the beam dynamics studies presented in this thesis were a crucial contribution to efficiently configure the machine during beam commissioning. The proposed injection schemes were a key aspect for reliably producing beams with the user-specific brightness targets already during the first operational year of the upgraded PSB. Furthermore, the presented results are a basis for pushing the beam performance in the coming years, such as the intensity of the high-intensity fixed target beams. The studies on automating the injection painting set-up will be an important foundation for increasing the operational efficiency of the PSB. Lastly, the feasibility tests for using neural networks to model and control complex electronic circuits, such as the painting kicker generator, lay the foundation for developing a generic way to solve similar tasks using machine learning techniques in the future.

Appendices

APPENDIX A

Transverse Beam Dynamics

A.1 Hamiltonian Formalism in Particle Accelerators

The Lagrange and Hamiltonian formalisms are powerful concepts introduced in classical mechanics, which simplify the formulation of the equations of motions for dynamic systems with constraints, e.g. the thread of a pendulum or the external fields in a particle accelerator. General background on Hamiltonian mechanics can be found in various textbooks, such as [199, Chp. 7]. The Hamiltonian description of accelerator physics is described e.g. in [55, Chp. 2],[49, Chp. 2.1] or [50, Chp.4.4]

The Hamiltonian of a relativistic charged particle with charge e in an electromagnetic field is

$$H\left(x, P_x, y, P_y, s, P_s; t\right) = \sqrt{c^2\left(\mathbf{P} - \frac{e}{c}\mathbf{A}\right)^2 + m_0^2 c^4} + e\Phi. \tag{A.1}$$

Here, $\mathbf{\Phi}$ is the electric potential and $\mathbf{A}$ the magnetic vector potential.

$$\mathbf{P} = m\mathbf{v} + e\mathbf{A} = \boldsymbol{\beta}_{\mathrm{r}}\gamma_{\mathrm{r}} m_0 c + e\mathbf{A} \tag{A.2}$$

is the canonical momentum, which differs from the mechanical momentum $m \cdot \mathbf{v}$.

For the application in particle accelerators, several transformations are applied to this Hamiltonian, as outlined in detail in [55, Chp. 2]:

- **Change independent variable from t to s:** For the description of the beam transport in a particle accelerator it is useful to transform Eq. (A.1) to a Hamiltonian, in which the longitudinal distance s is the independent variable and t the third coordinate, particularly when the guiding fields (cavities, magnets) are periodic functions of s.

- **Transformation to the Frenet-Serret coordinate system,** i.e. the coordinate system moving with the reference particle (see Section 1.1).

- **Expression by the longitudinal coordinate pair $\tilde{\delta}$ and z:** A canonical transformation allows describing the particle by the longitudinal coordinates

$$z = s/\beta_{\mathrm{r}} - ct, \tag{A.3}$$

i.e. the longitudinal difference of a particle position relative to the reference particle, and

$$\widetilde{\delta} = \frac{E}{cP_0} - \frac{1}{\beta_\mathrm{r}} \tag{A.4}$$

,

i.e. the respective energy deviation. The resulting generalised coordinate and momenta pairs are (x, p_x), (y, p_y) and $(z, \widetilde{\delta})$

- **Scaling with reference momentum and paraxial approximation:** The Hamiltonian is often additionally scaled with the reference momentum p_0. This simplifies the approximation by Taylor series expansion for particles with small deviations from the reference particle (paraxial approximation). The scaled canonical momenta, Hamiltonian and vector potentials are

$$\begin{aligned} \widetilde{H}_s &= H_s/p_0 \\ \mathbf{a} &= e/p_0 \cdot \mathbf{A} \\ \widetilde{p}_x &= \frac{P_x}{p_0} = \frac{\beta_{x,\mathrm{r}}\gamma_\mathrm{r} mc + eA_x}{p_0}. \end{aligned} \tag{A.5}$$

The resulting Hamiltonian to describe the movement of a relativistic, charged particle in electromagnetic fields relative to the reference trajectory in the Frenet-Serret coordinate system is

$$\begin{aligned} &\widetilde{H}_{s,\delta}\left(x, \widetilde{p}_x, y, \widetilde{p}_y, z, \widetilde{\delta}; s\right) = -p_s = \\ &\frac{\widetilde{\delta}}{\beta_\mathrm{r}} - \left(1 + \frac{x}{\rho}\right)\sqrt{\left(\widetilde{\delta} + \frac{1}{\beta_\mathrm{r}} - \frac{e\Phi}{cp_0}\right)^2 - (\widetilde{p}_x - a_x)^2 - (\widetilde{p}_y - a_y)^2 - \frac{1}{\beta_\mathrm{r}^2\gamma_\mathrm{r}^2}} - \left(1 + \frac{x}{\rho}\right) a_s. \end{aligned} \tag{A.6}$$

The conjugate coordinate pairs $(x, \widetilde{p}_x)$, $(y, \widetilde{p}_y)$ and $(z, \widetilde{\delta})$ are transformable to the commonly used pairs (x, x'), (y, y') and (z, δ). When applying Hamilton's equations

$$\begin{aligned} \dot{q}_i &= \frac{\partial H}{\partial p_i} \\ -\dot{p}_i &= \frac{\partial H}{\partial q_i}, \end{aligned} \tag{A.7}$$

to this Hamiltonian, one obtains the respective equations of motion. q and p are the respective conjugate coordinates.

A.1.1 Paraxial Approximation, Action-Angle Coordinates and Floquet Transform

The resulting equations of motion are generally nonlinear - even in drift spaces. Nevertheless, the equations can be simplified given that the transverse momenta are usually much smaller than the total momentum p_0 and hence $\widetilde{p}_u \ll 1$. For drifts, dipoles and quadrupoles, this *paraxial approximation* can be used to derive equations of motion, which are linear in the canonical variables. However, rather than linearising the equations of motion obtained from the Hamiltonian Eq. (A.6), the Hamiltonian (Eq. (A.6)) itself is expanded up to second order in all dynamical variables. The linearised equations of motions are subsequently directly obtained when applying Hamilton's equations to this approximated Hamiltonian. Derivations of such approximated Hamiltonians for several elements can be found in [55, Chp. 3]. The Hamiltonians for a drift space, a dipole and a quadrupole are

$$\begin{aligned}
\widetilde{H}_{\text{Drift}} &\approx \frac{1}{2}\widetilde{p}_x^2 + \frac{1}{2}\widetilde{p}_y^2 + \frac{\widetilde{\delta}^2}{2\beta_\text{r}^2\gamma_\text{r}^2} + \mathcal{O}(3) \\
\widetilde{H}_{\text{Dip}} &\approx \frac{1}{2}\widetilde{p}_x^2 + \frac{1}{2}\widetilde{p}_y^2 + \frac{x^2}{2\rho^2} - \frac{1}{\beta_\text{r}\rho}x\widetilde{\delta} + \frac{\widetilde{\delta}^2}{2\beta_\text{r}^2\gamma_\text{r}^2} + \mathcal{O}(3) \qquad \text{(A.8)} \\
\widetilde{H}_{\text{Quad}} &\approx \frac{1}{2}\left(\widetilde{p}_x^2 + \widetilde{p}_y^2 + k_1\left(x^2 - y^2\right) + \frac{\widetilde{\delta}^2}{\beta_\text{r}^2\gamma_\text{r}^2}\right) + \mathcal{O}(3).
\end{aligned}$$

These expressions are derived using the magnetic rigidity Eq. (1.10) as well as the definition of normalised multipole strengths k_i from Eq. (1.11). For sextupoles and higher-order multipole fields, higher-order terms need to be considered in the Hamiltonian, which yields nonlinear equations of motion.

Disregarding the term describing the longitudinal motion as well as the coupling of transverse and longitudinal motion, one can write the two-dimensional Hamiltonian for the linear, transverse betatron motion in general form as [49, Chp. 2.4]

$$\tilde{H}_{\text{Lin}} \approx \frac{1}{2}\left(\widetilde{p}_x^2 + \widetilde{p}_y^2 + K_x(s)x^2 + K_y(s)y^2\right), \qquad \text{(A.9)}$$

with the focusing strengths $K_{x,y}(s)$.

The fact that linear motion describes a circle in normalised phase space (see Section 1.2.8) motivates a canonical transformation from Cartesian coordinates $(\bar{x}, \bar{x}')$ to radial coordinates, so-called action-angle coordinates (J, Φ) (see [49, Chp. 2.4]) The transformed linear Hamiltonian of the transverse motion in one plane is

$$H(J, \Phi, s) = \frac{J}{\beta(s)}. \qquad \text{(A.10)}$$

$H(J, \Phi, s)$ is independent of $\Phi(s)$ for linear motion and therefore the action $J(s) = \text{const.}$ a constant of motion. However, the Hamiltonian and the phase $\Phi(s)$ still depend on s. The Hamiltonian is hence not a constant of motion itself. A transformation for solving this problem is the *Floquet transform* (see e.g. [200, Chp. 3.2] or [49, Chp. 2.4]). In short, one conducts a canonical transformation to change the independent variable from s to the orbiting angle $\Theta = s/R$ with the average accelerator radius R. This transformation is particularly useful as the transformed linear Hamiltonian

$$\bar{H} = Q \cdot J = \text{const.} \qquad \text{(A.11)}$$

becomes a constant, with the orbital angle Θ as the new independent variable. This yields a periodicity in the phase coordinate Θ, which becomes useful as it facilitates the decomposition of higher-order terms and field errors into a Fourier series.

A.1.2 The Perturbed Hamiltonian

Nonlinear fields, field and alignment errors are generally small compared to the main linear guiding and focusing fields. [201] explains in detail, how such imperfections and deviations from the linear motion can be included as perturbation terms H_1 in the Hamiltonian

$$H = H_0 + H_1 = Q_x J_x + Q_y J_y + H_1, \tag{A.12}$$

with H_0 being the unperturbed Hamiltonian of the linear motion. The perturbation term can be expressed as a series of polynomials in x, p_x, y and p_y

$$H_1(x, p_x, y, p_y; \Theta) = \sum_N \sum_{\substack{J,K,L,M=0 \\ J+K+L+M=N}}^{N} b^{(N)}_{J,K,L,M}(\Theta) \cdot x^J p_x^K y^L p_y^M, \tag{A.13}$$

which can be written using the Floquet transform as

$$H_1(J_x, J_y, \Phi_x, \Phi_y; \Theta) = \sum_N \sum_N \sum_{\substack{j,k,l,m=0 \\ j+k+l+m=N}}^{N} h^{(N)}_{jklm}(\Theta) J_x^{(j+k)/2} J_y^{(l+m)/2} e^{i\left[(j-k)Q_x+(l-m)Q_y\right]\Theta}. \tag{A.14}$$

Developing the coefficients $h^{(N)}_{jklm}(\Theta)$, which contain the information of the perturbing potential, into a Fourier series yields

$$H_1 = \sum_N \sum_N \sum_{\substack{j,k,l,m=0 \\ j+k+l+m=N}}^{N} \sum_{-q}^{q} h^{(N)}_{jklmq} J_x^{(j+k)/2} J_y^{(l+m)/2} \cdot e^{i\left[(j-k)Q_x+(l-m)Q_y+q\right]\Theta}. \tag{A.15}$$

Assuming that the actions J_x and J_y only change little during one oscillation, one neglects high-frequency terms as mainly low-frequency terms

$$(j-k)Q_x + (l-m)Q_y + q \longrightarrow 0 \tag{A.16}$$

perturb the particle motion. Introducing the integers $\pm n_x = j - k$, $\pm n_y = l - m$ and $p = \pm q > 0$, one obtains the resonance condition

$$n_x Q_x + n_y Q_y = p \tag{A.17}$$

which is interpreted in Section 1.2.12.

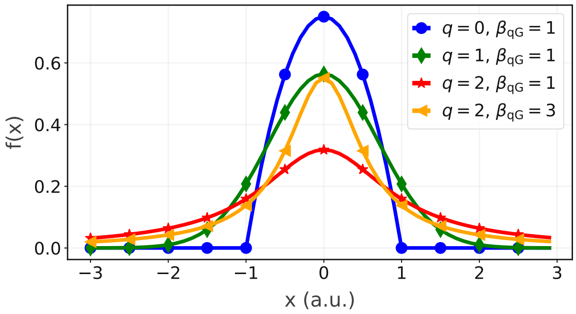

Figure A.1: Q-Gaussian distributions with different parameters.

A.2 Q-Gaussian Distribution

The q-Gaussian distribution is given by the probability density

$$f(x) = \frac{\sqrt{\beta_{qG}}}{C_q} e_q\left(-\beta_{qG} \cdot x^2\right), \tag{A.18}$$

based on the q-exponential function

$$e_q(x) = \begin{cases} \exp(x) & , \text{for} \quad q = 1 \\ (1 + (1-q) \cdot x)^{1/(1-q)} & , \text{for} \quad q \neq 1 \text{ and } (1 + (1-q) \cdot x) > 0 \\ 0 & , \text{for} \quad q \neq 1 \text{ and } (1 + (1-q) \cdot x) \leq 0 \end{cases} \tag{A.19}$$

and the normalisation factor

$$C_q = \begin{cases} \frac{2\sqrt{\pi}}{(3-q)\sqrt{1-q}} \frac{\Gamma\left(\frac{1}{(1-q)}\right)}{\Gamma\left(\frac{3-q}{2(1-q)}\right)} & , \text{for} \quad -\infty < q < 1 \\ \sqrt{\pi} & , \text{for} \quad q = 1 \\ \sqrt{\frac{\pi}{q-1}} \frac{\Gamma\left(\frac{3-q}{2(q-1)}\right)}{\Gamma\left(\frac{1}{(q-1)}\right)} & , \text{for} \quad 1 < q < 3 \end{cases} . \tag{A.20}$$

The tails are characterised by the single parameter q, with $q = 1$ for a Gaussian distribution, $q > 1$ for over- and $q < 1$ for underpopulated tails. For a given q-factor, $\beta_{qG} > 0$ defines the maximum amplitude of the distribution. The standard deviation can be computed for limited ranges as

$$\sigma_{qG} = \begin{cases} \frac{1}{\sqrt{\beta_{qG} \cdot (5-3q)}} & , \text{for} \quad q < 5/3 \\ \infty & , \text{for} \quad 5/3 \leq q < 2 \\ \text{undefined} & , \text{for} \quad 1 < q < 3 \end{cases} \tag{A.21}$$

APPENDIX B

Supplementary Materials: Beam Measurements

B.1 Machine Configurations

B.1.1 KSW Reference Amplitude and Steering of the Injected Beam

In preparation for all measurements, the injected beam is steered to the nominal position at the foil using the BTV installed in the injection region. This corresponds to an expected offset of $x_{\mathrm{on-axis}} = -81$ mm, with simulated KSW and BSW contributions of $x_{\mathrm{KSW}} = -35$ mm and $x_{\mathrm{BSW}} = -46$ mm, respectively. Subsequently, the injection oscillations are minimised by adapting the KSW amplitude and the angle of the injected beam. The KSW amplitudes, which are required to minimise the injection oscillations are referred to as *on-axis* amplitudes $A_{0,\mathrm{on-axis}}$. For the machine configurations in 2021, these amplitudes differed up to 2 mm from the modelled $A_{0,\mathrm{on-axis}} = 35$ mm, as listed in Table B.1. The difference can be explained by various machine imperfections (closed orbit errors, alignment errors of the injection region, rotational alignment errors of KSW, calibration errors or KSW kicks and quadrupole focusing strengths in P1 and P16). In the experimental results presented in this thesis, $A_{0,\mathrm{on-axis}}$ mm is considered to correspond to $A_0 = 35$ mm in simulations and referenced accordingly. Table B.1 further lists the requested and measured KSW currents. All acquired currents at flat-top are within the specified accuracy of ±1%.

B.1.2 Longitudinal Settings

Figure B.1 illustrates the programmed RF voltage of the first (pink) and second harmonic (yellow) for the ISOLDE, LHC and INDIV beams. The longitudinal phase space can be reconstructed from measurements using longitudinal tomography [134]. Figure B.2 shows the longitudinal phase space for different users, which is reconstructed at the cycle times of the wire scan measurements.

Table B.1: KSW configurations in the measurement campaigns: KSW amplitudes A_0(on-axis) and related currents I_{KSW}, which are required to minimise injection oscillations when steering the injected beam to the reference position at the stripping foil ($x_{\mathrm{Foil}} = -81$ mm). The set WP is $Q_x/Q_y = 4.22/4.36$. The measured WP is $Q_x/Q_y = 4.22/4.39$, as the β-beating induced by the BSW is not corrected.

Ring	**A_0 on-axis (mm)**	**I_{KSW}; set (A) 1L4, 2L1, 16L1, 16L4**	**I_{KSW}; meas. (A) 1L4, 2L1, 16L1, 16L4**
1	35.4	37.9, 324.3, 370.2, 27.7	38.0, 323.9, 369.6, 27.6
2	34.5	37.0, 316.0, 360.8, 27.0	37.0, 315.5, 360.6, 27.0
3	33.8	36.2, 309.6, 353.5, 26.5	36.2, 308.1, 350.7, 26.2
4	33.1	35.5, 303.2, 346.2, 25.9	35.6, 302.2, 346.4, 25.9

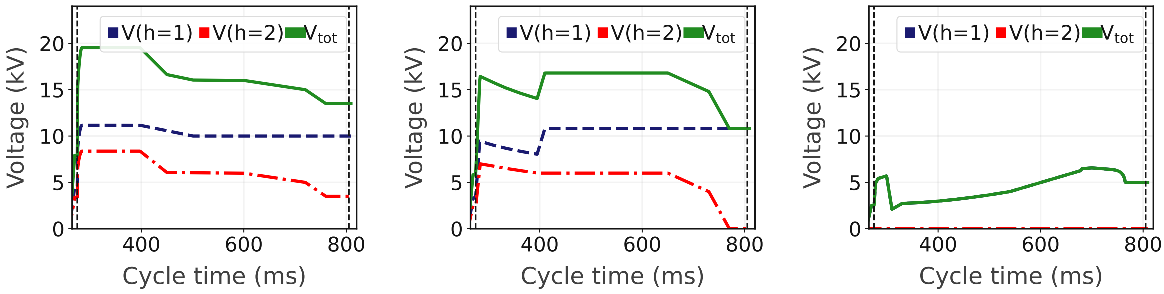

(a) ISOLDE

(b) LHC

(c) LHCINDIV

Figure B.1: PSB voltage programs for ISOLDE, LHC and INDIV beams in 2021.

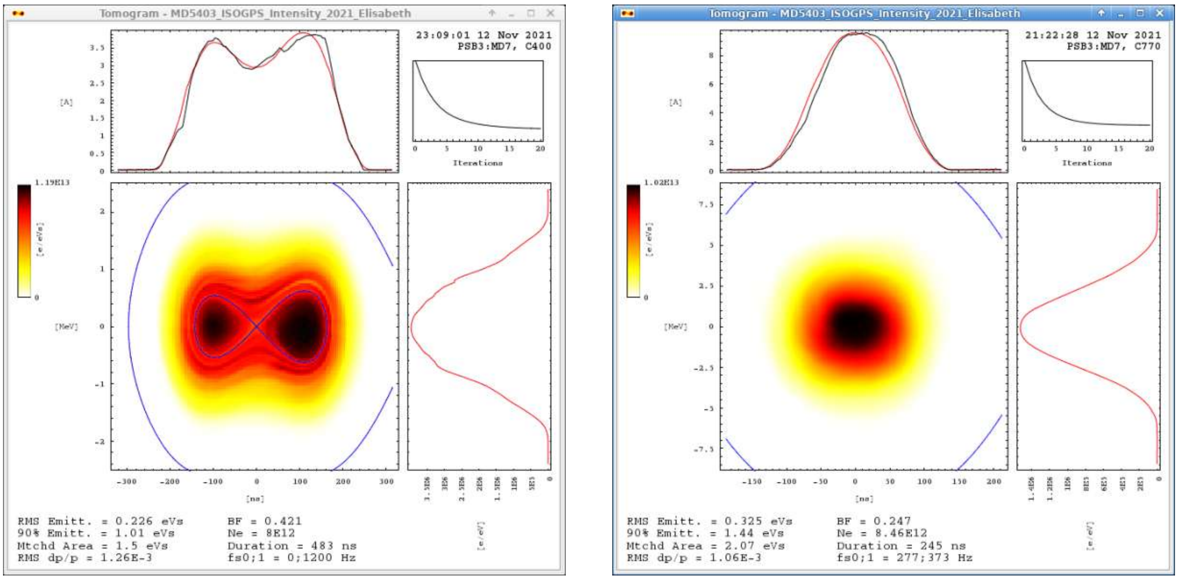

```
RMS Emitt. = 0.226 eVs          BF = 0.421
90% Emitt. = 1.01 eVs           Ne = 8E12
Mtchd Area = 1.5 eVs            Duration = 483 ns
RMS dp/p = 1.26E-3              fs0;1 = 0;1200 Hz
```

(a) ISOLDE, C400 (beginning of cycle)

```
RMS Emitt. = 0.325 eVs          BF = 0.247
90% Emitt. = 1.44 eVs           Ne = 8.46E12
Mtchd Area = 2.07 eVs           Duration = 245 ns
RMS dp/p = 1.06E-3              fs0;1 = 277;373 Hz
```

(b) ISOLDE, C770 (end of cycle)

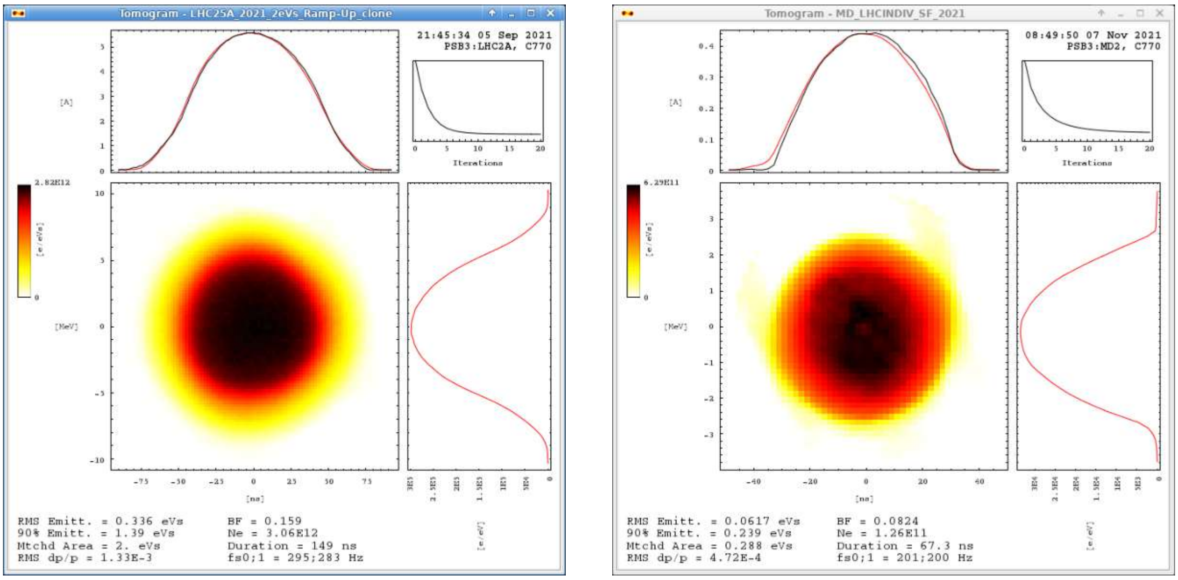

```
RMS Emitt. = 0.336 eVs          BF = 0.159
90% Emitt. = 1.39 eVs           Ne = 3.06E12
Mtchd Area = 2. eVs             Duration = 149 ns
RMS dp/p = 1.33E-3              fs0;1 = 295;283 Hz
```

(c) LHC, C770 (end of cycle)

```
RMS Emitt. = 0.0617 eVs         BF = 0.0824
90% Emitt. = 0.239 eVs          Ne = 1.26E11
Mtchd Area = 0.288 eVs          Duration = 67.3 ns
RMS dp/p = 4.72E-4              fs0;1 = 201;200 Hz
```

(d) INDIV, C770 (end of cycle)

Figure B.2: Tomographic reconstruction of the longitudinal phase space at the cycle times, at which the ISOLDE, LHC and LHCINDIV profile measurements are performed.

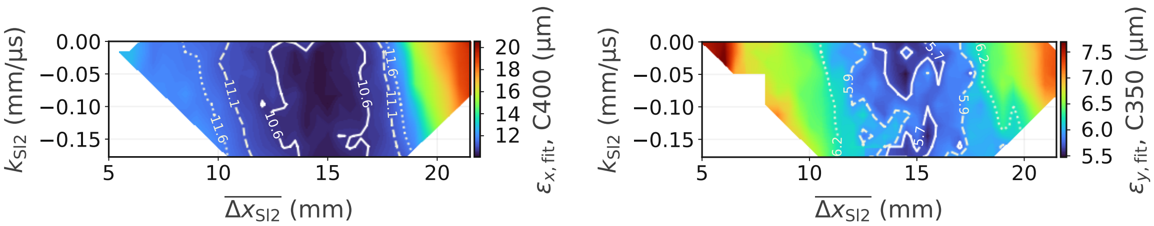

(a) Horiz. emittance (fit), C400

(b) Vert. emittance (fit), C350

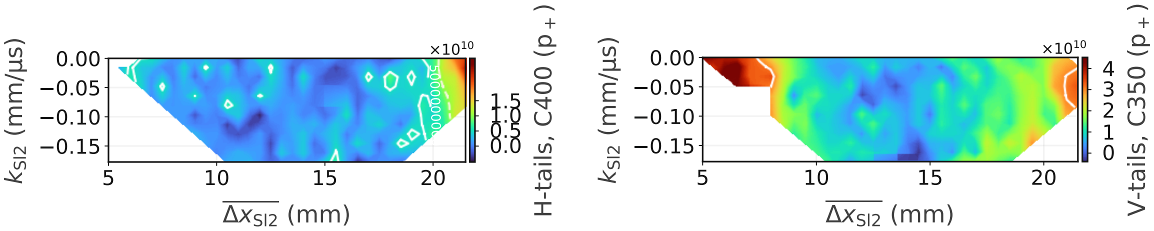

(c) Tail population with $x > x_{\text{thres}}$, C400

(d) Tail population with $y > y_{\text{thres}}$, C350

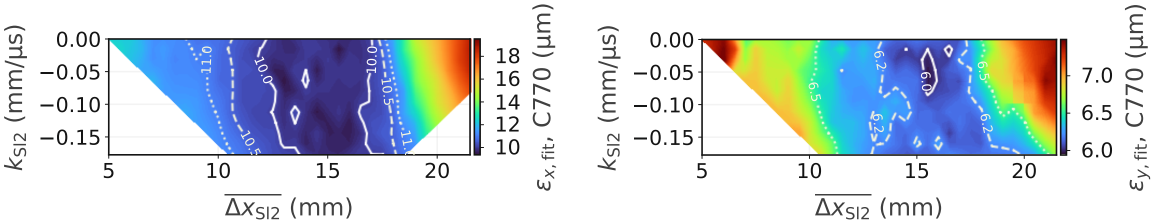

(e) Horiz. emittance (fit), C770

(f) Vert. emittance (fit), C770

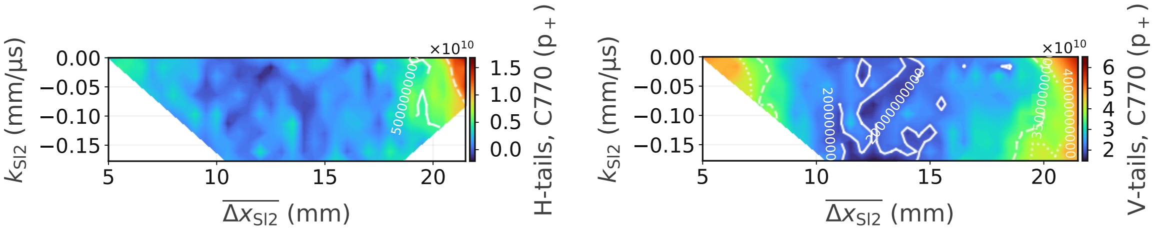

(g) Tail population with $x > x_{\text{thres}}$, C770

(h) Tail population with $y > y_{\text{thres}}$, C770

Figure B.3: Overview of various intensity and profile measurements when producing ISOLDE beams with different horizontal paintings (vertical on-axis injection, *Scan 2*).

B.2 High-Intensity Beam Painting Measurements

Figures B.3 and B.4 complement the in Section 4.3.5 presented results by illustrating the response of various beam loss, intensity and profile measurements to horizontal painting variations (Scan 2, Table 4.5). These measurements are the basis for the results presented in Figs. 4.21 to 4.23.

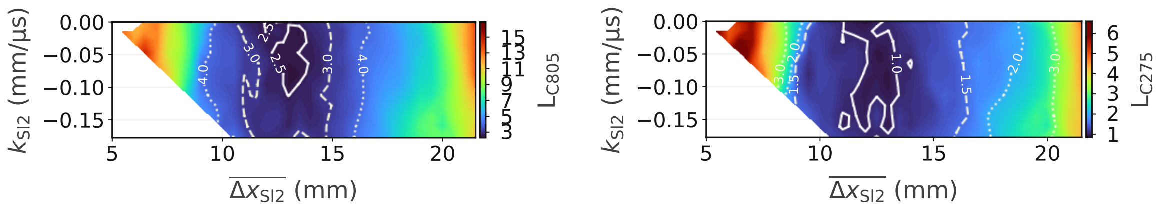

(a) Losses: injection and full cycle **(b)** Losses: injection and first ms

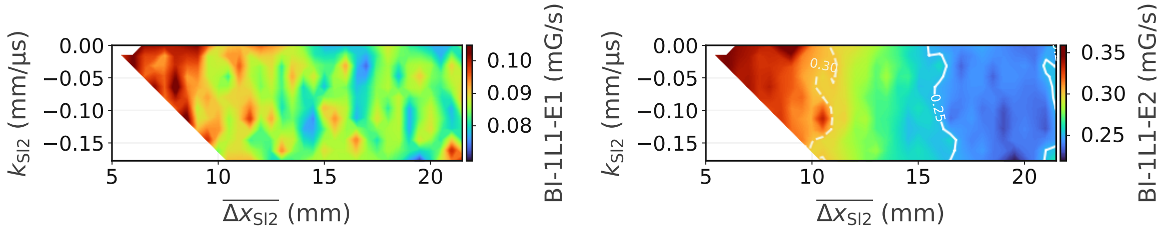

(c) Dose rate BI-BLM-1L1.E1 **(d)** Dose rate BI-BLM-1L1.E2

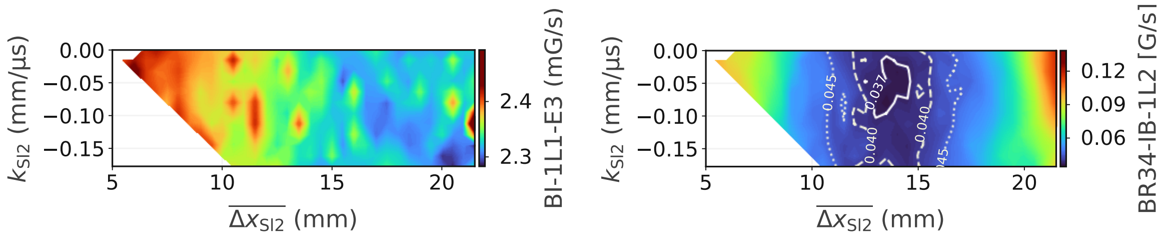

(e) Dose rate BI-BLM-1L1.E3 **(f)** Dose rate BR-BLM-1L2

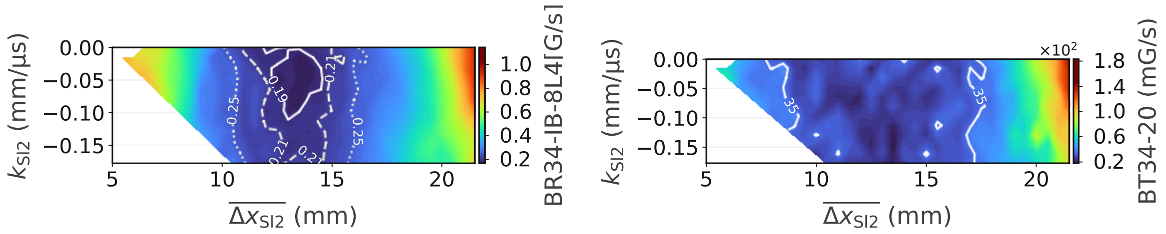

(g) Dose rate BR-BLM-8L4 **(h)** Dose rate BT-BLM-20

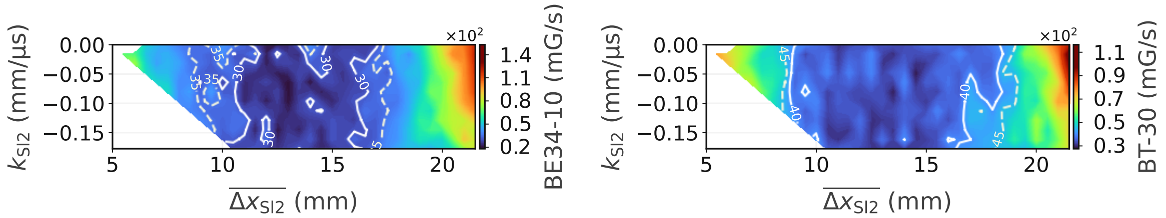

(i) Dose rate BE-BLM-10 **(j)** Dose rate BT-BLM-30

Figure B.4: Overview of various loss measurements when producing ISOLDE beams with different horizontal paintings (vertical on-axis injection, *Scan 2*).

Appendix C

Supplementary Materials: Injection Painting using Numerical Optimisers

C.1 Operational Constraints

Table C.1 summarises the bounds and constraints, which have to be respected when applying numerical algorithms to automate the injection painting optimisation for ISOLDE beams. The bounds and constraints are determined by operational or hardware limits.

Table C.1: Phase space painting with numerical optimisation algorithms: feature constraints as determined by operational (OP) and hardware limits (HW).

Features and constraints		Unit	Lower bound		Upper bound	
			Op.	Hw.	Op.	Hw.
Feature bounds (algorithm)						
A_0		mm	24	-	37	41[**]
A_1		mm	16	-	34	-
t_1		µs	6	5	30	30
k_{Sl2}		mm/µs	-0.178	-0.18	0	0
Δy		mm	-2	d.o.s[*]	7	d.o.s[*]
Additional constraints (penalty term)						
$(A_1/A_0)_{\mathrm{min}}$	$A_1 > (A_1/A_0)_{\mathrm{min}} \cdot A_0$	-	0.4	0.3	0.98	0.99
$k_{\mathrm{Sl1,max}}$	$A_1 > A_0 + k_{\mathrm{Sl1,max}} \cdot t_1$	mm/µs	-2.18	-2.2		
A_2		mm	0	0	A_1	A_1

[*] Depends on the reference steering of the injection beam.
[**] Depends on the WP.

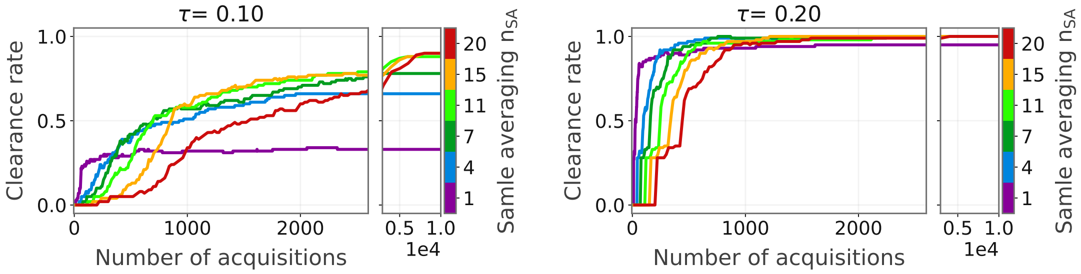

(a) pyBOBYQA with re-start ($\rho_{\text{beg}} = 0.5$)

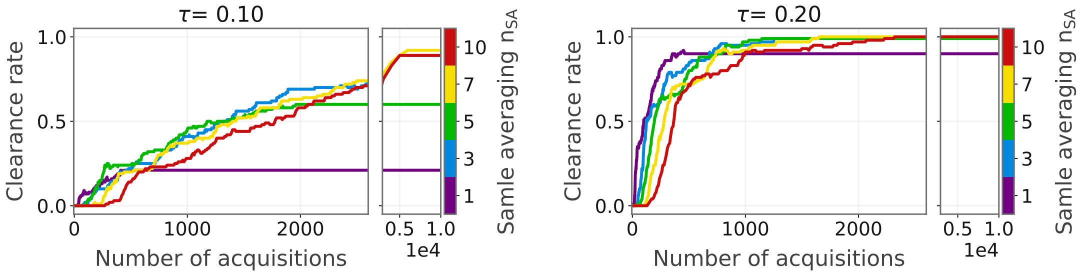

(b) pySOT (Radial Basis Function surrogate and DYCORS sampling strategy)

Figure C.1: Performance of different global optimisation algorithms on the surrogate model: sensitivity to statistical resampling rates.

C.2 Sensitivity to Noise Levels and Statistical Resampling Rates

Figures C.1 and C.2 complement the in Section 6.5 presented results by illustrating the data profiles for the different algorithms with varying resampling rates and hence effective noise levels. The *AUC* of these data profiles is summarised in Fig. 6.7b.

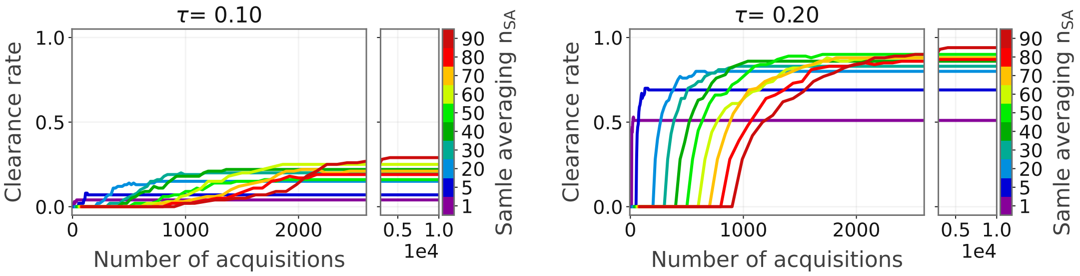

(a) pyBOBYQA ($\rho_{\text{beg}} = 0.5$)

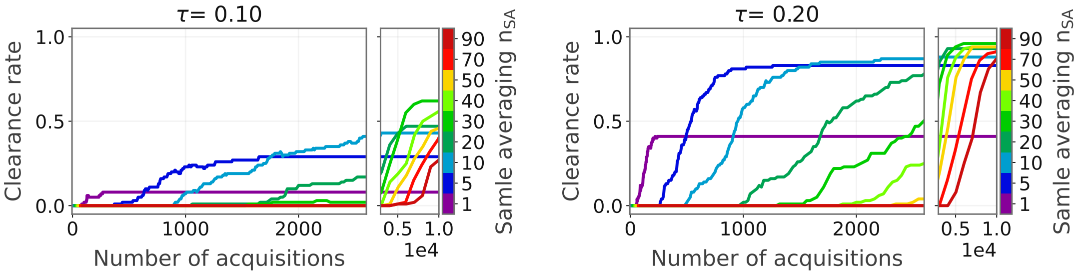

(b) Powell's Method

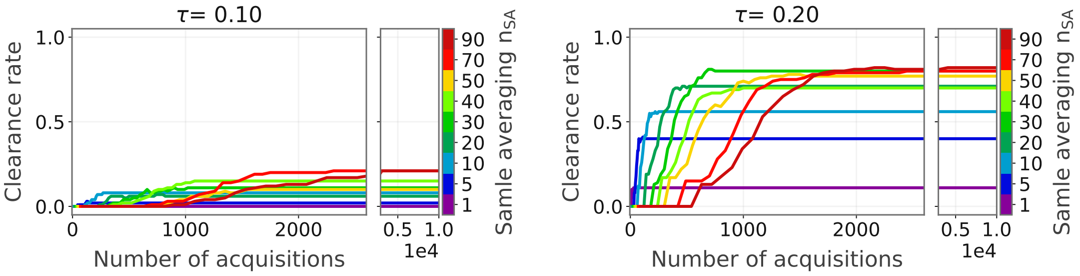

(c) COBYLA ($\rho_{\text{beg}} = 0.5$)

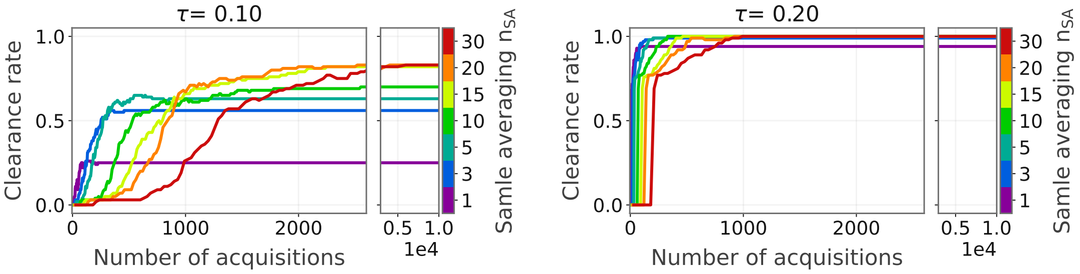

(d) Adaptive Nelder-Mead

Figure C.2: Performance of different local optimisation algorithms on the surrogate model: sensitivity to statistical resampling rates.

Bibliography

[1] B. Jonson and K. Riisager, "The ISOLDE facility," *Scholarpedia*, vol. 5, no. 7, p. 9742, 2010, revision #90796, DOI: `10.4249/scholarpedia.9742`.

[2] E. Chiaveri *et al.*, "Status and perspectives of the neutron time-of-flight facility n_TOF at CERN," *EPJ Web Conf.*, vol. 239, 2020, DOI: `10.1051/epjconf/202023917001`.

[3] L. Durieu, O. Ferrando, J.-Y. Hemery, J.-P. Riunaud, and B. Williams, "The CERN PS east area in the LHC era," in *Proc. 1997 Particle Accelerator Conference (PAC'97)*, vol. 1, 1997, pp. 228–230, DOI: `10.1109/PAC.1997.749601`.

[4] D. Banerjee *et al.*, "The North Experimental Area at the Cern Super Proton Synchrotron," 2021, [Online]. Available: `https://cds.cern.ch/record/2774716` (visited on 04/30/2022).

[5] S. Maury, "The Antiproton Decelerator (AD)," CERN, Geneva, Tech. Rep. CERN-PS-99-050-HP, 1999, [Online]. Available: `https://cds.cern.ch/record/405621` (visited on 04/30/2022).

[6] E. Mobs, *The CERN accelerator complex - 2019. Complexe des accélérateurs du CERN - 2019*, General Photo, Jul. 2019, [Online]. Available: `https://cds.cern.ch/record/2684277` (visited on 04/30/2022).

[7] CMS Collaboration, "Observation of a new boson at a mass of 125 GeV with the CMS experiment at the LHC," *Physics Letters B*, vol. 716, no. 1, pp. 30–61, 2012, ISSN: 0370-2693, DOI: `10.1016/j.physletb.2012.08.021`.

[8] ATLAS Collaboration, "Observation of a new particle in the search for the Standard Model Higgs boson with the ATLAS detector at the LHC," *Physics Letters B*, vol. 716, no. 1, pp. 1–29, 2012, DOI: `10.1016/j.physletb.2012.08.020`.

[9] G. Apollinari *et al.*, *High-Luminosity Large Hadron Collider (HL-LHC): Technical Design Report V. 0.1*, ser. CERN Yellow Reports: Monographs. Geneva: CERN, 2017, vol. 4, DOI: `10.23731/CYRM-2017-004`.

[10] H. Damerau *et al.*, *LHC Injectors Upgrade, Technical Design Report*. Geneva: CERN, Dec. 2014, DOI: `10.17181/CERN.7NHR.6HGC`.

[11] V. Kain *et al.*, "Achievements and Performance Prospects of the Upgraded LHC Injectors," in *Proc. 13th International Particle Accelerator Conference (IPAC'22)*, (Bangkok, Thailand), JACoW Publishing, Jun. 2022, DOI: `10.18429/JACoW-IPAC2022-WEIYGD1`.

[12] M. Vretenar *et al.*, *Linac4 design report*, ser. CERN Yellow Reports: Monographs. Geneva: CERN, 2020, vol. 6, DOI: `10.23731/CYRM-2020-006`.

[13] G. I. Budker, G. L. Dimov, A. G. Popov, Y. K. Sviridov, B. N. Sukhina, and I. Y. Timoshin, “Experiments on Charge-Exchange Injection of Protons into a Storage Ring,” *Journal of Nuclear Energy. Part C, Plasma Physics, Accelerators, Thermonuclear Research*, vol. 8, no. 6, pp. 692–694, Jan. 1966, DOI: `10.1088/0368-3281/8/6/309`.

[14] J. D. Simpson, “Operating Results from the ANL Booster,” *IEEE Transactions on Nuclear Science*, vol. 20, no. 3, pp. 198–201, 1973, DOI: `10.1109/TNS.1973.4327079`.

[15] C. W. Potts, “Negative Hydrogen Ion Injection into the Zero Gradient Synchrotron,” *IEEE Transactions on Nuclear Science*, vol. 24, no. 3, pp. 1385–1389, 1977, DOI: `10.1109/TNS.1977.4328953`.

[16] V. G. Dudnikov, “Charge exchange injection into accelerators and storage rings,” *Physics-Uspekhi*, vol. 62, no. 4, pp. 405–412, Apr. 2019, DOI: `10.3367/ufne.2019.02.038528`.

[17] G. I. Dimov, “Use of hydrogen negative ions in particle accelerators,” *Review of Scientific Instruments*, vol. 67, no. 10, pp. 3393–3404, 1996, DOI: `10.1063/1.1147513`.

[18] G. H. Rees, “Injection,” 1994, pp. 731–743, [Online]. Available: `https://cds.cern.ch/record/398435`.

[19] C. Bracco, “Phase Space Painting and H- Stripping Injection,” in *Proceedings of the CAS - CERN Accelerator School on Beam Injection, Extraction and Transfer*, vol. 5, 2018, pp. 141–150, DOI: `10.23730/CYRSP-2018-005.141`.

[20] V. C. Kempson, C. W. Planner, and V. T. Pugh, “Injection Dynamics and Multiturn Charge-Exchange Injection into the Fast Cycling Synchrotron for the SNS,” *IEEE Transactions on Nuclear Science*, vol. 28, no. 3, pp. 3085–3087, 1981, DOI: `10.1109/TNS.1981.4332017`.

[21] B. Jones, D. Adams, and C. Warsop, “Injection studies on the ISIS synchrotron,” in *2007 IEEE Particle Accelerator Conference (PAC)*, 2007, pp. 1640–1642, DOI: `10.1109/PAC.2007.4440849`.

[22] J. Beebe-Wang, Y. Y. Lee, D. Raparia, and J. Wei, “Transverse phase space painting for SNS accumulator ring injection,” in *Proc. of the 1999 Particle Accelerator Conference (PAC’99)*, (New York, NY), Mar. 1999, pp. 1743–1745, DOI: `10.1109/PAC.1999.794245`.

[23] J. Beebe-Wang, Y. Y. Lee, D. Raparia, J. Wei, C. R. Prior, and S. Machida, “Beam properties in the SNS accumulator ring due to transverse phase space painting,” in *Proc. of the 7th European Particle Accelerator Conference (EPAC’00)*, (Vienna, Austria), Jun. 2000, pp. 1465–1467, [Online]. Available: `https://accelconf.web.cern.ch/e00/papers/mop6A02.pdf` (visited on 08/10/2021).

[24] A. V. Fedotov *et al.*, “Halo and space-charge issues in the SNS ring,” in *Proc. of the 7th European Particle Accelerator Conference (EPAC’00)*, (Vienna, Austria), Jun. 2000, pp. 1289–1291, [Online]. Available: `https://accelconf.web.cern.ch/e00/PAPERS/TUP3B05.pdf` (visited on 08/10/2021).

[25] J. Beebe-Wang and J. Tang, “Injection painting optimization with fuzzy logic expert system,” in *Proc. of the 2001 Particle Accelerator Conference (PACS2001)*, (Chicago, IL, USA), vol. 3, Jun. 2001, pp. 1662–1664, DOI: `10.1109/PAC.2001.987140`.

[26] J. A. Holmes, T. Gorlov, N. J. Evans, M. Plum, and S. Cousineau, “Injection of a self-consistent beam with linear space charge force into a ring,” *Phys. Rev. Accel. Beams*, vol. 21, no. 12, 2018, DOI: `10.1103/PhysRevAccelBeams.21.124403`.

[27] M.-Y. Huang *et al.*, “Study on the anti-correlated painting injection scheme for the Rapid Cycling Synchrotron of the China Spallation Neutron Source,” *Nuclear Instruments and Methods in Physics Research Section A: Accelerators, Spectrometers, Detectors and Associated Equipment*, vol. 1007, p. 165 408, 2021, ISSN: 0168-9002, DOI: `10.1016/j.nima.2021.165408`.

[28] J. Qiu, J. Tang, S. Wang, and J. Wei, “Transverse phase space painting for the CSNS injection,” vol. 060626, pp. 1774–1776, 2006, [Online]. Available: `https://accelconf.web.cern.ch/e06/PAPERS/TUPLS115.PDF`.

[29] W. Tao, W. Sheng, Q. Jing, T. Jing-Yu, and Q. Qing, “Beam-loss driven injection optimization for CSNS/RCS,” *Chinese Physics C*, vol. 34, no. 2, pp. 218–223, Jan. 2010, DOI: `10.1088/1674-1137/34/2/012`.

[30] M.-Y. Huang, S. Wang, N. Huang, J. Qiu, S.-Y. Xu, and L.-S. Huang, “Study on the transverse painting during the injection process for CSNS/RCS,” in *Proc. of the 6th International Particle Accelerator Conference (IPAC’15)*, (Richmond, VA, USA), 2015, TUPTY015, DOI: `10.18429/JACoW-IPAC2015-TUPTY015`.

[31] M. Y. Huang, J. Qiu, S. Wang, and S. Y. Xu, “Study on the Injection Optimization and Transverse Coupling for CSNS/RCS,” in *Proc. of the 3rd International Particle Accelerator Conference (IPAC’12)*, (New Orleans, Louisiana, USA), vol. 1205201, 2012, pp. 3240–3242, DOI: `10.48550/ARXIV.1210.4613`.

[32] H. Hotchi *et al.*, “Beam loss reduction by injection painting in the 3-GeV rapid cycling synchrotron of the Japan Proton Accelerator Research Complex,” *Phys. Rev. ST Accel. Beams*, vol. 15, p. 040 402, 4 Apr. 2012, DOI: `10.1103/PhysRevSTAB.15.040402`.

[33] H. Hotchi, “Effects of the Montague resonance on the formation of the beam distribution during multiturn injection painting in a high-intensity proton ring,” *Phys. Rev. Accel. Beams*, vol. 23, no. 5, p. 050 401, 2020, DOI: `10.1103/PhysRevAccelBeams.23.050401`.

[34] I. Sakai *et al.*, “Phase space painting of charge exchange injection in the KEK booster,” in *Proc. of the 6th European Particle Accelerator Conference (EPAC 98)*, (Stockholm, Sweden), Jun. 1998, pp. 2137–2139, [Online]. Available: `https://accelconf.web.cern.ch/e98/PAPERS/MOP24C.PDF` (visited on 08/10/2021).

[35] A. I. Drozhdin, I. L. Rakhno, S. I. Striganov, and L. G. Vorobiev, “Modeling multiturn stripping injection and foil heating for high intensity proton drivers,” *Phys. Rev. ST Accel. Beams*, vol. 15, p. 011 002, 1 Jan. 2012, DOI: `10.1103/PhysRevSTAB.15.011002`.

[36] T. Kawakubo, “Analysis and measurement of beam dynamics in H^- charge-exchange injection,” *Nuclear Instruments and Methods in Physics Research Section A: Accelerators, Spectrometers, Detectors and Associated Equipment*, vol. 265, no. 3, pp. 351–363, 1988, DOI: `10.1016/S0168-9002(98)90001-8`.

[37] Y. Kamiya, “Elementary analysis of phase space painting,” in *Proc. of the 13th Particle Accelerator Conference (PAC’89)*, (Chicago, IL, USA), 1989, p. 660, [Online]. Available: `https://accelconf.web.cern.ch/p89/PDF/PAC1989_0660.PDF` (visited on 08/10/2021).

[38] A. Edelen *et al.*, *Opportunities in Machine Learning for Particle Accelerators*, 2018, DOI: `10.48550/ARXIV.1811.03172`.

[39] M. Scholz, “Simulationen zur H- Charge Exchange Injection in den CERN Proton Synchrotron Booster mit Linac4,” CERN-THESIS-2010-201, Presented on 2010, 2010, [Online]. Available: `http://cds.cern.ch/record/1331831` (visited on 08/10/2021).

[40] E. Benedetto, C. Bracco, V. Forte, B. Mikulec, V. Raginel, and G. Rumolo, “Transverse Emittance Preservation Studies for the CERN PS Booster Upgrade,” in *Proc. of the 54th ICFA Advanced Beam Dynamics Workshop on High-Intensity, High Brightness and High Power Hadron Beams (HB2014)*, (East-Lansing, MI, USA), 2015, THO4LR05. 5 p, [Online]. Available: `https://cds.cern.ch/record/2159007` (visited on 08/10/2021).

[41] C. Carli, M. Aiba, M. Chanel, B. Goddard, M. Martini, and W. Weterings, “Lattice Issues of the CERN PSB with H^- Charge Exchange Injection Hardware,” in *Proc. of the Particle Accelerator Conference 2009 (PAC09)*, (Vancouver, Canada), 2010, [Online]. Available: `https://accelconf.web.cern.ch/pac2009/papers/th6pfp036.pdf` (visited on 08/10/2021).

[42] V. Forte, E. Benedetto, and M. McAteer, “CERN Proton Synchrotron booster space charge simulations with a realistic model for alignment and field errors,” *Phys. Rev. Accel. Beams*, vol. 19, p. 124 202, 12 Dec. 2016, DOI: `10.1103/PhysRevAccelBeams.19.124202`.

[43] C. Bracco *et al.*, “Injection Painting and Associated HW for 160 MeV PSB H-,” in *Proc. of the 46th ICFA Advanced Beam Dynamics Workshop on High-Intensity and High-Brightness Hadron Beams (HB2010)*, (Morschach, Switzerland), Sep. 2010, [Online]. Available: `https://epaper.kek.jp/HB2010/papers/tuo2b02.pdf` (visited on 08/10/2021).

[44] C. Bracco *et al.*, “Studies on Transverse Painting for H- Injection into the PSB,” in *Proc. of the 2nd International Particle Accelerator Conference (IPAC’11)*, (San Sebastian, Spain), Sep. 2011, [Online]. Available: `https://accelconf.web.cern.ch/IPAC2011/papers/THPS052.pdf` (visited on 08/10/2021).

[45] J. L. Abelleira *et al.*, “Painting Schemes for CERN PS Booster H^- Injection,” in *Proc. of the 6th International Particle Accelerator Conference (IPAC’15)*, (Richmond, VA, USA), 2015, DOI: `10.18429/JACoW-IPAC2015-THPF083`.

[46] C. Bracco *et al.*, *PSB injection beam dynamics*, presented at LIU Day 2014, Apr. 2014, [Online]. Available: `https://indi.to/v2Rk4` (visited on 06/12/2021).

[47] V. Forte, J. Abelleira, E. Benedetto, C. Bracco, M. Cieslak-Kowalska, and G. D. Giovanni, “3D Emittances Tailoring Techniques and Optimization with Space Charge for the Future CERN PS Booster Operations with Linac4,” in *Proc. of the 7th International Particle Accelerator Conference (IPAC’16)*, (Busan, Korea), Jun. 2016, pp. 660–663, DOI: `10.18429/JACoW-IPAC2016-MOPOR025`.

[48] M. Cieslak-Kowalska, J. Abelleira, E. Benedetto, and C. Bracco, “Evolution of High Intensity Beams in the CERN PS Booster after H- Injection and Phase Space Painting,” in *Proc. of the 7th International Particle Accelerator Conference (IPAC’16)*, (Busan, Korea), Jun. 2016, pp. 656–659, DOI: `10.18429/JACoW-IPAC2016-MOPOR024`.

[49] S. Y. Lee, *Accelerator Physics*, 4th. World Scientific, 2019, DOI: `10.1142/11111`.

[50] H. Wiedemann, *Particle Accelerator Physics*, ser. Graduate Texts in Physics. Springer International Publishing, 2015, DOI: `10.1007/978-3-319-18317-6`.

[51] J. Rossbach and P. Schmüser, “Basic course on accelerator optics,” in *Proc. of the CAS - CERN Accelerator School: 5th General Accelerator Physics Course*, (Jyväskylä, Finland), Feb. 1992, DOI: `10.5170/CERN-1994-001.17`.

[52] J. Buon, “Beam Phase Space and Emittance,” in *Proc. of the CAS - CERN Accelerator School: 5th General Accelerator Physics Course*, (Jyväskylä, Finland), Feb. 1992, DOI: `10.5170/CERN-1994-001.89`.

[53] B. J. Holzer, “Beam optics and lattice design for particle accelerators,” in *Proc. of the CAS - CERN Accelerator School: High Power Hadron Machines*, (Bilbao, Spain), Mar. 2013, DOI: `10.5170/CERN-2013-001.171`.

[54] E. J. N. Wilson, “Transverse beam dynamics,” in *Proc. of the CAS - CERN Accelerator School: 5th General Accelerator Physics Course*, (Jyväskylä, Finland), Feb. 1992, DOI: `10.5170/CERN-1994-001.131`.

[55] A. Wolski, *Beam Dynamics in High Energy Particle Accelerators*. Imperial College Press, 2014, DOI: `10.1142/p899`.

[56] F. Bordry *et al.*, “Accelerator engineering and technology: Accelerator technology,” in *Particle Physics Reference Library : Volume 3: Accelerators and Colliders*. Cham: Springer International Publishing, 2020, pp. 337–517, DOI: `10.1007/978-3-030-34245-6_8`.

[57] G. Floquet, “Sur les équations différentielles linéaires à coefficients périodiques,” fr, *Annales scientifiques de l’École Normale Supérieure*, vol. 2e série, 12, pp. 47–88, 1883, DOI: `10.24033/asens.220`.

[58] CERN - BE/ABP Accelerator Beam Physics Group, *MAD - Methodical Accelerator Design*, [Online]. Available: `http://mad.web.cern.ch/mad/` (visited on 01/02/2022).

[59] F. Asvesta *et al.*, “Resonance Compensation for High Intensity and High Brightness Beams in the CERN PSB,” in *Proc. of 64th ICFA Advanced Beam Dynamics Workshop on High Intensity and High Brightness Hadron Beams (HB2021)*, 2022, pp. 40–45, DOI: `10.18429/JACoW-HB2021-MOP06`.

[60] V. Forte, “Performance of the CERN PSB at 160 MeV with H^- charge exchange injection,” CERN-THESIS-2016-063, presented on 03-06-2016, [Online]. Available: `https://cds.cern.ch/record/2194937` (visited on 07/13/2022).

[61] T. Prebibaj *et al.*, *Emittance measurements*, presented at LIU-PSB Beam Dynamics WG #19, CERN, Geneve Switzerland, 2017, [Online]. Available: `https://indico.cern.ch/event/832290/` (visited on 05/10/2022).

[62] A. Oeftiger, H. Bartosik, A. J. Findlay, S. Hancock, and G. Rumolo, “Flat Bunches with a Hollow Distribution for Space Charge Mitigation,” in *Proc. of the 7th International Particle Accelerator Conference (IPAC’16)*, (Busan, Korea), May 2016, DOI: `10.18429/JACoW-IPAC2016-MOPOR023`.

[63] G. Strebini *et al.*, *De-convolution algorithm to properly remove dispersive profile for emittance calculations*, presented at LIU-PS Beam Dynamics WG meeting #5, CERN, Geneve Switzerland", 2017, [Online]. Available: `https://indico.cern.ch/event/676527/` (visited on 05/10/2022).

[64] R. Jones, M. Gasior, T. Lefevre, H. Schmickler, and K. Wittenburg, “Introduction to beam instrumentation and diagnostics,” in *Proc. of CAS - CERN Accelerator School: Advanced Accelerator Physics Course*, (Trondheim, Norway), vol. 3, Aug. 2013, p. 353, DOI: `10.5170/CERN-2014-009.23`.

[65] S. Papadopoulou, F. Antoniou, T. Argyropoulos, M. Hostettler, Y. Papaphilippou, and G. Trad, “Impact of non-Gaussian beam profiles in the performance of hadron colliders,” *Phys. Rev. Accel. Beams*, vol. 23, p. 101 004, 10 Oct. 2020, DOI: `10.1103/PhysRevAccelBeams.23.101004`.

[66] G. Franchetti, “Space Charge in Circular Machines,” in *Proc. of CAS - CERN Accelerator School: Intensity Limitations in Particle Beams*, (Geneva, Switzerland), vol. 3, 2017, p. 353, DOI: `10.23730/CYRSP-2017-003.353`.

[67] K. Li, “Collective Effects – an introduction,” in *Proc. of the CAS - CERN Accelerator–School course on Introduction to Accelerator Physics 2021*, (Kaunas, Lithuania), Jul. 2021, DOI: `10.48550/ARXIV.2107.06109`.

[68] K. Schindl, “Space charge,” in *Proc. of CAS - CERN Accelerator School: Intermediate Accelerator Physics 2003*, (Zeuthen, Germany), 2006, DOI: `10.5170/CERN-2006-002.305`.

[69] I. Hofmann, *Space Charge Physics for Particle Accelerators*, ser. Particle Acceleration and Detection. Springer International Publishing, 2017, DOI: `10.1007/978-3-319-62157-9`.

[70] A. Shishlo, S. Cousineau, J. Holmes, and T. Gorlov, “The particle accelerator simulation code PyORBIT,” *Procedia Computer Science*, vol. 51, pp. 1272–1281, 2015, DOI: `10.1016/j.procs.2015.05.312`.

[71] E. Forest, A. Shishlo, J. Holmes, and A. Molodozhentsev, *Synopsis of the PTC and ORBIT integration*, KEK Internal Report (A), 2007.

[72] F. Schmidt, E. Forest, and E. McIntosh, “Introduction to the polymorphic tracking code: Fibre bundles, polymorphic Taylor types and "Exact tracking",” CERN, Geneva, Tech. Rep. CERN-SL-2002-044-AP, KEK-REPORT-2002-3, Jul. 2002, [Online]. Available: `http://cds.cern.ch/record/573082` (visited on 02/17/2022).

[73] M. Bassetti and G. A. Erskine, “Closed expression for the electrical field of a two-dimensional Gaussian charge,” CERN, Geneva, Tech. Rep. CERN-ISR-TH-80-06, 1980, [Online]. Available: `https://cds.cern.ch/record/122227` (visited on 04/30/2022).

[74] S. Kheifets, “Potential of a Three-Dimensional Gaussian Bunch,” DESY, Tech. Rep. PETRA Note 119, 1976, Hand written document, DOI: `10.3204/PUBDB-2017-01789`.

[75] B. W. S. L. Montague, *Fourth-order coupling resonance excited by space-charge forces in a synchrotron*, ser. CERN Yellow Reports: Monographs. Geneva: CERN, 1968, DOI: `10.5170/CERN-1968-038`.

[76] F. Asvesta, "Space Charge and Lattice Driven Resonances at the CERN Injectors," CERN-THESIS-2020-344. Presented 16 Sep 2020, 2020, [Online]. Available: `https://cds.cern.ch/record/2771289` (visited on 01/21/2022).

[77] S. Y. Lee, G. Franchetti, I. Hofmann, F. Wang, and L. Yang, "Emittance growth mechanisms for space-charge dominated beams in fixed field alternating gradient and proton driver rings," *New Journal of Physics*, vol. 8, no. 11, pp. 291–291, Nov. 2006, DOI: `10.1088/1367-2630/8/11/291`.

[78] B. Goddard, M. Aiba, C. Bracco, C. Carli, M. Meddahi, and W. Weterings, "Stripping Foil Issues for H-injection into the CERN PSB at 160 MeV," in *Proc. of 1st International Particle Accelerator Conference (IPAC'10)*, (Kyoto, Japan), Jun. 2010, [Online]. Available: `https://accelconf.web.cern.ch/IPAC10/papers/THPEB030.pdf`.

[79] F. Jones, *User's Guide to ACCSIM*, TRIUMF Design Note TRI-DN-90-17, 1990.

[80] T. T. Böhlen *et al.*, "The FLUKA Code: Developments and Challenges for High Energy and Medical Applications," *Nucl. Data Sheets*, vol. 120, pp. 211–214, 2014, DOI: `10.1016/j.nds.2014.07.049`.

[81] A. Ferrari, P. R. Sala, A. Fasso, and J. Ranft, "FLUKA: A multi-particle transport code (Program version 2005)," 2005.

[82] G. Moliere, "Theorie der Streuung schneller geladener Teilchen I. Einzelstreuung am abgeschirmten Coulomb-Feld," *Zeitschrift für Naturforschung A*, vol. 2, no. 3, pp. 133–145, 1947, DOI: `doi:10.1515/zna-1947-0302`.

[83] V. L. Highland, "Some practical remarks on multiple scattering," *Nuclear Instruments and Methods*, vol. 129, no. 2, pp. 497–499, 1975, DOI: `10.1016/0029-554X(75)90743-0`.

[84] J. D. Jackson, *Classical electrodynamics; 2nd ed.* New York, NY: Wiley, 1975, ISBN: 978-0-471-30932-1.

[85] A. Lechner, *Private communication*, 2019-10-29.

[86] C. Bracco, " Injection: Hadron Beams," in *Proc. of the CAS - CERN Accelerator School on Beam Injection, Extraction and Transfer (2017)*, (Erice, Italy), vol. 5, 2018, pp. 131–140, DOI: `10.23730/CYRSP-2018-005.131`.

[87] A. Lombardi, "Commissioning of CERN LINAC4," in *Proc. of 29th Linear Accelerator Conference (LINAC2018)*, (Beijing, China), 2018, DOI: `10.18429/JACoW-LINAC2018-TH1P01`.

[88] P. K. Skowroński *et al.*, "Summary of the First Fully Operational Run of Linac4 at CERN," in *Proc. of 13th International Particle Accelerator Conference (IPAC'22)*, (Bangkok, Thailand), Jun. 2022, DOI: `10.18429/JACoW-IPAC2022-MOPOST007`.

[89] R. Hradil, *Linac4*, General Photo, Apr. 2017, [Online]. Available: `https://cds.cern.ch/record/2260707` (visited on 04/20/2022).

[90] F. Asvesta *et al.*, *LHC Proton Beam Production*, presented at the Injectors and Experimental Facilities Workshop, Montreaux, Switzerland, 12/2021, [Online]. Available: `https://indico.cern.ch/event/1063281/` (visited on 12/10/2021).

[91] E. Renner *et al.*, *Beam Production for n_TOF and ISOLDE*, presented at the Injectors and Experimental Facilities Workshop, Montreaux, Switzerland, 12/2021, [Online]. Available: `https://indico.cern.ch/event/1063281/` (visited on 12/10/2021).

[92] P. Loïez and M. Brice, *The 1.4 GeV PS Booster in its tunnel. Le PS Booster à 1.4 GeV dans son tunnel*, General Photo, Feb. 2002, [Online]. Available: `http://cds.cern.ch/record/42643` (visited on 04/30/2022).

[93] M. Brice, *Charge-exchange injection system for the PS Booster. Système d'injection à échange de charge pour le PS Booster*, General Photo, Jun. 2019, [Online]. Available: `https://cds.cern.ch/record/2678082` (visited on 04/30/2022).

[94] *PSB Layout*, [Online]. Available: `http://psb-machine.web.cern.ch/layout.htm` (visited on 05/05/2022).

[95] A. Huschauer *et al.*, *Official optics repository of the CERN PSB*, CERN, Geneva, Switzerland, 2021, [Online]. Available: `https://gitlab.cern.ch/acc-models/acc-models-psb/-/tree/2021` (visited on 11/05/2021).

[96] K. Hanke, "Past and Present Operation of the CERN PS Booster," *International Journal of Modern Physics A*, vol. 28, no. 13, p. 1 330 019, 2013, DOI: `10.1142/S0217751X13300196`.

[97] Nanocrystalline soft magnetic material FINEMET®, Hitachi Metals.

[98] M. Paoluzzi *et al.*, "Design of the New Wideband RF System for the CERN PS Booster," in *Proc. of 7th International Particle Accelerator Conference (IPAC'16)*, (Busan, Korea), 2016, DOI: `10.18429/JACoW-IPAC2016-MOPMW024`.

[99] V. Forte, C. Bracco, G. D. Giovanni, M. Fraser, A. Lombardi, and B. Mikulec, "Multi-Particle Simulations of the Future CERN PSB Injection Process with Updated Linac4 Beam Performance," in *Proc. of 61st ICFA Advanced Beam Dynamics Workshop (HB'18)*, (Daejeon, Korea), Jul. 2018, pp. 278–283, DOI: `10.18429/JACoW-HB2018-WEP2PO007`.

[100] B. Balhan, C. Baud, J. Borburgh, and M. Hourican, "Design and Construction of the CERN PS Booster Charge Exchange Injection Chicane Bumpers," in *Proc. of 9th International Particle Accelerator Conference*, (Vancouver, Canada), May 2018, DOI: `10.18429/JACoW-IPAC2018-WEPMF082`.

[101] T. Prebibaj *et al.*, "Injection Chicane Beta-Beating Correction for Enhancing the Brightness of the CERN PSB Beams," in *Proc. of 64th ICFA Advanced Beam Dynamics Workshop on High Intensity and High Brightness Hadron Beams (HB2021)*, 2022, DOI: `10.18429/JACoW-HB2021-MOP18`.

[102] L. Feliciano *et al.*, "A New Hardware Design for PSB Kicker Magnets (KSW) for the 35 mm Transverse Painting in the Horizontal Plane," in *Proc. of 6th International Particle Accelerator Conference (IPAC'15)*, (Richmond, VA, USA), Jun. 2015, DOI: `10.18429/JACoW-IPAC2015-THPF086`.

[103] G. Gräwer, “A multi-waveform pulsed current generator for slow kicker magnets,” in *Proc. of 21st European Conference on Power Electronics and Applications (EPE’19)*, (Genova, Italy), Sep. 2019, DOI: `10.23919/EPE.2019.8915536`.

[104] W. Weterings, C. Bracco, L. Jorat, R. Noulibos, and P. van Trappen, “First experience with carbon stripping foils for the 160 MeV H^- injection into the CERN PSB,” *AIP Conference Proceedings*, vol. 1962, no. 1, p. 030 003, 2018, DOI: `10.1063/1.5035520`.

[105] C. Bracco *et al.*, “Commissioning of the Stripping Foil Units for the Upgrade of the PSB H^- Injection System,” in *Proc. of 8th International Particle Accelerator Conference (IPAC’17)*, (Copenhagen, Denmark), May 2017, DOI: `10.18429/JACoW-IPAC2017-MOPIK041`.

[106] C. Bracco, L. Jorat, R. Noulibos, P. Van Trappen, and W. Weterings, “Measurements with the stripping foil test stand in the Linac4 Transfer Line,” in *Proc. of 29th World Conference of the International Nuclear Target Development Society (INTDS2018)*, (East Lansing, USA), 2020, DOI: `10.1051/epjconf/202022901003`.

[107] ACF-Metals, 2239 E. Kleindale Road, Tucson, Arizona, U.S.A.

[108] Kaneka Coorperation, Nakanoshima, Kita-ku, Osaka, 530-8288.

[109] GSI Helmholtzzentrum für Schwerionenforschung GmbH, Planckstraße 1, 64291 Darmstadt.

[110] *PSB Injection Line Layout*, [Online]. Available: `http://psb-machine.web.cern.ch/inject.htm` (visited on 05/05/2022).

[111] V. Kain, “Emittance Preservation,” in *Proc. of CAS - CERN Accelerator School: Beam Injection, Extraction and Transfer*, (Erice, Italy), 2018, DOI: `10.23730/CYRSP-2018-005.345`.

[112] M. Reiser, “Free energy and emittance growth in nonstationary charged particle beams,” *Journal of Applied Physics*, vol. 70, no. 4, pp. 1919–1923, 1991, DOI: `10.1063/1.349474`.

[113] I. Karpov, V. Kornilov, and O. Boine-Frankenheim, “Early transverse decoherence of bunches with space charge,” *Phys. Rev. Accel. Beams*, vol. 19, p. 124 201, 12 Dec. 2016, DOI: `10.1103/PhysRevAccelBeams.19.124201`.

[114] I. Karpov, O. Boine-Frankenheim, and V. Kornilov, “Transverse Decoherence of Ion Bunches with Space Charge and Feedback System,” in *54th ICFA Advanced Beam Dynamics Workshop on High-Intensity and High-Brightness Hadron Beams (HB2014)*, (East-Lansing, MI, USA), 2015, MOPAB11, [Online]. Available: `https://accelconf.web.cern.ch/HB2014/papers/mopab11.pdf`.

[115] E. Renner, *Tolerances of the beam parameters at the PSB injection*, presented at Linac4 HW and Beam Commissioning Working Group Meeting, Geneva, Switzerland, Mar. 2020, [Online]. Available: `https://indico.cern.ch/event/893670/` (visited on 05/02/2022).

[116] A. Lombardi and J.-B. Lallement, *Linac4 transfer line matching for different debuncher settings*, presented at Injectors Performance Panel meeting #7, CERN, Geneve Switzerland, Apr. 2021, [Online]. Available: `https://indico.cern.ch/event/906075/` (visited on 08/10/2022).

[117] J. Wenniger, “YASP Steering Program User Guide,” CERN, Geneva, Tech. Rep., 2005, [Online]. Available: `https://jwenning.web.cern.ch/documents/YASP/YASP-user-guide.pdf` (visited on 01/20/2021).

[118] B. Autin and Y. Marti, “Closed orbit correction of A.G. machines using a small number of magnets,” CERN, Geneva, Tech. Rep. CERN-ISR-MA-73-17, Mar. 1973, [Online]. Available: `https://cds.cern.ch/record/790199` (visited on 01/20/2021).

[119] W. H. Press, S. A. Teukolsky, W. T. Vetterling, and B. P. Flannery, *Numerical Recipes 3rd Edition: The Art of Scientific Computing*, 3rd ed. Cambridge University Press, 2007, ISBN: 0521880688.

[120] B. Goddard, “Expected delivery precision of the injected LHC beam,” CERN, Geneva, Tech. Rep. LHC-Project-Note-337, Feb. 2004, [Online]. Available: `https://cds.cern.ch/record/719045` (visited on 10/11/2021).

[121] T. Stadlbauer, *Private communication*, 15.05.2020.

[122] J.-M. Cravero, *Private communication*, 19.05.2020.

[123] A. Huschauer *et al.*, *Official optics repository of the CERN transfer lines*, 2021, [Online]. Available: `https://gitlab.cern.ch/acc-models/acc-models-tls/-/tree/2021/psb_injection` (visited on 11/05/2021).

[124] E. Renner *et al.*, “Beam Commissioning of the New 160 MeV H^- Injection System of the CERN PS Booster,” in *Proc. of 12th International Particle Accelerator Conference (IPAC’21)*, (Campinas, SP, Brazil), Aug. 2021, DOI: `10.18429/JACoW-IPAC2021-WEPAB210`.

[125] H. Bartosik *et al.*, *PyORBIT_Examples*, 2021, [Online]. Available: `https://gitlab.cern.ch/pyorbit/pyorbit_examples.git` (visited on 02/15/2020).

[126] F. Asvesta, *Private communication*, 20.07.2022.

[127] F. Asvesta *et al.*, “High intensity studies in the CERN Proton Synchrotron Booster,” in *Proc. of 13th International Particle Accelerator Conference (IPAC’22)*, (Bangkok, Thailand), Jun. 2022, DOI: `10.18429/JACoW-IPAC2022-WEPOTK011`.

[128] F. Asvesta *et al.*, “Identification and characterization of high order incoherent space charge driven structure resonances in the CERN Proton Synchrotron,” *Phys. Rev. Accel. Beams*, vol. 23, p. 091 001, 9 Sep. 2020, DOI: `10.1103/PhysRevAccelBeams.23.091001`.

[129] E. Renner *et al.*, “Optimised Transverse Painting Schemes for the New 160 MeV H^- Injection System at CERN,” in *Proc. of 64th ICFA Advanced Beam Dynamics Workshop on High Intensity and High Brightness Hadron Beams (HB2021)*, 2022, DOI: `10.18429/JACoW-HB2021-MOP19`.

[130] J. Abelleira Fernandez, “Beam Dynamics Study on LIU High Intensity Beams in the BT Line,” Tech. Rep. EDMS 1537199 v.1.0, 2015, CERN Internal report, Geneva, Switzerland.

[131] H. Bartosik, G. P. Di Giovanni, B. Mikulec, and F. Schmidt, “PS Booster Beam Absorber/Scraper after LS2,” Tech. Rep. EDMS 1578463 v.2.1, 2018, CERN Internal report, Geneva, Switzerland.

[132] S. Machida, “Space-charge-induced resonances in a synchrotron,” *Nuclear Instruments and Methods in Physics Research Section A: Accelerators, Spectrometers, Detectors and Associated Equipment*, vol. 384, no. 2, pp. 316–321, 1997, DOI: `10.1016/S0168-9002(96)00884-4`.

[133] R. Veness *et al.*, “Installation and Test of Pre-series Wire Scanners for the LHC Injector Upgrade Project at CERN,” in *Proc. 8th International Particle Accelerator Conference (IPAC’17)*, (Copenhagen, Denmark), May 2017, DOI: `10.18429/JACoW-IPAC2017-MOPAB121`.

[134] S. Hancock, “A simple algorithm for longitudinal phase space tomography,” CERN, Geneva, Tech. Rep., May 1997, [Online]. Available: `https://cds.cern.ch/record/1174559` (visited on 08/20/2021).

[135] S. Albright, F. Antoniou, F. Asvesta, H. Bartosik, C. Bracco, and E. Renner, “New Longitudinal Beam Production Methods in the CERN Proton Synchrotron Booster,” in *Proc. of 12th International Particle Accelerator Conference (IPAC’21)*, (Campinas, SP, Brazil), Aug. 2021, pp. 4130–4133, DOI: `10.18429/JACoW-IPAC2021-THPAB183`.

[136] E. Renner, *PSB simulation studies for post LS2 operation*, presented at 4th ICFA Mini-Workshop on Space Charge, Geneva, Switzerland, 2018, [Online]. Available: `https://indico.cern.ch/event/828559/contributions/3528369/` (visited on 07/29/2021).

[137] S. van der Meer, “Calibration of the effective beam height in the ISR,” CERN, Geneva, Tech. Rep., 1968, [Online]. Available: `https://cds.cern.ch/record/296752` (visited on 10/07/2021).

[138] H. Bartosik and G. Rumolo, “Production of single Gaussian bunches for Van der Meer scans in the LHC injector chain,” Aug. 2013, [Online]. Available: `https://cds.cern.ch/record/1590405` (visited on 10/07/2021).

[139] E. Renner and F. Asvesta, *Production scheme for beams in the PSB: LHC single bunches*, presented at Injectors Performance Panel meeting #7, CERN, Geneve Switzerland, Apr. 2021, [Online]. Available: `https://indico.cern.ch/event/906075/` (visited on 05/05/2022).

[140] T. Hastie, R. Tibshirani, and J. Friedman, *Elements of Statistical Learning: Data Mining, Inference, and Prediction*, 2nd ed. Springer Science & Business Media, 2009, DOI: `10.1007/978-0-387-84858-7`.

[141] M. J. Zaki and M. J. Wagner, *Data Mining and Analysis: Fundamental Concepts and Algorithms*, 2nd. Cambridge University Press, Mar. 2020, p. 562, ISBN: 978-1108473989.

[142] S. L. Brunton and J. N. Kutz, *Data-Driven Science and Engineering: Machine Learning, Dynamical Systems, and Control*. Cambridge University Press, 2019, DOI: `10.1017/9781108380690`.

[143] R. S. Sutton and A. G. Barto, *Reinforcement Learning: An Introduction*. MIT press, 2018, ISBN: 9780262193986.

[144] I. Goodfellow, Y. Bengio, and A. Courville, *Deep Learning*. MIT Press, 2016, [Online]. Available: `http://www.deeplearningbook.org` (visited on 07/13/2022).

[145] N. Srivastava, G. Hinton, A. Krizhevsky, I. Sutskever, and R. Salakhutdinov, “Dropout: A simple way to prevent neural networks from overfitting,” *Journal of Machine Learning Research*, vol. 15, no. 1, pp. 1929–1958, Jan. 2014, DOI: `10.5555/2627435.2670313`.

[146] K. Hornik, M. Stinchcombe, and H. White, “Multilayer feedforward networks are universal approximators,” *Neural Networks*, vol. 2, no. 5, pp. 359–366, 1989, DOI: `10.1016/0893-6080(89)90020-8`.

[147] L. Breimann and O. Sheridan-Methven, “Random Forests,” *Machine Learning*, vol. 45, no. 5–32, 2001, DOI: `10.1023/A:1010933404324`.

[148] L. Breiman, “Bagging predictors,” *Machine Learning*, vol. 24, no. 2, pp. 123–140, Aug. 1996, DOI: `10.1007/BF00058655`.

[149] M. Krzywinski and N. Altman, “Classification and regression trees,” *Nature Methods*, vol. 14, no. 8, pp. 757–758, Aug. 2017, DOI: `10.1038/nmeth.4370`.

[150] J. Nocedal and S. Wright, *Numerical Optimization*, ser. Springer Series in Operations Research and Financial Engineering. Sprfinger New York, 2006, DOI: `10.1007/978-0-387-40065-5`.

[151] D. Wolpert and W. Macready, “No free lunch theorems for optimization,” *IEEE Transactions on Evolutionary Computation*, vol. 1, no. 1, pp. 67–82, 1997, DOI: `10.1109/4235.585893`.

[152] P. Virtanen *et al.*, “SciPy 1.0: Fundamental Algorithms for Scientific Computing in Python,” *Nature Methods*, vol. 17, pp. 261–272, 2020, DOI: `10.1038/s41592-019-0686-2`.

[153] V. Nissen and J. Propach, “Optimization with noisy function evaluations,” in *Proc. of 5th International Conference on Parallel Problem Solving from Nature (PPSN V)*, (Amsterdam, Netherlands), 1998, pp. 159–168, DOI: `10.1007/BFb0056859`.

[154] V. Beiranvand, W. Hare, and Y. Lucet, “Best practices for comparing optimization algorithms,” *Optimization and Engineering*, vol. 18, no. 4, pp. 815–848, Dec. 2017, DOI: `10.1007/s11081-017-9366-1`.

[155] S. Soritz, D. Moser, and H. Gruber-Wölfler, “Comparison of derivative-free algorithms for their applicability in self-optimization of chemical processes,” *Chemistry–Methods*, 2022, DOI: `10.1002/cmtd.202100091`.

[156] C. Audet and W. Hare, *Derivative-Free and Blackbox Optimization*. Springer International Publishing, 2017, DOI: `10.1007/978-3-319-68913-5`.

[157] C. T. Kelley, *Iterative Methods for Optimization*, ser. Frontiers in Applied Mathematics. Society for Industrial and Applied Mathematics, 1999, DOI: `10.1137/1.9781611970920`.

[158] P. Pardalos, V. Rasskazova, and M. Vrahatis, *Black Box Optimization, Machine Learning, and No-free Lunch Theorems*, ser. Springer optimization and its applications. Springer, 2021, DOI: `10.1007/978-3-030-66515-9`.

[159] L. M. Rios and N. V. Sahinidis, “Derivative-free optimization: a review of algorithms and comparison of software implementations,” *Journal of Global Optimization*, vol. 56, no. 3, pp. 1247–1293, Jul. 2013, DOI: `10.1007/s10898-012-9951-y`.

[160] T. G. Kolda, R. M. Lewis, and V. Torczon, “Optimization by Direct Search: New Perspectives on Some Classical and Modern Methods,” *SIAM Review*, vol. 45, pp. 385–482, 2003, DOI: `10.1137/S003614450242889`.

[161] C. Blum and A. Roli, “Metaheuristics in combinatorial optimization: Overview and conceptual comparison,” *ACM Computing Surveys*, vol. 35, no. 3, pp. 268–308, Sep. 2003, DOI: `10.1145/937503.937505`.

[162] J. Larson, M. Menickelly, and S. M. Wild, “Derivative-free optimization methods,” *Acta Numerica*, vol. 28, pp. 287–404, 2019, DOI: `10.1017/S0962492919000060`.

[163] A. R. Conn, N. I. M. Gould, and P. L. Toint, *Trust Region Methods*, ser. Series on Optimization. 2000, DOI: `10.1137/1.9780898719857`.

[164] V. Kain and N. Madysa, *Generic Optimisation Frontend and Framework (GeOFF)*, 2021, [Online]. Available: `%7Bhttps://gitlab.cern.ch/vkain/acc-app-optimisation%7D` (visited on 06/15/2021).

[165] C. Cartis, J. Fiala, B. Marteau, and L. Roberts, “Improving the flexibility and robustness of model-based derivative-free optimization solvers,” 2018, DOI: `10.48550/ARXIV.1804.00154`.

[166] S. Appel and S. Reimann, “Beam Line Optimization using Derivative-Free Algorithms,” in *Proc. of 10th International Particle Accelerator Conference (IPAC’19)*, (Melbourne, Australia), vol. 1350, IOP Publishing, May 2019, p. 012 104, DOI: `10.1088/1742-6596/1350/1/012104`.

[167] S. Hirlaender *et al.*, “Automatisation of the SPS Electrostatic Septa Alignment,” in *Proc. of 10th International Particle Accelerator Conference (IPAC’19)*, (Melbourne, Australia), May 2019, DOI: `doi:10.18429/JACoW-IPAC2019-THPRB080`.

[168] R. Roussel, A. Hanuka, and A. Edelen, “Multiobjective bayesian optimization for online accelerator tuning,” *Phys. Rev. Accel. Beams*, vol. 24, p. 062 801, 6 Jun. 2021, DOI: `10.1103/PhysRevAccelBeams.24.062801`.

[169] J. A. Nelder and R. Mead, “A Simplex Method for Function Minimization,” *The Computer Journal*, vol. 7, no. 4, pp. 308–313, Jan. 1965, DOI: `10.1093/comjnl/7.4.308`.

[170] F. Gao and L. Han, “Implementing the Nelder-Mead Simplex Algorithm with Adaptive Parameters,” *Computational Optimization and Applications*, vol. 51, no. 1, pp. 259–277, 2012, DOI: `10.1007/s10589-010-9329-3`.

[171] M. J. D. Powell, “An efficient method for finding the minimum of a function of several variables without calculating derivatives,” *The Computer Journal*, vol. 7, no. 2, pp. 155–162, Jan. 1964, DOI: `10.1093/comjnl/7.2.155`.

[172] M. J. D. Powell, “A Direct Search Optimization Method That Models the Objective and Constraint Functions by Linear Interpolation,” in *Advances in Optimization and Numerical Analysis*, Springer Netherlands, 1994, pp. 51–67, DOI: `10.1007/978-94-015-8330-5_4`.

[173] M. J. D. Powell, “Direct search algorithms for optimization calculations,” vol. 7, pp. 287–336, 1998, DOI: `10.1017/S0962492900002841`.

[174] M. J. D. Powell, "A View of Algorithms for Optimization Without Derivatives," Department of Applied Mathematics and Theoretical Physics, University of Cambridge, Tech. Rep. DAMTP2007/NA03, Jan. 2007, [Online]. Available: `http://www.damtp.cam.ac.uk/user/na/NA_papers/NA2007_03.pdf` (visited on 03/16/2022).

[175] C. Cartis, L. Roberts, and O. Sheridan-Methven, "Escaping local minima with derivative-free methods: A numerical investigation," 2018, DOI: `10.48550/ARXIV.1812.11343`.

[176] M. J. D. Powell, "The BOBYQA algorithm for bound constrained optimization without derivatives," University of Cambridge, Tech. Rep. DAMTP 2009/NA06, 2009, [Online]. Available: `http://www.damtp.cam.ac.uk/user/na/NA_papers/NA2009_06.pdf` (visited on 03/15/2022).

[177] J. R. R. A. Martins and A. Ning, *Engineering Design Optimization*. Cambridge University Press, 2021, DOI: `10.1017/9781108980647`.

[178] K. K. Vu, C. D'Ambrosio, Y. Hamadi, and L. Liberti, "Surrogate-based methods for black-box optimization," *International Transactions in Operational Research*, vol. 24, no. 3, pp. 393–424, 2017, DOI: `10.1111/itor.12292`.

[179] J. Močkus, "On bayesian methods for seeking the extremum," in *Proc. Optimization Techniques IFIP Technical Conference*, (Novosibirsk, Russia), 1975, pp. 400–404, DOI: `10.1007/3-540-07165-2_55`.

[180] D. Rullière, A. Faleh, F. Planchet, and W. Youssef, "Exploring or reducing noise?" *Structural and Multidisciplinary Optimization*, vol. 47, no. 6, pp. 921–936, Jun. 2013, DOI: `10.1007/s00158-012-0874-5`.

[181] E. Cantú-Paz, "Adaptive Sampling for Noisy Problems," in *Proc. of Genetic and Evolutionary Computation Conference (GECCO 2004)*, (Seattle, Washington, US), Jun. 2004, pp. 947–958, DOI: `10.1007/978-3-540-24854-5_95`.

[182] T. Head *et al.*, *Scikit-optimize*, version v0.5.2, Mar. 2018, DOI: `10.5281/zenodo.1207017`.

[183] D. Eriksson, D. Bindel, and C. A. Shoemaker, "pySOT and POAP: An event-driven asynchronous framework for surrogate optimization," *arXiv preprint arXiv:1908.00420*, 2019.

[184] R. G. Regis and C. A. Shoemaker, "Combining radial basis function surrogates and dynamic coordinate search in high-dimensional expensive black-box optimization," *Engineering Optimization*, vol. 45, no. 5, pp. 529–555, May 2013, DOI: `10.1080/0305215X.2012.687731`.

[185] J. J. Moré and S. M. Wild, "Benchmarking derivative-free optimization algorithms," *SIAM Journal on Optimization*, vol. 20, pp. 172–191, 2009, DOI: `10.1137/080724083`.

[186] S. Kamyab, Z. Azimifar, R. Sabzi, and P. Fieguth, "Deep learning methods for inverse problems," en, *PeerJ Computer Science*, vol. 8, e951, May 2022, DOI: `10.7717/peerj-cs.951`.

[187] A. Daw, A. Karpatne, W. Watkins, J. Read, and V. Kumar, *Physics guided neural networks for modelling of non-linear dynamics*, 2022, DOI: `10.48550/ARXIV.1710.11431`.

[188] M. Raissi, P. Perdikaris, and G. Karniadakis, “Physics-informed neural networks: A deep learning framework for solving forward and inverse problems involving nonlinear partial differential equations,” *Journal of Computational Physics*, vol. 378, pp. 686–707, 2019, DOI: `10.1016/j.jcp.2018.10.045`.

[189] G. Gräwer, “Precise generation of a complex, bipolar, piecewise linear current waveform for a slow kicker magnet,” in *Proc. of 19th IEEE Pulsed Power Conference (PPC 2013)*, (San Francisco, CA, US), Jun. 2013, DOI: `10.1109/PPC.2013.6627427`.

[190] B. Friedland, *Control System Design: An Introduction to State-space Methods*, ser. Control theory. McGraw-Hill, 1986, ISBN: 9780070224414.

[191] A. Paszke *et al.*, “PyTorch: An Imperative Style, High-Performance Deep Learning Library,” in *Proc. of 33rd Conference on Neural Information Processing Systems (NeurIPS 2019)*, (Vancouver, Canada), 2019, pp. 8024–8035, DOI: `10.48550/arXiv.1912.01703`.

[192] F. Pedregosa *et al.*, “Scikit-learn: Machine Learning in Python,” *Journal of Machine Learning Research*, vol. 12, pp. 2825–2830, 2011, DOI: `10.48550/arXiv.1201.0490`.

[193] K. Pearson, “LIII. On lines and planes of closest fit to systems of points in space,” *The London, Edinburgh, and Dublin Philosophical Magazine and Journal of Science*, vol. 2, no. 11, pp. 559–572, 1901, DOI: `10.1080/14786440109462720`.

[194] N. Halko, P. G. Martinsson, and J. A. Tropp, “Finding Structure with Randomness: Probabilistic Algorithms for Constructing Approximate Matrix Decompositions,” *SIAM Review*, vol. 53, no. 2, pp. 217–288, 2011, DOI: `10.1137/090771806`.

[195] A. L. Maas, A. Y. Hannun, and A. Y. Ng, “Rectifier nonlinearities improve neural network acoustic models,” in *Proc. of ICML Workshop on Deep Learning for Audio, Speech and Language Processing*, (Atlanta, GA, US), Jun. 2013.

[196] S. Ioffe and C. Szegedy, *Batch Normalization: Accelerating Deep Network Training by Reducing Internal Covariate Shift*, 2015, DOI: `10.48550/ARXIV.1502.03167`.

[197] L. Ilya and F. Hutter, “Decoupled Weight Decay Regularization,” in *Proc. of International Conference on Learning Representations (ICLR 2019)*, (New Orleans, LA, US), 2019.

[198] G. Van Rossum and F. L. Drake, *Python 3 Reference Manual*. Scotts Valley, CA: CreateSpace, 2009, ISBN: 1441412697.

[199] M. Bartelmann, B. Feuerbacher, T. Krueger, D. Lüst, A. Rebhan, and A. Wipf, *Theoretische Physik*. Springer Spektrum, Oct. 2014, DOI: `10.1007/978-3-642-54618-1`.

[200] T. Sagota, *Coordinate Transformations and Nonlinear Dynamics*, presented at USPAS Accelerator Physics 2017, University of California, Davis, 2017, [Online]. Available: `http://toddsatogata.net/2017-USPAS/Lectures/NonlinearDynamics.pdf` (visited on 05/05/2022).

[201] G. Guignard, “A general treatment of resonances in accelerators,” in *Proc. of CERN Academic Training Lectures*, (Geneva, Switzerland), CERN, Geneva, 1977 - 1978, CERN, Geneva: CERN, 1978, DOI: `10.5170/CERN-1978-011`.

Index